SEARCH FOR THE DECAY $K_L \rightarrow \pi^0 \gamma\gamma$

BY

VAIA PAPADIMITRIOU

DECEMBER 1990

THE UNIVERSITY OF CHICAGO

SEARCH FOR THE DECAY $K_L \rightarrow \pi^0 \gamma\gamma$

A DISSERTATION SUBMITTED TO
THE FACULTY OF THE DIVISION OF PHYSICAL SCIENCES
IN CANDIDACY FOR THE DEGREE OF
DOCTOR OF PHILOSOPHY

DEPARTMENT OF PHYSICS

BY VAIA PAPADIMITRIOU

CHICAGO, ILLINOIS
DECEMBER 1990

PPB2272

ACKNOWLEDGEMENTS

I would like first to express my gratitude to my advisor, Roland Winston, for supervising my education throughout these years and for his very helpful guidance and continuous encouragement all along the way.

I owe special thanks to Bruce Winstein for several important and insightful suggestions regarding this analysis. I learned a lot from Hitoshi Yamamoto and I greatly appreciate the many discussions with him regarding the work reported here. Many thanks go also to Taku Yamanaka who played a key role in the many Monte Carlo generations needed for this analysis. I would like to especially thank Yau Wah who guided me when I first joined this group and with whom I worked in the Cluster Finder project.

I have enjoyed working and learning together with my fellow students Lawrence Gibbons, Magnus Karlsson and Ritchie Patterson and have benefitted from the specific experience of all of them. Their careful work in their individual projects was very crucial to the success of the experiment.

I appreciate stimulating discussions and useful suggestions from Bob Hsiung, Tony Barker, Sunil Somalwar and Roy Briere.

It was a pleasure to work with G. Makoff and M. Woods (from Chicago), E. Swallow (from Elmhurst), G. J. Bock, R. Coleman, J. Enagonio, K. Stanfield and R. Stefanski (from Fermilab), G. Blair, G. D. Gollin, J. K. Okamitsu and R. Tschirhart (from Princeton), J. C. Brisson, P. Debu, B. Peyaud, R. Turlay and B. Vallage (from Saclay). Their efforts contributed greatly to the success of this experiment.

Finally, I wish to thank my parents for their unlimited encouragement and moral support throughout these years.

TABLE OF CONTENTS

	page
ACKNOWLEDGEMENTS	ii
LIST OF ILLUSTRATIONS	vii
LIST OF TABLES	xix
ABSTRACT	xxii

Chapter

1. INTRODUCTION	**1**
1.1 Discussion of the Theory	2
1.1.1 Historical Overview	3
1.1.2 Current theoretical interest	5
1.2 Experimental status of the $K_L \rightarrow \pi^0\gamma\gamma$ decay before the current search	18
2. THE EXPERIMENT	**20**
2.1 Principles of the measurement	20
2.2 Beamline	21
2.3 The Detector and its calibration	25
2.3.1 The charged particle spectrometer	25
2.3.2 The calorimeter	34
2.3.3 The background rejection anticounters	41
3. THE CLUSTER FINDER TRIGGER PROCESSOR	**51**
3.1 Overview	51
3.2 Description	53

3.2.1 The front end electronics 53
3.2.2 The Cluster Boards 55
3.2.3 The control cards 58
3.2.4 The CAMAC interface 67
3.3 Operation 68
3.4 Results 71

4. TRIGGER DESCRIPTION 76
4.1 Trigger logic 76
4.2 Running conditions 82
4.3 Information recorded for every event and electronic readout 88
4.4 Cluster Finder external logic 90
4.5 Special runs 91

5. DATA RECONSTRUCTION - DATA REDUCTION . . . 96
5.1 Event reconstruction 96
5.1.1 Photon measurements 97
5.1.2 Decay kinematics 99
5.2 Data reduction 101
5.3 Data Summary Tapes 114

6. BACKGROUND REJECTION - HIGHER LEVEL ANALYSIS 116
6.1 Background from $K_L \rightarrow \pi^+\pi^-\pi^0$ 116
6.2 Background from $K_L \rightarrow 2\pi^0$ 118
6.3 Background from $K_L \rightarrow 3\pi^0$ 123
6.3.1 Photon veto cuts 124
6.3.2 z decay vertex cut 126
6.3.3 Center of energy cut 126
6.3.4 Fusion cuts 128
6.3.5 Further "double fusion" rejection 148

6.4 Background from accidentals 150
6.5 Other backgrounds 155
6.6 Summary of all cuts 156

7. MONTE CARLO 167
7.1 Event generation 168
7.1.1 Beam simulation 168
7.1.2 Detector simulation 172
7.1.3 Cluster simulation 179
7.1.4 ADC simulation 183
7.1.5 HCF simulation 183
7.1.6 Photon conversion, Bremsstrahlung, Multiple scattering 183
7.2 Signal Monte Carlo 184
7.2.1 Data-Monte Carlo comparison for signal . . . 184
7.2.2 Acceptance determination 193
7.3 Background Monte Carlo 203
7.3.1 The standard $3\pi^0$ background Monte Carlo . . . 203
7.3.2 Complementary $3\pi^0$ background Monte Carlos . 222
7.4 Data-Monte Carlo comparisons for $\pi^0\gamma\gamma$ candidates . . 230

8. SYSTEMATIC ERROR DETERMINATION 235
8.1 Overview 235
8.2 Photon veto adjustment and systematic error 236
8.3 Systematic error due to fusions 247
8.4 Systematic error due to energy resolution 248
8.5 Systematic error due to the lead Mask cut 254
8.6 Summary of systematics 256

9. UPPER LIMIT CALCULATION FROM THE 20% OF THE DATA 259
9.1 Upper limit using the CHPT model 259
9.2 Upper limit using the phase space hypothesis 264

10. UPDATE FROM THE FULL DATA SET 266
10.1 Overview 266
10.2 Data-Monte Carlo comparisons 270
10.3 Calculation of the branching ratio for the $K_L \rightarrow \pi^0\gamma\gamma$ decay 277
10.4 Summary - Conclusions 280

REFERENCES 283

LIST OF ILLUSTRATIONS

Figure page

1. Diagrams showing η-pole dominance for the $K_2 \rightarrow \pi^0\gamma\gamma$ and $K_2 \rightarrow \gamma\gamma$ decays 4
2. Baryon-antibaryon intermediate state diagram for the $K^0 \rightarrow \pi^0\gamma\gamma$ decay 4
3. Pion loop diagrams for the $K_2 \rightarrow \pi^0\gamma\gamma$ decay 6
4. $K_2 \rightarrow \pi^0\gamma\gamma$ contribution to the $K_2 \rightarrow \pi^0 e^+e^-$ decay 7
5. One-loop diagrams for the $K^0 \rightarrow \pi^0\gamma\gamma$ decay 11
6. $\gamma\gamma$ invariant mass spectrum for the $K_L \rightarrow \pi^0\gamma\gamma$ decay calculated on the basis of CHPT 12
7. $\gamma\gamma$ invariant mass distribution for the $K_L \rightarrow \pi^0\gamma\gamma$ decay produced from a Monte Carlo using the phase space hypothesis 12
8. $\gamma\gamma$ invariant mass spectrum for the $K_L \rightarrow \pi^0\gamma\gamma$ decay calculated on the basis of the pion rescattering model (taken from Reference [20]) 14
9. Vector meson dominance diagram for the $K_2 \rightarrow \pi^0\gamma\gamma$ decay . 15
10. $\gamma\gamma$ invariant mass squared spectrum for the $K_L \rightarrow \pi^0\gamma\gamma$ decay calculated on the basis of the VMD model (taken from Reference [24]) 16
11. $\gamma\gamma$ invariant mass squared spectrum for the $K_L \rightarrow \pi^0\gamma\gamma$ decay calculated on the basis of a combination of pion loop and VMD models (taken from Reference [24]) 17
12. The target and collimators 23

LIST OF ILLUSTRATIONS -- (continued)

13. The decay volume and detector 24
14. Side view of the regenerator 25
15. V and T scintillator banks and DRAC and DRAN photon veto counters 29
16. Side view of V and T bank and the Pb converter 30
17. Cell geometry of drift chamber wires 31
18. Beam view of the C Bank 32
19. Beam view of the B Bank 33
20. The lead glass electromagnetic calorimeter 35
21. A lead glass block with its optical fiber and its read out system 36
22. Beam view of the Mu1 Bank 39
23. Distribution of the gains and resolutions of the adders from one calibration file 42
24. Beam view and side view of AM 44
25. Cross-section of a VA counter 45
26. Beam view of theVacuum-antis 46
27. Beam view of the MA and LGA photon veto counters . . . 47
28. Beam view and side view of the Collar-anti photon veto . . 48
29. One of the three units of the Back-anti photon veto 49
30. An on-line event display of energy deposited in the lead glass array for a four-cluster event 52
31. General hardware layout of the Cluster Finder trigger processor 54
32. Relationship of the six cells of an EPLD between themselves and with cells of neighbor EPLDs 57
33. The algorithm with which two cells of an EPLD (odd1 and even1) belonging to column 1 and to the odd and even row respectively operate 60
34. Illustration of synchronization between CAMAC and the trigger processor 70

35. Distribution of the number of software clusters without the Cluster Finder in the trigger 72
36. Distribution of the number of hardware clusters with the Cluster Finder in the trigger 72
37. Energy distribution of lead glass blocks above the Cluster Finder threshold 73
38. Cluster Finder thresholds for each one of the 804 lead glass blocks in ADC counts 74
39. Cluster Finder resolutions in ADC counts for each one of the 804 lead glass blocks 74
40. Data taking "running modes" from the beginning of August of 1987 till the end of November of 1987 85
41. Data taking "running modes" from the beginning of December of 1987 till the 15th of February of 1988 86
42. Cluster Finder external logic 92
43. z decay vertex distribution for $K \rightarrow \pi^0\gamma\gamma$ candidates at a very early analysis stage 102
44. z decay vertex distribution for $K \rightarrow \pi^0\gamma\gamma$ candidates at the data reduction stage in the region upstream of 140 m . 104
45. m_{π^0} distribution for $K \rightarrow \pi^0\gamma\gamma$ candidates at the data reduction stage in the region upstream of 140 m 105
46. $m_{\gamma\gamma}$ distribution for $K \rightarrow \pi^0\gamma\gamma$ candidates at the data reduction stage, in the region upstream of 140 m 106
47. An example of a fused cluster from $3\pi^0$ background Monte Carlo 108
48. m_{π^0} distribution for $K \rightarrow \pi^0\gamma\gamma$ candidates at the data reduction stage after all the cuts have been applied . . . 109
49 $m_{\gamma\gamma}$ distribution for $K \rightarrow \pi^0\gamma\gamma$ candidates at the data reduction stage after all the cuts have been applied . . . 110

50. z decay vertex distribution for $K \rightarrow \pi^0\gamma\gamma$ candidates at the data reduction stage after all the cuts have been applied 111
51. Illustration of $2\pi^0$'s from a $K_L \rightarrow 3\pi^0$ decay getting superimposed 112
52. Photon pairings for the reconstruction of the z decay vertex in the $K \rightarrow 2\pi^0$ decay 120
53. Best χ^2 versus reconstructed kaon mass for $K_L \rightarrow 2\pi^0$ decays 121
54. m_{π^0} distribution for $K_S \rightarrow 2\pi^0$ decays starting from the assumption that the decay originates from a kaon 122
55. $m_{\gamma\gamma}$ distribution for $K_S \rightarrow 2\pi^0$ decays starting from the assumption that the decay originates from a kaon 122
56. Disallowed topologies for cluster centers at the edges of the array 125
57. Center of energy distribution for $K_L \rightarrow 3\pi^0$ decays satisfying the "four-cluster" trigger requirement 127
58. The 16 block ring outside the 3 x 3 blocks belonging to each cluster, on which fusion algorithm 1 operates . . . 129
59. Maximum energy in two consecutive blocks in the 16 block ring surrounding the blocks belonging to the cluster versus the cluster energy for $K_S \rightarrow 2\pi^0$ decays 130
60. Maximum energy in two consecutive blocks in the 16 block ring surrounding the blocks belonging to the cluster versus the cluster energy for $K_L \rightarrow \pi^0\gamma\gamma$ candidates 131
61. Example of a fused cluster from $3\pi^0$ background Monte Carlo 132
62. Rows and columns within a cluster on which fusion algorithm 2 operates 132

63. Valmax, as explained in the text, for each cluster versus the cluster energy for $K_S \rightarrow 2\pi^0$ decays 134
64. Valmax, as explained in the text, for each cluster versus the cluster energy for $K_L \rightarrow \pi^0\gamma\gamma$ candidates . . . 135
65. Corner and side blocks on which fusion algorithm 3 operates 136
66. The minimum ratio for the energy of a side block to the energy of a corner block among all corner blocks of a cluster versus the energy of the corner block for $K_S \rightarrow 2\pi^0$ events 137
67. The minimum ratio for the energy of a side block over the energy of a corner block among all corner blocks of a cluster versus the energy of the corner block for $K_L \rightarrow \pi^0\gamma\gamma$ candidates 138
68. Distribution of the energy in ADC counts of the block with the maximum energy within an "in time" adder, as described in the text, for $K_S \rightarrow 2\pi^0$ decays 139
69. Distribution of the energy in ADC counts of the block with the maximum energy within an "in time" adder, as described in the text, for $K_L \rightarrow \pi^0\gamma\gamma$ candidates 140
70. Nine lead glass blocks belonging to a cluster 141
71. Rtopmid versus Rmaxcen, as defined in the text, for $K_S \rightarrow 2\pi^0$ decays 142
72. Rtopmid versus Rmaxcen, as defined in the text, for $K_L \rightarrow \pi^0\gamma\gamma$ candidates 143
73. Rlefmid versus Rmidmid, as defined in the text, for $K_S \rightarrow 2\pi^0$ decays 144
74. Rlefmid versus Rmidmid, as defined in the text, for $K_L \rightarrow \pi^0\gamma\gamma$ candidates 145

75. Rbotmid versus Rmincen, as defined in the text, for $K_S \rightarrow 2\pi^0$ decays 146
76. Rbotmid versus Rmincen, as defined in the text, for $K_L \rightarrow \pi^0\gamma\gamma$ candidates 147
77. Overlapping clusters in a "double fusion" event from $3\pi^0$ background 149
78. Energy distributions of photons belonging to the same π^0 from $K_L \rightarrow \pi^0\gamma\gamma$ events with $m_{\gamma\gamma}$ greater than about 270 MeV 151
79. Energy in the lead glass calorimeter outside the 5 x 5 block area belonging to each cluster for $K_L \rightarrow \pi^0\gamma\gamma$ candidates from the "chg/n, neutral" running mode . . . 153
80. Energy in the lead glass calorimeter outside the 5 x 5 block area belonging to each cluster for $K_L \rightarrow \pi^0\gamma\gamma$ candidates from the "neutral" running mode 153
81. Adder ratio distribution for $K_L \rightarrow \pi^0\gamma\gamma$ candidates after stage 20 154
82. Adder ratio distribution for accidental events 154
83. Total energy distribution for $\pi^0\gamma\gamma$ candidates 158
84. Distribution of the difference between the invariant mass distribution of the two photons in the $K_L \rightarrow \pi^+\pi^-\pi^0$ decay and the nominal π^0 mass 160
85. z decay vertex distribution for $K_L \rightarrow \pi^0\gamma\gamma$ candidate events after stage 11 162
86. π^0 invariant mass for $K_L \rightarrow \pi^0\gamma\gamma$ candidates after stage 11 . 163
87. $\gamma\gamma$ invariant mass for $K_L \rightarrow \pi^0\gamma\gamma$ candidates after stage 11 . 163
88. Distribution of the energy of the maximum energy cluster for $K_L \rightarrow \pi^0\gamma\gamma$ candidates 164
89. $\gamma\gamma$ invariant mass for $K_L \rightarrow \pi^0\gamma\gamma$ candidates after all the non kinematics related fusion cuts 165

90. $\gamma\gamma$ invariant mass for $K_L \rightarrow \pi^0\gamma\gamma$ candidates after the kinematics related double fusion rejection cut 165
91. π^0 invariant mass distribution for $K_L \rightarrow \pi^0\gamma\gamma$ candidates after all cuts 166
92. $\gamma\gamma$ invariant mass for $K_L \rightarrow \pi^0\gamma\gamma$ candidates after all cuts . 166
93. Monte Carlo energy distributions of photons hitting the most upstream photon veto counters 173
94. Monte Carlo energy distributions of photons hitting the Collar-anti and Back-anti veto counters 175
95. Detection efficiency for the Sweeper-anti photon veto as a function of photon energy 177
96. Photon probability for hitting the vacuum pipe outside the VA2 photon veto and depositing there more than 0.1 MeV of energy 178
97. Energy distribution of electrons and positrons taken from calibration data and used for the cluster library . . 181
98. Data-Monte Carlo comparison for the z decay vertex distribution for $K_L \rightarrow 3\pi^0$ decays 185
99. Kaon energy distribution for $K_L \rightarrow 3\pi^0$ decays 186
100. Cluster energy distribution for $K_L \rightarrow 3\pi^0$ decays 187
101. Photon illumination at the lead Mask, x view 188
102. Photon illumination at the lead Mask, y view 188
103. Photon illumination at the HDRA, x view 189
104. Photon illumination at the HDRA, y view 189
105. Photon illumination at the lead glass, x view 190
106. Photon illumination at the lead glass, y view 190
107. Distribution of the distance between clusters for $K_L \rightarrow 3\pi^0$ decays 191
108. z decay vertex distribution for $K_L \rightarrow 2\pi^0$ decays 192
109. Distribution of the best χ^2 variable for $K_L \rightarrow 2\pi^0$ decays . . 192

110. Kaon energy distribution for $K_L \rightarrow 2\pi^0$ decays 194
111. Cluster energy distribution for $K_L \rightarrow 2\pi^0$ decays 194
112. Data-Monte Carlo comparison in $K_S \rightarrow 2\pi^0$ decays for the maximum energy, "maxsum", in two consecutive blocks of the 16 block ring surrounding the cluster . . . 195
113. Data-Monte Carlo comparison for "maxsum" in $K_S \rightarrow 2\pi^0$ decays for certain cluster energy range 196
114. Data- Monte Carlo comparison for "valmax", as explained in the text, for $K_S \rightarrow 2\pi^0$ decays 197
115. Data-Monte Carlo comparison for the minimum ratio of the energy of a side block to the energy of a corner block among all corner blocks of a cluster for $K_S \rightarrow 2\pi^0$ decays . 198
116. z decay vertex distribution for $K_L \rightarrow \pi^0\gamma\gamma$ Monte Carlo events using the CHPT model 199
117. π^0 invariant mass for $K_L \rightarrow \pi^0\gamma\gamma$ Monte Carlo events after all the analysis cuts except the m_{π^0} cut 200
118. $\gamma\gamma$ invariant mass for $K_L \rightarrow \pi^0\gamma\gamma$ Monte Carlo events after all the analysis cuts 200
119. $\gamma\gamma$ invariant mass for $K_L \rightarrow \pi^0\gamma\gamma$ Monte Carlo events requiring that the reconstructed π^0 is also the true π^0 . . 201
120. $\gamma\gamma$ invariant mass after all the analysis cuts for $K_L \rightarrow \pi^0\gamma\gamma$ Monte Carlo using the phase space assumption 202
121. Acceptance versus the $\gamma\gamma$ invariant mass for $K_L \rightarrow \pi^0\gamma\gamma$ decays 203
122. Difference between the reconstructed and generated decay vertex for $K_L \rightarrow 3\pi^0$ background Monte Carlo decays . . . 206
123. Fraction of events with zero, one and two missing photons as a function of the reconstructed z decay vertex from $K_L \rightarrow 3\pi^0$ background Monte Carlo decays 207

124. $\gamma\gamma$ invariant mass after all cuts from $K_L \rightarrow 3\pi^0$ background Monte Carlo events 208
125. Illustration of a $3\pi^0$ background event with two fused clusters 210
126. Illustration of three photons overlapping in a single cluster in a $3\pi^0$ background event 211
127. $\gamma\gamma$ invariant mass after all cuts from $K_L \rightarrow 3\pi^0$ background Monte Carlo events with no missing photons 212
128. Distance between photons in fused clusters from $3\pi^0$ background decays after all the $\pi^0\gamma\gamma$ analysis cuts 213
129. Illumination of photons that belong to fused clusters at the lead glass array from $3\pi^0$ background decays after all the $\pi^0\gamma\gamma$ analysis cuts 214
130. Data-Monte Carlo comparison between $K_L \rightarrow \pi^0\gamma\gamma$ candidates and $3\pi^0$ background events for the maximum energy, "maxsum", in two consecutive blocks of the 16 block ring surrounding the cluster 215
131. Data-Monte Carlo comparison for "maxsum" between $K_L \rightarrow \pi^0\gamma\gamma$ candidates and $3\pi^0$ background Monte Carlo for certain cluster energy range 216
132. Data-Monte Carlo comparison for "valmax", as explained in the text, between $K_L \rightarrow \pi^0\gamma\gamma$ candidates and $3\pi^0$ background Monte Carlo 217
133. Data-Monte Carlo comparison between $K_L \rightarrow \pi^0\gamma\gamma$ candidates and $3\pi^0$ background Monte Carlo for the minimum ratio of the energy of a side block to the energy of a corner block among all corner blocks of a cluster 218
134. Data-Monte Carlo comparison between $K_L \rightarrow \pi^0\gamma\gamma$ candidates and $3\pi^0$ background Monte Carlo for the variable 9/25 . . 219

135. The four photon invariant mass distribution for $K_L \rightarrow 2\pi^0$ events 220
136. 90% c.l. upper limit based on $3\pi^0$ and $2\pi^0$ background . . 221
137. z decay vertex distribution for events with at least one photon hitting the SA, outside the lead Mask, the lead Mask and VA1 223
138. z decay vertex distribution for events with at least one photon hitting the VA2, the HDRA, VA3 and VA4 224
139. z decay vertex distribution for events with at least one photon hitting MA and LGA 225
140. $\gamma\gamma$ invariant mass distribution for $K_L \rightarrow 3\pi^0$ background Monte Carlo events with at least one photon hitting the SA veto system 226
141. $\gamma\gamma$ mass distribution for events with at least one photon hitting outside the lead Mask and the lead Mask 227
142. $\gamma\gamma$ mass distribution for events with at least one photon hitting VA2 and the HDRA 228
143. Generated z decay vertex versus generated energy for $K_L \rightarrow 3\pi^0$ background Monte Carlo events 229
144. Generated z decay vertex versus generated energy and reconstructed z decay vertex from $3\pi^0$ background Monte Carlo 231
145. Data-Monte Carlo comparison for the z decay vertex distribution for $\pi^0\gamma\gamma$ candidates and background events from the 20% of the data 232
146. Data-Monte Carlo comparison for the $\gamma\gamma$ mass distribution for $\pi^0\gamma\gamma$ candidates and background events from the 20% of the data 233
147. Data-Monte Carlo comparison for the z decay vertex distribution for $\pi^0\gamma\gamma$ candidates and background events from

the 20% of the data and before any photon veto adjustment . 237

148. Chi-square for the z vertex distribution as a function of the change of rejection efficiency for photons projecting outside the lead Mask for 10% and 20% reduction to the VA1 and VA2 cuts 240

149. Chi-square for the z vertex distribution as a function of the change of rejection efficiency for photons projecting outside the lead Mask for 30% and 40% reduction to the VA1 and VA2 cuts 241

150. Chi-square minima in the plane of rejection efficiency change of photons projecting outside the lead Mask and rejection efficiency change for the VA1 and VA2 photon vetoes. The squares indicate points with chi-squares about 1σ higher than the minima, the open circle the final choice of our cuts and the "+"s the points across which the systematic was finally calculated. 242

151. Chi-square minima in the plane of rejection efficiency change of photons projecting outside the lead Mask and rejection efficiency change for the VA1 and VA2 photon vetoes. The "+"s correspond to the points across which the systematic was finally calculated. The numbers next to all the points indicate the number of events for $m_{\gamma\gamma} \geq 0.300$ GeV and the ones in parentheses the corresponding number for a broader mass region. 244

152. $\gamma\gamma$ invariant mass distribution 249

153. Data-Monte Carlo comparison for the best χ^2 distribution for $K_L \rightarrow 2\pi^0$ decays and for different resolution smearings . 252

154. Likelihood function as a function of added events per bin in the $m_{\gamma\gamma}$ distribution 255

155. m_{π^0} distribution of $K_L \rightarrow \pi^0\gamma\gamma$ candidates that are rejected by the lead Mask cut after all other cuts 257

156. $m_{\pi}0$ distribution of $K_L \rightarrow \pi^0\gamma\gamma$ candidates that are rejected by the lead Mask cut after photon veto and some of the fusion cuts 257

157. Kaon mass distribution for $K_L \rightarrow 2\pi^0$ decays after similar cuts with the $\pi^0\gamma\gamma$ analysis and in the decay region 110-128 m 261

158. Data-Monte Carlo comparison for the $\gamma\gamma$ mass distribution between $\pi^0\gamma\gamma$ candidates and background events based on the full data set 272

159. Data-Monte Carlo comparison for the z decay vertex distribution between $\pi^0\gamma\gamma$ candidates and background events for the whole $\gamma\gamma$ mass region 273

160. Data-Monte Carlo comparison for the z decay vertex distribution between $\pi^0\gamma\gamma$ candidates and background events for the high $\gamma\gamma$ mass region 274

161. Data-Monte Carlo comparison for the m_{π^0} distribution between $\pi^0\gamma\gamma$ candidates and $3\pi^0$ and $2\pi^0$ background events in the range $0.264 \text{ GeV} < m_{\gamma\gamma} < 0.280 \text{ GeV}$ 275

162. Data-Monte Carlo comparison for the m_{π^0} distribution between $\pi^0\gamma\gamma$ candidates and background events for the high $\gamma\gamma$ mass region 276

163. Data-Monte Carlo comparison for the m_{π^0} distribution between $\pi^0\gamma\gamma$ candidates and background events plus $\pi^0\gamma\gamma$ signal Monte Carlo, for $m_{\gamma\gamma} \geq 0.280 \text{ GeV}$ 279

LIST OF TABLES

Table page

1. Positions and dimensions of the detector elements 26
2. Radiation and interaction lengths of detector elements . . 28
3. Instructions in the main sequence 61
4. Instructions for testing purposes and for special service in the system 62
5. Instructions controlling the loading of data, address and PROM address from CAMAC to System Controller. . . . 68
6. Instructions controlling the reading of data, address and PROM address latched at System Controller to CAMAC. . 69
7. Prescale factors of different trigger types 84
8. Trigger composition of spill in "chg, neutral" running mode 84
9. Trigger composition of spill in "neutral" running mode . 87
10. Trigger composition of spill in "chg/n, neutral" running mode 87
11. Information recorded for the energy of the signal in the counter banks 89
12. "Dead time" of the experiment for various running conditions 90
13. Effect of software cluster finding on the number of hardware clusters 98
14. Probability for the presence of one or two accidental clusters at the lead glass array, as a function of the $\pi^0\gamma\gamma$ analysis cuts 155

LIST OF TABLES -- (continued)

15. The effect of cuts (applied in series) on the sample of $\pi^0\gamma\gamma$ candidates 157
16. Parameter values in Malensek's formula 169
17. Photon veto efficiencies 176
18. Percentages of events with zero, one and two missing photons in different $m_{\gamma\gamma}$ regions from $K_L \to 3\pi^0$ background Monte Carlo 209
19. Effect of the change of photon veto gains on the $3\pi^0$ background 246
20. Effect of the change of photon veto resolutions on the $3\pi^0$ background. 246
21. Data-Monte Carlo comparison for the $\gamma\gamma$ invariant mass distribution in the "double fusion" region. The kinematic "double fusion" cut is applied 250
22. Data-Monte Carlo comparison for the $\gamma\gamma$ invariant mass distribution in the "double fusion" region. The kinematic "double fusion" cut has been removed 250
23. Effect of the change of the energy resolution in $3\pi^0$ background Monte Carlo. Only non fused clusters are smeared 253
24. Effect of the change of the energy resolution in $3\pi^0$ background Monte Carlo. All clusters are smeared . . . 253
25. Summary of systematic errors and their effects on the $3\pi^0$ background 258
26. Numbers of $K_L \to \pi^0\gamma\gamma$ and $K_L \to 2\pi^0$ data events in the different running modes of the experiment 267
27. Acceptances for the $K_L \to \pi^0\gamma\gamma$ and $K_L \to 2\pi^0$ decay modes for the different running modes of the experiment 268
28. Normalization factors for the $K_L \to 3\pi^0$ and $K_L \to 2\pi^0$ backgrounds for the different running modes of the

experiment 270

29. Background prediction corresponding to the different running modes of the experiment, for $m_{\gamma\gamma} \geq 0.280$ GeV . 271

30. Background prediction corresponding to the different running modes of the experiment, for $m_{\gamma\gamma} \geq 0.300$ GeV . 271

31. Branching ratio for $m_{\gamma\gamma} \geq 0.280$ GeV and $m_{\gamma\gamma} \geq 0.300$ GeV using the Chiral Perturbation Theory 281

ABSTRACT

The decay $K_L \rightarrow \pi^0\gamma\gamma$ is of interest in the context of both Chiral Perturbation Theory and the VMD model and for its contribution to the decay $K_L \rightarrow \pi^0 e^+e^-$. Using the full data set from Fermilab experiment E731 we report on an observation of the $K_L \rightarrow \pi^0\gamma\gamma$ decay and assuming Chiral Perturbation Theory we have calculated a branching ratio of $(2.2\pm0.7\pm0.8) \times 10^{-6}$ for decays with $\gamma\gamma$ invariant mass above 0.280 GeV. We have also calculated a branching ratio and an upper limit for decays with $\gamma\gamma$ invariant mass above 0.300 GeV.

This work is dedicated to my parents

Δημήτριο and Δέσποινα

CHAPTER 1

INTRODUCTION

Much of our current understanding of the structure of the standard model has been gained from the study of rare decays of the K meson. Rare kaon decays played an important role in the establishment of parity violation and the indirect CP violation, studies of form factors, studies of neutral currents and the prediction of charm. At present, rare kaon decay experiments still remain at the forefront of high precision attempts to better understand the nature of CP violation ($K \rightarrow 2\pi$, $K_L \rightarrow \pi^0 e^+ e^-$, μ polarization in $K_L \rightarrow \mu\mu$), to test the accuracy of the standard model predictions ($K^+ \rightarrow \pi^+ \nu\bar{\nu}$) and to discover new physics beyond the model ($K_L \rightarrow \mu e$, $K^+ \rightarrow \pi^+ \mu^+ e^-$). The rare kaon process that we are going to concentrate on in this thesis is the $K_L \rightarrow \pi^0 \gamma\gamma$ decay which is interesting both by itself, and because of its contribution in the $K_L \rightarrow \pi^0 e^+ e^-$ decay as will become clear below.

1.1 Discussion of the Theory

Before we proceed further we would like to mention some elements of the phenomenology of the neutral kaon system which will be helpful in our discussion.

The strong eigenstates of the neutral kaon are the $|K^0\rangle$ and the $|\overline{K^0}\rangle$ which have strangeness +1 and -1 respectively. $|K^0\rangle$ and $|\overline{K^0}\rangle$ are not eigenstates of the weak Hamiltonian because weak interactions do not conserve strangeness and they can mix these states. By forming linear combinations of them one can construct the CP eigenstates which are known as $|K_1\rangle$ and $|K_2\rangle$.

$$|K_1\rangle = \frac{1}{\sqrt{2}}\left(|K^0\rangle + |\overline{K^0}\rangle\right) \qquad \text{CP=+1}$$

$$|K_2\rangle = \frac{1}{\sqrt{2}}\left(|K^0\rangle - |\overline{K^0}\rangle\right) \qquad \text{CP=-1}$$

If CP were conserved then $|K_1\rangle$ and $|K_2\rangle$ would be physical particles with definite masses and lifetimes. Since CP is not conserved, the real physical particles which are eigenstates of the weak interaction Hamiltonian are the $|K_L\rangle$ and $|K_S\rangle$.

$$|K_L\rangle = \frac{1}{\sqrt{2(1+|\varepsilon|^2}}\left((1+\varepsilon)|K^0\rangle - (1-\varepsilon)|\overline{K^0}\rangle\right)$$

$$|K_S\rangle = \frac{1}{\sqrt{2(1+|\varepsilon|^2}}\left((1+\varepsilon)|K^0\rangle + (1-\varepsilon)|\overline{K^0}\rangle\right)$$

where ε is a small parameter with amplitude $|\varepsilon|=(2.26\pm0.02) \times 10^{-3}$.

1.1.1 Historical Overview

The decay $K_L \rightarrow \pi^0\gamma\gamma$ was of theoretical interest in the late 1960's for several reasons. A major one was that this decay could be a background to the CP violating decay $K_L \rightarrow 2\pi^0$; because it is difficult to experimentally distinguish the two decays, it was desirable to know their relative branching ratio. Another reason was that, as a radiative nonleptonic decay of the K meson, it could help in better understanding of the dynamics of weak nonleptonic processes. Also at that time it was experimentally reported that the decay $\eta \rightarrow \pi^0\gamma\gamma$ had a large branching ratio and this suggested that $K_L \rightarrow \pi^0\gamma\gamma$ might also have a large branching ratio because of the closeness of the masses of the K_L and η mesons [1, 2].

Various attempts were made to estimate $\Gamma(K_L \rightarrow \pi^0\gamma\gamma)$ but most of them were rather qualitative in nature. One of the proposed models [2] assumed that $\Gamma(K_2 \rightarrow \pi^0\gamma\gamma)$ is approximately equal to $\Gamma(K^+ \rightarrow \pi^+\gamma\gamma)$ although there exist diagrams contributing to $K^+ \rightarrow \pi^+\gamma\gamma$ but not to $K_2 \rightarrow \pi^0\gamma\gamma$ decay. Based on that hypothesis, on lifetime measurements for K^+ and K_L and on the value of $\Gamma(K^+ \rightarrow \pi^+\gamma\gamma)/\Gamma(K^+ \rightarrow \text{all})$ that was thought at that time to be 0.4%-1%, one could estimate that $\Gamma(K_2 \rightarrow \pi^0\gamma\gamma)/\Gamma(K_2 \rightarrow \text{all})$ lay in the range $1.7\text{x}10^{-2}$ to $4.2\text{x}10^{-2}$. Using the current value [3] for the above branching ratio which is $B(K^+ \rightarrow \pi^+\gamma\gamma) < 1\text{x}10^{-6}$ one can calculate $B(K_2 \rightarrow \pi^0\gamma\gamma) < 5\text{x}10^{-7}$. Another approach [2] was to use current algebra and PCAC (Partially Conserved Axial Current) theory and relate $\Gamma(K_2 \rightarrow \pi^0\gamma\gamma)$ with $\Gamma(K_1 \rightarrow \gamma\gamma)$ with the "soft pion" method. This approach led to $\Gamma(K_2 \rightarrow \pi^0\gamma\gamma)/\Gamma(K_2 \rightarrow \text{all})$ lying in the range 10^{-6} to $2\text{x}10^{-3}$ and more likely near the lower limit. This big uncertainty was due to the corresponding uncertainty in the theoretical prediction for the $K_1 \rightarrow \gamma\gamma$ branching ratio at the time. Using the current value for this branching ratio we find that $\Gamma(K_2 \rightarrow \pi^0\gamma\gamma)/\Gamma(K_2 \rightarrow \text{all})$ would be approximately equal to $1.5 \text{ x } 10^{-6}$ using the method just described. A third model [2] considered a dominance of

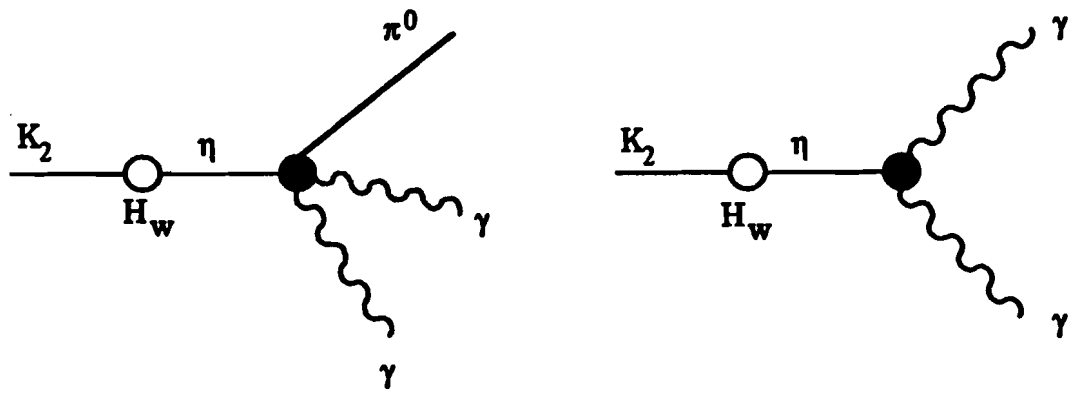

Figure 1. Diagrams showing η-pole dominance for the $K_2 \to \pi^0\gamma\gamma$ and $K_2 \to \gamma\gamma$ decays.

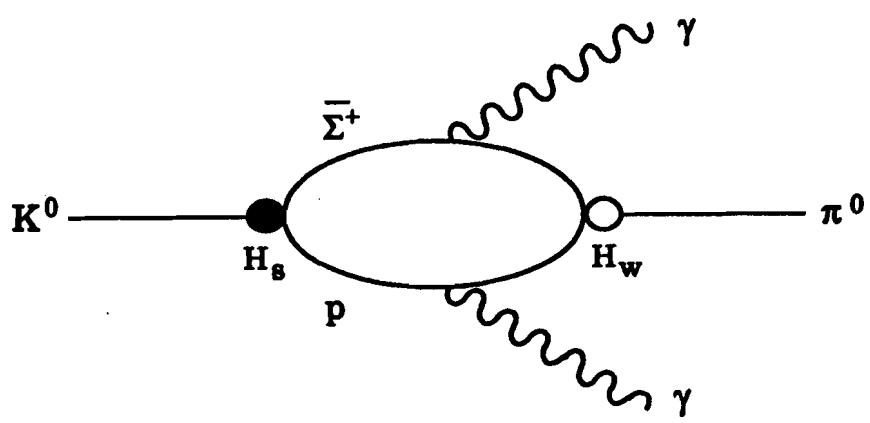

Figure 2. Baryon-antibaryon intermediate state diagram for the $K^0 \to \pi^0\gamma\gamma$ decay. Instead of $p\overline{\Sigma^+}$ one could have also $\Xi^- \overline{\Sigma^-}$ etc.

diagrams such as in Figure 1 assuming that η-pole dominates both $K_2 \rightarrow \pi^0\gamma\gamma$ and $K_2 \rightarrow \gamma\gamma$ and expecting that $\Gamma(K_2 \rightarrow \pi^0\gamma\gamma)/\Gamma(K_2 \rightarrow \gamma\gamma)$ is approximately equal to $\Gamma(\eta \rightarrow \pi^0\gamma\gamma)/\Gamma(\eta \rightarrow \gamma\gamma)$. Using for the above branching ratios the values that were known at the time, $\Gamma(K_2 \rightarrow \pi^0\gamma\gamma)/\Gamma(K_2 \rightarrow \text{all})$ was estimated to be $\sim 0.75\times10^{-3}$. If one uses current values, the branching ratio becomes 1.04×10^{-6}. A fourth model [2] that led to an upper limit for $K_2 \rightarrow \pi^0\gamma\gamma$ considered diagrams with a baryon-antibaryon intermediate state like the one in Figure 2 which led to $\Gamma(K_2 \rightarrow \pi^0\gamma\gamma)/\Gamma(K_2 \rightarrow \text{all}) \sim 5\times10^{-5}$. From most "reasonable" models at that time it seemed that $\Gamma(K_2 \rightarrow \pi^0\gamma\gamma)$ would be rather small relative to $\Gamma(K_2 \rightarrow 2\pi^0)$ but no strong statement could be made about the $\gamma\gamma$ mass spectrum. In 1969 there was set an upper limit [4] of 2.4×10^{-4} for the decay $K_L \rightarrow \pi^0\gamma\gamma$ from a rare kaon decay experiment performed at the Princeton-Pennsylvania Accelerator. In 1972 a "pion loop" model [5] appeared in the literature suggesting the diagrams shown in Figure 3 where the divergence of the first two diagrams exactly cancels the divergence of the third. The branching ratio was calculated to be 6.8×10^{-7} and the differential decay rate as a function of the $\gamma\gamma$ invariant mass squared was rising sharply near $m_{\gamma\gamma}^2 = 4m_{\pi^0}^2$. In the same reference one can also find a model independent lower bound for the decay by using unitarity. The bound is calculated to be 1.45×10^{-8} by considering only $m_{\gamma\gamma} > 346.6$ MeV.

1.1.2 Current theoretical interest

The theoretical and experimental interest for the $K_L \rightarrow \pi^0\gamma\gamma$ decay has been renewed in the last four years for at least three reasons: First, this decay provides an opportunity to test the standard model in the context of chiral symmetry. Second, it provides a CP-conserving intermediate state for the $K_L \rightarrow \pi^0 e^+e^-$ decay which has been the subject of recent experimental [6-8] and theoretical [9] attention as a possible new window

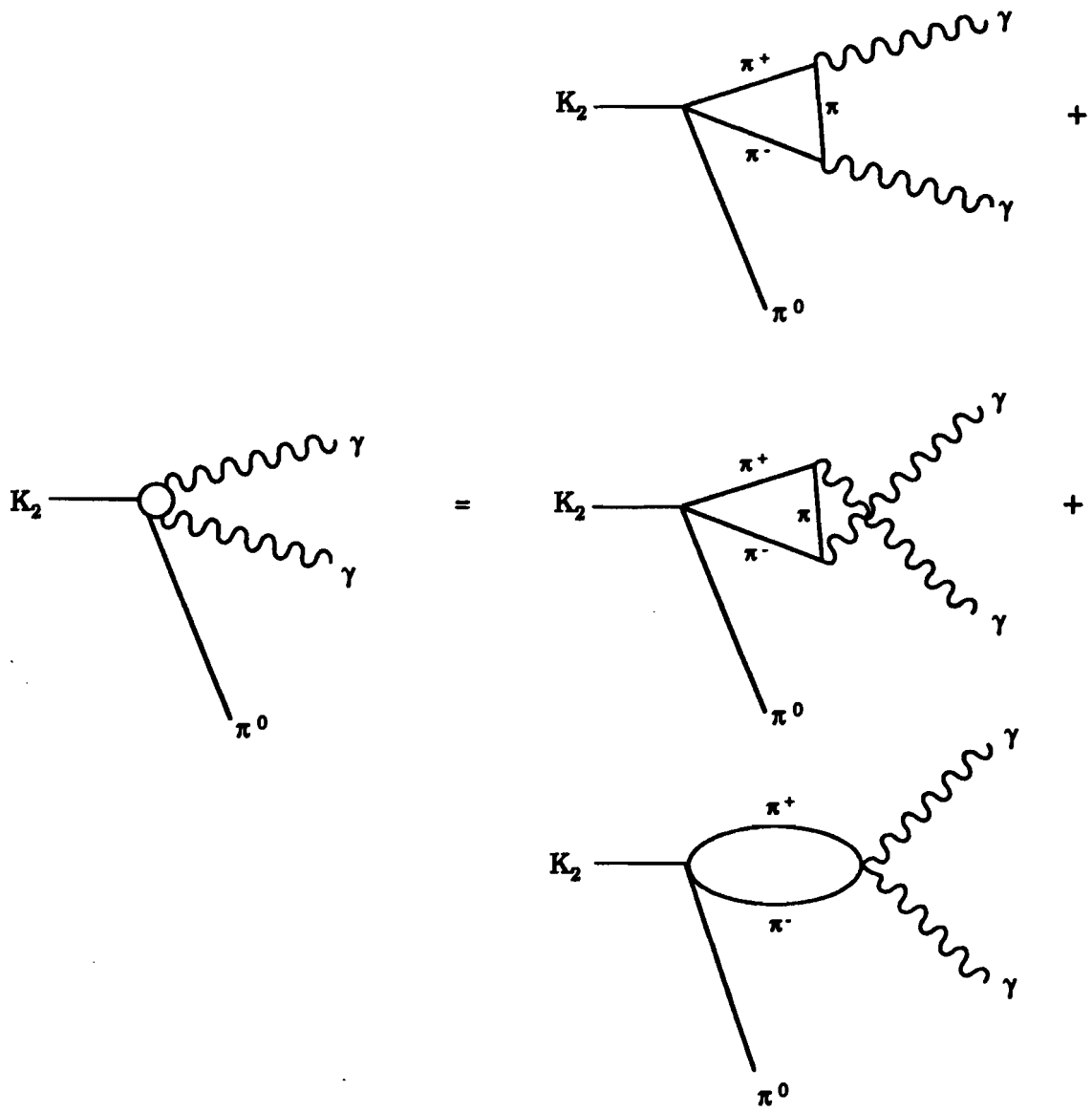

Figure 3. Pion loop diagrams for the $K_2 \rightarrow \pi^0\gamma\gamma$ decay.

to explore direct CP violation. Third, if the branching ratio of this mode were at the level of the upper limit [4, 10] set in 1969 it could be a background to the $K_L \to 2\pi^0$ decay for precision experiments [11, 12] measuring ε'/ε.

As far as the relation between $K_L \to \pi^0\gamma\gamma$ and $K_L \to \pi^0 e^+e^-$ is concerned, $K_L \to \pi^0\gamma\gamma$ contributes to the amplitude of $K_L \to \pi^0 e^+e^-$ as the CP conserving channel whose contribution to the total amplitude is not known exactly and is the subject of theoretical discussions. K_L can be written as $K_L = K_2 + \varepsilon K_1$ where K_2 and K_1 are the CP odd and CP even eigenstates respectively. The $K_L \to \pi^0 e^+e^-$ amplitude has three contributions: a) a CP conserving contribution through an intermediate state of two real or virtual photons. This contribution is of order $O(G_F\alpha^2)$ and one has as shown in Figure 4:

$K_2 \to \pi^0\gamma\gamma \to \pi^0 e^+e^-$

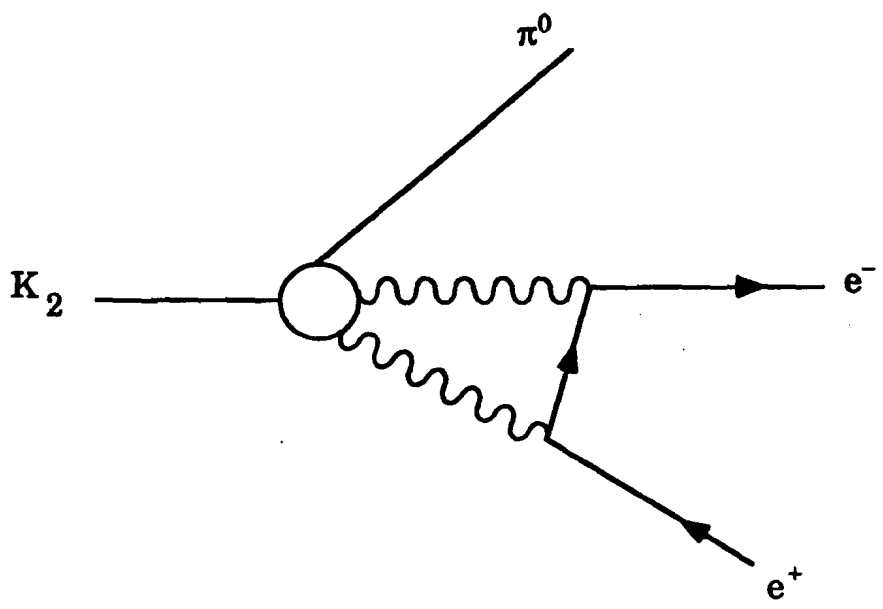

Figure 4. $K_2 \to \pi^0\gamma\gamma$ contribution to the $K_2 \to \pi^0 e^+e^-$ decay.

The branching ratio of $K_L \to \pi^0 e^+ e^-$ based on this amplitude alone would be $\sim 10^{-14}$ according to Chiral Perturbation Theory (CHPT) up to $O(P^4)$ and $\sim 10^{-11}$ according to the Vector Meson Dominance model (VMD) if we want to consider the most extreme theoretical models for the decay $K_L \to \pi^0 \gamma\gamma$; b) a CP violating contribution through the small εK_1 component of K_L where $K_1 \to \pi^0 \gamma^* \to \pi^0 e^+ e^-$. Here CP violation occurs in the mass matrix and the e^+e^- pair comes out of one virtual photon. This amplitude is of order $O(G_F \alpha \varepsilon)$ and the branching ratio based on this amplitude alone is predicted [9] to be $\sim 6 \times 10^{-12}$; c) a CP violating contribution through the large K_2 component of K_L where the e^+e^- pair originates from one virtual photon-"electromagnetic penguin"-, a Z bozon-"Z penguin"- or through a "W box" diagram. In this case CP violation occurs in the decay amplitude and the amplitude is of order $O(G_F \alpha \varepsilon'_{\pi^0 e^+ e^-})$. The branching ratio due to this amplitude alone is predicted [9] to be $\sim 10^{-11}$. It can be easily seen that the decay $K_L \to \pi^0 e^+ e^-$ is expected to have $\varepsilon'_{\pi^0 e^+ e^-}/\varepsilon$ of order 1 in contrast with the $K \to 2\pi$ system where $\varepsilon'_{2\pi}/\varepsilon$ is of order 10^{-3}-10^{-4} and therefore very hard to measure. However in the decay $K_L \to \pi^0 e^+ e^-$ one has to face the problem that the branching ratio is expected to be very small, in the range 0.4×10^{-12}-0.6×10^{-9}. The highest branching ratio, 0.6×10^{-9}, comes from Weinberg's model [13]. Using the $K_L \to \pi^0 e^+ e^-$ process to study direct CP violation which is a very appealing (and may be necessary) avenue one has to untangle the CP conserving and the two CP violating amplitudes. This requires first, measurement of the decay $K_L \to \pi^0 \gamma\gamma$ and study of its Dalitz plot which will help to distinguish between the various theoretical models. Second one would need either to study the interference between $K_L \to \pi^0 e^+ e^-$ and $K_S \to \pi^0 e^+ e^-$ or to measure their branching ratios and study their Dalitz plots.

It would be interesting now to take a closer look at the various theoretical approaches that predict the branching ratio and Dalitz plot distribution of the $K_L \to \pi^0 \gamma\gamma$ decay. Recently this decay has been analyzed

in the framework of CHPT [14, 15] together with other rare kaon decays such as $K_{L,S} \to \gamma\gamma$, $K_{L,S} \to \pi^0 \ell^+ \ell^-$ (ℓ stands for lepton), $K^+ \to \pi^+ \ell^+ \ell^-$ and $K_S \to \pi^0 \gamma\gamma$. CHPT has been used for the systematic determination of the low energy structure of the Green functions in QCD by using massless QCD as the unperturbed system and studying the deviations from chiral symmetry by treating the quark masses as perturbations [16, 17]. It is a nice framework for the study of the $K_L \to \pi^0 \gamma\gamma$ mode because the characteristic momenta are small compared with the natural scale of chiral symmetry breaking which is about 1 GeV and the only hadrons involved are pseudoscalar mesons. In order to calculate in CHPT the various matrix elements of a given operator that are necessary for the evaluation of a decay one makes a correspondance between the operator in the underlying quark-gluon theory and the meson operators that have the same chiral transformation properties in an effective theory [18]. The effective lagrangian in CHPT as in most phenomenological theories involves fields that transform in a well defined way under an internal symmetry group like $SU(3)_L x SU(3)_R$ and consists of a main part that is invariant under the group and of a part that breaks the symmetry. The effective chiral lagrangian used for the study of the decay $K_L \to \pi^0 \gamma\gamma$ has the general form:

$$L_{eff} = L_{str} - F_{\mu\nu} F^{\mu\nu} + L_{em} + \frac{1}{\sqrt{2}} G_F s_1 c_1 c_3 (L_{\Delta S=1} + L^{em}{}_{\Delta S=1})$$

where L_{str} describes the strong interactions among the octet of pseudoscalar mesons, $F_{\mu\nu}$ is the electromagnetic tensor, L_{em} is the hadronic lagrangian in the presence of electromagnetic interactions and $L^{em}{}_{\Delta S=1}$, $L_{\Delta S=1}$ denote the strangeness changing weak interactions with or without electromagnetic interactions respectively. G_F is the Fermi constant and s_1, c_1, c_3 are Cabibbo-Kobayashi-Maskawa matrix elements. One can organize the effective lagrangian in terms of increasing powers of momentum (increasing numbers of derivatives) and terms with small powers of momentum will dominate at low energies . This decay has been calculated to lowest non-trivial order in CHPT including one-loop

contributions which correspond to $O(P^4)$ because to lowest order, $O(P^2)$, the amplitude for non-leptonic radiative K decays with at most one pion in the final state vanishes [19]. The decay amplitude is finite at one loop, hence no counterterms are required. In Reference [15], where the standard basis is used, there are 24 Feynman diagrams corresponding to the decay $K_2^0 \rightarrow \pi^0\gamma\gamma$. In Reference [14] the covariant kinetic and mass terms of order G_F which are quadratic in the pseudoscalar fields are simultaneously diagonalized and in this basis there are no off-diagonal propagators like K-π nor vertices of the type $K\pi\gamma$. The effective lagrangian in this diagonal basis consists of a part that contains the quartic terms in the K and π fields of the $\Delta S=1$ weak lagrangian and of a part that arises from the strong interaction lagrangian. The four Feynman diagrams introduced by the one loop calculation are shown in Figure 5 and the branching ratio is calculated to be [14]

$$\Gamma(K_L \rightarrow \pi^0\gamma\gamma)/\Gamma(K_L \rightarrow \text{all}) = 6.8\text{x}10^{-7} \qquad (1.1)$$

The predicted invariant mass spectrum of the two photons that do not originate from the π^0 is very characteristic and it is shown in Figure 6. The spectrum peaks at about 325 MeV and the distribution is vanishing at low $\gamma\gamma$ masses. In Figure 7 we show for comparison the same spectrum derived from Monte Carlo using the phase space hypothesis. This last spectrum is shown at the generation stage, that is, it is not affected by any experimental acceptance.

The branching ratio given above is calculated by assuming CP invariance for the decay. If one considers CP violation then the K_1 component of the K_L state can induce a CP violating amplitude at the tree level such that

$$A(K_L \rightarrow \pi^0\gamma\gamma)_{tree} = \varepsilon A(K_1 \rightarrow \pi^0\gamma\gamma) \approx \varepsilon A(K_S \rightarrow \pi^0\gamma\gamma) \qquad (1.2)$$

where $|\varepsilon| = (2.26 \pm 0.02) \times 10^{-3}$. At the tree level diagram the two photons originate from a π^0, an η or an η' and in that case the pion pole dominates the total rate for $K_L \rightarrow \pi^0\gamma\gamma$. Of course the $m_{\gamma\gamma}$ region around the nominal

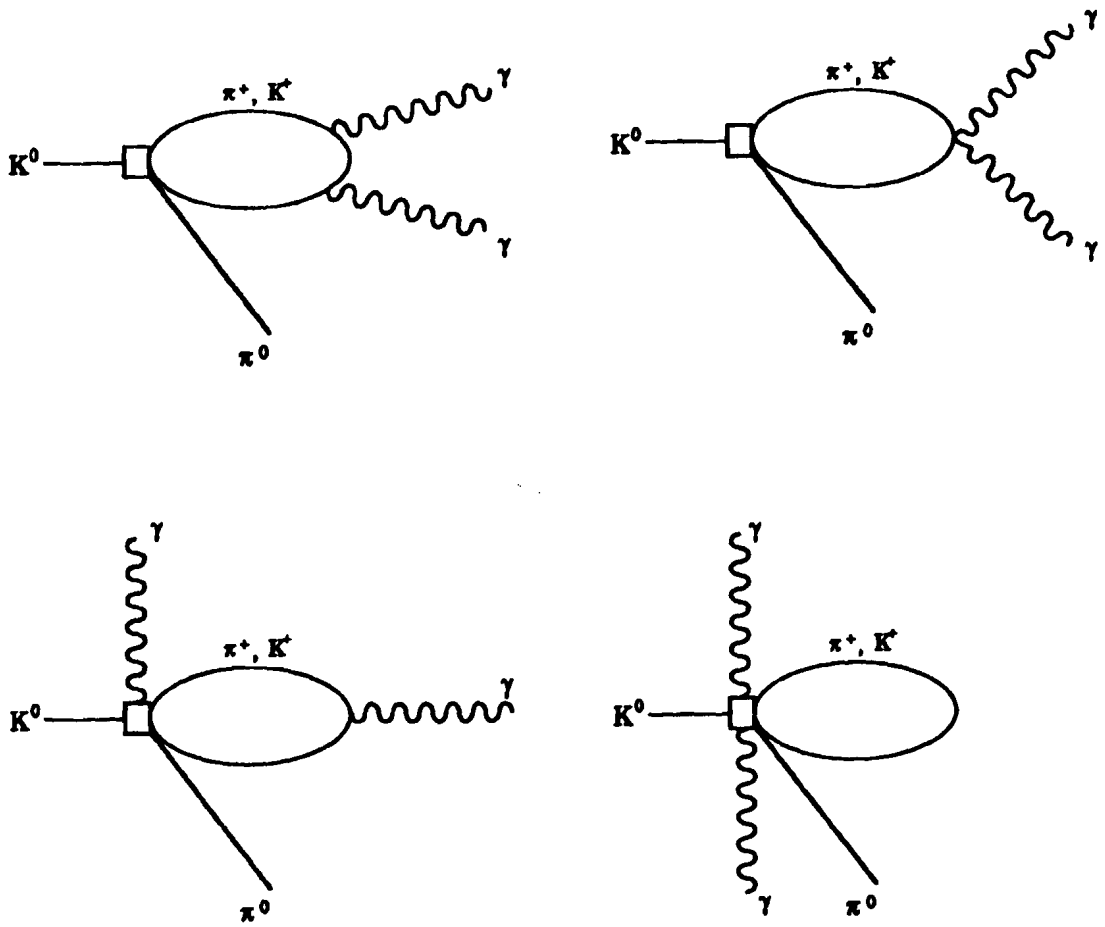

Figure 5. One-loop diagrams for the $K^0 \to \pi^0\gamma\gamma$ decay. The boxes denote weak and weak-electromagnetic vertices given by the effective lagrangian described in the text.

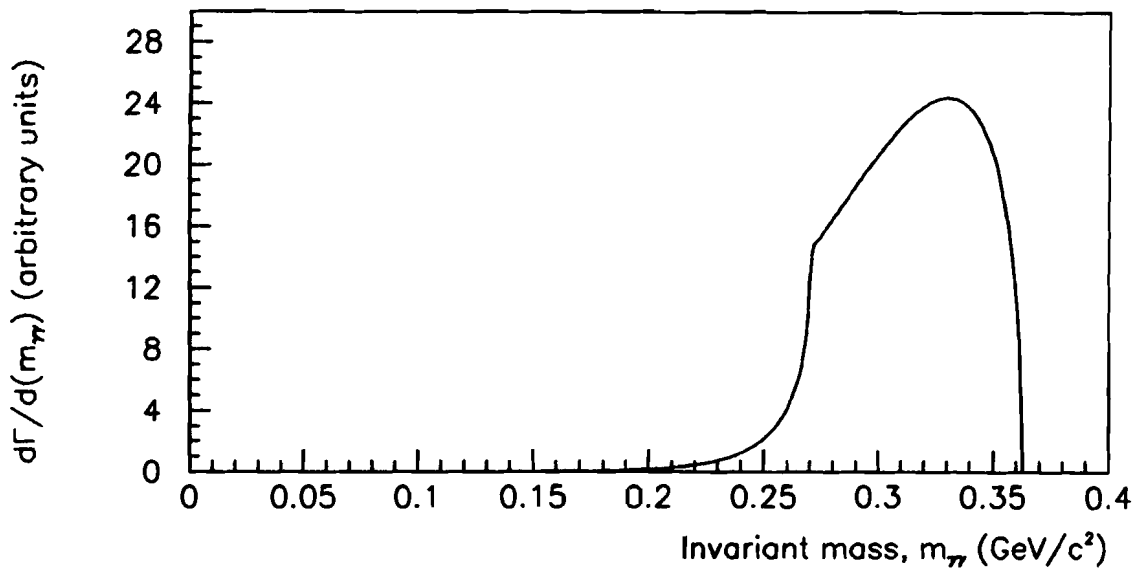

Figure 6. $\gamma\gamma$ invariant mass spectrum for the $K_L \rightarrow \pi^0\gamma\gamma$ decay calculated on the basis of CHPT.

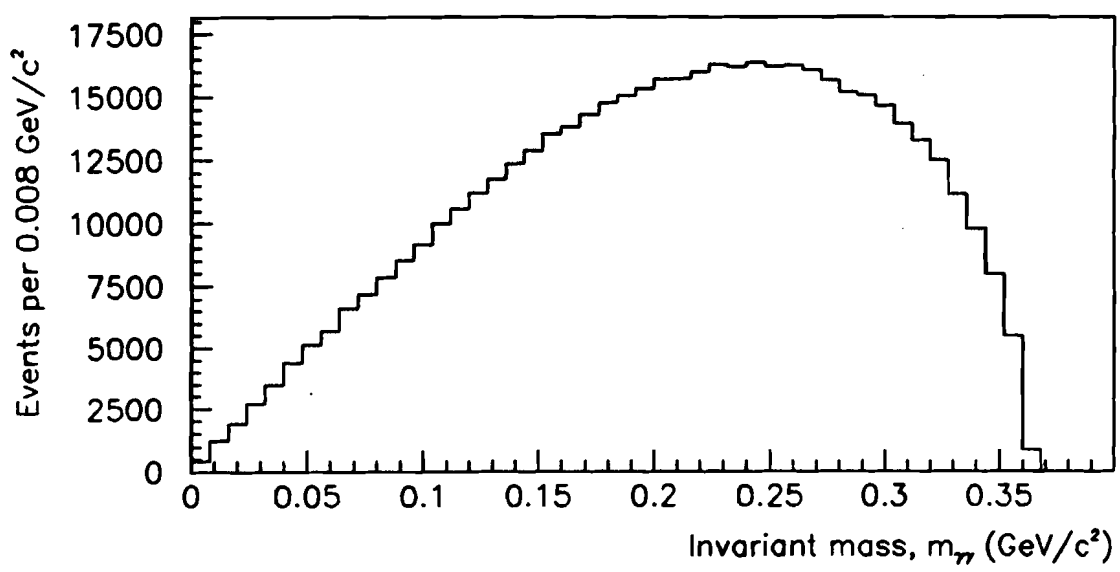

Figure 7. $\gamma\gamma$ invariant mass distribution for the $K_L \rightarrow \pi^0\gamma\gamma$ decay produced from a Monte Carlo using the phase space hypothesis.

π^0 mass is not interesting experimentally because it is dominated by $K_L \to 2\pi^0$ background. However if one considers $m_{\gamma\gamma}$ greater than about 223 MeV,[1] then the amplitude given in Equation (1.2) can be safely neglected: by using the known values of the K_L and K_S lifetimes and the predicted $\Gamma(K_S \to \pi^0\gamma\gamma)/\Gamma(K_S \to \text{all})$ value from CHPT for $m_{\gamma\gamma} \geq 222.6$ MeV which is 3.8×10^{-8} it turns out that the tree amplitude is ~6000 times smaller than the loop amplitude. Therefore one can test the prediction of CHPT for the one loop amplitude by considering only $m_{\gamma\gamma} \geq 222.6$ MeV. In that case the branching ratio is still given by Equation (1.1). To justify why CHPT predicts that the branching ratio of $K_L \to \pi^0 e^+ e^-$ based on the 2γ amplitude alone would be $\sim 10^{-14}$ one should mention that with two real photons there are two possible Lorentz invariant amplitudes that can be formed for $K_L \to \pi^0\gamma\gamma$ up to $O(P^4)$. One corresponds to the S wave configuration of the photon pair and is the coefficient of $F_{\mu\nu}^{(1)}F_{\mu\nu}^{(2)}$. It introduces a factor of m_e (which is very small) when it is contracted with the amplitude for $\gamma\gamma \to e^+e^-$ as a result of helicity conservation and therefore it is strongly suppressed. The other amplitude corresponds to a D wave configuration of the photon pair and it is not proportional to m_e. It is the coefficient of a tensor which contains two more powers of momentum and one expects its contribution to be suppressed by angular momentum barrier factors.

A pion-rescattering model [20] which has similarities with the model described in Reference [5] has been also discussed recently. This model assumes that the decay $K_L \to \pi^0\gamma\gamma$ is dominated by a $\pi^+\pi^-\pi^0$ intermediate state where the charged pions rescatter to two photons. The branching ratio is estimated to be 7.5×10^{-7} and the predicted $m_{\gamma\gamma}$ spectrum is shown in Figure 8. In the same reference the branching ratio of $K_L \to \pi^0\gamma\gamma$ in the CHPT framework is also recalculated to be 6.3×10^{-7}.

The $K_L \to \pi^0\gamma\gamma$ decay has been also looked for recently in the

[1] A cut at $m_{\gamma\gamma} > 223$ MeV makes almost no difference for the behavior of the one loop amplitude as can be seen from Figure 6.

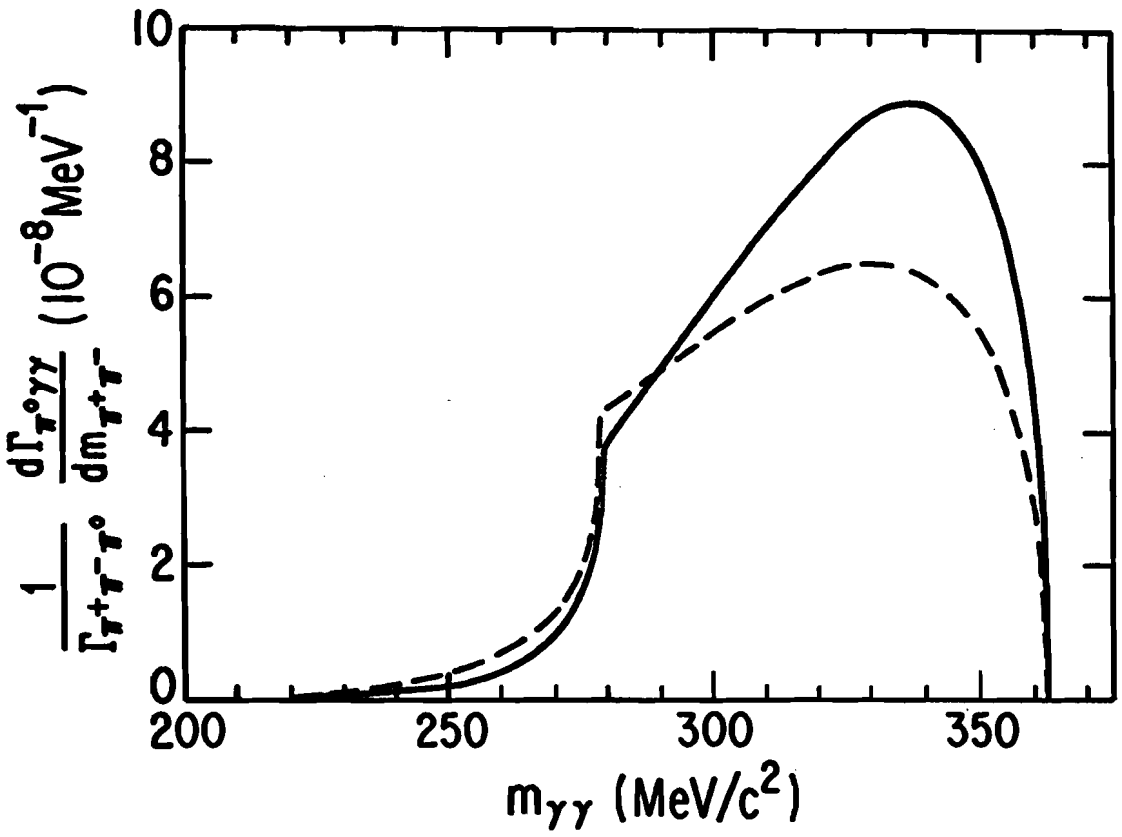

Figure 8. $\gamma\gamma$ invariant mass spectrum for the $K_L \rightarrow \pi^0\gamma\gamma$ decay calculated on the basis of the pion rescattering model (taken from Reference [20]). The spectrum is normalized to the total width for $K_L \rightarrow \pi^+\pi^-\pi^0$. The solid and the dashed lines indicate the pion rescattering model and the CHPT predictions respectively.

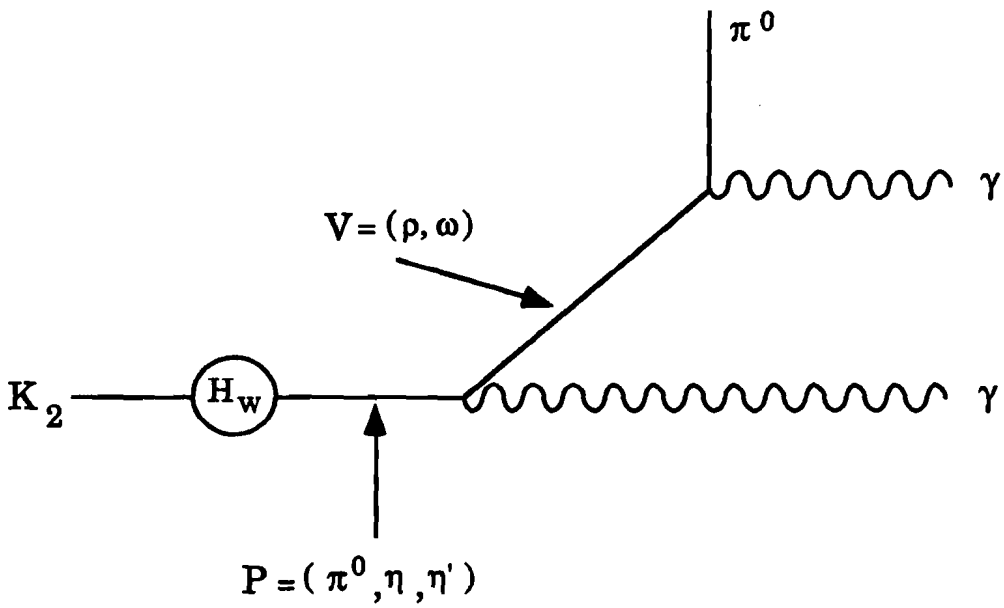

Figure 9. Vector meson dominance diagram for the $K_2 \rightarrow \pi^0\gamma\gamma$ decay.

framework of the VMD [21, 22] which assumes first a weak transition of K_2 to a pseudoscalar meson (π^0 or η or η') and then two radiative transitions as shown in Figure 9. The branching ratio was calculated to be $\Gamma(K_L \rightarrow \pi^0\gamma\gamma)/\Gamma(K_L \rightarrow \text{all}) = 1.8\text{x}10^{-6}$. The same authors calculated that $\Gamma(K_L \rightarrow \pi^0 e^+e^-)_{2\gamma}/\Gamma(K_L \rightarrow \text{all})$ would be about four orders of magnitude smaller. In this model the 2γ contribution to $K_L \rightarrow \pi^0 e^+e^-$ is comparable with the 1γ contribution. If the $K_L \rightarrow \pi^0\gamma\gamma$ decay contributes strongly to the decay $K_L \rightarrow \pi^0 e^+e^-$ this is going to happen only through a VMD amplitude because the loop contribution is proportional to the electron mass and therefore negligible. The $\gamma\gamma$ mass spectrum in the VMD model has an enhancement at low masses as shown in Figure 10.

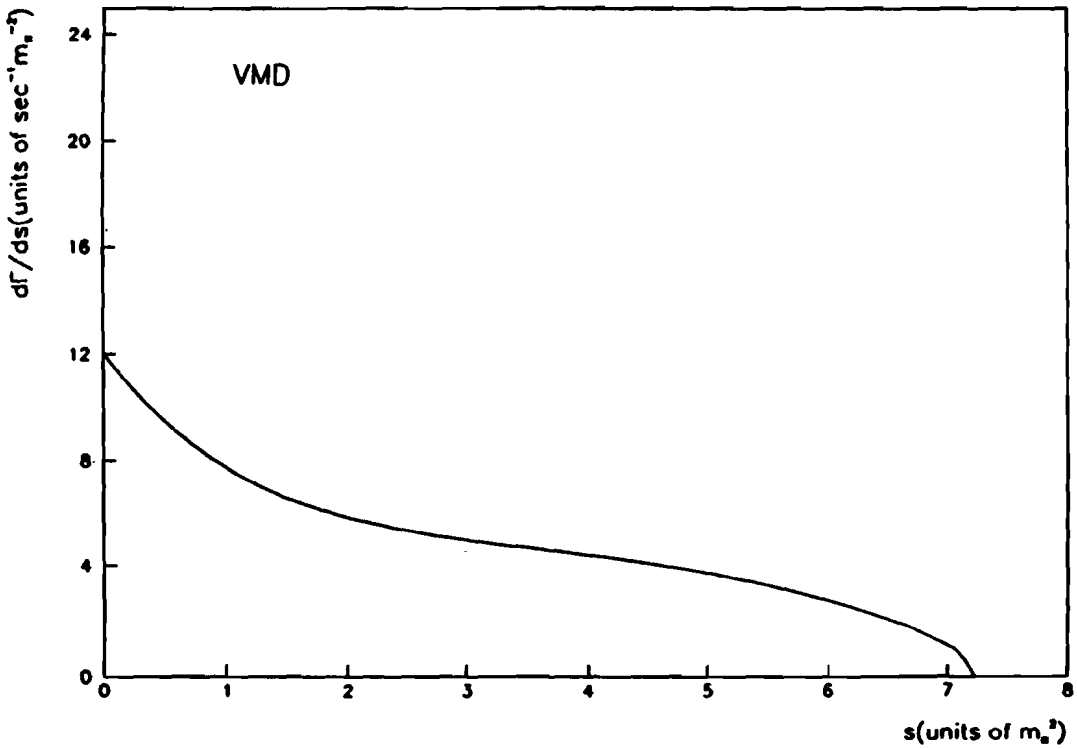

Figure 10. $\gamma\gamma$ invariant mass squared spectrum for the $K_L \rightarrow \pi^0\gamma\gamma$ decay calculated on the basis of the VMD model (taken from Reference [24]).

It was recently shown [23] that if one takes into account the P-wave pion loop besides the S-wave one that CHPT up to $O(P^4)$ does, then one gets the same results as the ρ vector meson dominance model obtains for the $K_L \rightarrow \pi^0\gamma\gamma$ decay.

Interestingly enough the interference between the real part of a "pion loop" amplitude mentioned earlier in the historical overview and the VMD amplitude has been considered [24]. When the interference is constructive the $\gamma\gamma$ mass spectrum looks like the one in Figure 11a and the most probable value for the branching ratio is estimated to be 3.9×10^{-6}. When the interference is destructive the mass spectrum looks like the one in Figure 11b and the central value of the branching ratio is estimated to

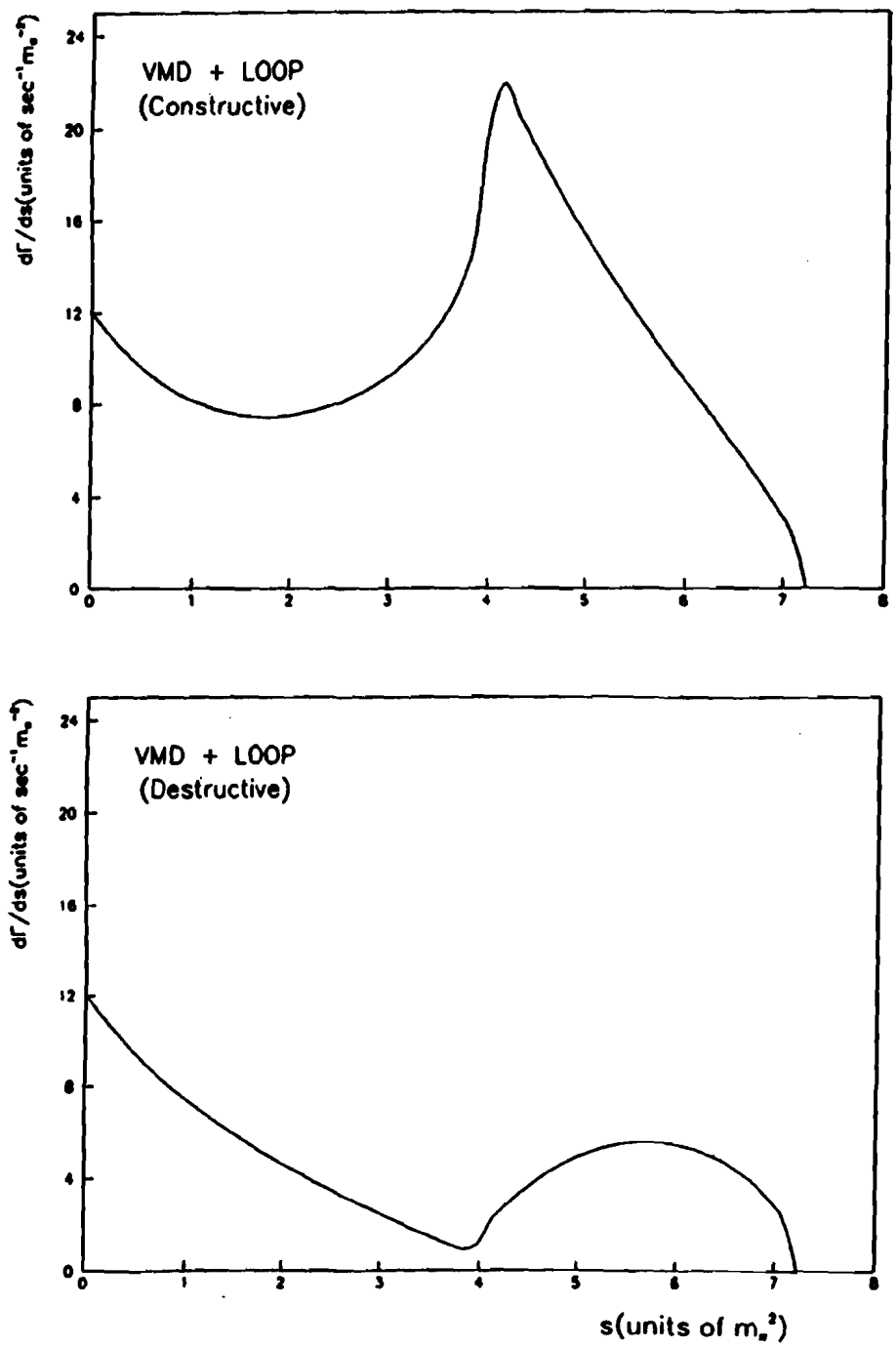

Figure 11. $\gamma\gamma$ invariant mass squared spectrum for the $K_L \rightarrow \pi^0\gamma\gamma$ decay calculated on the basis of a combination of pion loop and VMD models (taken from Reference [24]). a) constructive interference; b) destructive interference.

be 1.8×10^{-6}. These predictions have a range of uncertainty and according to Reference [24] the first number lies in the range 2.7×10^{-6} -6.2×10^{-6} and the second number lies in the range 1.17×10^{-6}-3.2×10^{-6}.

A similar approach [25] with the one in Reference [24] which uses both pion and kaon loops estimates the branching ratio to be 2.25×10^{-6} for constructive interference and 1.03×10^{-6} for destructive interference.

Recently the authors of Reference [14] have incorporated vector mesons in the chiral lagrangian [26] by considering also a lagrangian which is responsible for vector exchange contribution in $K \rightarrow \pi\gamma\gamma$ to $O(P^6)$. Considering different possibilities for the importance of the effective vector coupling they predict that the branching ratio of $K_L \rightarrow \pi^0\gamma\gamma$ lies in the range 6.7×10^{-7}-3.0×10^{-6} with more probable values smaller than 10^{-6}. It is pointed out though that neither of the current available approaches can provide a precise prediction for the transition $K_L \rightarrow \pi^0 e^+e^-$ via two photon exchange and experimentalists are urged to measure the $K_L \rightarrow \pi^0\gamma\gamma$ decay which can settle the issue whether the amplitude of $K_L \rightarrow \pi^0 e^+e^-$ is predominantly CP violating or not.

1.2 Experimental status of the $K_L \rightarrow \pi^0\gamma\gamma$ decay before the current search

For the decay $K_L \rightarrow \pi^0\gamma\gamma$ there was set an upper limit [4, 10] of 2.4×10^{-4} in 1969 by a rare kaon decay experiment performed at the Princeton-Pennsylvania Accelerator. The experimental procedure was to measure accurately the momentum of one photon by converting it in a lead sheet and then momentum analyzing the resulting e^+e^- pair with a magnetic spectrometer. It was assumed (and it was true ~95% of the time for the events used) that the photon in the magnetic spectrometer was one of the two direct photons in the decay. As far as the theoretical status was concerned, the exact form of the matrix element involved in the decay was not known at that time and the one used by the above experiment was

deduced from symmetry principles by requiring it to be Lorentz, gauge and CP invariant and also symmetric in the two photons. Its amplitude squared was $|M|^2 = |G_1|^2 m_{\gamma\gamma}^4$ where G_1 was a model dependent function that was assumed to be constant by the above experiment. The $m_{\gamma\gamma}$ spectrum based on this matrix element peaked at about 0.360 GeV and the above limit was set for $m_{\gamma\gamma} > 0.240$ GeV where the acceptance was expected to be $(70 \pm 8)\%$.

An analysis of a data set that consisted of approximately 20% of our data enabled us to improve this limit by a factor of about 90, yielding an upper limit of 2.7×10^{-6} for $m_{\gamma\gamma} \geq 0.300$ GeV which was published [27] in the summer of 1989. In the summer of 1990, the NA31 group at CERN reported [28] an observation of the decay. We will refer to this observation in some more detail in Chapter 9. Following our publication we have further refined our analysis, used more Monte Carlo statistics for background studies, and have included the remaining 80% of the data. We will describe our experimental procedure, analysis and results in the following chapters.

The rest of this thesis is organized as follows: In Chapters 2, 3 and 4 we will describe the detector that we used to perform our experiment, a hardware trigger processor that increased significantly our statistical power and the trigger requirements. In Chapters 5 and 6 the data collection and analysis will be described in detail, and in Chapter 7 we will describe the Monte Carlo simulation program and will perform data-Monte Carlo comparisons. After the determination of our systematic error in Chapter 8, we will proceed in Chapter 9 with the derivation of an upper limit for the $K_L \rightarrow \pi^0\gamma\gamma$ decay based on the 20% of the data. As will become clear by the end of that chapter, we improved our original limit by another factor of 1.5. Finally, in Chapter 10, we will present a new result based on 100% of the data set.

CHAPTER 2

THE EXPERIMENT

In this chapter we will discuss the principles of the measurement of the $K_L \rightarrow \pi^0\gamma\gamma$ branching ratio and also the apparatus with which the data were collected. The calibration of the several pieces of the detector will be also discussed together with the description of the apparatus.

2.1 Principles of the measurement

The branching ratio of the decay $K_L \rightarrow \pi^0\gamma\gamma$ is measured by comparing the rate of $K_L \rightarrow \pi^0\gamma\gamma$ to that of $K_L \rightarrow 2\pi^0$ and is given by Equation (2.1),

$$BR(K_L \rightarrow \pi^0\gamma\gamma) = \frac{N_{\pi^0\gamma\gamma}}{A_{\pi^0\gamma\gamma}} \times \frac{A_{2\pi^0}}{N_{2\pi^0}} \times BR(K_L \rightarrow 2\pi^0) \qquad (2.1)$$

where $N_{\pi^0\gamma\gamma}$ denotes the observed number of $K_L \rightarrow \pi^0\gamma\gamma$ decays, $N_{2\pi^0}$ denotes the observed number of $K_L \rightarrow 2\pi^0$ decays, and $A_{\pi^0\gamma\gamma}$ and $A_{2\pi^0}$ denote the acceptance of the detector for $K_L \rightarrow \pi^0\gamma\gamma$ and $K_L \rightarrow 2\pi^0$ decays respectively.

BR($K_L \rightarrow 2\pi^0$) is the world average for the branching ratio of the $K_L \rightarrow 2\pi^0$ decay which is known to be (0.0909±0.0029)%. The data used in this thesis for the extraction of the $K_L \rightarrow \pi^0\gamma\gamma$ branching ratio were collected by the E731 fixed target experiment performed at the Meson Center beamline at Fermilab. K_L decays into $\pi^0\gamma\gamma$ and $2\pi^0$ were detected at the same time, in the same neutral beam and satisfied the same trigger requirements and therefore any accelerator instabilities, electronic drifts associated with the electronics of detector elements or changes in detector resolution affected both rates in the same way. The data analysis that leads to the determination of $N_{\pi^0\gamma\gamma}$ and $N_{2\pi^0}$ will be basically described in Chapters 5 and 6. The acceptances are calculated by a Monte Carlo simulation which will be described in detail in Chapter 7. Data for the $K_L \rightarrow \pi^0\gamma\gamma$ search were collected simultaneously with those for the measurement of the ε'/ε parameter of direct CP violation for which the experiment was optimized. The fact that the experiment was optimized for a precision measurement led to very detailed understanding of the detector and its performance and this had very positive effects on the measurement of the BR($K_L \rightarrow \pi^0\gamma\gamma$). On the other hand the experiment was not designed to study rare kaon decays and this, as will become clear below, made it a real challenge to extract this branching ratio.

2.2 Beamline

A beam of 800 GeV protons was delivered to our experiment by the Fermilab accelerator in the form of one 22 s spill every minute (duty factor of 37%). The 22 s spill had an RF (radio frequency) substructure of 2 ns proton buckets every 18.8 ns and we had about 10^9 such buckets hitting our target per spill, with about 500-1000 protons per bucket. The primary beam illuminated a Be target of one interaction length which was placed

at a targeting angle of 4.8 mrad; the targeting angle was in the horizontal plane and it was chosen so that we have both high kaon flux and good kaon to neutron ratio in the secondary beam produced. A set of sweeping magnets immediately downstream of the target as shown in Figure 12 removed charged particles from the secondary beam and a two hole collimator at ~15 m downstream of the target followed by 3 collimation and sweeping magnet stations (at ~15 m, ~48 m and ~78 m from the target respectively) produced two well-collimated, vertically separated beams at our spectrometer. Photons were removed from the beams by first converting them through 7.5 cm of Pb in the holes of the two hole collimator and then removing the resulting electron-positron pairs by sweeping magnets downstream of the Pb. The neutron to kaon ratio achieved in the beams was approximately 1:1. To reduce the interactions of the beams with material, the beams entered vacuum (~10 mTorr) almost immediately downstream of the two hole collimator. The vacuum continued till the Vacuum window which was located at ~159 m from the target and had a radius of 0.6 m. The Vacuum window consisted of two thin foils of Kelvar 29 and mylar to minimize the multiple scattering of charged particles.

Figure 13 shows the decay region and the detector starting roughly 100 m downstream of the target. At this point there is a negligible K_S component to the beams since we are several K_S lifetimes away from the target. A regenerator is located at 110 m from the target with the purpose of producing K_S for the ε'/ε measurement. The regenerator, shown in Figure 14, consists of four 19 cm B_4C blocks; three of these are followed by 0.635 cm of scintillator and the fourth is followed by 1.27 cm of Pb and 0.635 cm of scintillator. In coherent regeneration we had K_S produced along the initial direction of K_L but in diffractive and inelastic regeneration the K_S was regenerated at a finite angle with respect to the K_L. The regenerator moved from one beam to the other between each pulse of the

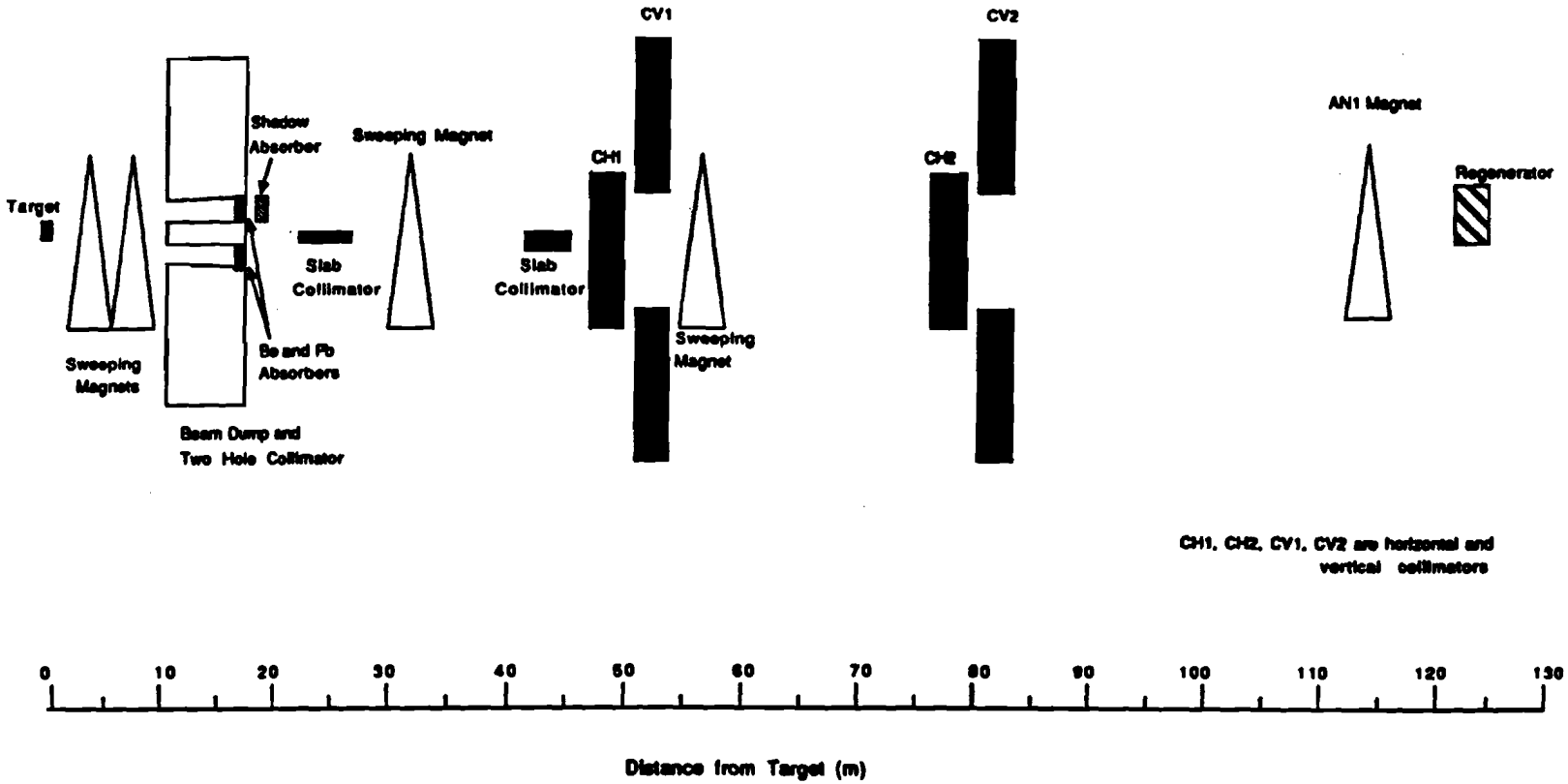

Figure 12. The target and collimators.

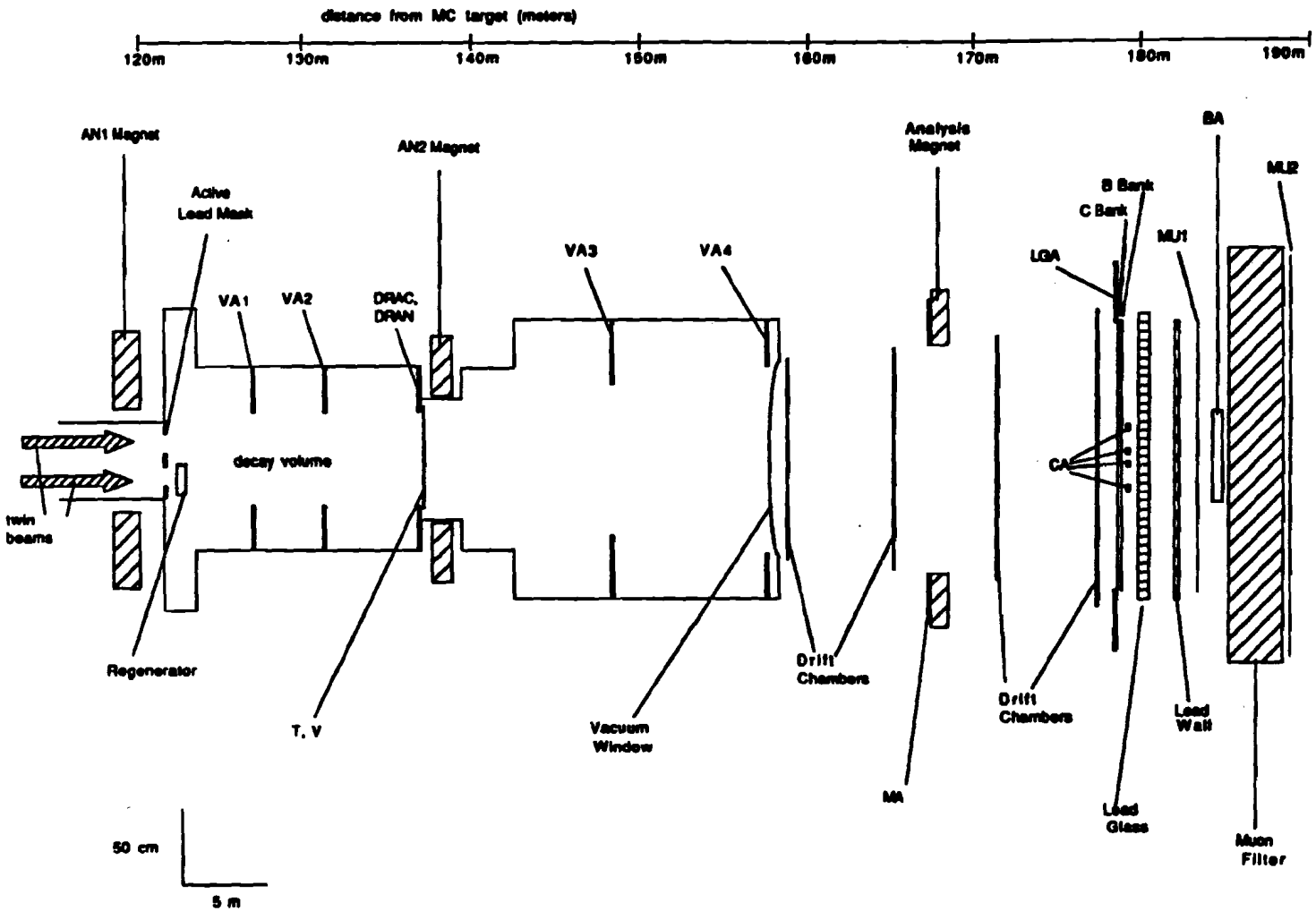

Figure 13. The decay volume and detector.

accelerator, so that one of the beams (the vacuum beam) was a pure K_L beam and the other (the regenerator beam) was a mixture of K_L and K_S. The K_L in the regenerator beam were (6.35±0.03)% of the K_L coming from the vacuum beam. For the $K_L \rightarrow \pi^0\gamma\gamma$ measurement only the vacuum beam was used.

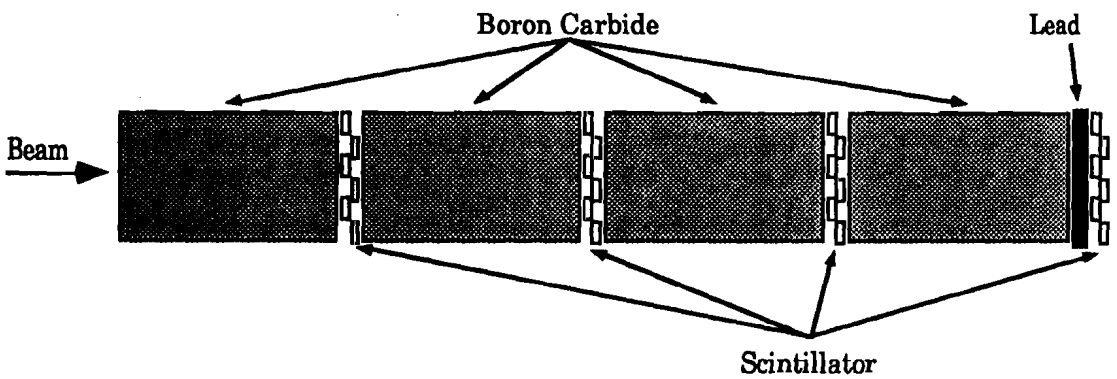

Figure 14. Side view of the regenerator.

2.3 The Detector and its calibration

We have shown already in Figure 13 a schematic of our detector. The positions and dimensions of the individual detector elements are given in Table 1 and their radiation lengths are given in Table 2.

2.3.1 The charged particle spectrometer

The charged particle spectrometer (see Figure 13) consisted of 5 scintillator counter banks, 4 drift chambers and two magnets. The first two counter banks (V and T) were located about 138 m from the target and their counter planes were 2.3 cm apart. The V bank was upstream of the T bank and the V counters were positioned horizontally while the T counters were positioned vertically, as can be seen in Figures 15 and 16.

TABLE 1. Positions and dimensions of the detector elements.

Detector element	Z location (wrt target)	Transverse dimensions (width x height)
PA	116.118 m	
SA	117.81 m-121.36 m	16.2 cm x 28.58 cm
Lead Mask (AM)	121.893 m	
Regenerator	123.550 m	
VA1	127.855 m	inner edge radius: 30.3 cm; outer edge radius: 59.5 cm
VA2	132.819 m	inner edge radius: 30.3 cm; outer edge radius: 59.5 cm
V	137.792 m	
T	137.815 m	
DRAC	137.826 m	
DRAN	137.866 m	
Separator Magnet	139.008 m	
VA3	149.309 m	inner edge radius is 50.2 cm; outer edge radius is 88.5 cm
VA4	158.291 m	inner edge radius is 60.6 cm; outer edge radius is 88.9 cm
Vacuum Window	158.965 m	
Chamber 1	159.292 m	1.27 m x 1.27 m
Chamber 2	165.867 m	1.42 m x 1.57 m
MA	166.836 m	inner edge: 1.82 m x 1.49 m; outer edge: 2.09 m x 2.13 m
Analyzing magnet	168.865 m	
Chamber 3	171.857 m	1.57 m x 1.73 m
Chamber 4	178.004 m	1.78 m x 1.78 m

TABLE 1. -- (continued)

Detector element	Z location (wrt target)	Transverse dimensions (width x height)
LGA	178.710 m	inner edge diameter : 1.8 m outer edge diameter : 2.64 m clipped height : 2.11 m
C Bank	179.502 m	1.9 m x 1.8 m
B Bank	179.520 m	2.0 m x 2.1 m
CA	180.700 m	Pb, Cu and scintillator square rings: inner edge side: 4.6" outer edge side: 6.9"
Lead Glass	181.089 m	approximate radius is 0.91 m
Mu1	183.996 m	2.0 m x 2.2 m counter dimensions: a) 35" x 4.5" b) 49.5" x 3.5"
BA	185.047 m	20.32 cm x 40.64 cm counter dimensions: 0.25" thick, 1" wide and a) 19.75" long (vert. strips) b) 11.75" long (horiz. strips)
Mu2	189.914 m	2.54 m x 2.44 m

TABLE 2. Radiation and interaction lengths of detector elements.

Detector Element	Number of Radiation lengths	Number of Interaction lengths
HDRA V	0.0033	
Lead sheet	0.11	
HDRA T	0.0033	
Vacuum window	0.0025	
Drift Chamber 1	0.0034	
Drift Chamber 2	0.0040	
Drift Chamber 3	0.0038	
Drift Chamber 4	0.0021	
Field wire	0.0057	
Sense wire	0.0064	
B bank	0.04	
C bank	0.04	
Collar-anti	8.1	
Lead Glass	18.74	2.2
Lead Wall	21.4	0.7
Back-anti	28.1	1.3
Muon filter		19.1

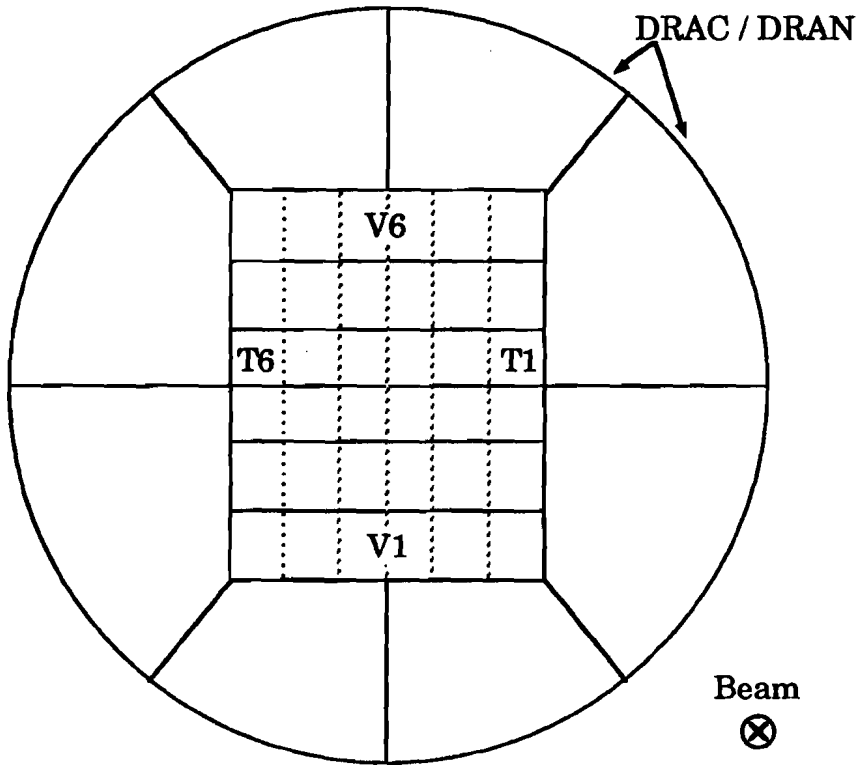

Figure 15. V and T scintillator banks and DRAC and DRAN photon veto counters.

The V and T counters are made of NE110 scintillator 1 mm thick and, as shown in Figure 16, between their planes one could slide in at will a Pb sheet converter of 0.5 mm thickness and supported by 3 mil thick mylar foil. 1 mil (25 μm) thick aluminum mylar on both sides of the Pb converter protected the counters when the converter slid in. The combination of the V and T counter banks, together with the DRAC and DRAN photon veto counters which will be described in section 2.3.5, and the Pb sheet converter were known as the "HDRA". A signal in V or in T scintillator banks was required for the "charged" trigger and the V bank was used as

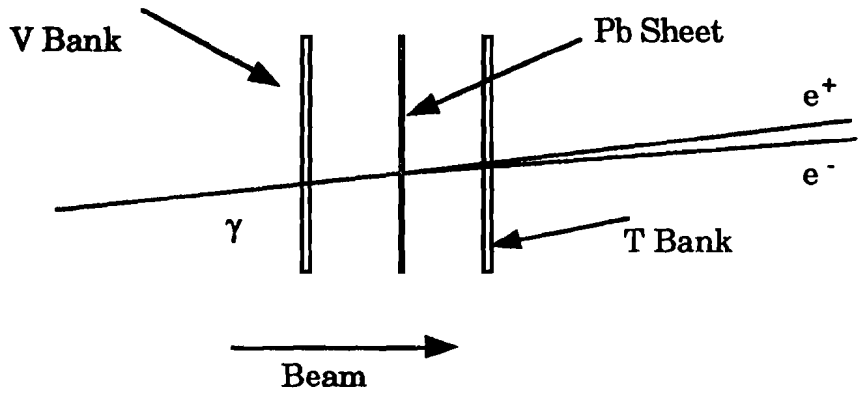

Figure 16. Side view of V and T bank and the Pb converter.

a veto in the "neutral" trigger as will be explained in Chapter 4. A magnet downstream from the T bank (the Separator magnet or AN2) gave a transverse kick of 28.3 MeV to the e^+ and e^- produced by photon conversion at the Pb sheet. This kick was suitably chosen so that the pair reconverges to the glass after another kick by the Analyzing magnet, AN4, further downstream.

Trajectories and momenta of charged particles were measured by a system of 4 drift chambers, two on either side of the AN4 magnet. Each chamber had two horizontal and two vertical planes of wires with 1.1 cm distance between planes. The field-shaping wires and the sense wires were arranged in a hexagonal cell geometry as shown in Figure 17 and the sense wire spacing was 0.635 cm. The chamber gas was a mixture of 50/50 argon-ethane with about 0.5% ethanol. Later in the run isopropanol was used instead of the ethanol to avoid aging. The average drift velocity for electrons was 45 μm/ns and the longest drift times were approximately 250ns. The operating voltage for the field wires was 2650 V. The signals of the sense wires were amplifiied and discriminated at the chambers and were led to Le Croy 4291B TDC's which operated in "common stop" mode.

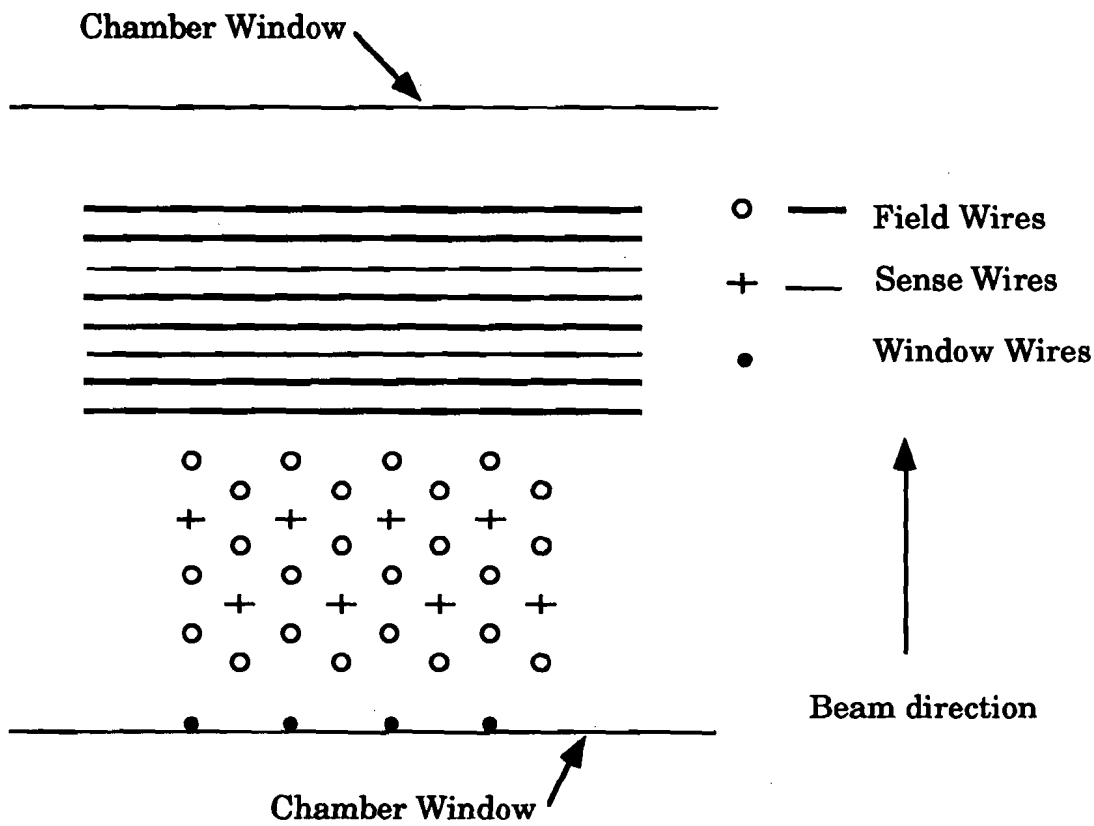

Figure 17. Cell geometry of drift chamber wires.

The wire plane efficiencies were measured to be about 99% except from the upstream vertical plane in chamber 1 whose efficiency was ranging between 93-96% and the upstream vertical plane 2 which was at least 95% efficient. The position resolution was 100 μm/plane and the two track resolution, that is the minimum distance that two tracks should have in order to be recognized as two seperate tracks, was about 1 cm. The relative location and orientation of the chambers was determined by muon alignment runs which gave clean single tracks through the spectrometer. The time at which a charged particle passed through the chambers was measured by TDCs and it was related to its distance from a sense wire by

using the drift time distributions for the relevant wire planes. The tracks were bent in the x-view by the AN4 magnet and the momentum of a track was determined by using the bend angle between the track segments upstream and downstream of the magnet.

The AN4 magnet located between chambers 2 and 3 gave to the π^+, π^- and e^+,e^- a transverse kick of ± 200 MeV/c or ± 100 MeV/c depending on the trigger. AN4 gave to the $e^+$and e^- an equal and opposite kick to the one given to them by the Separator magnet so that the pair converges to a single cluster in the calorimeter. Between each of the drift chambers there were positioned Helium bags with thin mylar windows in order to minimize multiple scattering of the charged particles.

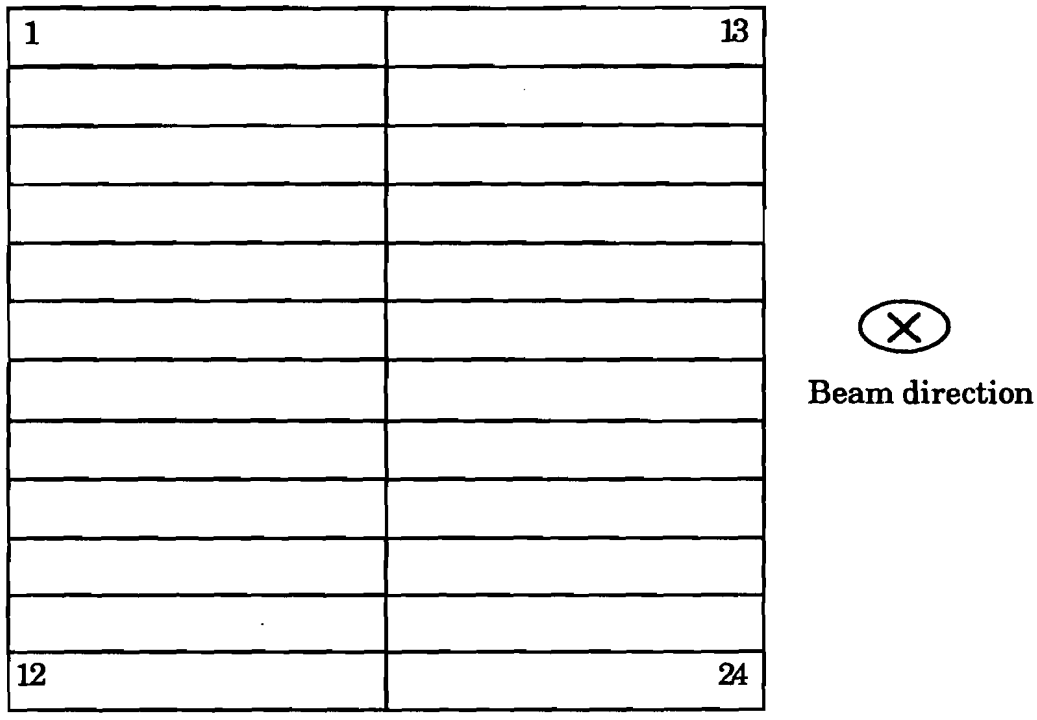

Figure 18. Beam view of the C Bank.

Downstream of the chamber system and immediately upstream of the lead glass there were located two more scintillator counter banks (the C and B banks). The C bank was upstream of the B bank and the C counters were positioned horizontally while the B counters were positioned vertically. There were 24 counters in the C bank and 30 counters in the B bank as shown in Figures 18 and 19.

Finally a 3.2 m iron filter downstream of the lead glass, the Muon filter, filtered out all charged particles except from muons which were identified by a scintillator counter bank (Mu2) of 32 counters located at the end of our spectrometer.

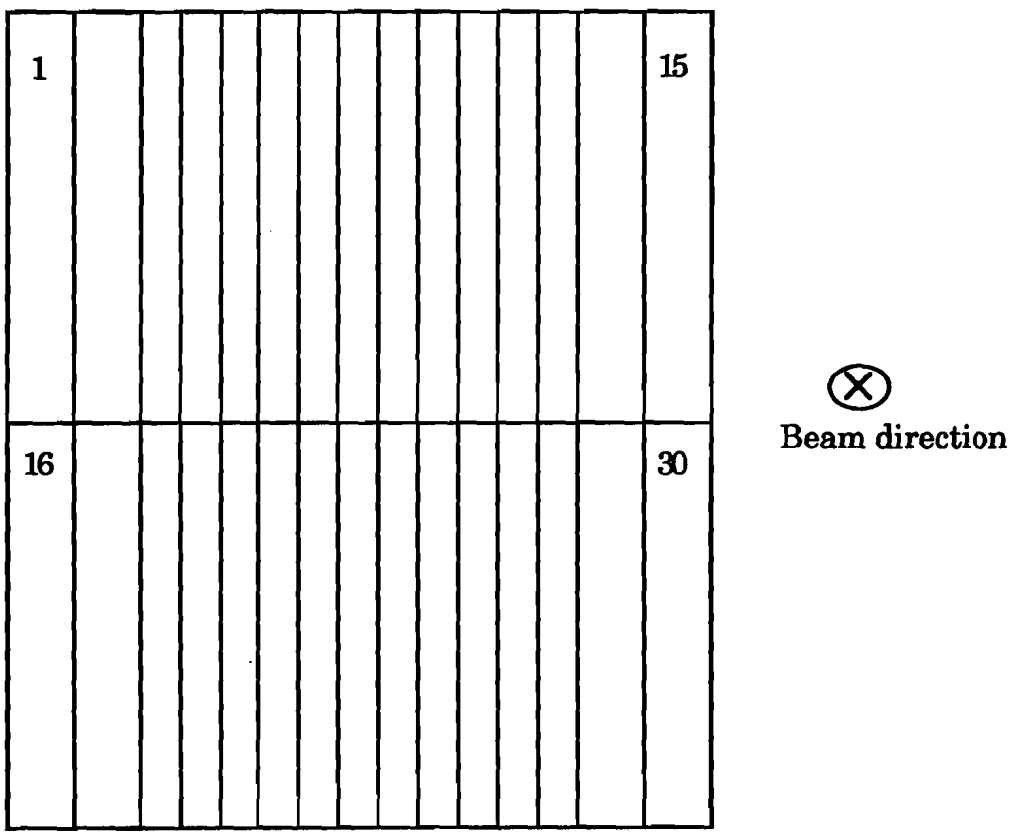

Figure 19. Beam view of the B Bank.

2.3.2 The calorimeter

2.3.2.1 Description

The electromagnetic calorimeter which is shown in Figure 20 was one of the most important portions of the apparatus since it was used for the measurement of energies and positions of photons and electrons. It consisted of 804 lead glass blocks which were stacked in a circular array and were optically isolated from each other. The lead glass used was Schott Optical Glass Type F2 with radiation length 3.25 cm. The dimensions of the individual blocks were 5.81 cm in x by 5.81 cm in y by 60.96 cm in z and the array was placed in a temperature controlled, light-tight house. Each of the blocks was read by a single 10-stage, Amperex XP2202-FL photomultiplier with a bi-alkali photocathode and was sensitive mostly to blue light. A filter placed between the photocathode and the block absorbed the short wavelengths up to about 4300 A^0. The photomultipliers ran at approximately 1000 V and their signals after a delay of 275 ft (447 ns) of RG-58 cable were distributed to 10 G10 backplanes. There, there were two paths: a) about $5x10^{-3}$ of the signal of each phototube was capacitively picked off at the flash cards plugged at the back of the backplanes in order to be used by a trigger proccessor for cluster finding purposes as will be explained in Chapter 3; b) the signal was led with shielded 25 channel ribbon cables to the ADCs which measure the integrated charge of the phototube signal. The ADCs were 12-bit Le Croy 1885N using the full dynamic range. Their gain was 0.05 pC/count for the low range and 0.4 pC/count for the high range and the ADC gate was 150 ns wide. A 1 GeV electromagnetic shower in the glass corresponds to approximately 210 counts at the ADCs. The signal recorded by the ADCs is proportional to the total *Čerenkov* light produced by shower particles weighted by light attenuation. Gain stability as a function of beam intensity was improved by continuously illuminating the front faces of the glass blocks with dc light supplied by LEDs. The voltage

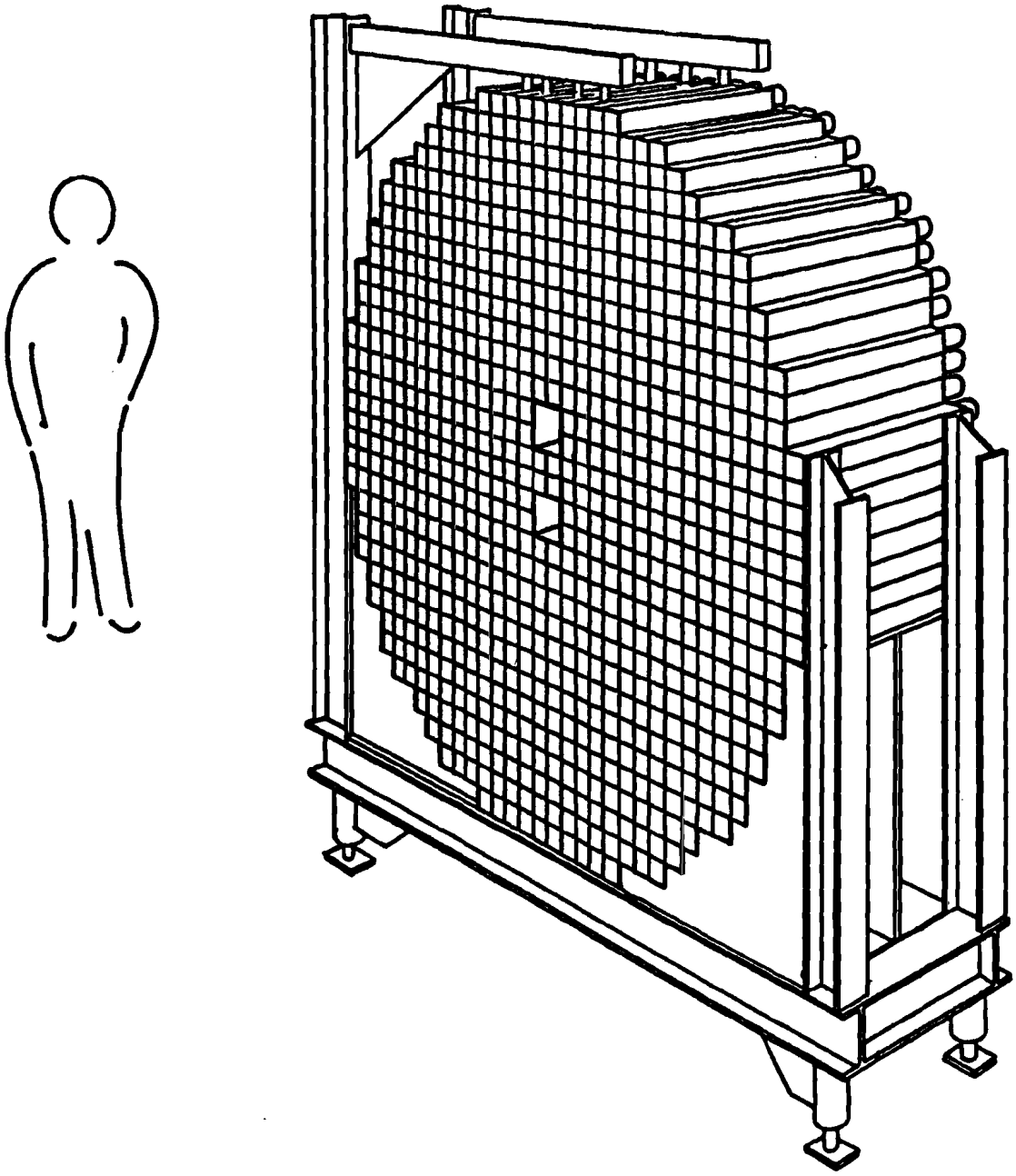

Figure 20. The lead glass electromagnetic calorimeter.

of the LEDs was in the range of 2.2-2.4 V and this low level light reduced the gain change that the blocks experience when the intensity changes drastically (e.g at the beginning of each spill). Short-term monitoring of gain stability of the blocks was done with a Xenon flasher system. The flasher was triggered at 1 Hz during the beam spill and its light was transmitted to the 804 blocks by fiber optics. A lead glass block with its photomultiplier, filter and flasher fiber is shown in Figure 21.

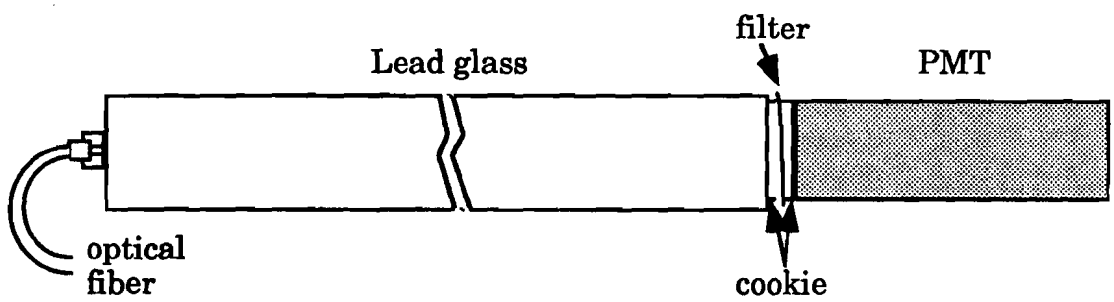

Figure 21. A lead glass block with its optical fiber and its read out system.

The pedestals of the lead glass ADCs were subtracted on line and the number subtracted for each channel was an average of ADC counts observed in this channel between spills. In reality the pedestals between spills were different from the pedestals during the spill by a couple of counts, that is by about 10 MeV, and this difference depended on beam intensity, on the elapsed time since the previous gate and on the ADC module. Therefore, the data had to be corrected for this effect. The array was read in a "sparse read out" mode, that is, after pedestal subtraction was done, only blocks containing shower energy above some threshold were read. This threshold was 5 ADC counts for neutral mode data and 20 ADC counts for charged mode data corresponding to about 25 MeV and

100 MeV of shower energy respectively. The glass resolution for electrons has been measured from electron calibration data to be $1.5\% + \frac{5\%}{\sqrt{E}}$. This was done by fitting a gaussian to E/p (E is the energy and p the momentum of the electron) distributions in different momentum bins and by subtracting in quadrature from the widths of the fitted gaussians the expected contributions of momentum resolution due to chamber resolution and multiple scattering. The constant term is due to absorption and to shower fluctuations. The resolution for photons was roughly $2.5\% + \frac{5\%}{\sqrt{E}}$. If one wants to be more specific there were high order polynomial curves that were fitting better the photon resolution as a function of energy but there was good evidence from EGS study that the photon resolution is about 1% worse than the electron resolution. The absorptions of the lead glass blocks were mostly in the range α=0.034-0.042 inverse radiation lengths but the absorptions of blocks around the beam holes were larger due to heavier radiation damage in that region (the absorption per cm was increasing proportionally to the dose). In order to restore the transmission of the blocks we shined on them a 400 W mercury vapor lamp four times during the run, for about 24-48 hours each time, restoring about 50% of their transmission every time. The absorption or attenuation contributes to what we call nonlinearity of the calorimeter which consists of the fact that the number of photons from an electromagnetic shower seen by a phototube, or the measured energy by the ADCs, is not exactly proportional to the energy of the particle that caused the shower. In fact the measured energy, E_{meas}, of a photon that travels through x radiation lengths in a lead glass block of absorption coefficient α, due to the fact that x depends logarithmically on E_{tr}, has a power law dependence on its true energy, E_{tr}:

$$E_{meas} = E_{tr} e^{-\alpha x} = C_1 E_{tr}^{C_2}$$

where C_1 and C_2 depend on α. The measured energies of our clusters were corrected for this effect by being basically raised to the power of 0.979.

We are going to use in following chapters this nonlinearity of the calorimeter to explain the characteristics of some kinematic distributions.

Analog sums of lead glass signals from subarrays of 7-9 blocks were formed to produce 92 "adder" signals the sum of which gave the total energy of the array, ET, which was used in the trigger. This total energy was also ADCed for both delayed buckets and for early buckets within the gate, giving a good monitor of the accidental activity at the calorimeter. The gate of the adders was much shorter than the one of the lead glass (30 ns compared with 150 ns for the lead glass) and gave them the ability to identify "in time" or "out of time" accidental events. This was particularly useful for the charged mode where the hardware cluster finder processor described in Chapter 3 was not used in the trigger.

We did not have a hadron calorimeter in the experiment but hadronic events were identified and rejected in the neutral mode trigger by using in veto the Mu1 scintillator counters, located downstream of the lead glass calorimeter and of a 12 cm thick lead wall. The Mu1 bank consisted of 45 counters and it is shown schematically in Figure 22. Both beams pass through a single hole in this bank. The electromagnetic showers were completely contained in the 40 radiation lengths provided by the lead glass and the lead wall but hadronic showers were not and usually gave large pulse heights in Mu1.

2.3.2.2 Calibration

The electromagnetic calorimeter was calibrated by using electrons and positrons collected during special runs in the experiment. For these runs the intensity was approximately 1×10^{11} protons on target per spill and the normal 1 interaction length Be target was replaced by a 1/3 interaction length Cu target. The normal absorbers were also replaced by a 48" Be absorber in order to reduce the neutron flux and the conversion propability of the photons. A 1/16" thick Cu foil was inserted in the photon dominated neutral beams about 6.4 m downstream of the

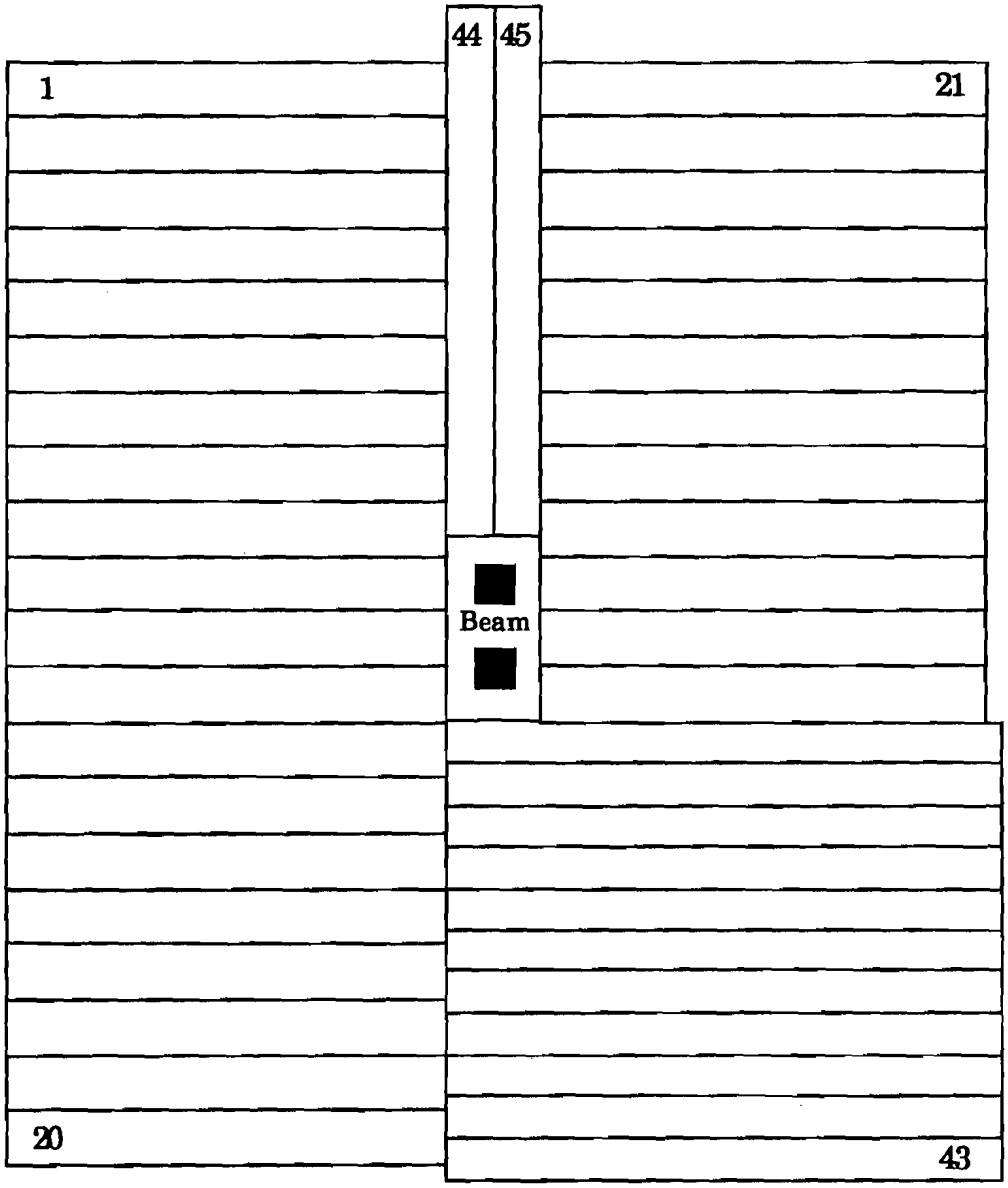

Figure 22. Beam view of the Mu1 Bank.

target and provided 0.11 radiation lengths of material for the conversion of the photons to electron-positron pairs. For the last month of the run the

Cu foil was replaced by a 0.02 radiation length foil consisting of 0.005" Cu and 0.003" Ti in order to reduce the produced Bremmstrahlung. As the e^+e^- pairs travelled along the beamline, they were first split vertically by magnet AN1 located at 119 m from the target, and they were next split horizontally by the Separator magnet (AN2) located right after the HDRA. The Pb sheet was removed for the calibration runs. The AN4 magnet, further downstream, gave an additional horizontal kick to the pair. The current of the AN4 magnet was 1714 A and the currents of the magnets AN1, AN2 were properly adjusted so that electrons and positrons illuminate the whole array. The calibration run was using the "charged"trigger but the read out threshold for the calorimeter was the one used in the open mode trigger (5 ADC counts). During calibration and during normal data taking flasher pulseheights for all the blocks were recorded and this gave us a quick monitoring of the performance of the calorimeter. We had ten electron calibration runs during the experiment and the gains[1] of the blocks that we used in the analysis were the ones determined by the closest in time calibration run corrected at first order for the difference observed in the flasher pulseheights between calibration run and normal data taking period. A second order correction was applied to the gains by using electrons and positrons from Ke3 decays. When the incident particle was photon and not electron there was applied some additional correction to its energy. This last correction was due to the fact that the electromagnetic showers initiated by photons start deeper into the block than electron showers and therefore light attenuation is less for photons than for electrons. So for an electron and a photon of the same incident energy, the lead glass signal is larger for the photon by a factor of about 1.035 up to 20 GeV of energy and for our range of absorption coefficients. This factor is smaller for higher energies, it

[1]Gain is effectively the number by which we have to multiply the number of ADC counts corresponding to each block in order to determine the true fraction of the energy of the particle deposited in the block.

depends weakly on the energy of the particle up to 50 GeV and its determination was done with EGS Monte Carlo. A detailed description of the calibration of the lead glass and of the corrections applied to the energies of the clusters is given in Reference [29]. The overall gain scale was understood to about 0.2% at all energies.

The adder calibration was performed by using $K_L \rightarrow 3\pi^0$ decays for which we had lots of statistics. The gain of the adders, g(a), was defined as the mean of the distribution of the ratio of the ADC counts of the adder to the sum of the ADC counts of the lead glass blocks participating in the adder. The width of that distribution was called the "sigma" or the resolution of the adder. Twenty nine calibration files were used for the whole run and g(a) was ~0.1. The central adders had usually ~1.4-3.9K events in calibration files in tapes that were rich in $3\pi^0$ and ~500 events when we were recording predominently charged trigger events. Adders at the edges of the lead glass array had ~15-70 events or ~10 events for $3\pi^0$ rich or $3\pi^0$ poor tapes respectively. Typical non-edge and non-central adders had ~150-1400 events or 60-180 events for $3\pi^0$ rich or $3\pi^0$ poor tapes respectively. Gains and sigmas of the adders from one calibration file are shown in Figure 23.

2.3.3 The background rejection anticounters

The main background for the $K_L \rightarrow 2\pi^0$ and for the $K_L \rightarrow \pi^0\gamma\gamma$ decay modes is from the $K_L \rightarrow 3\pi^0$ decay in which one or more photons miss the lead glass calorimeter. In order to reduce this background there were built 13 planes of photon veto counters. Starting from upstream, the Pinching-anti (PA) was located 116.1 m from the target, it consisted of 6 scintillator counters and its function was to identify and veto charged particles with wide angle. The Sweeper-anti (SA) consisted of 6 scintillator counters covering the square beam pipe between 117.81 and 121.36 meters from the target. This counter was not in the trigger but

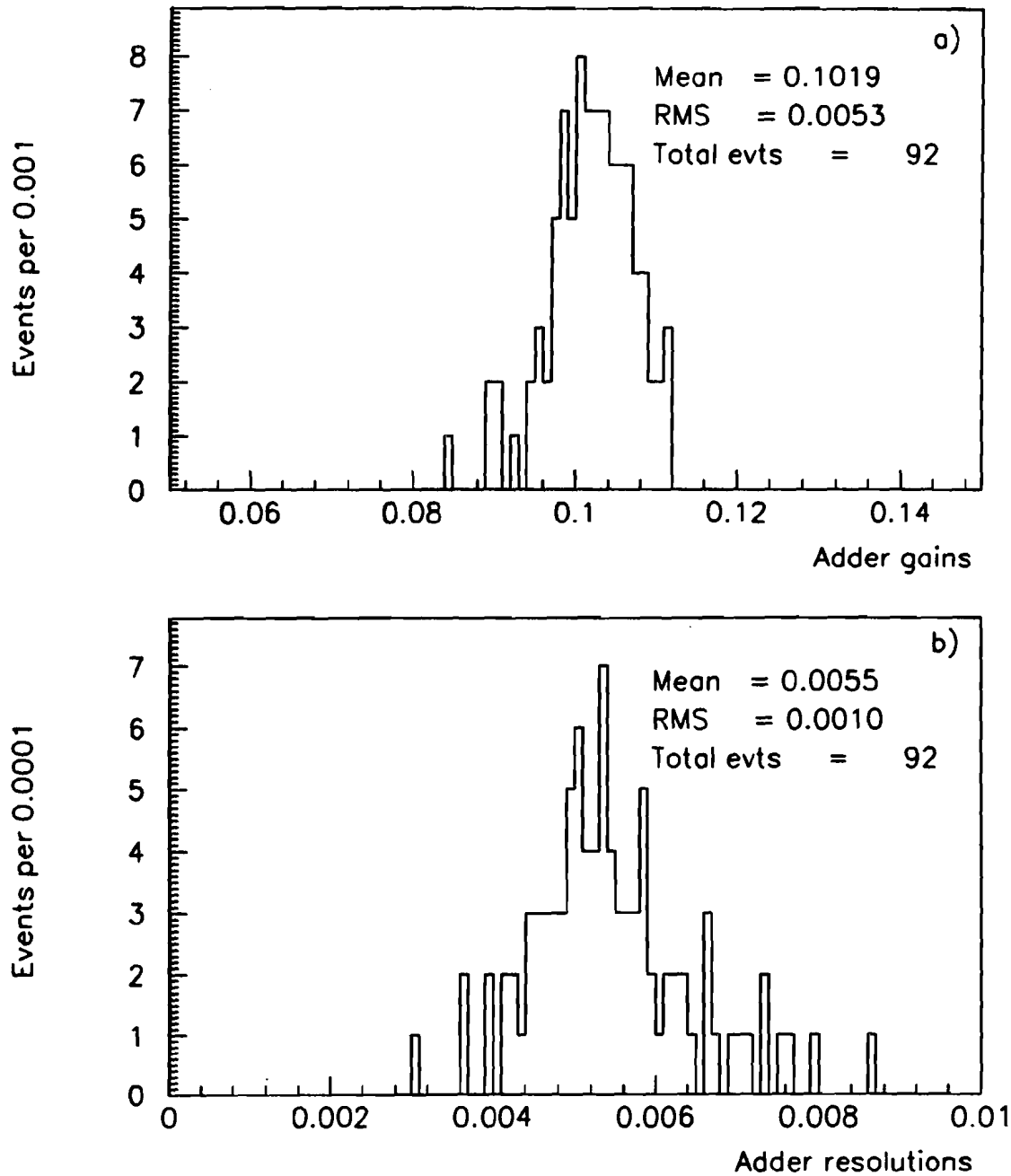

Figure 23. Distribution of the gains and resolutions of the adders from one calibration file.

was used off-line to identify soft photons that would otherwise hit outside the Mask-anti counters escaping detection. The Mask-anti system (AM or "Active Mask) consisted of 2 layers (see Figure 24). Each layer involves 1" Pb and 5 scintillator counters. The scintillator in each layer consists of three horizontal pieces of 2" width and two vertical pieces of 3" width. The thickness of each scintillator piece in each layer is 0.125" and there is overlap between horizontal and vertical pieces. The signals from the 5 counters in each layer are transferred to phototubes with optical fibers. The Pb Mask and the lead glass apertures were the defining apertures for data with neutral final states. Five planes of photon vetoes followed in vacuum. These planes were VA1, VA2, DRAC-DRAN, VA3 and VA4. VA stands for Vacuum-anti, DRAC stands for decay region-anti charged and DRAN stands for decay region-anti neutral. The VA units consisted of a scintillator plane for charged particle identification followed by two planes of lead-lucite sandwiches for photon identification. The lead-lucite planes were 3 radiation lengths each and consisted of 5 layers as shown in Figure 25. Cross section of the VAs along the direction of the beam is shown in Figure 26. DRAC and DRAN have been shown already in Figure 15. DRAC consisted of a layer of scintillator and DRAN of a layer of lead followed by a layer of scintillator. The MA (Magnet-anti) and LGA (Lead glass-anti) photon vetoes were of similar construction as the VAs and their cross sections along the beam are shown in Figure 27.

The Collar-anti system (CA) detected electrons and photons passing within 1/2 block away from the beam holes at the lead glass array. It consists of two similar subsystems-one for each beam- and it is shown in Figure 28. Each subsystem consists of a 1.75" thick square ring of Cu (3.1 r.l.), a 1.102" thick similar ring of Pb (5.0 r.l.), and a 0.25" thick square ring of scintillator providing more than 8 r.l. for the conversion of photons to e^+, e^- pairs. The light produced is detected by 8 phototubes -1 at each corner of the two subsystems. The above subsystems are mounted on

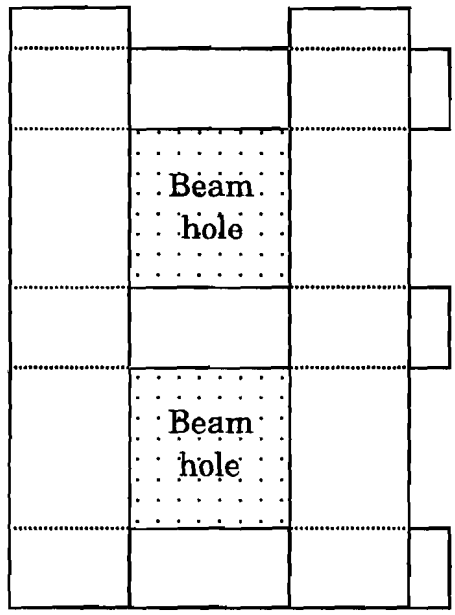

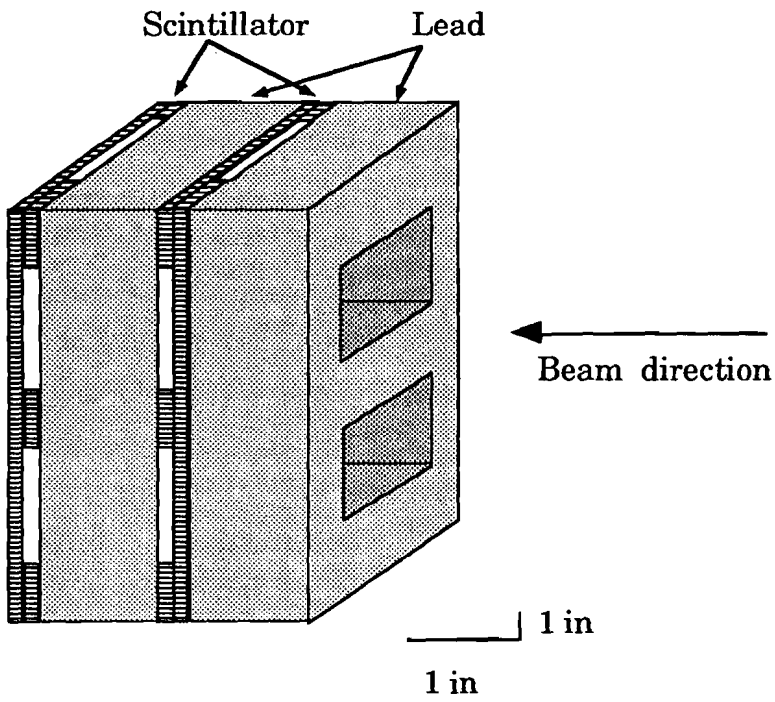

Figure 24. Beam view and side view of AM.

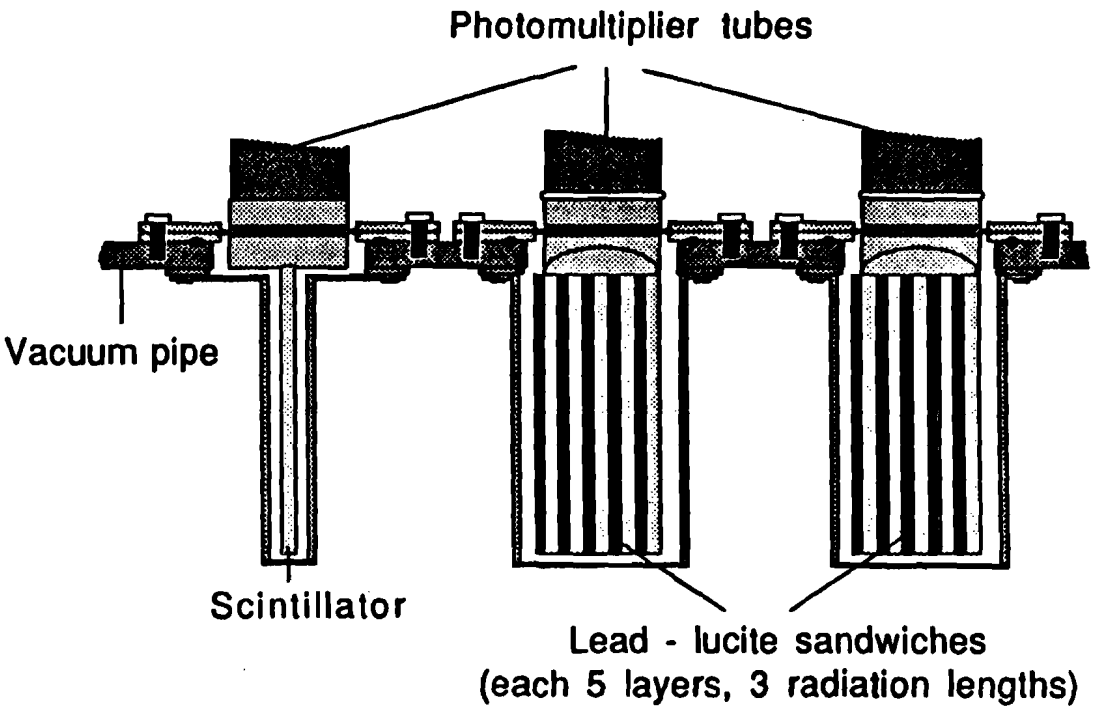

Figure 25. Cross-section of a VA counter.

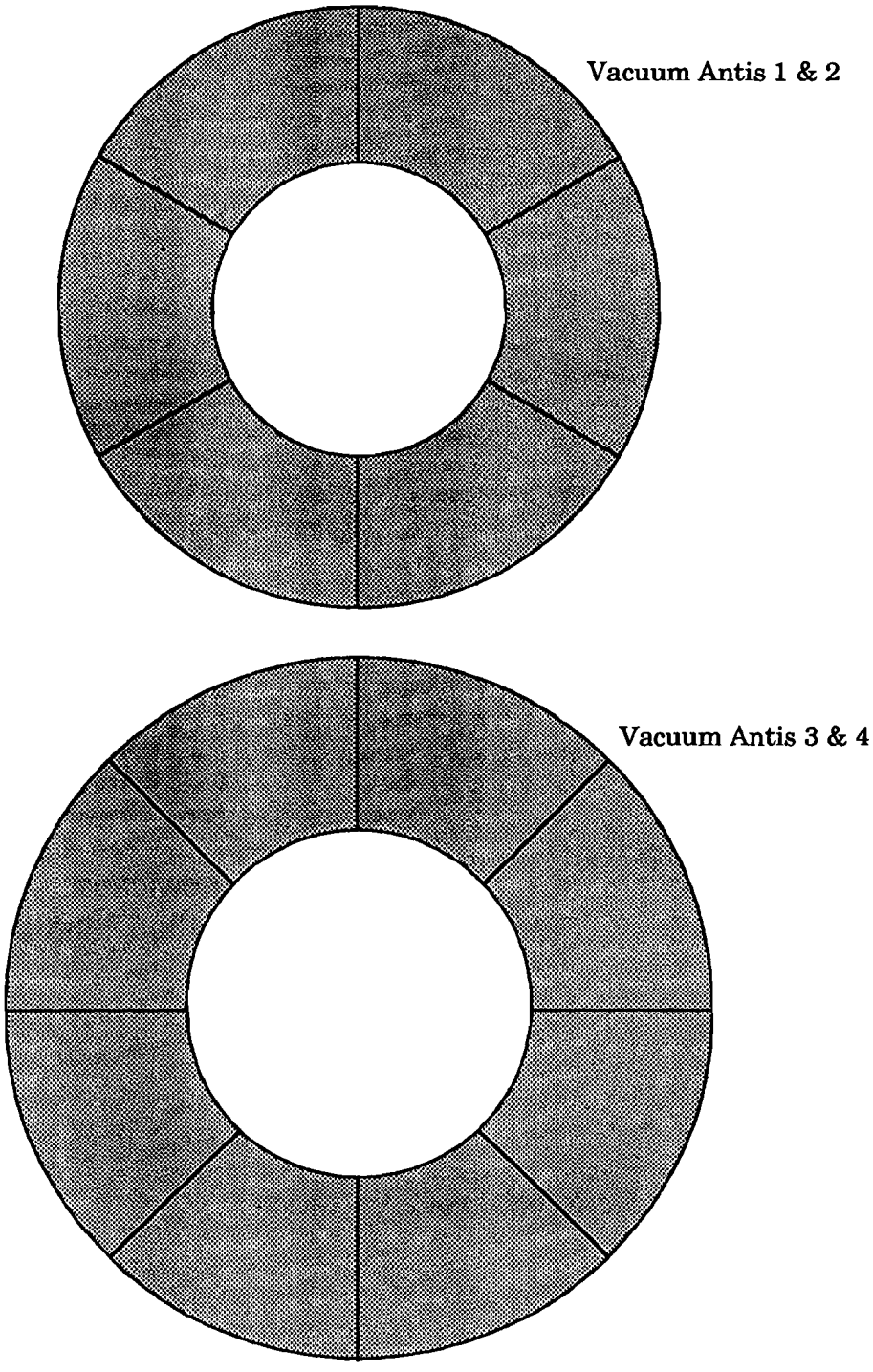

Figure 26. Beam view of theVacuum-antis.

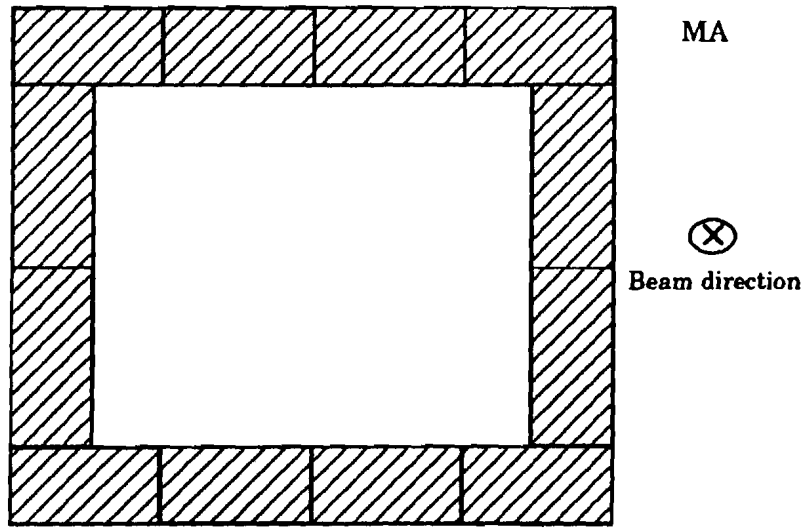

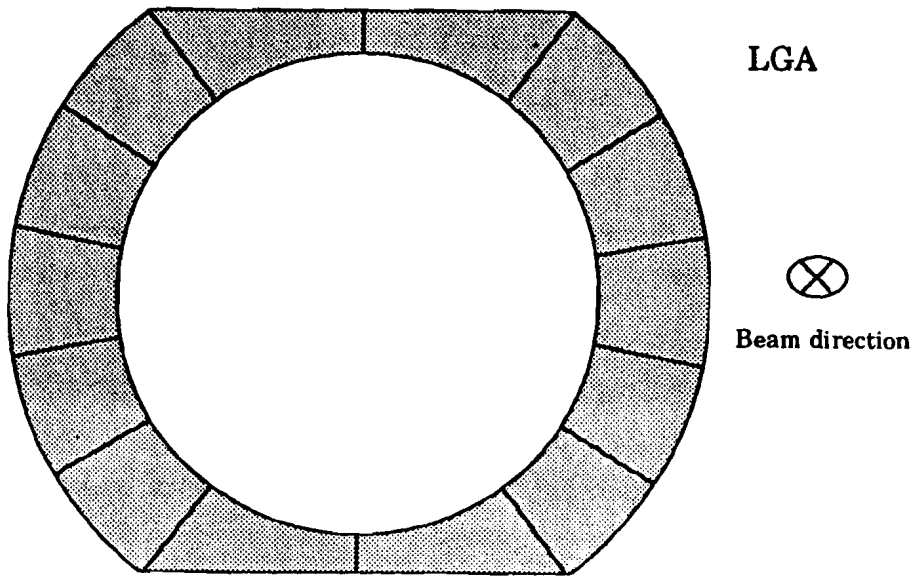

Figure 27. Beam view of the MA and LGA photon veto counters.

brass pipes 0.092" thick, identical to those going through the lead glass and they are aligned to the pipes passing through the lead glass holes. The inner edges of the Cu, the Pb and the scintillator square rings are determined by the pipes which are square of side about 4.6". The outer sides of the rings are about 6.9".

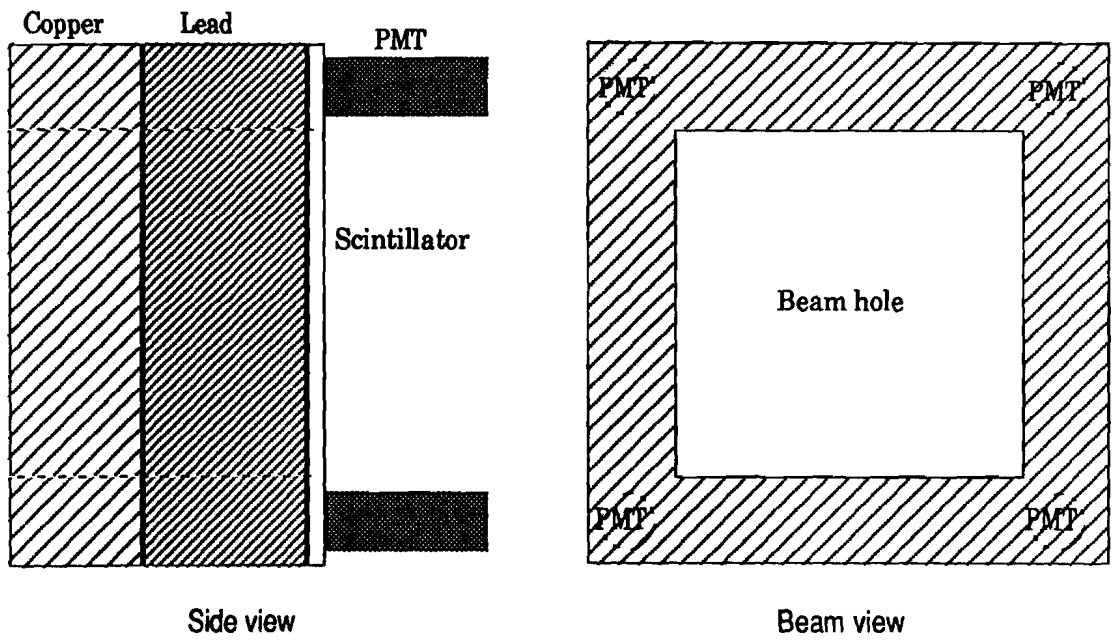

Figure 28. Beam view and side view of the Collar-anti photon veto.

Photons passing through the holes of the calorimeter were identified by the Back-anti (BA) counter system covering an area of 8"x16" around the center of the lead glass array and consisting of 3 similar units of lead lucite sandwitches (see Figure 29). Each unit consisted of a system of 8 vertical strips followed by a system of 16 horizontal strips of lucite counters. Both the vertical and the horizontal strips had 8 layers of lucite counters along the beam direction alternating with layers of 0.125" Pb.

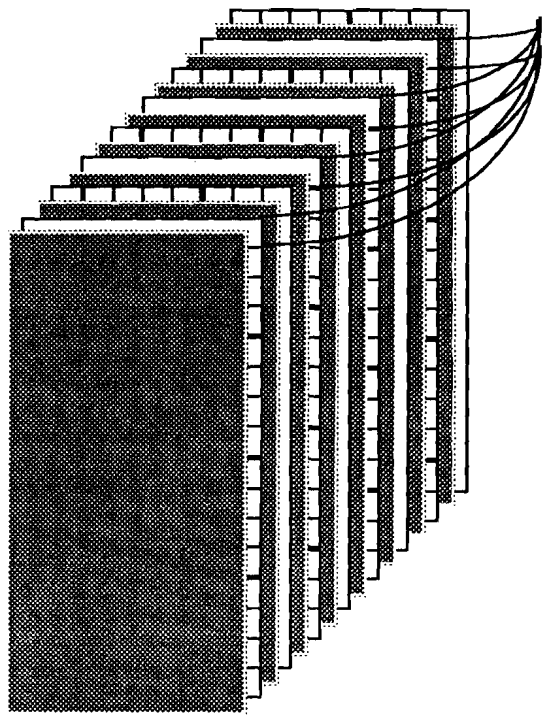

Figure 29. One of the three units of the Back-anti photon veto. The curved lines indicate a group of light pipes.

The light from all 8 lucite counters belonging to the same strip was guided with u.v. transmitting light pipes to a single phototube. So there were 72 phototubes to record the light from all 3 units of the BA system. The 24 vertical strips (8 from each unit) were used in the neutral trigger and this introduced some noise into these counters despite the attempt to minimize it. The BA defining counter (BA_{def}) was a piece of scintillator covering the same 8"x16" area as the BA and it was used in some special trigger that triggered on muons passing through the BA.

The calibration of the VAs, MA and LGA was done by using $K_L \rightarrow \pi^+\pi^- \pi^0$ decays where one of the photons from the π^0 decay has missed the calorimeter and has fired the anticounters. The decay vertex was derived from momentum information on the two charged pions. By assuming that the decay originated from a kaon whose direction was known by using the decay vertex information and knowing the target position it was possible to solve for the energy and the direction of the missing photon. The spatial resolution for the missing photon is $\sigma(r)$~15 cm, $\sigma(\phi)$~0.1 radians and the energy resolution $\sigma(E)$~15%-20%. These resolutions were derived from data-Monte Carlo comparison for $\pi^+\pi^- \pi^0$ events with one photon missing. The gain of each counter which is defined as $g(c) = \frac{energy_{meas}}{energy_{true}}$ had an uncertainty due to the counter itself and due to the reconstruction method. The former uncertainty was estimated again by data-Monte Carlo comparison and it was ~45% for VA1 and VA2, ~35% for VA3 and VA4, ~30% for MA and ~25% for LGA and DRAN.

BA was calibrated by muons required to project through each of the 8 lucite strips of and by $K_L \rightarrow \pi e \nu$ decays where the electrons hit BA. The muons used were taken from special tapes $B^*\mu^*BA_{def}$ providing ~300-1000 muons/counter and the $K_L \rightarrow \pi e \nu$ were selected from normal "charged" trigger data. The muon gains were used as a starting point and they were corrected by Ke3 to minimize the energy resolution. This correction was significant for the vertical but not the horizontal strips and especially for low energies where the noise level is more important. The correction also affected mostly strips in the first two units and especially the central ones. The resolution is $\frac{\sigma_E}{E} = \frac{40\%}{\sqrt{E}}$.

CHAPTER 3

THE CLUSTER - FINDER TRIGGER PROCESSOR

It was realized from the 1985 test run of the experiment that the four-cluster events which were of great importance for the ε'/ε measurement consisted of only about 10% of the total number of events as shown in Figure 35. Therefore it turned out necessary to build a trigger processor [30, 31] that would have the ability to trigger at four clusters and thereby improve the statistical power of the ε'/ε measurement.

3.1 Overview

As already discussed in Chapter 2, we used our lead glass calorimeter to measure energies and positions of electromagnetic showers (clusters). This calorimeter consisted of 804 blocks and it was organized in an array of 32 columns by 32 rows as shown in Figure 30. The Cluster Finder was used as a second level trigger to find and count the number of clusters associated with every event by scanning the rows of the array from bottom to top and the columns of the array from left to

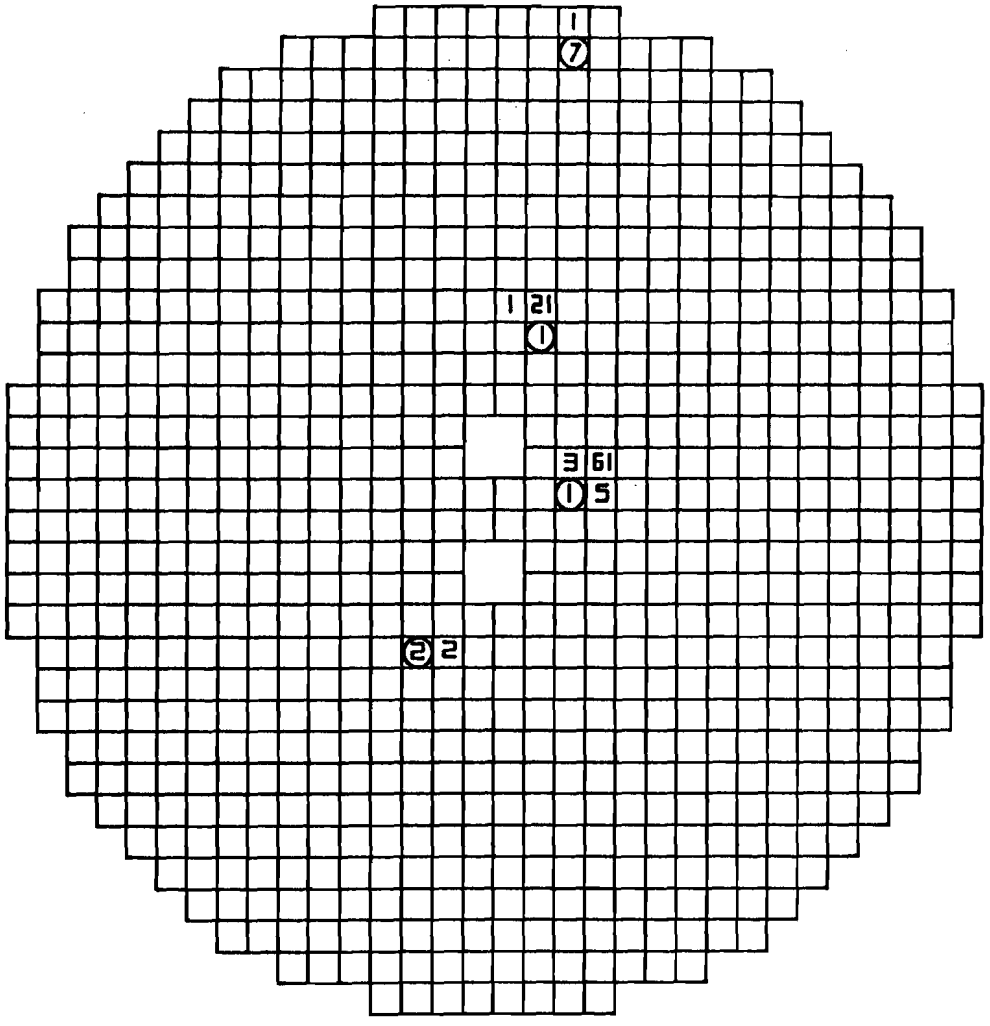

Figure 30. An on-line event display of energy deposited in the lead glass array for a four-cluster event. The numbers represent the amount of energy in GeV. The circled numbers indicate in which block the processor found the "seed" of a cluster.

right. In this chapter a cluster is defined as an island of connected glass blocks each with deposited energy above a preset threshold. The raw data (804 bits) were mapped onto the EPLDs (Erasable Programmable Logic Devices) located on two algorithm boards (the Cluster Boards) where the cluster finding is implemented. The controlling of the cluster finding was done by six cards: the Flash Card Controller, the Cluster Buffer, the Cluster Controller, the System Controller which consists of two cards and the Trigger I/O card. They communicate with each other by an S-100 bus backplane. The signals assigned on this bus include 32 data bits, 5 address bits, 6 instruction bits, 4 clocks (strobes A, B, C, D), two status bits (Status1 and Status2), 4 bits for the number of clusters and a reset. The operation of the processor depends critically on the System Controller which through its sequencer and memory generates instructions that the control cards decode with their corresponding EP600 or EP900 Altera EPLDs. The system operates in a form of parallel processing in the sense that all the control cards receive the same instruction at the same time and execute it if they are programmed to decode it. The processor communicates with CAMAC via an interface card, the CAMAC Card.

3.2 Description

The Cluster Finder consists of four subsystems: 1) the front end electronics, 2) two Cluster Boards with 150 EP900 Altera EPLDs where the cluster finding algorithm is implemented, 3) the control cards and 4) the CAMAC interface. Figure 31 shows the overall hardware structure of the processor.

3.2.1 The front end electronics

The front end electronics consists of 10 crates and backplanes loaded with Flash Cards and Buffer Cards. The photomultiplier signals from

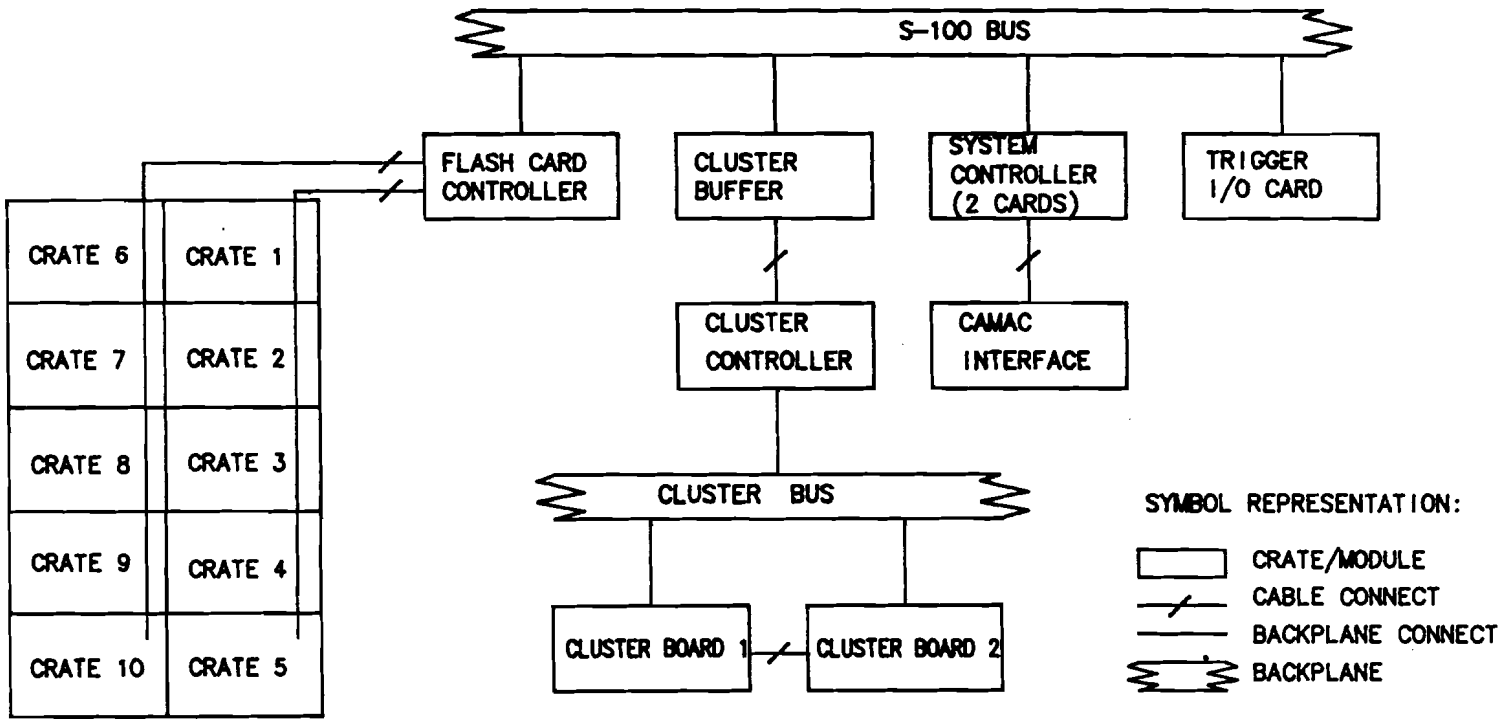

Figure 31. General hardware layout of the Cluster Finder trigger processor. Each one of the ten backplanes has three or four flash-ADC cards and a buffer card.

the 804 lead glass blocks after~ 450 ns cables delay, were led to the FASTBUS ADC main data acquisition modules. They were also fed to ten backplanes where they were capacitively picked off, amplified by a differential high impedance amplifier of gain 30, digitized by a 30 MHz 6-bit flash ADC and compared with a preset threshold through a 6-bit parallel digital comparator. The threshold was chosen to be about 1 GeV to optimize the event acceptance. Each crate's backplane contained 3 or 4 Flash Cards and a Buffer Card and each one of the Flash Cards was fed by 24 lead glass signals. The Buffer Card distributed the lead glass thresholds, the address of the data to be read and the flash ADC strobe to the Flash Cards. The impedance of the Flash Card system was about 10000 Ohms for each one of the 24 channels and the current drawn by each Card was approximately 1 A. About 0.5% of each phototube's signal was picked by the processor for cluster finding purposes. We checked the pulse heights of a signal with the Flash Cards plugged in and out of the backplanes and within our resolution we could not see a difference.

3.2.2 The Cluster Boards

The cluster finding process was executed by two Cluster Boards which were 3 layer printed circuit boards consisting of an array of 150 EP900 Altera EPLDs [32] and some control circuitry. We had the ability to use on the Boards a 3 V source besides a 5 V one, which turned out helpful in: a) reducing the power dissipation and b) speeding up the process by reducing the fall time in the response of the chips. (for each one of the Altera chips $\frac{dV}{dt}$ was fixed by the capacitance and the maximum current that the chip can sink; therefore the only way to reduce the fall time was to reduce the voltage difference between the source and ground) Each Board contained 75 EPLDs, 38 drivers, 115 resistors of 560 Ohms pulling up the Altera chips to 3 Volts, 6 resistors of 122 Ohms and 204 capacitors. The EP900 EPLDs were high speed 40 pin chip carriers with more than 900

gates each. They were allowing for 12 dedicated inputs, 24 I/O pins which can be configured for input, output or bidirectional operation and 2 synchronous clock inputs. Each EPLD contains logic for 6 lead glass blocks configured in a two row by three column region and provides six flags indicating whether the associated lead glass block had energy above or below threshold. Figure 32 shows the communication lines (links) between the six cells of an EPLD and the EPLD and its neighbor cells. The ICs are all CMOS. A HI (+5V) of the flag indicates that the lead glass block is below threshold and a LO (ground) indicates it is above threshold. In general, negative logic is used for the design of the boards so that the wire-or technique is applicable. In fact there are 32 wire-ors corresponding to the 32 columns of the array and each one of them has 32 inputs corresponding to the 32 rows. The EPLDs on the Cluster Boards recognize five basic input instructions which are generated by an EP900 Altera EPLD on the Cluster Controller card and through receivers and drivers are distributed to the appropriate pins at the EPLDs. The instructions are "write", "find address priority","read or find column priority", "associate" and "clear". These are global instructions that all the EPLDs execute simultaneously. First the data from the lead glass array has to be mapped onto the flags by using the "write" instruction. The data is received via 32 data lines corresponding to the 32 rows in the array and one column is being written at a time. We refer from now on to rows and columns as data and address respectively. An EPLD on the Cluster Boards loads one of its 6 flags LO if (i) the "write" instruction is active, (ii) its column input is LO and (iii) its row input is LO. Conversely, an EPLD will load one of its 6 flags HI if (i) the "write" instruction is active, (ii) the corresponding column input is LO, but (iii) the row input is HI. The flags are controlled by JK flip-flops and must be strobed whenever one wants to change the status of the flag. The flags will stay loaded until: (a) the "clear" instruction is active, or (b) new data is being written over or (c) the cluster "associates" and by doing so erases itself. After the data is mapped on to the cells of the EPLDs, clusters are found by

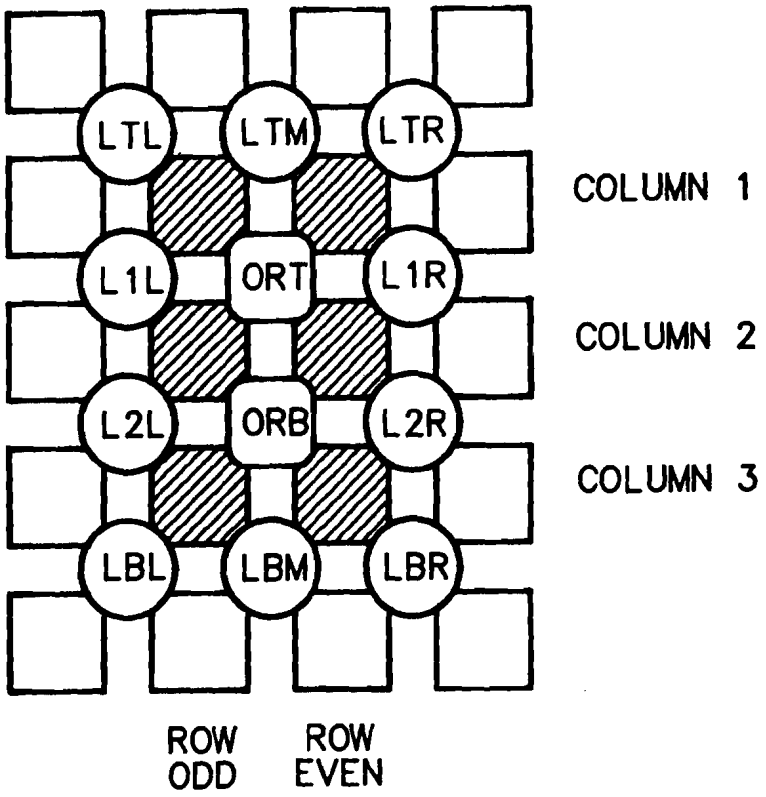

Figure 32. Relationship of the six cells of an EPLD between themselves and with cells of neighbor EPLDs. The circles are communication lines between the EPLD and cells of neighbor EPLDs. The first L in the three-letter acronyms stands for "link". For the other two letters, T stands for "top", B for "bottom", L for "left", R for "right" and M for "middle". 1 and 2 signify the first and second link that are both located either at the left - or the right-hand side of the EPLD. The curved boxes ORT (OR top) and ORB (OR bottom) are communication lines between the six cells of an EPLD.

identifying active cells and then searching for active neighboring cells. In order to find an active cell one searches first which of the 32 wired-or columns have hits on to them. One column is chosen during "find address priority" instruction (address seed) and then it is checked which of the rows in this column have been hit. One of them is picked during the "read" instruction (data seed) and the cell picked in this way is called a "seed"(see Figure 30). The identification of all the other neighboring cells of the same cluster begins during the "associate" instruction. The seed sends messages to its eight nearest neighbor blocks which, if they are hit, will send messages to their neighbors and so on like a chain reaction. In addition to sending out messages to its neighbors, a cell will simultaneously set its JK flip-flop to change its flag. The entire cluster in this way erases itself so that double counting is prevented. The "clear" command in the end clears all the flags. Figure 33a shows how two of the six cells in an EPLD operate with the "write", "read" and "clear" instructions. Figure 33b shows how these same cells operate with the "find address priority" and "associate" instructions. The functioning of the EPLDs was tested in two steps. In the first step a software package [32] which was used to design the logic was also used to simulate the functions and timing of the ICs. In the second step each programmed EPLD sitting on a test board and communicating with a PDP-11 computer had to recognize succesfully several patterns written on to it. EPLDs that passed this detailed test show no failures during the run.

3.2.3 The Control Cards

All control cards use negative logic in general and were built almost entirely with CMOS ICs. They operate using a set of 25 instructions defined in Tables 3 and 4.

Figure 33. The algorithm with which two cells of an EPLD (odd1 and even1) belonging to column 1 and to the odd and even row respectively operate. (a) Instructions "write", "read" and "clear". COL1 stands for Column 1 and RODD and REVEN for the odd and even rows respectively. (b) Instructions "find address priority" and "associate". L1LOE is the name of the wire that enables the output for L1L. OD1ORTOP stands for "the cell with flag ODD1 activates the OR gate ORTOP". EV1FIRETM stands for " the cell with flag EVEN1activates LTM". Other wire names have similar meanings. The prefix X in front of a wire name indicates inversion.

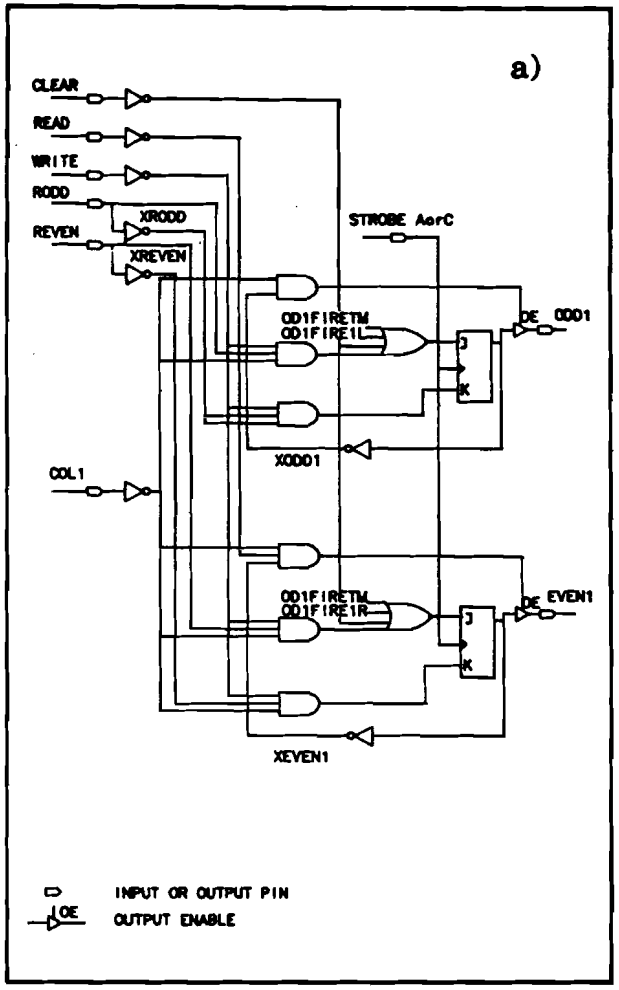
a)
CLEAR
READ
WRITE
RODD
REVEN
XRODD
XREVEN
STROBE AorC
OD1FIRETM
OD1FIRE1L
OE
ODD1
XODD1
COL1
OD1FIRETM
OD1FIRE1R
OE
EVEN1
XEVEN1
INPUT OR OUTPUT PIN
OE
OUTPUT ENABLE

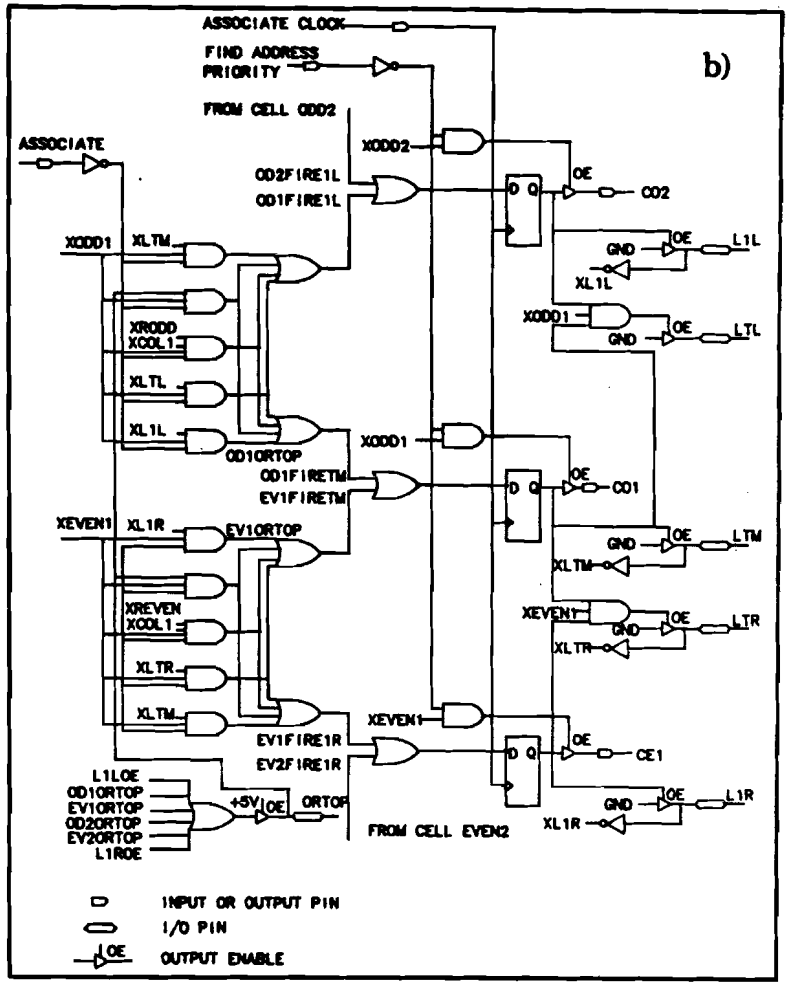
b)
ASSOCIATE CLOCK
FIND ADDRESS PRIORITY
FROM CELL ODD2
ASSOCIATE
XODD2
OD2FIRE1L
OD1FIRE1L
OE
CO2
XODD1
XLTM
GND
OE
L1L
XL1L
XRODD
XCOL1
XODD1
GND
OE
LTL
XLTL
XL1L
OD1ORTOP
XODD1
OD1FIRETM
EV1FIRETM
OE
CO1
XEVEN1
XL1R
EV1ORTOP
GND
OE
LTM
XLTM
XREVEN
XCOL1
XEVEN1
GND
OE
LTR
XLTR
XLTR
XLTM
XEVEN1
EV1FIRE1R
EV2FIRE1R
OE
CE1
L1LOE
OD1ORTOP
EV1ORTOP
OD2ORTOP
EV2ORTOP
L1ROE
+5V
OE
ORTOP
FROM CELL EVEN2
GND
OE
L1R
XL1R
INPUT OR OUTPUT PIN
I/O PIN
OE
OUTPUT ENABLE

TABLE 3. Instructions in the main sequence.[1]

INSTR. No	CONTROL CARDS	ACTION
1	System Controller A	Wait for trigger or CAMAC "start"
2	System Controller A	Clear address counter
3	System Controller B	Clear FIFO
4	Cluster Buffer	Clear cluster counter
5	Flash Card Controller Cluster Buffer Cluster Controller System Controller A,B	Transfer data from Flash Cards to Cluster Boards and to FIFO (This instruction is executed 32 times inside normal sequence)
6	Cluster Controller	EP900 EPLDs on Cluster Boards execute "Find Address Priority" instruction; address priority is picked and gets latched
7	Cluster Controller Cluster Buffer System Controller A,B Trigger I/O Card	Address priority is sent back to the Cluster Boards; number of clusters available to S-100 bus; the sequence is terminated when all clusters have been found or the maximum number of clusters has been exceeded
8	Cluster Controller	The flags of EP900 EPLDs are read and priority is picked and latched
9	Cluster Controller	Data priority is sent to Cluster Boards; "associate" instruction active, "associate" clock not active yet
10	Cluster Controller	"associate" instruction and "associate" clock are active
11	Cluster Controller Cluster Buffer System Controller B	"associate" instruction is active, "associate" clock not active; strobe C erases cluster; increment cluster counter; write seed to FIFO
12	Cluster Controller	Clock instruction

[1]Column 1 indicates the instruction number and column 2 the control cards that participate in the instruction.

TABLE 4. Instructions for testing purposes and for special service in the system.

INSTR. No	CONTROL CARDS	ACTION
13	Flash Card Controller Cluster Buffer System Controller A	Load lead glass thresholds and maximum number of clusters
14	Flash Card Controller Cluster Buffer System Controller B	Read lead glass thresholds and maximum number of clusters
15	Flash Card Controller System Controller A,B	Move data from Flash Cards to FIFO using address loaded from CAMAC
16	Flash Card Controller System Controller A,B	Move data from Flash Cards to FIFO using address loaded from address counter
17	System Controller A Cluster Buffer Cluster Controller	Write data from CAMAC to the Cluster Boards
18	System Controller A,B Cluster Buffer Cluster Controller	Read the Cluster Boards to the FIFO using address from address counter (this instruction is repeated 32 times)
19	System Controller A,B Cluster Buffer Cluster Controller	Read the Cluster Boards to the FIFO using address loaded from CAMAC
20	System Controller A,B	Move data from System Controller A to System Controller B
21	System Controller A,B	Move CAMAC loaded address through address counter to FIFO
22	Cluster Controller	"associate" instruction and "associate" clock are active
23	System Controller A Cluster Buffer Cluster Controller	CAMAC loaded data seed (32 bits) is loaded to Cluster Boards at a certain address
24	Cluster Controller Cluster Buffer System Controller B	Read to FIFO the 32 bits of data seed
25	System Controller A	Go to the idle state

3.2.3.1 Flash Card Controller

The main function of the Flash Card Controller is to transfer data stored in the Flash Cards via the S-100 bus backplane to either (i) the Cluster Boards or (ii) the FIFO (First In First Out) of the System Controller for testing purposes. The data are transferred in 32 steps which correspond to the 32 columns and each transfer is controlled by a 5-bit address. This address is loaded through the Flash Card Controller to two 50 pin cables with each cable daisy-chaining to 5 Flash Card backplanes. When the address reaches the Buffer Card of the backplanes, the Flash Cards load the corresponding data through the Flash Card Controller onto the 32 data bit lines of the S-100 bus backplane.

The other function of the Flash Card Controller is to load the lead glass threshold through the S-100 bus backplane to the two cables and then to the Buffer Cards of each backplane. The threshold uses 6 data bits on the S-100 bus. It can be read back by the system for testing purposes after it has been latched.

3.2.3.2 Cluster Buffer

The Cluster Buffer card is the interface between the S-100 bus backplane and the Cluster Controller. One of its functions is to receive data and address from the S-100 bus and load them to the Cluster Controller so that data are written on the Cluster Boards at the appropriate address. Data and address enter the Cluster Buffer from the S-100 bus backplane through the 32 data bits and the 5 address bits respectively and are driven to Cluster Controller by transceivers.

Another function of this card is to pass the data and address seed information from the Cluster Controller card to the S-100 bus backplane and from there to the FIFO. The seed uses 5 data bits for row and 5 address bits for column. The Cluster Buffer card passes also the 6 instruction bits and 4 strobes to the Cluster Controller and receives from there a message "DONE" (LO) signifying that all clusters have been found and counted. This message is passed to the S-100 bus backplane as Status1.

The maximum number of clusters permitted to be found in each event is loaded to this card via 4 data bits from the S-100 bus and is latched at instruction 13. It is read back to the FIFO of the System Controller together with the seed information and the number of clusters in the event at instruction 9.

On the Cluster Buffer there is also an 8-bit cluster counter that counts the number of clusters found in the event. The cluster counter adds "1" to the number of clusters during instruction 11. At instruction 7 the output of the counter is compared with the maximum number of clusters allowed and if an overflow exists, a LO is sent to the S-100 bus as Status2. The same instruction outputs the number of clusters to the S-100 bus. The number of found clusters is available as 4 data bits which is latched at the FIFO and also as 4 "cluster lines" which are inputs to the Trigger I/O card.

3.2.3.3 Cluster Controller

The Cluster Controller is an interface between the Cluster Boards and the rest of the system controlling the writing and reading of the Cluster Boards. It generates 5 global instructions and it handles the cluster seed search. It connects to the Cluster Boards by a custom wire-wrap backplane (a MUPAC cluster bus) with about 300 pins distributed on three connectors each with three rows. One of the main functions of the card is to transfer data from the Cluster Buffer card through transceivers and write them with the "write" instruction to the Cluster Boards. The address is decoded with a 5 to 32 converter. After the data are written the array is ready to be scanned for clusters. The column that contains a seed is found by a priority circuit which consists of four 8-line to 3-line priority encoders, 12 two-input "and" gates and a latch. The priority column is then chosen, latched and required to output the row data. A second similar priority circuit decodes and latches the row priority. Both the data

and address seed information are contained in 32 bits each and are encoded into 5 bits by using 32 to 5 bit converters. The seed is then transferred to the Cluster Buffer and to the S-100 bus backplane. The functions of the Cluster Controller are controlled by an EP900 Altera EPLD located on the card. The card also produced a 100 ns clock (associate clock) by "oring" of the four strobes. This clock is used by the EP900 EPLDs on the Cluster Boards at instructions during the cluster finding process.

3.2.3.4 System Controller

The System Controller (CPU of the system) consists of two cards each containing an EP600 Altera EPLD that controls the functions of the card. The first one, System Controller A, has the sequencer and an EPROM. It generates a four phase clock for synchronization and also the address of the data to be read or written through an address counter. The second one, System Controller B contains the FIFO.

System Controler A

a) The sequencer consists of three 4-bit counters which are connected through the "Ripple Carry" output and an "enable" input pin. Its 11 output lines are the address inputs to the EPROM and its 11 inputs is the address of the PROM loaded from CAMAC for testing purposes. At normal cluster finding operation the address of the PROM is incremented automatically through the sequencer counters. The sequencer clock is effectively the complementary output of a flip-flop, which is set either by trigger or by CAMAC. The sequencer is stopped by one of the two conditions: (i) a LO pulse has to be fed to the synchronous clear input of the three sequencer counters or (ii) a HI on the sequencer clock. The first condition is satisfied either during instruction 7 and when Status1 or Status2 is a LO or during instruction 25 which is designed just to bring the system at an idle state. The second condition is satisfied by giving a LO input to the clock flip-flop during either one of the above mentioned instructions. The EPROM is 2048 word x 8 bit and consists of a 7 bit row

decoder, a 4 bit column decoder, an 128 x128 programmable array and a multiplexer. The contents of the memory location become available at 8 output lines at strobe A.

b) The 4 phase clock has a cycle of 400 ns and consists of four strobes (A, B, C, D) each seperated by approximately 100 ns. It is generated by the combination of two delay lines, two flip-flops, an 8-bit shift register which features serial inputs and an asynchronous clear, two dual pulse synchronizers, "nand", "or" and "inverting" gates and four switches. In Reference [31] one can find a more detailed description of this clock.

c) The address counter gets incremented at strobe A during instructions that write data to the Cluster Boards or read data either from the Flash Cards or from the Cluster Boards. One can also preload the address counter through CAMAC.

System Controller B

System Controller B communicates through two 50 pin twisted pair cables with CAMAC and through the S-100 bus backplane with the rest of the system. Its main function is to store the seed, number of clusters and maximum number of clusters as well as the 804 flags in the FIFO. Eight FIFO 64x4-bit chips are used. The Master Resets of all 8 chips are connected and during instruction 3 they are pulsed LO to accept data at the first location. These data enter the FIFO when the "Shift In" input of each chip is brought HI during instructions 7,11,15 and 18 and at the appropriate strobes. When data is shifted to the outputs of all 8 chips, CAMAC Card creates a shift-out pulse that is sent to the FIFO and data is buffered to the CAMAC Card. There is also a status buffer on System Controller B that could be read through CAMAC to indicate the status of the system.

3.2.3.5 Trigger I/O card

The Trigger I/O card is located in the S-100 crate. One of its major functions is to accept the master trigger from outside and output a "start"

signal onto the S-100 bus backplane. This "start" signal starts the sequence of instructions at the System Controller. Another major function of the Trigger I/O card is to output a "reject" or an "accept" trigger for the event on the basis of the number of clusters found. The number of clusters enters the card through the 4 "cluster lines" of the S-100 bus and is decoded into 10 mutually exclusive outputs (0-9 clusters) through a demultiplexer. Each one of the 10 outputs could be prescaled if desired. An "accept" or "reject" TTL signal is issued for the event during instruction 7 and when Status1 or Status2 have a LO. Another signal indicates if the sequence has stopped or not and at the end of the sequence the number of clusters is available externally through a 20-pin cable. In this experiment we accepted all the events with four clusters in the final state. The six cluster events were taken unprescaled or prescaled by a factor 4 or 8. Other numbers of clusters were prescaled by factors 64 or 128 or 256 at different time periods. Special data have been taken with the Cluster Finder out of the trigger for diagnostic purposes.

3.2.4 The CAMAC interface

The CAMAC Card is the interface between CAMAC and the System Controller cards. One of its main functions is to receive each of the 32 bit words from the FIFO as two sequential 16 bit words appropriate for CAMAC. With the CAMAC Card, data, address and PROM address can be loaded for testing purposes to the System Controller through four instructions as shown in Table 5 and they can be read back to the CAMAC Card as shown in Table 6. When PROM address is loaded from CAMAC, the synchronization between CAMAC and the rest of system which has a 400 ns cycle is achieved as shown in Figure 34.

3.3 Operation

Twenty-five instructions (besides the 5 global instructions mentioned earlier) were defined to complete all the tasks required for normal cluster finding operation and for diagnostics (Tables 3 and 4). The system first oaded the lead glass threshold to the Flash Cards and the maximum number of clusters to the comparator located on the Cluster Buffer and

TABLE 5. Instructions controlling the loading of data, address and PROM address from CAMAC to System Controller.

CAMAC Subaddress Code	CAMAC Function Code	CAMAC Strobe	Description
A(1)	F(16)	S1	16 bits of data (Data1-Data16) are transferred through 16 "write" lines of CAMAC and drivers to System Controller A and get latched
A(2)	F(16)	S1	16 bits of data (Data17-Data32) are transferred through 16 "write" lines of CAMAC and drivers to System Controller A and get latched
A(3)	F(16)	S1	5 bits of data address are transferred through 5 "write" lines of CAMAC and a driver to System Controller A and get latched
A(4)	F(16)	S1	11 bits of PROM address are transferred through 11 "write" lines of CAMAC and drivers to System Controller A and get latched

TABLE 6. Instructions controlling the reading of data, address and PROM address latched at System Controller to CAMAC.

CAMAC Subaddress Code	CAMAC Function Code	Description
A(1)	F(0)	16 bits of data (Data1-Data16) are read back to CAMAC through 16 "read" lines
A(2)	F(0)	16 bits of data (Data17-Data32) are read back to CAMAC through 16 "read" lines
A(3)	F(0)	5 bits of data address are read back to CAMAC through 16 "read" lines
A(4)	F(0)	11 bits of PROM address are read back to CAMAC through 11 "read" lines

then it was in an idle state waiting for a CAMAC instruction or for a trigger "start" to start a main sequence of instructions within which the loading of the data and the cluster finding operation is performed.

The main sequence first includes three instructions that clear the address counter located on the System Controller A, the FIFO located on System Controller B and the cluster counter located on Cluster Buffer. In the subsequent instruction the data are transferred from the Flash Cards to the Cluster Boards and to the FIFO. This instruction was executed 32 times transferring one row (32 bits) at a time. After the data had been written onto the Cluster Boards a cluster finding group of 7 instructions followed. With the first instruction the address priority was encoded from 32 into 5 lines and latched. The second instruction transferred this

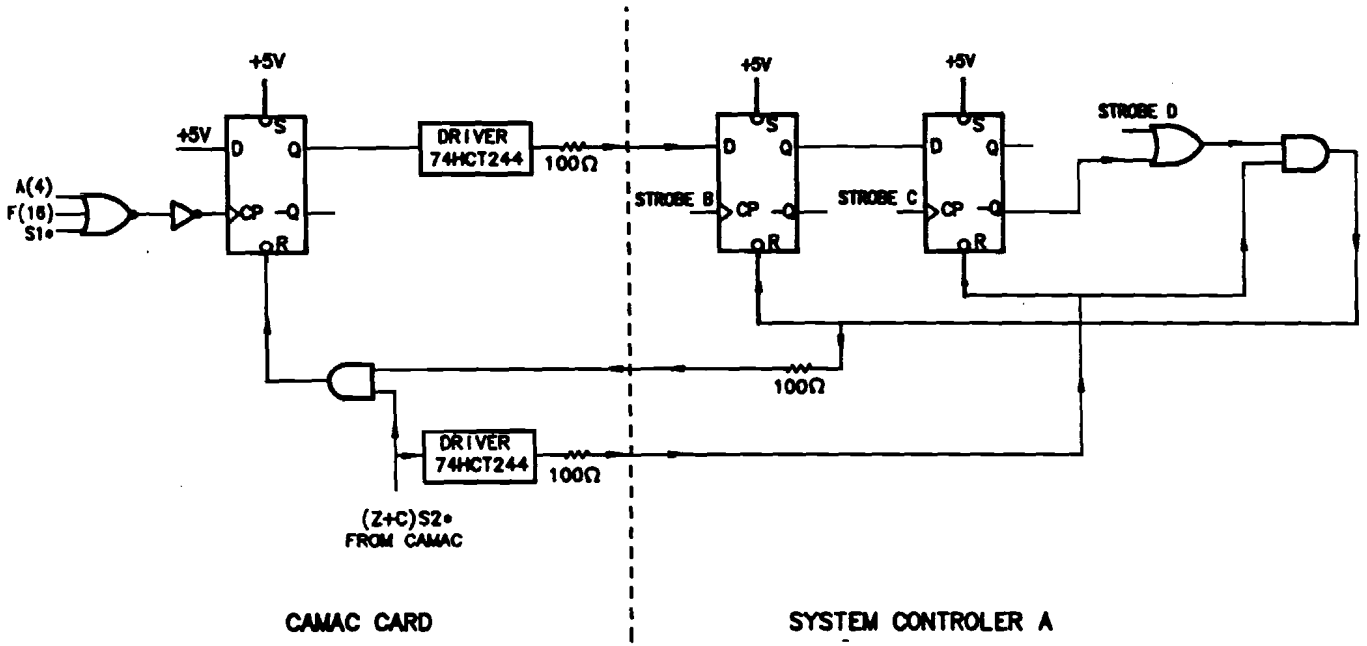

Figure 34. Illustration of synchronization between CAMAC and the trigger processor. A(4) and F(16) are CAMAC subaddress and function codes respectively, and S1*, S2* are CAMAC strobes. Z and C are the "initialize" and "clear" CAMAC controls.

priority back to the Cluster Boards. At this instruction the sequence terminated when there were no more clusters or when the maximum number of clusters had been reached. At the third instruction the flags of the EP900 Altera EPLD's were read and the column priority picked and latched. At the fourth instruction the data seed was sent to the array along with the associate request (no clock activated yet). The association continued during the fifth and sixth instruction. During the C strobe of the sixth instruction the cluster was erased after communicating with a 7x7 block neighborhood and the cluster counter was incremented by "1". The seventh instruction was a clock instruction providing some flip-flops inside the EP900 EPLDs with the necessary pulse to stabilize their status. The cluster finding group of instructions could be repeated 10 times (allowing for 10 clusters to be found). A typical "four cluster" event took about 25 μs to be processed.

3.4 Results

The Cluster Finder processor was used in the data-taking run between August 1987 and February 1988 and reduced the trigger rate by about a factor of 10 while contributing less than 2% dead time to the online data acquisition system. Figure 35 shows the distribution of the number of clusters per event (determined by software) from special runs during which the processor was taken out of the trigger. One can notice that the "four cluster" events for which we wanted maximum acceptance are only about 10% of the total number of events. Figure 36 shows the distribution of the number of clusters from a normal data taking period, with the processor in the trigger, during which we recorded four and six cluster events without any prescaling. Figure 37 shows the distribution of the energy of any block above the Cluster Finder threshold. The sharp edge indicates that the relative gains of all 804 glass blocks were matched

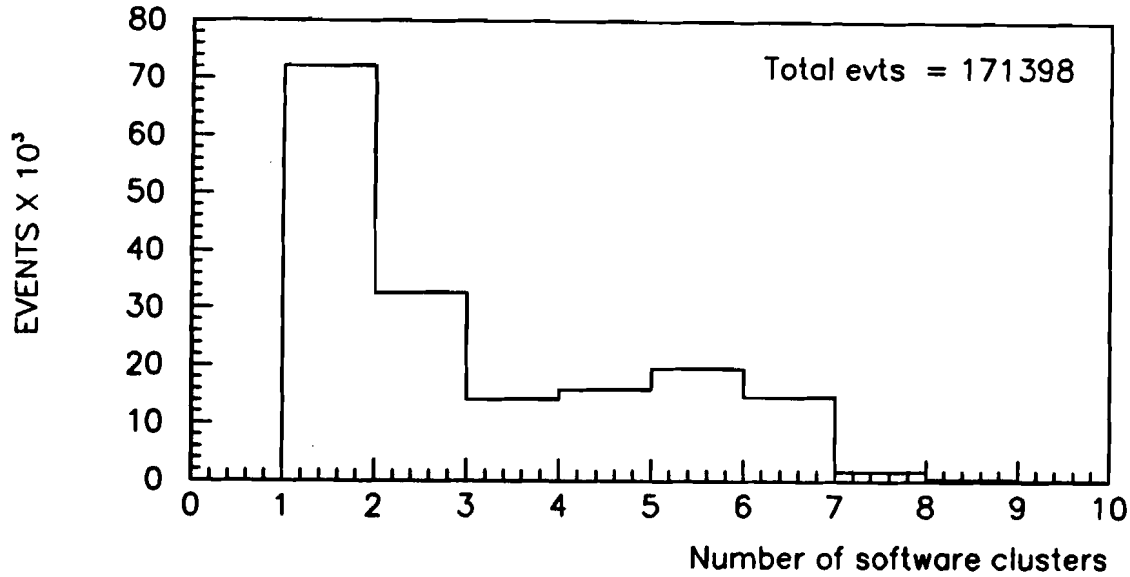

Figure 35. Distribution of the number of software clusters without the Cluster Finder in the trigger.

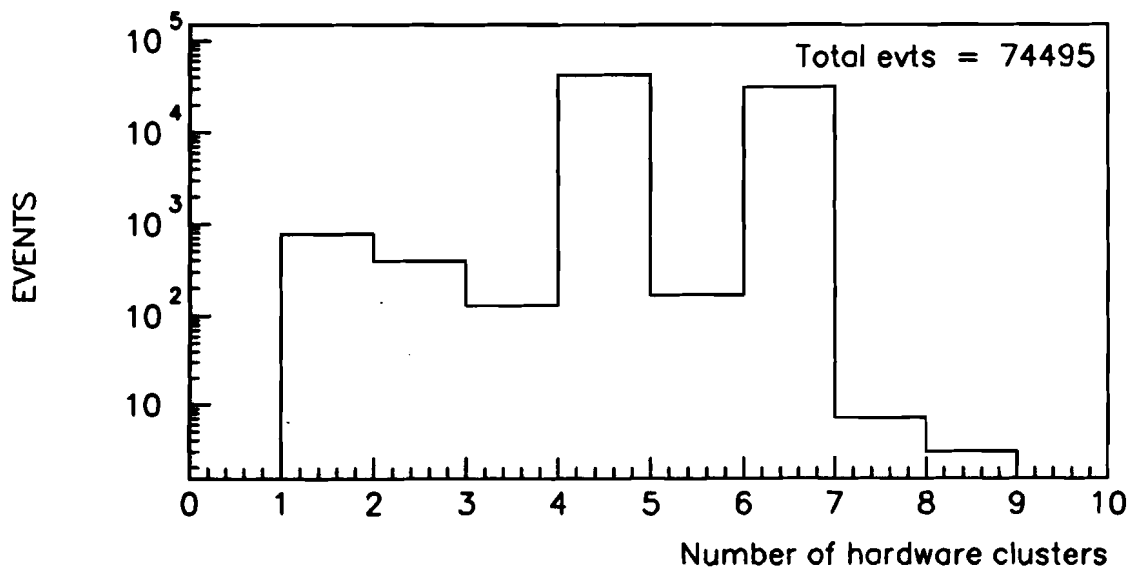

Figure 36. Distribution of the number of hardware clusters with the Cluster Finder in the trigger.

online to within about 5%. Because of this gain variation, the thresholds of the Cluster Finder are not a step function but an error function. The Cluster Finder thresholds were determined by using some of the $K_L \rightarrow 3\pi^0$ events that were taken during the last month of running for which lots of statistics were available. For every block there was plotted in bins of 2 counts of the corresponding ADC channel a ratio indicating how often the block had energy above the HCF threshold compared with how often it had any energy. This ratio was fitted with the error function

$$\frac{1}{\sqrt{2\pi}} \int_{-\infty}^{+\infty} e^{-\frac{x^2}{2\sigma^2}} dx$$

where x represents ADC counts. For each block we found the center and the width (σ) of the gaussian which are plotted in Figures 38 and 39.

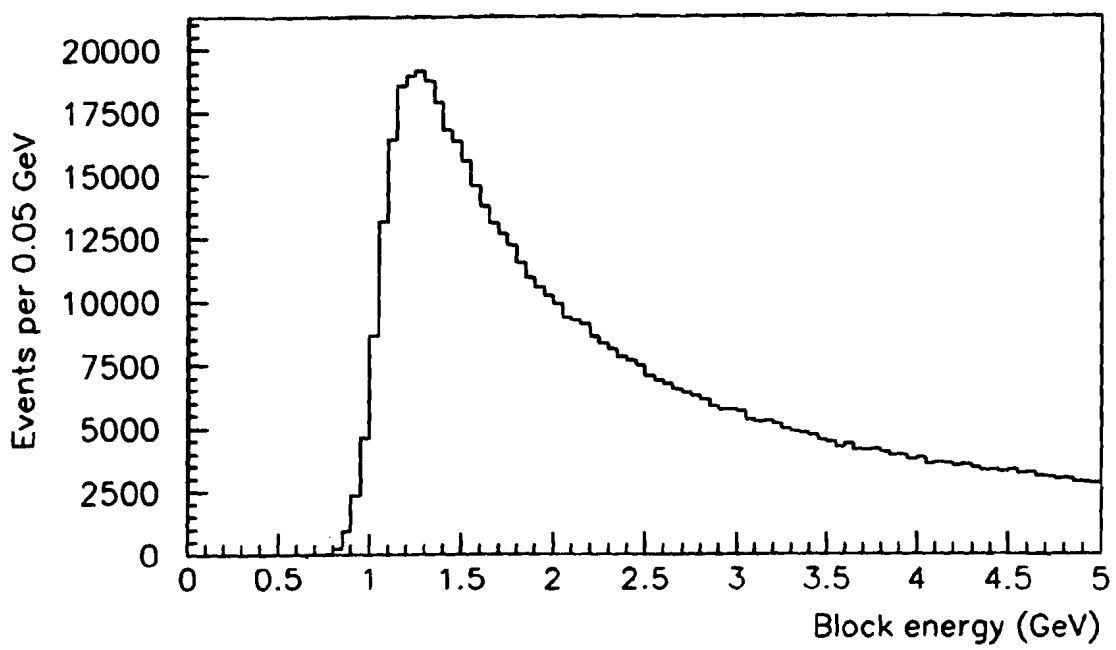

Figure 37. Energy distribution of lead glass blocks above the Cluster Finder threshold. The threshold was set at about 1 GeV.

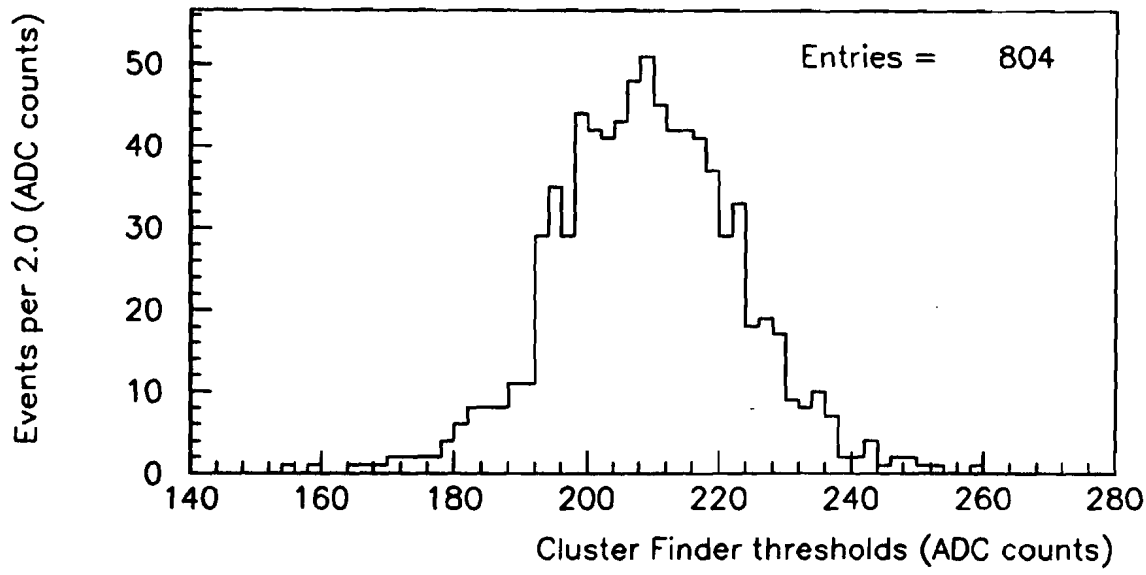

Figure 38. Cluster Finder thresholds for each one of the 804 lead glass blocks in ADC counts. 210 counts correspond to about 1 GeV.

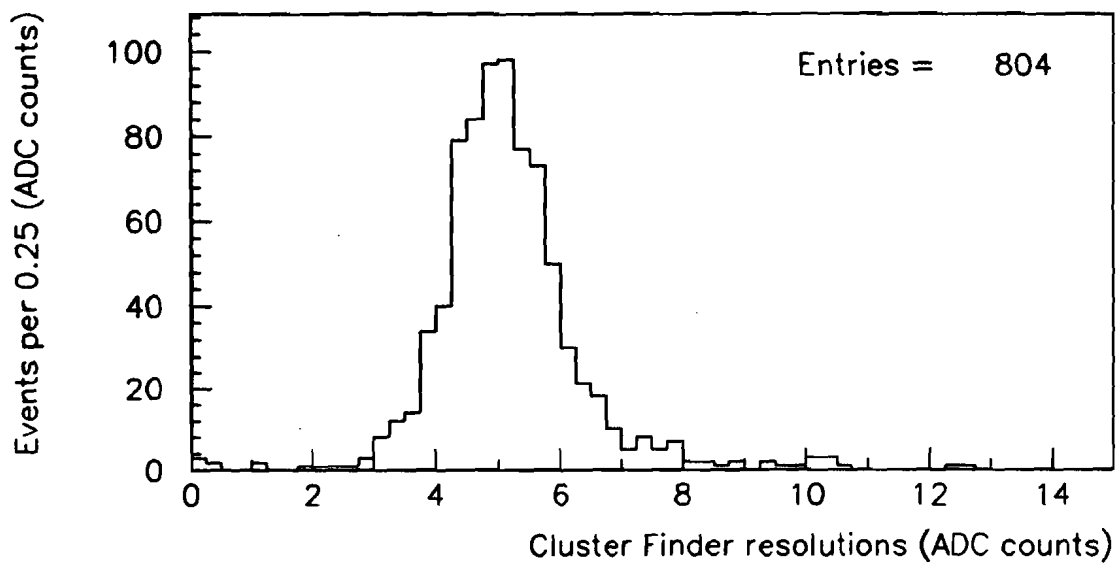

Figure 39. Cluster Finder resolutions in ADC counts for each one of the 804 lead glass blocks.

From now on we will call thresholds the centers of the gaussians and resolutions their widths. The data used for the threshold determination were $3\pi^0$ from 40 raw tapes from which 20 were recorded earlier and 20 were recorded later in the last month of the run. Comparison of the thresholds in these two subperiods showed that they were reasonably stable. The Monte Carlo generation program has used the threshold information in the emulation of the HCF and in this way the agreement between data and Monte Carlo was improved.

In all our recent publications [6, 11, 27, 33] referring to searches of the $K_{L,S} \rightarrow \pi^0 e^+e^-$ and $K_L \rightarrow \pi^0\gamma\gamma$ rare decays and the ε'/ε and $\Delta\phi$ measurements the data on which we based our results used the "four-cluster" sample provided the Cluster Finder. The statistical power we got would be impossible without the processor. The same processor will be also used in the Fermilab experiments E-773 and E-779 [34, 35].

CHAPTER 4

TRIGGER DESCRIPTION

The data described in this thesis were taken during the 1987-1988 fixed target run at the Fermilab Tevatron. We started writing data to tape in early July 1987 and we finished in the middle of February 1988. The first month of data taking was largely devoted to studying and understanding the detector and therefore the usuable data start from August 1987. In order to collect enough statistics for the ε'/ε measurement we ran at high intensity with an efficient trigger which minimized the dead time and increased the signal to noise ratio. This chapter describes the trigger logic and the different modes in which the experiment was operated.

4.1 Trigger logic

The timing in the experiment was determined by using timing signals from the accelerator. The timing of all the triggers was defined by the 53 MHz RF signal described in section 2.2 which reflects the spill

substructure determined by the accelerator. Besides RF, four fixed timings were given to us every minute: T1, T2, T5 and T6 from which T5 signaled the beginning and T6 the end of the 22 second spill. Five seconds after T2 we began to read out an event by initializing FASTBUS and CAMAC and starting to accumulate pedestals and flashers. At T5, which signaled the beginning of spill, we recorded the low and high range pedestals for both the lead glass and other ADCs. These pedestals are averages of the accumulated pedestals up to that time; they are the same for all the events in the spill and they are subtracted from the signal of the corresponding ADCs. T6 signaled the end of spill and also disabled all the triggers. In the time interval between T5 and T6 there was open a 0.5 s gate for the scaler which monitored the temperature of the base of one phototube in the calorimeter, the temperature of the front face of a block near the pipe, the air temperature in the lead glass house and the temperature at the top of the crate of the lead glass ADCs. In addition to the temperature scaler there were other scalers providing information on the number of protons on target during the spill, the number of events satisfying each one of the various triggers discussed below, and the number of counts in the counter banks during the spill. The scalers were read out 0.1 s after T6 and 3 s after T2 an end of readout signal was given to the memory modules in order to prepare for the reading of the next event.

Several types of triggers were used in this experiment, often simultaneously, both prescaled or non-prescaled. They were the "neutral" trigger, the "charged" trigger, the "Kμ3" trigger, the "downstream Ke3" trigger, the "Pb sheet π^0" trigger the "B*μ" trigger, and the "accidental" trigger. These triggers were ameliorated as we learned more about the data and the way they were finally set up will be described shortly. We will first define the triggers as a function of their logic elements and then explain the individual elements. One can find information on the relevant detector components in Chapter 2.

We will start with the "neutral" trigger with which we collected $K_L \rightarrow \pi^0\gamma\gamma$ candidates, $K_{L,S} \rightarrow 2\pi^0$ events and events of several other decay modes.

$$\text{neutral trigger} = \text{RF} * \text{EThi} * \text{HCF} * \text{BA}\gamma * \overline{PA} * \overline{AM} * \overline{RA} * \overline{VA2_{sc}} * \overline{VA3_{sc}} * \overline{VA4_{sc}} * \overline{VA4_{ll}} * \overline{V_{Sum}} * \overline{LGA_{ll}} * \overline{CA} * \overline{Mu1}$$

Photons and electrons deposited all their energy at the lead glass calorimeter. The total energy measured by the calorimeter, ET, was the energy of the kaon if one considers decays that involve only photons and electrons, if all the decay particles are detected at the lead glass, and if one ignores accidental activity at the glass. In this trigger and in other triggers described below we require that ET is greater than ~28 GeV (EThi). PA and AM scintillators were in veto in order to reject events with charged particles from upstream of the lead Mask. RA was in veto, as is also done in "charged" trigger, in order to reject inelastically regenerated events. The scintillators of VA2, VA3 and VA4 were also set in veto in order to reduce inelastic background coming from the regenarator and also accidental activity. The analog sum of the VA4 and the analog sum of the LGA lead lucite counters was in veto in order to reduce the $K_L \rightarrow 3\pi^0$ background. The Collar-anti was put in veto, $\overline{CA}$, to reject events with photons very close to the beams. Events with such photons usually experience significant energy losses down the beam holes and, if kept, it would be difficult to handle them properly. The trigger rate was fairly insensitive to the threshold of CA veto if it ranged between 1.9 μ and 10.8 μ (where μ stands for one muon equivalent). The threshold of the veto was chosen to be 9.5 μ so that the chance of vetoing in albedo is reduced. BAγ stands for $(BA_{I+II} * \overline{BA_{III}})$ where BA_{I+II} indicates that the sum of the energy in the first and second BA units should be more than 5 GeV and $\overline{BA_{III}}$ indicates that the energy in the third unit should be less than 10 GeV. Only the energy in the 8 vertical strips of each unit is included in the sum.

An analog sum of the V counters was formed and was put in veto, $\overline{V_{Sum}}$, requiring in this way no charged particles upstream of the V bank plane. In this trigger events with hadrons, ($K_L \rightarrow \pi^+\pi^-\pi^0$), were suppressed by using the Mu1 counter bank in veto. An analog sum was formed of the pulse heights of the Mu1 counters to distinguish events with only photons and electrons from those involving hadrons. The threshold for the Mu1 sum was 3.5 μ for about the first 1/6 of the run and it became 2.1 μ for the rest of the run. Events with pulse height in Mu1 greater than this threshold were vetoed. "HCF" in the description of the triggers indicates that the hardware cluster finder (HCF) was used in the trigger with certain requirements about the number of clusters in each event. HCF was a second level trigger arriving about 20 μs after the first level trigger and could abort the event. In the "neutral" trigger we recorded all events with a four-cluster final state. The HCF requirements for events with different numbers of clusters can be found in section 3.2.3.5.
The remaining triggers are:

$$\text{Charged trigger} = \text{RF} * (V_{Sum}+T_{Sum}) * C_u * C_d * B_e * B_w * 2B * Ch2 * \overline{Mu2} * \overline{PA} * \overline{AM} * \overline{RA} * \overline{VA2_{sc}} * \overline{VA3_{sc}} * \overline{VA4_{sc}} * \overline{LGA_{ll}}$$

This trigger was designed to accept $K_L \rightarrow \pi^+\pi^-$ decays for the ε'/ε measurement; it also accepted Ke3 and $K_L \rightarrow \pi^+\pi^-\pi^0$ decays. By requiring a signal in the V or the T bank or in both, the decays satisfying this trigger were required to occur upstream of the HDRA. For the B and C counter banks the number of charged particles passing through them was determined from the number of hit counters. Therefore in the trigger logic the logic elements 2B or 3B for example were true if at least two or at least three B counters respectively were hit. For $K_{L,S} \rightarrow \pi^+\pi^-$ decays one expects in general from momentum conservation that the two charged particles should be produced in opposite directions with respect to the beam from which the decay occured. Therefore we use combinations of

logic elements like B_e*B_w indicating that at least one B counter in the east half of the B bank and at least one counter in the west half of the B bank are hit. The central counters 8 and 23 were shared by the east west logic. Similarly C_u*C_d was required indicating that at least one counter in the up half of the C bank and at least one counter in the down half of the C bank were hit. Again the central counters 6,7 and 18,19 were shared by up and down halves. The Chamber 2 logic (Ch2) which was implemented to improve the signal to noise ratio in the $K_L \rightarrow \pi^+\pi^-$ decay by reducing the Ke3 ($K_L \rightarrow \pi^{\pm} e^{\mp} \nu$) and $K_L \rightarrow \pi^+\pi^-\pi^0$ backgrounds, required that we have at least two hits at Chamber 2, located one at the right half and one at the left half of the upstream vertical wire plane or one at the right half and one at the left half of the downstream vertical wire plane. Ch2 was a second level trigger element arriving about 0.5 μs after the first level trigger.

$$\text{K}\mu3 \text{ trigger} = \text{RF} * (V_{Sum}+T_{Sum}) * C_u * C_d * B_e * B_w * 2B * \text{Mu2} * \overline{PA} * \overline{AM} * \overline{RA} * \overline{VA2_{sc}} * \overline{VA3_{sc}} * \overline{VA4_{sc}} * \overline{LGA_{ll}}$$

This trigger was designed to accept $K_L \rightarrow \pi^{\pm}\mu^{\mp}\nu$ decays and it was very similar to the "charged" trigger. The only differences were that Mu2 was in veto in the "charged" but it was in coincidence in the "Kμ3" trigger and the Ch2 logic was not used in the "Kμ3" trigger.

$$\text{Pb sheet } \pi^0 \text{ trigger} = \text{RF} * \overline{VA4_{ll}} * \overline{V_{Sum}} * T_{Sum} * \overline{LGA_{ll}} * C_u * C_d * B_e * B_w * 2B * \overline{3B} * \overline{CA} * \text{ETlo} * \text{Mu1} * \text{HCF}$$

Events in this trigger consisted of π^0s produced at the Pb sheet ($\overline{V_{Sum}}$ * T_{Sum}) which were accompanied by two tracks. They were collected to help in the understanding of energy resolution and energy scale, since they were produced at a known z location. The HCF requirement was 3 or 4 hardware clusters per event in this trigger. The total energy in the calorimeter, ET, was required to be greater than ~9 GeV (ETlo).

$$\text{Downstream Ke3 trigger} = RF * \overline{V_{Sum}} * \overline{T_{Sum}} * C_u * C_d * B_e * B_w * 2B * \overline{3B} * \overline{VA4_u} * \overline{LGA_u} * \overline{CA} * ETlo * Mu1 * \overline{Mu2}$$

This trigger was useful for lead glass calibration studies. The advantage of the Ke3 electrons over the ones collected within dedicated electron calibration runs is that Ke3s were collected at the same time and under the same conditions as the data.

$B^*\mu$ trigger = RF * 1B * Mu2

In this trigger besides the default requirements of at least one hit at B bank and Mu2 bank firing, we also had occasionally more requirements for special study purposes, usually photon veto studies. These requirements were (VA + DRAC) or (AM + RA) or BA_{def} or similar requirements.

Finally the "accidental" trigger was designed to look at accidental, non-kaon decays. This was done by having 2 scintillator counters look at the target at some fixed angle in such a way that they monitor the beam activity but are uncorrelated with activity in the detector. In the early part of the run the "accidental" trigger required that two downstream counters at approximate *z* location 155 m from the target fired in coincidence and for the remaining of the run it was required that two upstream counters at approximate *z* location 40 m from the target fired in coincidence. In the later case, the counters were 5.5 apart in *z* and a ray passing through both of them projected at the plane of the Analyzing magnet (AN4) to a point about 11.6 m west of the magnet center. The timing of the "accidental" trigger started being defined by RF only in the last month of the run.

4.2 Running conditions

We had three basic running modes in this experiment: the "neutral" mode, the "chg, neutral" mode and the "chg/n, neutral" mode. During the "neutral" running mode we recorded simultaneously K_L and K_S decays that satisfied the "neutral" trigger. The Pb sheet, mentioned in Chapter 2, was in place during this period inducing conversions of the photons hitting it about 6.5% of the time. The Separator magnet (AN2), immediately downstream of the HDRA, caused an opening angle of the e^+, e^- pair produced at the Pb sheet by giving to it a 28 MeV transverse momentum kick. The current of the Analyzing magnet, further downstream, was set to 857 A corresponding to a P_T kick of 100 MeV of opposite polarity to the one given by the AN2 magnet. Therefore the e^+, e^- pair reconverged at the lead glass. The opening up of the pair by the Separator Magnet helped in finding the vertex of the decay and its reconvergence helped in reducing the amount of noise that would be introduced in the event if we had two seperate clusters for the e^+ and the e^-. This 'double' cluster often included at least one bremsstrahlung photon produced by the electron or the positron. Events with conversions at the Pb sheet are rejected from the final $\pi^0\gamma\gamma$ sample. During this running mode we recorded all the events having a 4 hardware-cluster final state. We often refer to these as a "four-cluster" sample. Events with 6 hardware clusters were prescaled by a factor of either 4 or 8 and events with different numbers of clusters were prescaled by much larger factors given in section 3.2.3.5. During the "neutral" running mode we also recorded "Pb sheet π^0" and "Downstream Ke3" decays for calibration and special study purposes.

During the "chg, neutral" running mode we recorded simultaneously K_L and K_S decays that satisfied mainly the "charged" trigger and also the "Kμ3" and the "neutral" triggers. In the early part of this period we did not record any "neutral" trigger events (this running

mode is indicated as "chg" in Figures 40 and 41) but for the rest of the time we also simultaneously recorded "neutral" triggers without any prescaling. The "neutral" triggers were about 6% or 10% of the "charged" triggers for a wider or shorter photon veto ADC gate respectively. The lead glass sparse readout threshold was 100 MeV instead of 25 MeV in this mode which makes the analysis of the "neutral" triggers more complicated.

For the last 25% of the data the running mode was "chg/n, neutral", where n indicates the prescaling of the "charged" trigger. During this running mode we simultaneously recorded K_L and K_S decays that satisfied the "neutral", the "charged" and the "Kμ3" trigger. The "charged" trigger was prescaled by a factor either 4 or 8 and we recorded all the events with 4 or 6 hardware clusters in the "neutral" trigger. The Pb sheet was removed and the current of the AN4 magnet was 1714 A, corresponding to a P_T kick of 200 MeV. The polarity of the magnet was reversed roughly every 30 tapes for the last two and a half months of the run in order to remove systematic effects in the measurement of Re(ε) from the Ke3 decay. The Ke3 decay was satisfying the normal "charged" trigger requirements within this running mode. During all the running modes we recorded also events satisfying the "B*μ" and the "accidental" triggers as well as flashers and pedestals. Prescale factors for the different trigger types during the run are given in Table 7. A summary of the run plan and the running mode as a function of time during the run is described in Figures 40 and 41. Quite often during the run we had special run periods which are described in more detail below and roughly every two weeks we performed lead glass calibration. The intensities we ran at were approximately 6×10^{11} pts (protons on target per spill) for the "chg, neutral" mode, 1×10^{12} pts for the "neutral" mode and 7×10^{11} for the "chg/n, neutral" mode. Examples of the trigger composition of the events recorded during each spill are given in Tables 8, 9 and 10.

TABLE 7. Prescale factors of different trigger types.

Trigger Type	Running mode	Prescale factor
Kμ3	"chg, neutral"	4, 25
	"chg/n, neutral"	50, 100
Accidental	"chg, neutral"	100, 5
	"neutral"	10, 20, 100, 200
	"chg/n, neutral"	5, 20
Pb Sheet π^0	"neutral"	7, 10, 20, 40
B*μ	"chg, neutral"	2^{13}, 2^{15}
	"neutral"	2^{13}, 2^{15}, 2^{16}
	"chg/n, neutral"	2^{7}, 2^{16}
Downstream Ke3	"neutral"	600, 800, 999

TABLE 8. Trigger composition of spill in "chg, neutral" running mode.

Trigger type	Number of events per spill, at 6.2×10^{11} pts	Prescale factor
neutral	970	
charged	9862	
Kμ3	351	25
Accidental	155	5
B*μ	398	2^{13}
flasher	21	
pedestal	36	

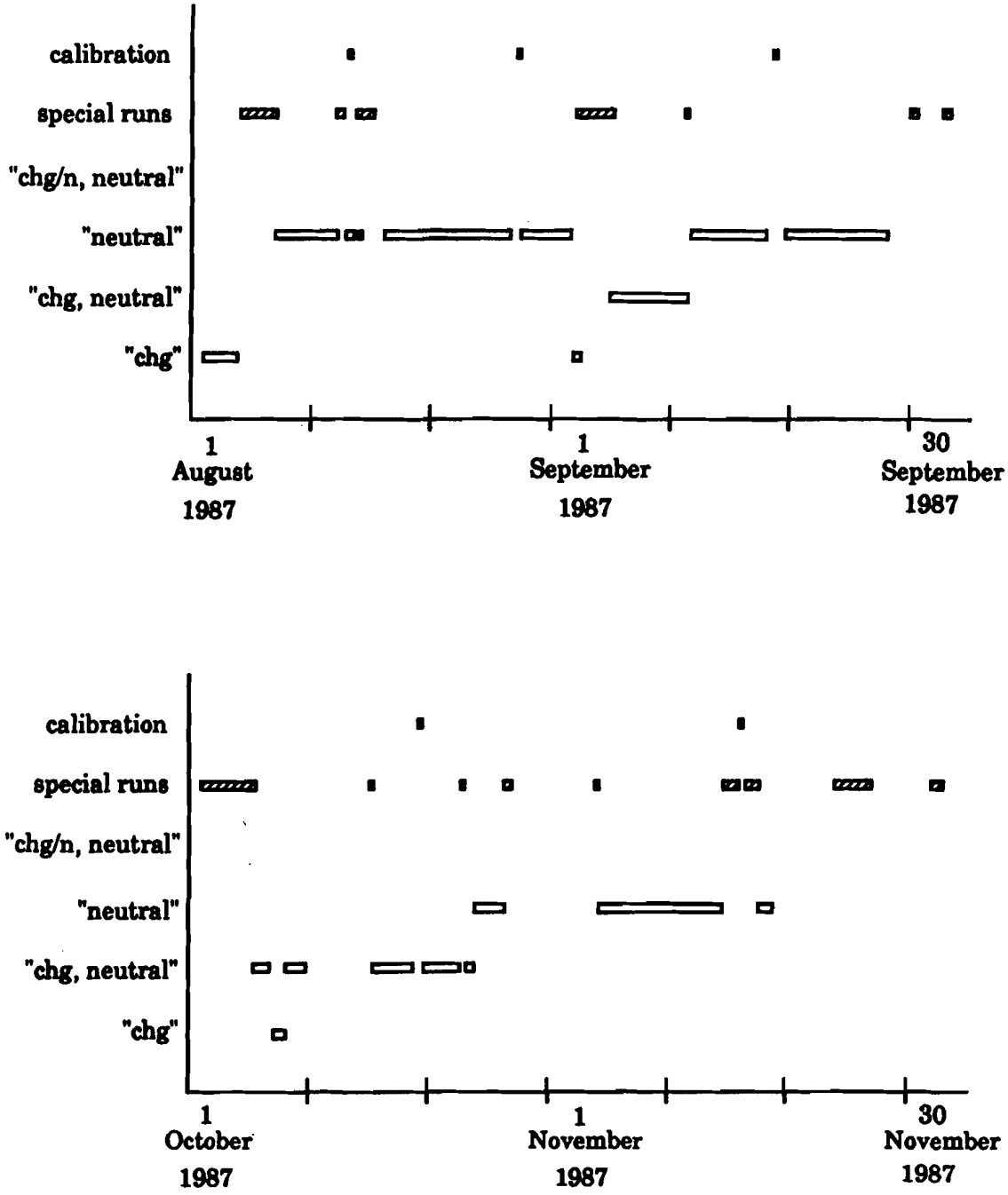

Figure 40. Data taking "running modes" from the beginning of August of 1987 till the end of November of 1987.

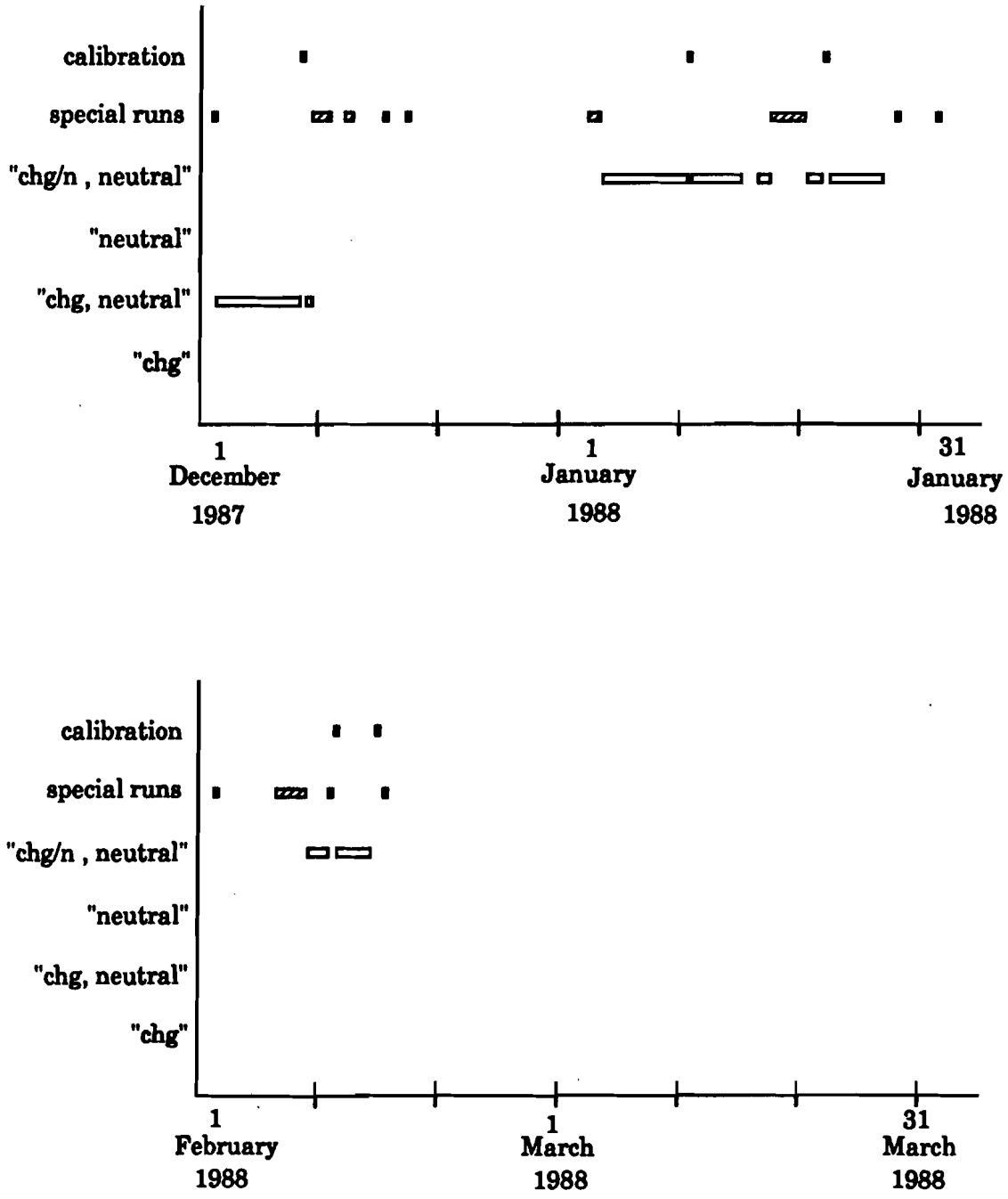

Figure 41. Data taking "running modes" from the beginning of December of 1987 till the 15th of February of 1988.

TABLE 9. Trigger composition of spill in "neutral" running mode.

Trigger type	Number of events per spill, at 9.8 x 10^{11} pts	Prescale factor
neutral	2889	
charged	0	
Downstream Ke3	81	600
Pb sheet π^0	87	7
Accidental	17	200
B*μ	130	2^{16}
flasher	24	
pedestal	62	

TABLE 10. Trigger composition of spill in "chg/n, neutral" running mode.

Trigger type	Number of events per spill, at 8.3 x 10^{11} pts	Prescale factor
neutral	3100	
charged	3216	8
Kμ3	174	100
Accidental	69	20
B*μ	114	2^{16}
flasher	22	
pedestal	46	

4.3 Information recorded for every event and electronic readout

For every event the information saved was the run number, the spill number, the event number within the run, information on the beam and the trigger conditions and sufficient information for the reconstruction of the event from the lead glass, the chambers and the counter banks.

As far as the beam conditions are concerned, we recorded the number of protons per spill hitting the target, profiles of the proton beam and the instantaneous beam intensity which was monitored by a scaler, the RA scaler, that recorded the number of counts in the Regenerator-anti (RA) bank in a time interval of 100 μs after the trigger. There was also saved some latch information indicating the position of the regenerator and the movable absorber with respect to the two beams. For the trigger conditions, we recorded the type of trigger that the event satisfied; if the event satisfied the "neutral", the "Pb sheet π^0" or the "accidental" triggers, we recorded the HCF hit pattern, the "seed" block for each cluster and also the number of hardware clusters found by HCF.

As mentioned also in Chapter 2, we saved digitized pulse height information for every block in the lead glass that was above the sparse read out threshold. We also had ADC information on the adder signals and the total energy of the lead glass array. The energy of the array was recorded for the "in time" bucket, ET, and also for preceding and following buckets (ETearly and ETlate respectively). From the chambers, we saved wire number and TDC information for every wire that was hit. The counter banks were ADCed and/or latched. When they were ADCed we had pulse height information on their signals; when they were latched we knew that the particular counter had or did not have energy deposit above some threshold which was usually equivalent to the signal of one (or fraction of one) minimum ionizing particle. The information saved for the energy of the signal in each one of the counter banks is summarized in Table 11.

TABLE 11. Information recorded for the energy of the signal in the counter banks.

Detector element	ADC	latch
PA		×
SA		×
Lead Mask (AM)		×
RA		×
VAs (scintillator)		×
VAs (lead-lucite)	×	
MA (scintillator)		×
MA (lead-lucite)	×	
LGA (scintillator)		×
LGA (lead-lucite)	×	
DRAC	×	×
DRAN	×	
CA	×	
BA	×	
BA_{def}		×
V counters	×	×
T counters	×	×
C Bank		×
B Bank	×	×
Mu2		×
Mu1	×	
ACC1 and ACC2		×

We used the Le Croy 1885N ADC operating in either high or low dynamic range. We used a gate of 150 ns for the lead glass ADCs and a 30 ns gate for all the other ADCs. The photon veto ADC gate though was shortened to 15 ns about half way through the run. The width of the gate used for the latches was 50 ns for PA, the VAs, MA, LGA, ACC1 and ACC2 and 25 ns for the remaining counters.

The arrival times of signals at AM, RA, the VAs, MA, LGA, DRAC, CA, BA, T, V, B, Mu2 and Mu1 with respect to the trigger were measured by Le Croy 4291B TDCs (time to digital converters) which operated in a "common start" mode. The time of each event with respect to the beginning of the spill or "time into the spill" was also recorded.

The "dead time" of the experiment which is the percentage of the time during which the detector was insensitive to new triggers because of digitization and readout of signals, was easily calculated by substracting from 1 the ratio of muon events written to tape for every spill to events satisfying the B*μ trigger in the same spill. This "dead time" is given approximately for all three running modes in Table 12.

TABLE 12. "Dead time" of the experiment for various running conditions.

running mode	"Dead time"
"neutral"	20%-40%
"chg/n, neutral"	40%-60%
"chg, neutral"	55%-70%

4.4 Cluster Finder external logic

The hardware cluster finder (HCF) was used whenever we had an event that was satisfying the "neutral", the "Pb sheet π^0", or the "accidental" trigger requirements. As described in section 3.2.3.5, the HCF has as output 10 ECL signals indicating the number of clusters found after prescaling (0-9), an "accept" or "reject" signal which is the "OR" of all the number of clusters after prescaling and a "done" signal

that was available every time HCF finished cluster finding, independent of prescaling. An event was "HCF consistent" if one of the following 5 conditions, which are also illustrated in Figure 42, was satisfied: 1) the event satisfied the "neutral" trigger and had 4 hardware clusters, 2) the event satisfied the "neutral" trigger and had 6 hardware clusters, 3) the event satisfied the "Pb sheet π^0" trigger and had 3 or 4 hardware clusters, 4) the event satisfied the "accidental" trigger and 5) the "done" signal was available. In this last case we accepted any number of clusters but the "Ignore HCF result" prescaler was set at 64, 128 or 256. These events were saved for study purposes. An "HCF consistent" event was read out if the "done" signal was available. If the event was not "HCF consistent" a "fast clear" was applied.

This external logic was fairly flexible and allowed us to change our requirements from the Cluster Finder if we wanted. If for some reason we decided to remove HCF from the trigger then the only thing that had to be done was to change the prescaling value of the "Ignore HCF result" prescaler to 0. For example, if we wanted to record events satisfying the "neutral" trigger with any number of clusters greater than 2, then the "neutral" trigger signal would have to be plugged in the free input of the "special" gate and the prescaling factors for 0, 1 and 2 clusters would have to be set to Maximum (2^{10}).

4.5 Special runs

Besides the muon runs that were performed on a daily basis for chamber alignment, and the electron calibration runs that were performed roughly every two weeks and used for the understanding of the lead glass, we performed more special runs. These runs focused on studies that would help us to understand our trigger vetoes and systematic effects in the experiment. They included studies of the

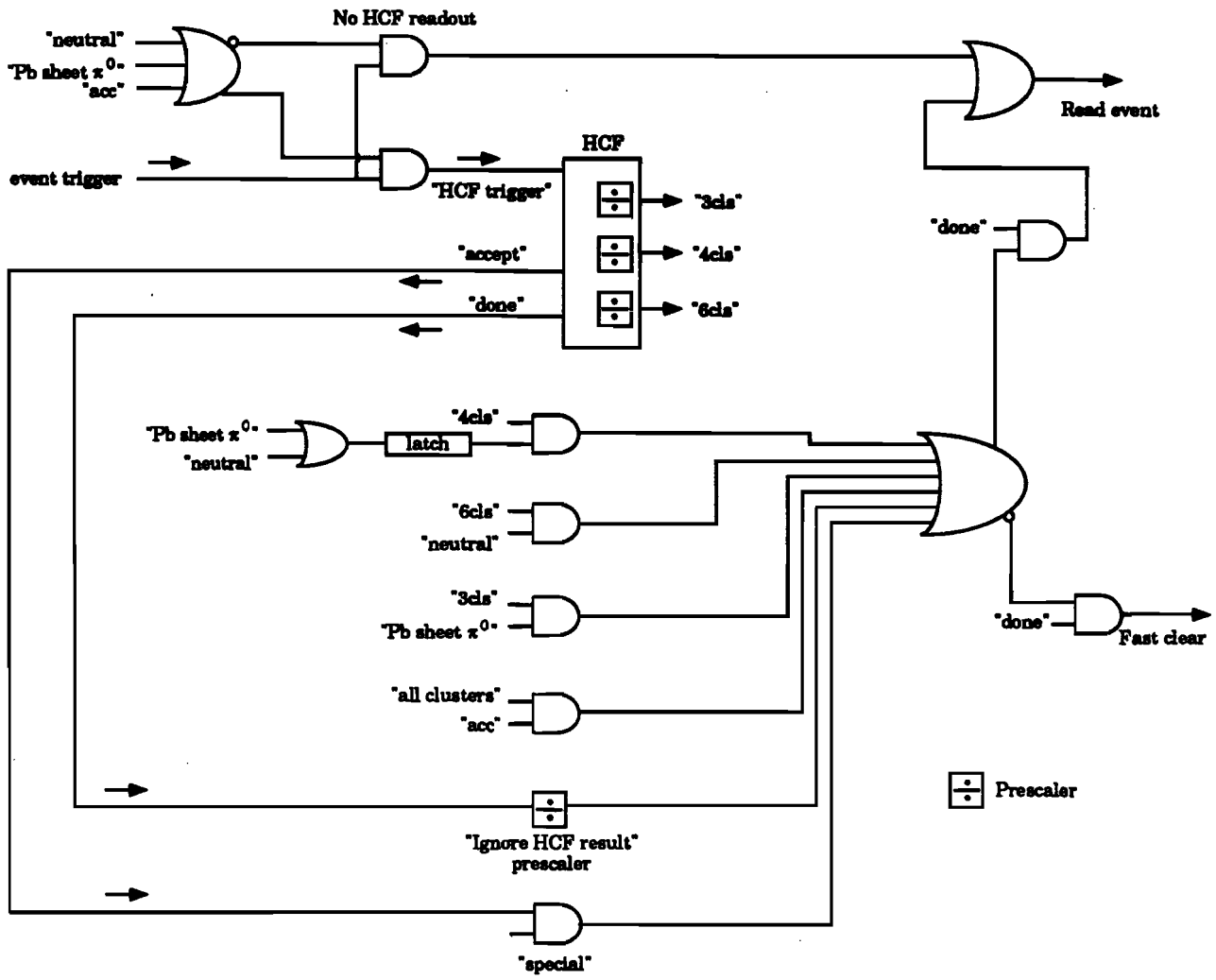

Figure 42. Cluster Finder external logic.

regeneration at the Pb sheet and at the V and T counter banks, of the beam shape and the scattering of the beam at the absorber, of the inelastic background, the lead glass response under special conditions and the effect of the hardware cluster finder on the trigger. The main special runs performed are described below:

1) In order to study regeneration at the Pb sheet converter, we wrote within the "charged" trigger 7.9M events with the Pb sheet in place and a two radiation length Pb curtain inserted in front of the lead glass array and upstream of the B bank. The function of the Pb curtain was to reject Ke3 and $K_L \rightarrow \pi^+\pi^-\pi^0$ decays by causing electromagnetic showering of the electron of the Ke3 and the photons of the $\pi^+\pi^-\pi^0$ decays. Events generating signals greater than 5 MIP (minimum ionizing particles) at a single B counter were rejected. The trigger used for this special run was the following:

$((\text{charged-}(V_{Sum}+T_{Sum})) * 2C * \overline{B5}))/2$

The "2" in the denominator indicates that the "charged" trigger was prescaled by a factor of 2.

2)In order to study regeneration at the T or the V counters 7.6M events were written with identical conditions and identical trigger as in the previous run except that the Pb sheet was removed.

3) For the study of the tails of the vacuum beam and the study of the $3\pi^0$ and accidental backgrounds in the same beam one of the two beams was plugged and the regenerator and absorber instead of changing beams every spill they stayed fixed at the plugged beam. In this way and by using the "chg/n, neutral" trigger we recorded 2.3M charged and neutral trigger events with the lower beam plugged and an equivalent number of events with the upper beam plugged.

4) The Regenerator-anti (RA), as mentioned in Chapter 2, was important in detecting and vetoing inelastic scattering in the regenerator beam. Therefore, to study the inelastic background, we had to take RA out of the veto in the various triggers. These runs were performed within the

"chg/n, neutral" running mode. 1.9M events were recorded with the lower beam plugged and with the absorber and the regenerator in the upper beam. Another 88K events were recorded with the same conditions but with the absorber in the lower beam. By plugging the upper beam and having the regenerator and absorber in the lower beam we recorded earlier in the run 1.8M events by using the (neutral-$\overline{RA}$) and (charged-$\overline{RA}$) triggers. We also recorded 1.94M charged triggers with the (charged-$\overline{RA}$) trigger and no beam plugged.

5) In order to study the scattering in the absorber, we used the "charged" trigger and we placed the movable absorber in the vacuum beam while the regenerator beam was plugged. We recorded 3.2M events with the vacuum beam being the lower beam and another 3.0M events with the vacuum beam being the upper beam.

The two following special runs were performed for the study of the lead glass response.

6) Within the "chg/n, neutral" mode and with the 2 radiation lengths Pb curtain inserted upstream of the lead glass and downstream of the B bank, about 550K events were recorded in order to study the change in the lead glass energy resolution.

7) For the electron calibration of the lead glass array we performed a special run during which we used a thin foil for the conversion of photons, introducing in this way less bremsstrahlung. In that special run only about 50% of the triggers came from conversions in the foil. The remainder of the conversions originated at the T and V counters. For the last month of the run we used this thin foil for electron calibration (see section 2.3.2.2)

8) To study the effects of having HCF in the trigger, we removed it from the "neutral" trigger and recorded 970K events with the Pb sheet out of place and 1.03M events with the Pb sheet in place. In both cases the "neutral" trigger was prescaled by a factor of 5. The HCF was taken out of the trigger by changing the prescale rate of the prescaler to "ignore HCF

result" from 2^8 to 2^0. These events were used to study the thresholds and resolutions of the 804 HCF channels as discussed in Chapter 3.

9)In order to study the efficiency of V_{sum} and T_{sum} we recorded 2.45M events satisfying the trigger:

(charged-(V_{Sum}+T_{Sum}))

10) A special gate timing study was performed for the lead glass ADC gate, by using electron calibration data. In this study we shifted the timing of the ADC gate by a few nanoseconds in either direction and collected data where the gate comes at the usual time, 1 ns early, 1 ns late and 3 ns late. Between 70 to 90K triggers were recorded for each category. These data have been used in studying the change in the $\frac{E}{p}$ for electrons and positrons as a function of gate timing. The concern was that if the timing of the gate shifted in the data or the time of the gate was different for the "neutral" and "charged" triggers, this perhaps could lead to a shift in the measured energies since different amounts of the tail of the signal would lie outside the gate. The change we observed in $\frac{E}{p}$ in this study was very small and therefore of no concern.

CHAPTER 5

DATA RECONSTRUCTION - DATA REDUCTION

This chapter discusses the principles of the reconstruction of the $K_L \rightarrow \pi^0\gamma\gamma$ decay and the way the data were processed to form Data Summary Tapes. The $\pi^0\gamma\gamma$ analysis will be discussed in detail in the next chapter. Here we will discuss some of the cuts that were used for the data reduction.

5.1 Event reconstruction

The topology for a $K_L \rightarrow \pi^0\gamma\gamma$ event as well as the one for a $K_L \rightarrow 2\pi^0$ event consists of 4 photons depositing all of their energy in the lead glass calorimeter. The reconstrucion of the event involves determination of the beam from which the kaon originates (vacuum or regenerator) and reconstruction of the decay vertex, the invariant mass of the two photons that form a π^0, m_{π^0}, and the invariant mass of the two independent photons, $m_{\gamma\gamma}$. For this reconstruction one first needs to determine the

energies and positions of the photons involved in the event as described briefly below.

5.1.1 Photon measurements

Both the $K_L \rightarrow \pi^0\gamma\gamma$ and $K_L \rightarrow 2\pi^0$ decays satisfied the "neutral" trigger and they were required to have 4 hardware clusters. After the HCF returned the number of hardware clusters there was another level of cluster finding performed in software. The HCF returned the block number that contained the "seed" for each hardware cluster (see Chapter 3). The "seed" was not necessarily the block with the maximum energy in the cluster; rather it was the block that the HCF identified first as belonging to the hardware cluster in its scanning of rows and columns of the array. The software cluster finding started from this "seed" and searched for local maximum of block energy in the immediate neighborhood of the "seed". The energies of the blocks in a 3 x 3 block region around the local maximum are summed to form the raw energy of a software cluster and the block with the maximum energy is considered as its center. There was a considerable number of cases where within one hardware cluster the software cluster finding would identify two clusters. Special care was taken for the estimation of the energy of the individual overlapped clusters but events with these types of clusters were not included in the final data sample; in the data reduction which is described below we rejected events for which the numbers of hardware and software clusters did not match. Table 13 gives the percentage of the time that the software cluster finding identifies 4, 5 or 6 clusters among 4 hardware clusters and similarly the percentage of the time that the software cluster finder identifies 6, 7 or 8 clusters among 6 hardware clusters. The information is taken from raw data before any analysis cuts are applied. The reason for having disagreement of about 20% between the hardware and software cluster finding for 4 hardware clusters is

TABLE 13. Effect of software cluster finding on the number of hardware clusters.

4 hardware clusters		6 hardware clusters	
4 software clusters	81.83%	6 software clusters	97.27%
5 software clusters	16.37%	7 software clusters	2.52%
6 software clusters	1.73%	8 software clusters	0.19%

primarily due to $K_L \rightarrow 3\pi^0$ background and also due to accidental activity and photon conversions upstream of the Analyzing magnet. The disagreement of about 2.7% between the hardware and software cluster finding for 6 hardware clusters is due to accidental activity which varies with the beam intensity and photon conversions.

After the cluster was identified its observed raw energy had to undergo several corrections before it is converted to the energy of the incident particle. First we had to correct for the pedestal effect mentioned in Chapter 2. This correction was done after studying shifts of the π^0 mass in the $K_L \rightarrow \pi^+\pi^-\pi^0$ decay mode as a function of the counting rate of the RA scaler and "time into the spill". Second we had to correct for the loss of energy due to our ADC readout threshold which was studied and determined from full readout calibration data. For the readout threshold of 25 MeV per block, the loss of energy below threshold is less than 1% for cluster energies above 4 GeV and it can reach 2.5% at 2 GeV. In the presence of pedestal shifts the correction is more complicated and it is described in Reference [29]. We also had to correct for any leakage of energy outside the 3 x 3 block region considered as a software cluster. This leakage was estimated to be 3.1% from study of the data and from EGS studies. A fourth correction took care of any leakage of energy outside the array. If any of the 9 blocks belonging to a cluster were missing because the cluster was located near the outer edge of the array

or near the central beam pipes, an extra correction was applied to the energy of the cluster by including simulated energies at the missing blocks; the simulated energy was 0.6% or 1.1% of the energy of the cluster for missing corner blocks or side blocks respectively. We had also to take into account the electron-photon difference. When the clusters were photons and not electrons there was applied a correction to their energy which is mentioned in section 2.3.2.2 and which decreased the observed energy of the photon by a few percent. Finally we had to correct for nonlinearity which was discussed in Chapter 2 and which decreased the energy of the cluster. Some of the corrections mentioned above tend to increase and some others tend to decrease the observed energy of a cluster. The net correction in general was small, on the order of a few percent; it was about 2% for cluster energies above 10 GeV.

The exact position of the cluster within the central block is basically determined by forming the ratios of energy of the left and right columns of the cluster to that of the central column and similarly the ratios of the top and bottom row of the cluster to that of the central row. The x and y coordinates of the position of the cluster are closer to the column and row whose ratio of energy to the energy of the central column or row is the largest. The average global position resolution derived from electron calibration data studies is 2.8 mm.

5.1.2 Decay kinematics

In order to find the decay vertex for a $K_L \rightarrow \pi^0\gamma\gamma$ candidate we had to assume that the decay originated from a kaon. Since the final state contains only neutral particles (photons) it is not possible to determine the vertex by tracking information. The z vertex of the decay is defined as $z=z_{Pbg}-z_{gl}$ where z_{Pbg} is the distance of the lead glass array from the target and z_{gl} is the the distance of the decay vertex from the lead glass. z_{gl} can be found by using Equation (5.1),

$$m_{nK}^2 = \sum_{i=1}^{4} E_i^2 - \sum_{i=1}^{4} \overline{P_i^2} = \frac{\sum_{j>i}^{4}\sum_{i=1}^{4} E_i E_j r_{ij}^2}{z_{gl}^{\ 2}} \qquad (5.1)$$

where E_i, E_j are the energies of clusters i, j respectively after all corrections, $\overline{P_i}$ is the momentum of particle i corresponding to energy E_i, r_{ij} is the distance of the two clusters and m_{nK} is the nominal kaon mass. Using the z_{gl} derived from the above equation one can form the invariant mass of any two photons γ_i, γ_j as:

$$m_{\gamma_i\gamma_j} = \frac{E_i E_j r_{ij}^2}{z_{gl}^{\ 2}}. \qquad (5.2)$$

There are six ways to choose out of four photons a pair that is going to be the π^0 candidate. If the four photons are labeled as γ_1, γ_2, γ_3, γ_4 then six pairings of photons can be formed:

$m_{\gamma_1\gamma_2}$ $m_{\gamma_3\gamma_4}$

$m_{\gamma_1\gamma_3}$ $m_{\gamma_2\gamma_4}$

$m_{\gamma_1\gamma_4}$ $m_{\gamma_2\gamma_3}$

$m_{\gamma_2\gamma_3}$ $m_{\gamma_1\gamma_4}$

$m_{\gamma_2\gamma_4}$ $m_{\gamma_1\gamma_3}$

$m_{\gamma_3\gamma_4}$ $m_{\gamma_1\gamma_2}$

where the first column corresponds to the mass of the π^0 candidate, m_{π^0}, and the second column corresponds to the mass of the $\gamma\gamma$ candidate, $m_{\gamma\gamma}$. In order to choose the right pairing all the masses of the first column are compared to the nominal π^0 mass, $m_{n\pi^0}$, which is 134.964 MeV and the pairing that has the mass of its π^0 candidate closest to this value is picked as the right one. The π^0 candidate mass is in addition required to be close to $m_{n\pi^0}$. The selection criteria for $K_L \rightarrow \pi^0\gamma\gamma$ candidates were chosen so that we could achieve big rejection for the dominant $K_L \rightarrow 2\pi^0$ and $K_L \rightarrow 3\pi^0$ backgrounds without eliminating the signal. These criteria were applied in two stages. In the first one which was the data reduction

during which first level data summary tapes (DSTs) were produced, the selection criteria were loose enough to be safe for any possible changes in various calibration files or energy corrections that might be needed later. In the second stage tighter analysis cuts were applied on data in first level or second level DSTs.

5.2 Data reduction

The data reduction in the experiment occured in two different time periods. In the summer of 1988 we reduced about 20% of our data corresponding to the bulk of the events satisfying the "chg/n, neutral" trigger and after having studied and analyzed them we had the second or main data reduction beginning in the fall of 1989. The selection criteria applied during the main data reduction in the experiment were the following:

. The event should satisfy the "neutral" trigger requirement.

. Regenerator and absorber should be in the same beam.

. The event should have 4 hardware clusters.

. The event should have 4 software clusters.

. There should be less than 2 tracks in either the x or y views of the chambers. (This prevents contamination of the sample by $\pi^+\pi^-\pi^0$ events)

Figure 43 shows the distribution of the z vertex of the decay for events satisfying the "neutral" trigger after these three requirements. This sample corresponds to about 50% of our data and is taken from the second data reduction in the experiment. The mean of the distribution is shifted towards the calorimeter due the presence of the $K_L \rightarrow 3\pi^0$ background. The distribution has a prominent excess of events at about 123 m from the target, which can be seen more clearly in Figure 44, due to $K_S \rightarrow 2\pi^0$ decays and background from the regenerator.

. The z vertex of the decay should lie less than 140 m away from the target

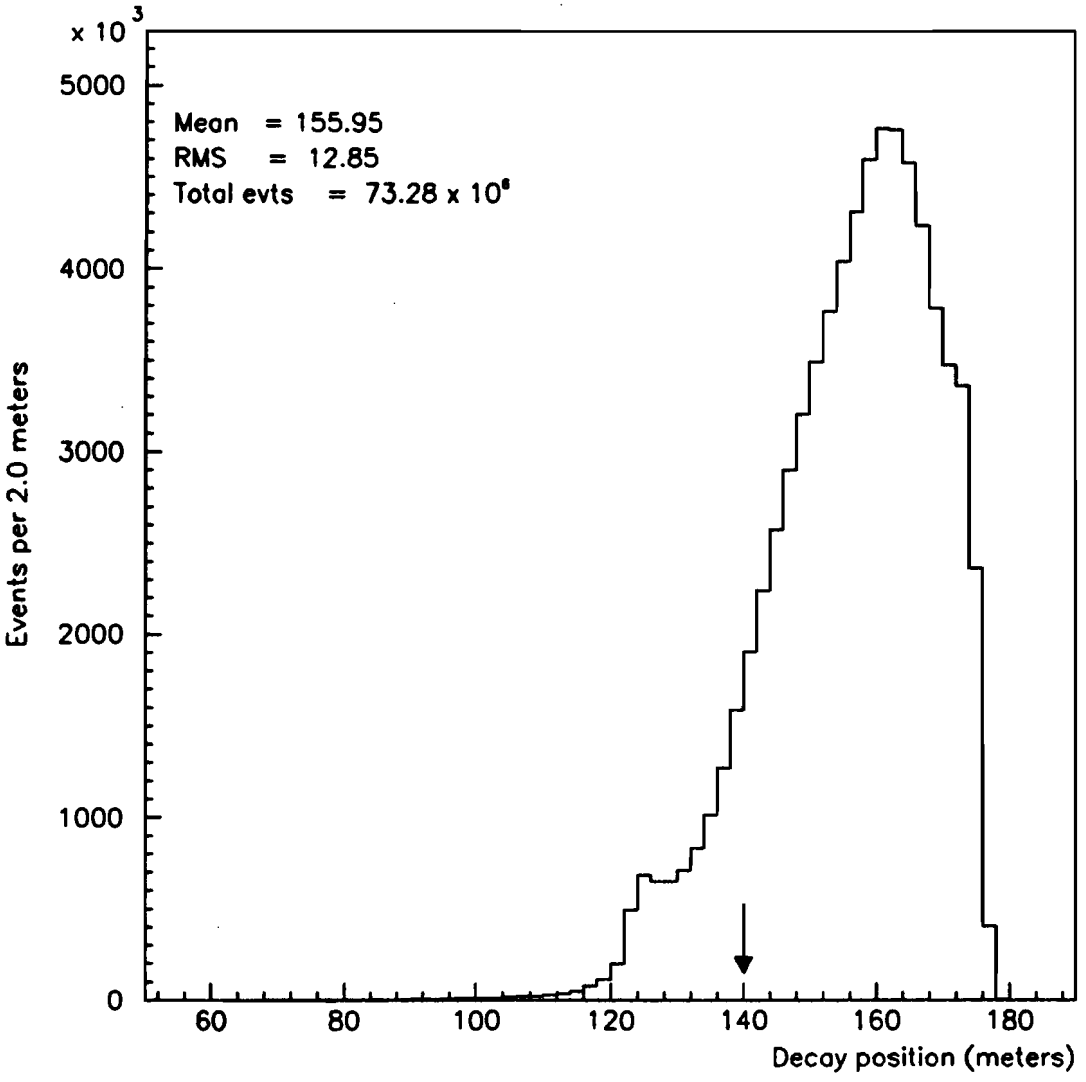

Figure 43. z decay vertex distribution for $K \rightarrow \pi^0\gamma\gamma$ candidates at a very early analysis stage. The sample corresponds to about 50% of our data. Only events reconstructing upstream of the arrow were accepted during data reduction.

and this cut is indicated with the arrow in Figure 43. This cut was applied in order to reduce the dominant $K_L \rightarrow 3\pi^0$ background as will become clear later. Right after this cut the z vertex distribution and the candidate π^0 and $\gamma\gamma$ mass distributions from the same sample of data are shown in Figures 44 and 45 and 46. The very prominent peak at around 135 MeV in Figure 46 indicates the presence of $K \rightarrow 2\pi^0$ background.

· m_{π^0} should be within ±12 MeV from the nominal mass of the π^0 and the cut is indicated in Figure 45 with the arrows. Till this point the event could perfectly well be a $K \rightarrow 2\pi^0$ candidate.

· In order to reject the $K \rightarrow 2\pi^0$ decays from this sample as a first step it was required that $m_{\gamma\gamma}$ is away from the nominal π^0 mass by ±9 MeV and the cut is indicated again with the arrows in Figure 46. A second step will be discussed in Chapter 6.

· In order to reduce the $K_L \rightarrow 3\pi^0$ background where at least one of the photons has skipped detection by the lead glass calorimeter, the center of energy of the event was required to be in the beam area. The x and y coordinates of the center of energy are defined as:

$$XCE = \frac{\sum_{i=1}^{ncl} x_i E_i}{\sum_{i=1}^{ncl} E_i} \quad \text{and} \quad YCE = \frac{\sum_{i=1}^{ncl} y_i E_i}{\sum_{i=1}^{ncl} E_i}$$

where *ncl* is the number of clusters in the event and E_i, x_i, y_i are the energy and position coordinates of each cluster. In more detail it was required that:

$-7 \text{ cm} \leq XCE \leq +7 \text{ cm}$

$-19 \text{ cm} \leq YCE \leq +19 \text{ cm}$ and $ABS(YCE) \geq 4.5 \text{ cm}$

Events from both the vaccum and regenerator beams were kept at this level.

. In order to reduce this background even further the photon veto counters were scanned and some safe cuts were applied on the energy deposit in the lead lucite part of the VAs, MA and LGA and also on the energy at DRAC and DRAN. The photon veto cuts were adjusted according to the

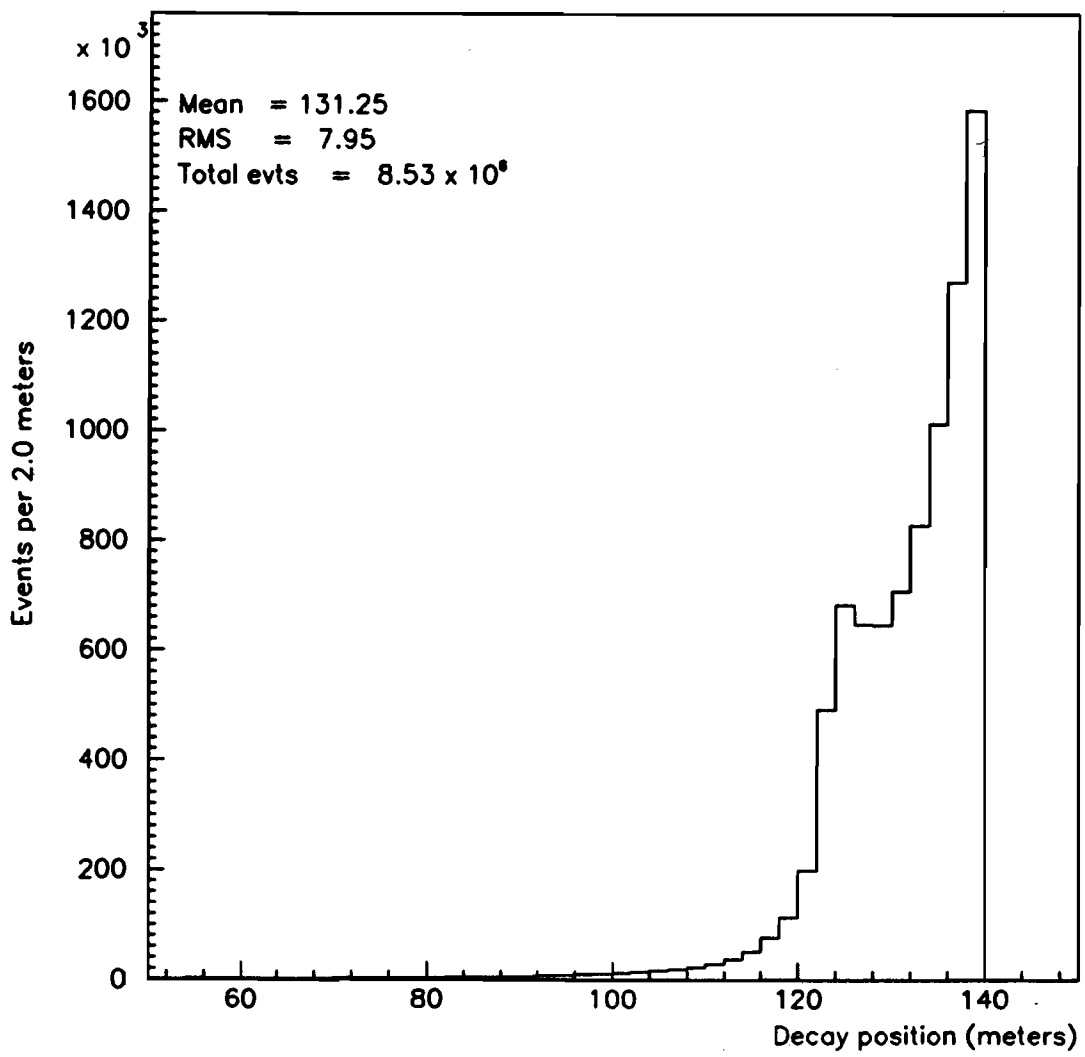

Figure 44. z decay vertex distribution for $K \rightarrow \pi^0\gamma\gamma$ candidates at the data reduction stage in the region upstream of 140 m. The "knee" at about 123 m from the target corresponds to decays from the regenerator beam.

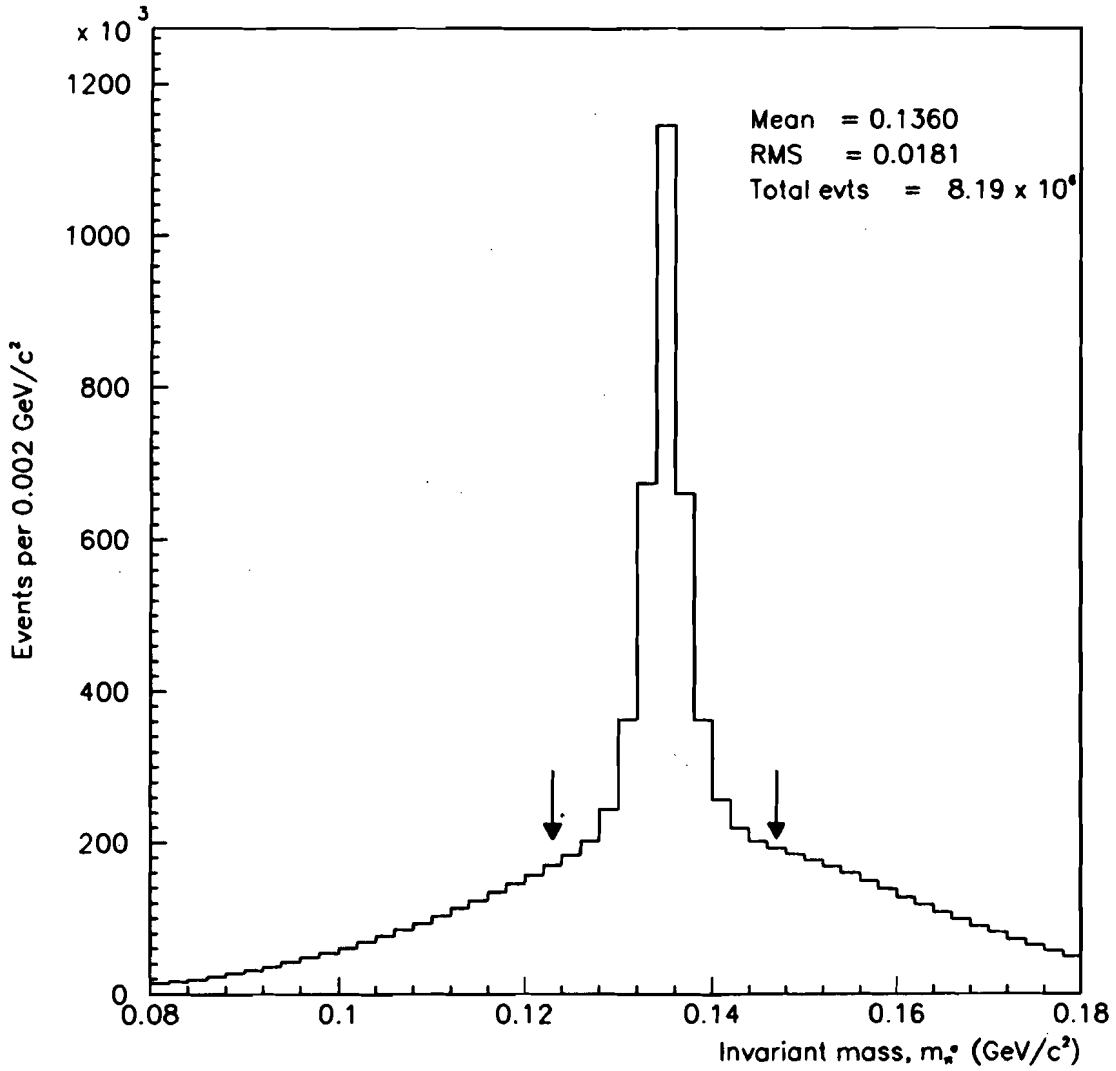

Figure 45. m_{π^0} distribution for $K \rightarrow \pi^0\gamma\gamma$ candidates at the data reduction stage in the region upstream of 140 m. Only events reconstructing within the arrows were accepted.

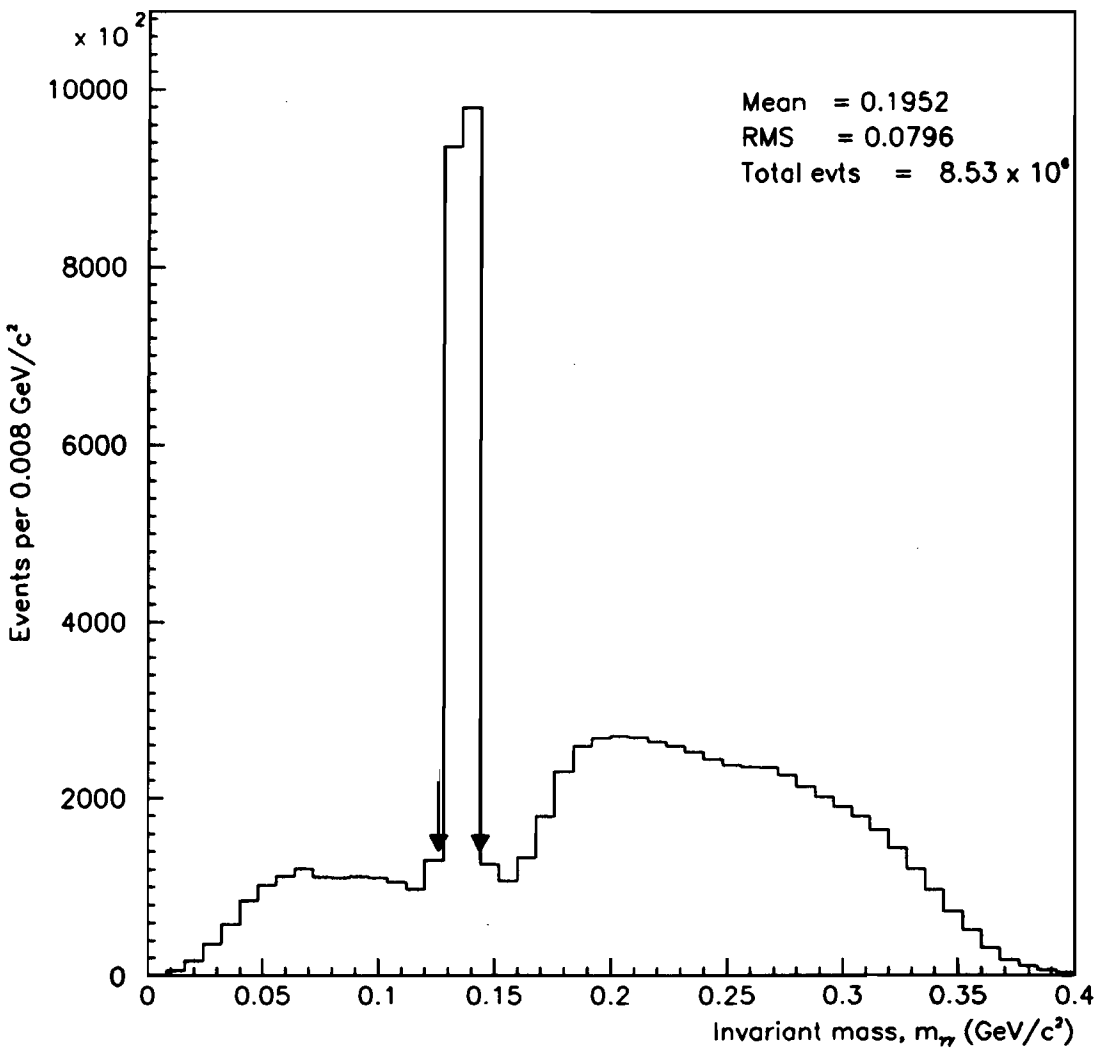

Figure 46. $m_{\gamma\gamma}$ distribution for $K \rightarrow \pi^0\gamma\gamma$ candidates at the data reduction stage, in the region upstream of 140 m. The peak at around 0.135 GeV corresponds to $K \rightarrow 2\pi^0$ background. Events reconstructing within the arrows were rejected.

run number to account for a change of the photon veto gate from 30 ns to 15 ns which was made approximately in the middle of the run. For the 15 ns gate period it was in particular required that:

1)Energy in VA1 $\leq$ 20.0 μ
2)Energy in VA2 $\leq$ 4.0 μ
3)Energy in VA3 $\leq$ 1.5 μ
4)Energy in VA4 $\leq$ 1.5 μ
5)Energy in MA $\leq$ 2.0 μ
6)Energy in LGA $\leq$ 2.5 μ
7)Energy in DRAC $\leq$ 1.5 μ
8)Energy in DRAN $\leq$ 1.5 μ

where μ corresponds to a muon equivalent.
For the 30 ns gate the cuts were looser for almost all the counters.
. In order to reduce the $K_L \rightarrow 3\pi^0$ background where at least two of the photons fuse (land on top of each other), it was required that all 4 clusters in each event satisfied a "fusion" criterion which consisted in the following: if any of the corner blocks in the 3 x 3 block area of a cluster has energy more than 1 GeV then its energy is compared with the energy of the two side blocks next to it. For example in Figure 47 where we have a fused cluster from a $3\pi^0$ decay the energy of block A was compared with the energy of blocks B and C. If its energy was more than 1 GeV greater than the energies of the side blocks the event was rejected. The event in Figure 47 is an example of a fused cluster from a $3\pi^0$ Monte Carlo event satisfying the 4 cluster requirement.
. Finally in order to reduce $K_L \rightarrow 3\pi^0$ background with missing photons even further it was also required that no latches associated with the Sweeper-anti veto counters fired . After all this requirements the m_{π^0}, the $m_{\gamma\gamma}$ and the z vertex distributions are presented in Figures 48 , 49 and 50 respectively. m_{π^0} in Figure 48 seems to be shifted to high masses. The stage at which m_{π^0} is presented here is of course very early but this shift

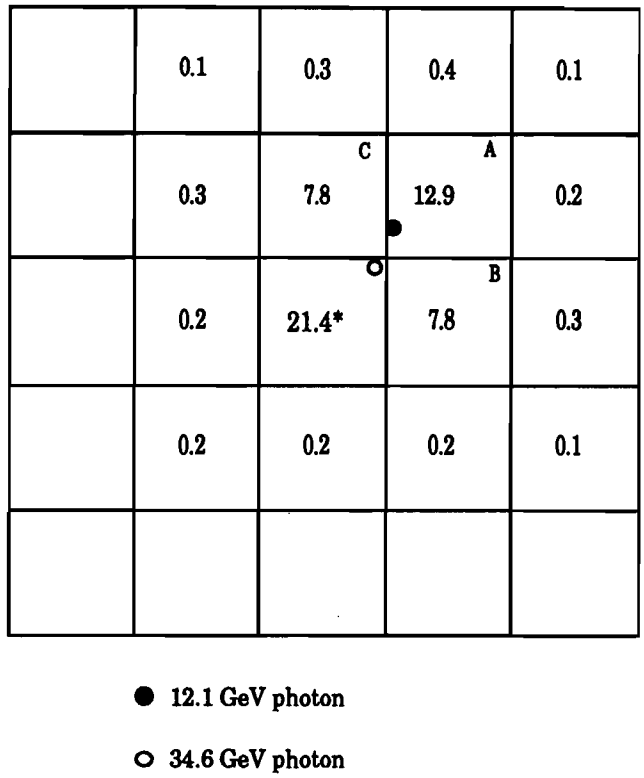

Figure 47. An example of a fused cluster from $3\pi^0$ background Monte Carlo. The circles indicate the positions of the photons.

could be due to three reasons. The first is that the nonlinearity, as will be explained in section 7.3.1.1, can shift $m_{\pi}0$ high for events involving fused clusters. Another reason is that in $3\pi^0$ background with missing photons the decay vertex will be artificially shifted towards the glass which can result in higher masses for the π^0 candidate as can be seen from Equation (5.2). The shift could also be due to a general tendency of any accidental background present at this stage. Figure 49 shows the $\gamma\gamma$ effective mass for the "non π^0" photon pair. There are two prominent characteristics in that plot. The one is a gap around 135 MeV which is due to the cut that

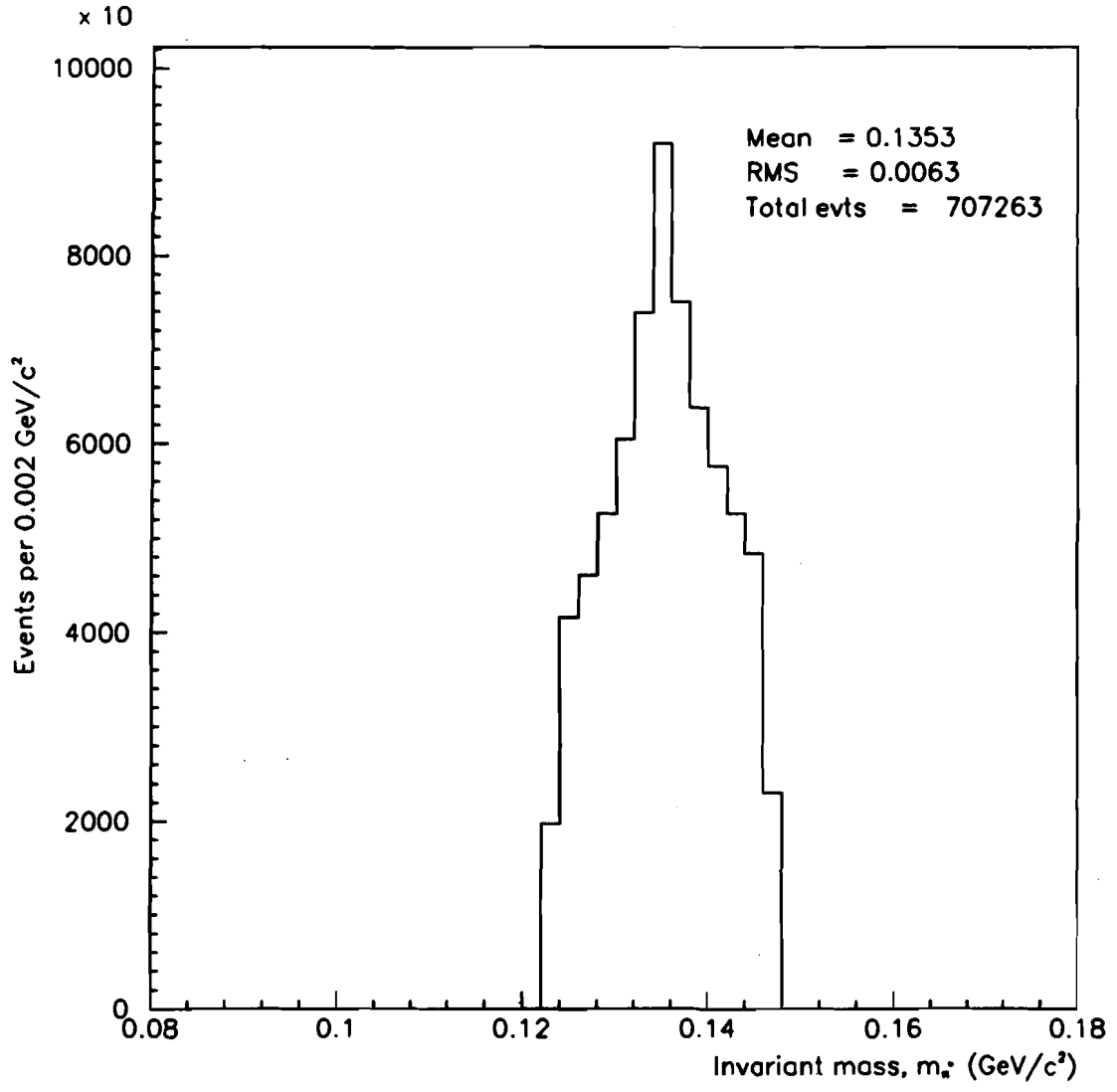

Figure 48. m_{π^0} distribution for $K \rightarrow \pi^0\gamma\gamma$ candidates at the data reduction stage after all the cuts have been applied.

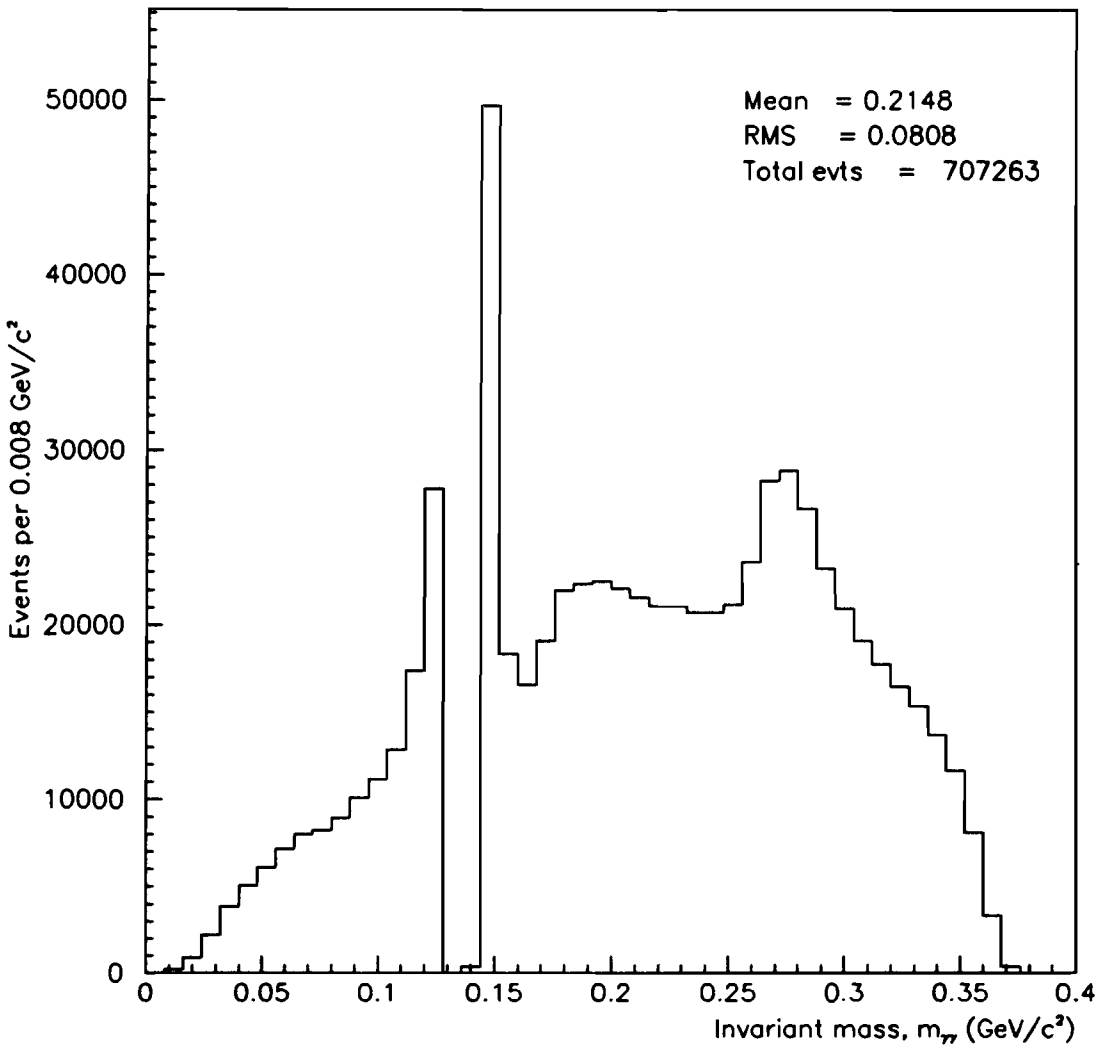

Figure 49. $m_{\gamma\gamma}$ distribution for $K \rightarrow \pi^0\gamma\gamma$ candidates at the data reduction stage after all the cuts have been applied. The spikes around 0.135 GeV correspond to $K \rightarrow 2\pi^0$ background.

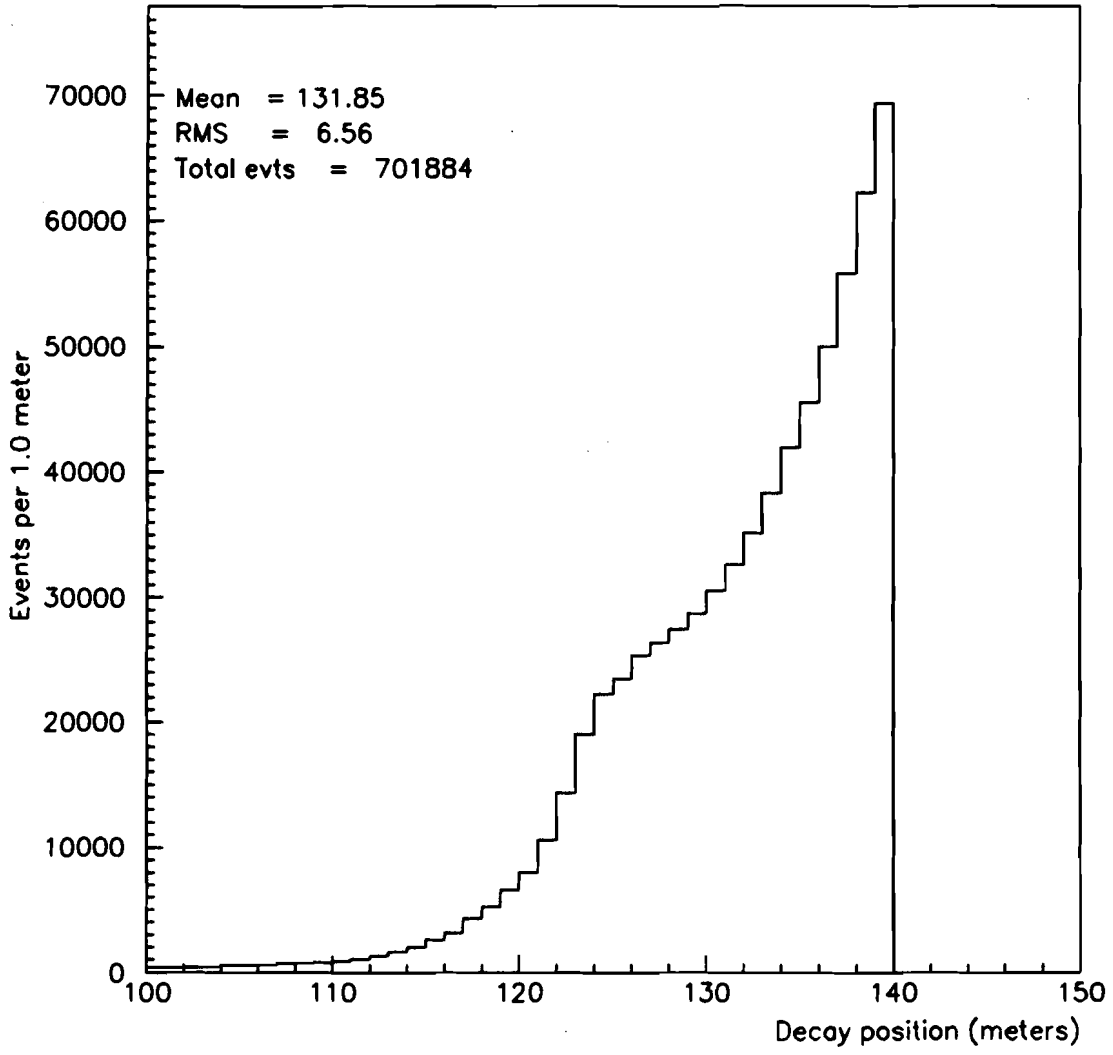

Figure 50. z decay vertex distribution for $K \rightarrow \pi^0\gamma\gamma$ candidates at the data reduction stage after all the cuts have been applied. The "knee" at about 123 m is not prominent now.

excludes $\gamma\gamma$ masses around the π^0 mass and the second is a "double fusion" peak at about $m_{\gamma\gamma}$ 270 MeV. This peak arises when $2\pi^0$'s in the $K_L \rightarrow 3\pi^0$ decay get superimposed as illustrated in Figure 51. The $3\pi^0$'s are labeled as π_a^0, π_b^0, π_c^0 and the photons to which they decay are γ_{1a} γ_{2a}, γ_{1b} γ_{2b} and γ_{1c} γ_{2c} respectively. γ_{1a} and γ_{2a} correspond to two distinct clusters in the lead glass array but each photon from π_b^0 overlaps with a photon from π_c^0 (in this case γ_{1b} overlaps with γ_{1c} and γ_{2b} overlaps with γ_{2c}). If the 4-momenta of γ_{1b}, γ_{2b}, γ_{1c}, γ_{2c} are labeled as P_1, P_2, q_1, q_2

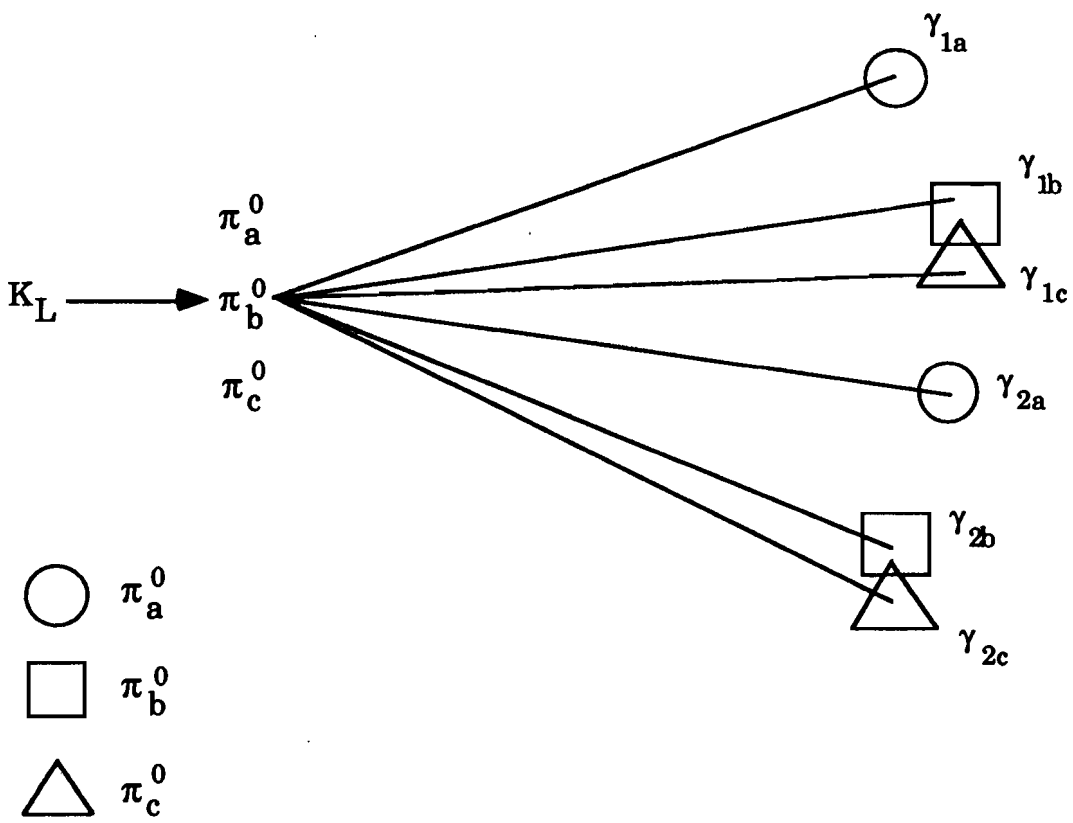

Figure 51. Illustration of $2\pi^0$'s from a $K_L \rightarrow 3\pi^0$ decay getting superimposed. Each photon from one π^0 overlaps with a photon from the other π^0.

respectively then we have:

$2P_1 P_2 = m^2_{n\pi^0}$ (5.3)

$2q_1 q_2 = m^2_{n\pi^0}$

Since photons γ_{1b}, γ_{1c} are unresolvable and similarly γ_{2b}, γ_{2c} are unresolvable,

$P_1 = aq_1$ (5.4)

$P_2 = bq_2$

By using Equations (5.3) and (5.4) we have the condition

$ab=1$ (5.5)

and if we form the square of the the $\gamma\gamma$ effective mass we have that

$m_{\gamma\gamma}^2 = 2(P_1+q_1)(P_2+q_2) = (2+a+b)m^2_{n\pi^0}$ (5.6)

Equation 5.5 implies that min(a+b)=2

This concludes that $m_{\gamma\gamma}$ should have a threshold at about 270 MeV for this particular case of fusions.

In the first data reduction period the selection criteria were similar. The changes in the cuts consisted basically in the following:

. There should not be even number of tracks simultaneously in both the x and y views of the chambers.

. The z vertex was required to lie within 145 m from the target.

. $m_{\pi}0$ should be within ± 10 MeV from the nominal mass of the π^0.

. $m_{\gamma\gamma}$ should be away from the nominal π^0 mass by ± 10 MeV.

. The photon veto ADC gate was 15 ns for these data and the cuts were very similar with the ones mentioned above for the 15 ns gate.

. It was required that no latches associated with the C bank fired in order to reject events with photon conversions.

5.3 Data Summary Tapes

Approximately 5330 tapes of raw data were written during the run, including tapes for calibration data and special runs. The data reduction and production of DSTs (Data Summary Tapes) for the full data set was performed, as mentioned above, at two different time periods after the completion of the run, using the ACP computer at Fermilab. In the first data reduction 995 raw data tapes were reduced to 215 first level DSTs. Since these 995 tapes were about 20% of the total number of tapes with analysis data we call this set "the 20% of the data" although in reality it is about 27%. The DST data were seperated according to their trigger type and the criteria that each analysis satisfied in several streams. The $K_L \rightarrow \pi^0\gamma\gamma$ candidates occupied 2 tapes and they were saved in their raw data format. One can get a feeling for the reduction factor of each one of the cuts applied in this data reduction for $K_L \rightarrow \pi^0\gamma\gamma$ by looking at their effect on 5 raw tapes. After the requirement for 4 hardware and 4 software clusters and the tracking requirement, we started with 80,670 events. The z vertex cut at 145 m from the target reduces this number to 14,373. The m_{π^0} cut reduces this number to 6,480 and after the $m_{\gamma\gamma}$ cut we have 4,200 events. After the center of energy requirement we are left with 2,910 events and the photon veto cuts reduced this number to 1,970. The requirement for C latches not firing gave us 1,420 events and the fusion cut reduced it even more to 930 events. In the end the sweeper-anti requirement reduced this number to 762 events for these five raw tapes. Out of the 995 tapes, 174,330 events passed the cuts.

During the second period of data reduction we reduced seperately the data from the "neutral" and the "chg, neutral" running modes. The reduction factors were 1 DST tape for 8 raw tapes for the "neutral" trigger and 1 DST tape for 5 raw data tapes for the "chg, neutral" trigger. The $K_L \rightarrow \pi^0\gamma\gamma$ candidates were saved into DSTs together with $K_L \rightarrow \pi^0\pi^0\gamma\gamma$ candidates and we had 8 DSTs from the "neutral" and 1 DST from the

"chg, neutral" running mode reductions. Two second level DSTs were produced for $K_L \rightarrow \pi^0\gamma\gamma$ from the "neutral" trigger by keeping only $K_L \rightarrow \pi^0\gamma\gamma$ events with z decay vertex less than 138 m from the target and no C or B latches firing. The raw event format was preserved for these data during all levels of reduction.

CHAPTER 6

BACKGROUND REJECTION - HIGHER LEVEL ANALYSIS

The backgrounds that are going to be discussed in this chapter are due to the $K_L \rightarrow \pi^+\pi^-\pi^0$, $K_L \rightarrow 2\pi^0$, $K_L \rightarrow 3\pi^0$ decays and background coming from accidental events. These backgrounds and the cuts used to remove them are going to be addressed one by one and in the end of the chapter will be presented a summary of all cuts used in the analysis. Several mass and decay vertex distributions at different stages of the analysis as well as the final distributions used for the extraction of an upper limit for the $K_L \rightarrow \pi^0\gamma\gamma$ decay will also be presented at the last section of this chapter.

6.1 Background from $K_L \rightarrow \pi^+\pi^-\pi^0$

$K_L \rightarrow \pi^+\pi^-\pi^0$ decays satisfying the "neutral" trigger, that is occuring downstream of the HDRA, can generate 4 clusters in the lead glass

calorimeter from which the two originate from a π^0 and therefore simulate a $K_L \rightarrow \pi^0\gamma\gamma$ decay. This potential background was easily removed by requiring that no tracks are found in either the x or the y projection of the chambers and that the B and C latches do not fire. If there is still $\pi^+\pi^-\pi^0$ background left in the $\pi^0\gamma\gamma$ sample even after these requirements it has to belong to one of the following three categories: i) The charged pions are not detected and therefore no tracks are reconstructed, and the B and C latches do not fire. The π^+, π^- though emit two bremsstrahlung photons which are detected at the calorimeter and therefore the event satisfies the "four-cluster" requirement. ii) Two accidental photons substitute for the two missing charged pions and the event again satisfies the "four-cluster" requirement. iii) One accidental and one bremsstrahlung photon substitute for the missing clusters.

The probability to have any of these cases occuring is very small because first of all the probability to have both pion tracks missing and no signal at the B and C latches is very small. To verify that, we generated $K_L \rightarrow \pi^+\pi^-\pi^0$ decays satisfying the conditions of the "neutral" trigger , that is downstream of the HDRA till the lead glass, and it turned out that out of 150K accepted decays no one survived the tracking and B, C latches' requirements. Therefore the survival probability of such events is less than 6.7×10^{-5}. Second the probability for an electron with energy greater than 1.5 GeV to emit a bremsstrahlung photon in our detector downstream of the HDRA and upstream of the B and C banks is 1-2% and therefore for the pion would be further suppressed by a factor of about 3×10^5. If one takes into account that both pions would have to emit such a photon and also the fact that the angle between the emitted photon and the charged pion direction is very small and if one misses the pions one is very likely to miss the radiated photons too, case i) is very rare indeed. As far as the accidentals are concerned, it will be shown later in Table 14 that the probability to have one accidental cluster at the glass after all cuts is

about 6.2×10^{-5} and the probability to have two accidental clusters is less than 2.95×10^{-6}. This, together with the very small probability of losing both tracks and having no latches firing at the B and C banks makes cases ii) and iii) very improbable. In fact, the $\pi^+\pi^-\pi^0$ background with both tracks missing the B and C banks and two accidental clusters substituting for them is predicted to exist in our data sample at a branching ratio level of less than about 2.3×10^{-9}. This calculation was done on the basis of a Monte Carlo study and by using the probability (90% confidence level) of having two accidental clusters at the glass.

6.2 Background from $K_L \rightarrow 2\pi^0$

The $K_L \rightarrow 2\pi^0$ decay is one of the larger potential backgrounds for the $K_L \rightarrow \pi^0\gamma\gamma$ decay. Both decays have a four-cluster final state and in principle none of the clusters is associated with any track except from the cases of having photon conversions. We will first discuss the reconstruction for a $K_L \rightarrow 2\pi^0$ decay because this will make it easier to understand the cuts used to remove them from the $K_L \rightarrow \pi^0\gamma\gamma$ sample. This reconstruction is done as following: for a $2\pi^0$ decay there are four clusters in the calorimeter and there are 3 distinct ways to choose 2 pairs of photons that correspond to two π^0's. The distance z from the lead glass of the longitudinal decay vertex of a particle of mass m that decays in n photons can be calculated from Equation (6.1), where E_i ,E_j are the photon energies and r_{ij} is their distance measured in the calorimeter.

$$m^2 = \frac{1}{2}\sum_{i=1}^{n}\sum_{j>i}^{n}\frac{E_iE_jr_{ij}^2}{z^2} \qquad (6.1)$$

The distance from the glass for each of the two π^0s in the $K_L \rightarrow 2\pi^0$ decay is then calculated by the same equation after substituting m with the nominal π^0 mass, $m_{n\pi^0}$. This distance has an error σ_z that depends on the

uncertainty in the energy and position measurements involved in the calculation. As illustrated in Figure 52 , each one of the 3 pairings mentioned above gives 2 z estimates Z_1 and Z_2 (one for each π^0) which are combined to give a weighted average *AVERZ*:

$$AVERZ = \frac{\frac{Z_1}{\sigma_{Z_1}^2} + \frac{Z_2}{\sigma_{Z_2}^2}}{\frac{1}{\sigma_{Z_1}^2} + \frac{1}{\sigma_{Z_2}^2}}$$

The correct pairing is picked by forming a χ^2 for each pairing as shown in Equation (6.2) and picking the pairing with the smallest (best) χ^2.

$$\chi^2 = \frac{(AVERZ - Z_1)^2}{\sigma_{Z_1}^2} + \frac{(AVERZ - Z_2)^2}{\sigma_{Z_2}^2} \qquad (6.2)$$

Then the kaon mass, m_K, is reconstructed by using Equation (5.1) after substituting *AVERZ* for z_{gl} and m_K for m_{nK}. In Figure 53 is plotted the best χ^2 versus m_K for $K_L \rightarrow 2\pi^0$ decays. The low mass events are mostly due to $3\pi^0$ background. The distribution is plotted after photon veto cuts but before cuts that remove fusions. The rejection of the $K_L \rightarrow 2\pi^0$ background in the $K_L \rightarrow \pi^0\gamma\gamma$ decay has been done in two steps. First it was required that $|m_{\gamma\gamma} - m_{n\pi^0}| > 14$ MeV. One can get a feeling of how many $2\pi^0$s get rejected with this cut by reconstructing the $K \rightarrow 2\pi^0$ decay assuming the kaon mass as is done for $K \rightarrow \pi^0\gamma\gamma$ and selecting the two pairs of photons that form the two π^0s in a similar way as in $\pi^0\gamma\gamma$ analysis. Then the mass of the pair of photons which is selected to be the π^0 candidate is plotted in Figure 54 and the mass of the pair of photons which is selected to be the $\gamma\gamma$ candidate is plotted in Figure 55. These plots are from a sample of $K_S \rightarrow 2\pi^0$ data corresponding to 2 first level DSTs, in the decay region 110 m-133 m and after photon veto cuts have been applied. The dip at around 135 MeV in $m_{\gamma\gamma}$ in Figure 55 is due to our requirement that the two clusters that form the π^0 candidate are the ones whose mass is the closest to $m_{n\pi^0}$ and therefore necessarily $m_{\gamma\gamma}$ is away from $m_{n\pi^0}$. The

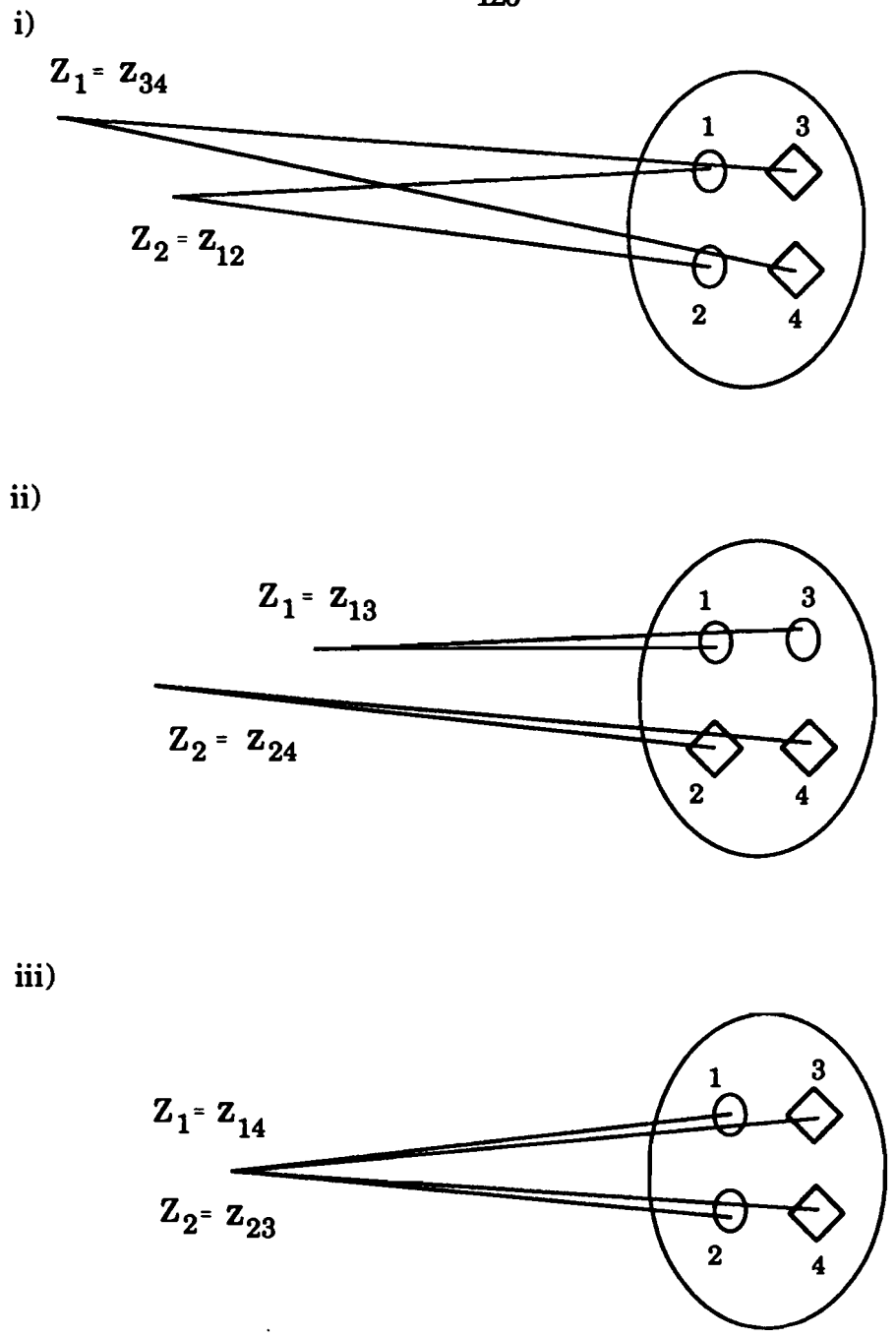

Figure 52. Photon pairings for the reconstruction of the z decay vertex in the $K \rightarrow 2\pi^0$ decay. As explained in the text the top two pairings are incorrect because they give inconsistent z determinations. The bottom pairing is the true pairing.

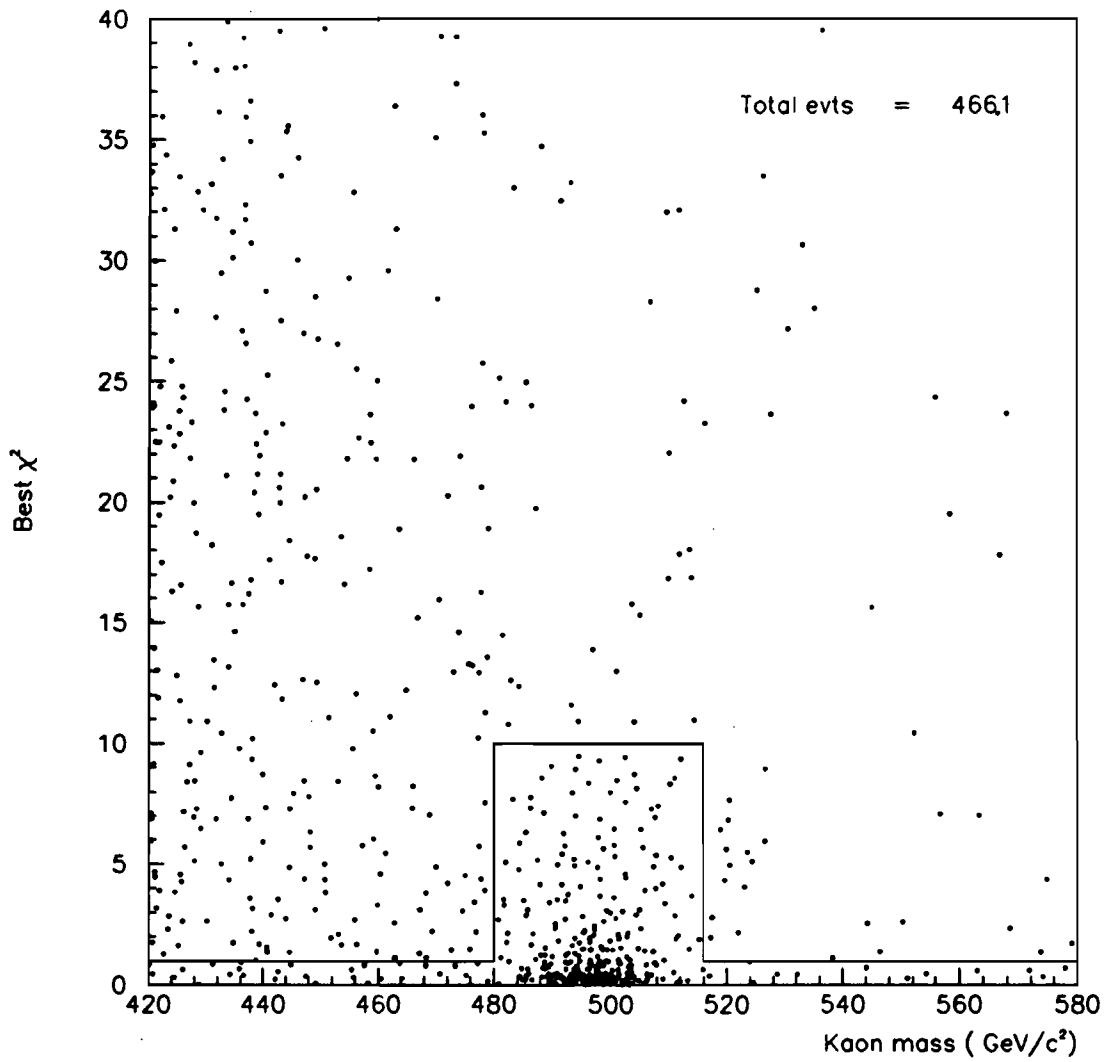

Figure 53. Best χ^2 versus reconstructed kaon mass for $K_L \rightarrow 2\pi^0$ decays.

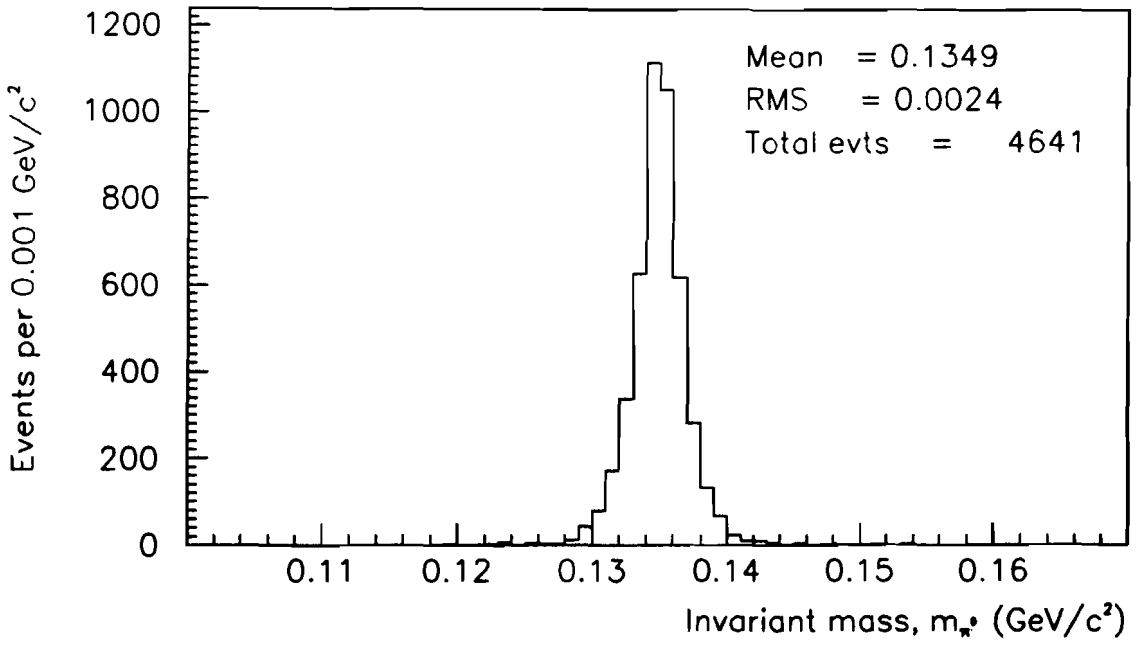

Figure 54. $m_{\pi}0$ **distribution for** $K_S \rightarrow 2\pi^0$ **decays starting from the assumption that the decay originates from a kaon.**

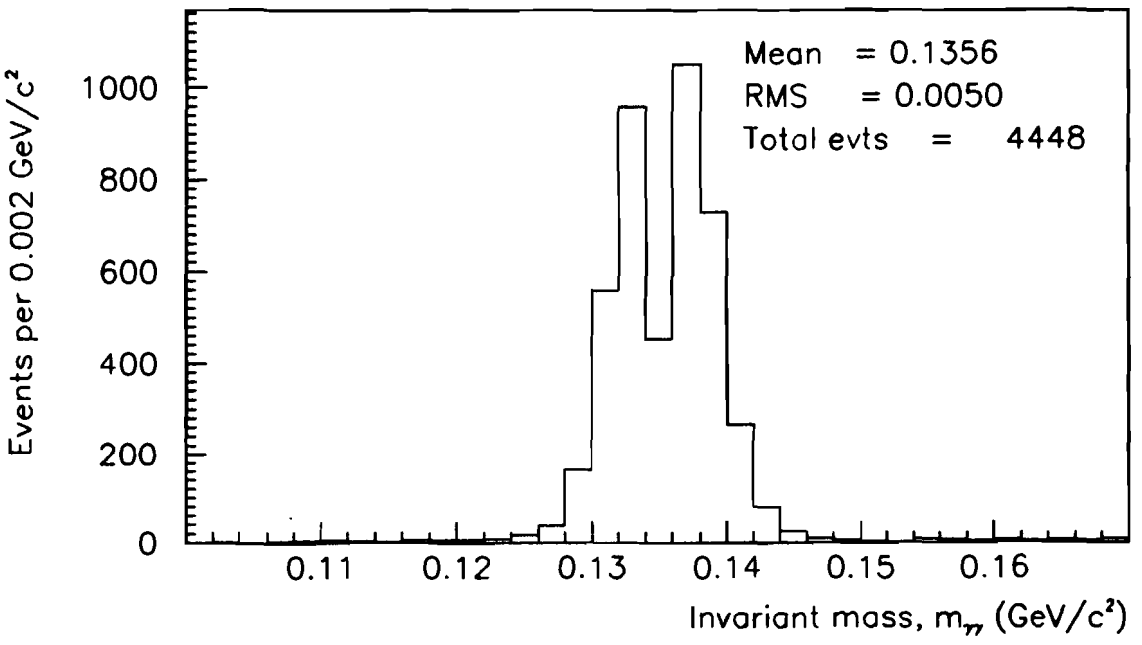

Figure 55. $m_{\gamma\gamma}$ **distribution for** $K_S \rightarrow 2\pi^0$ **decays starting from the assumption that the decay originates from a kaon. The dip at about 135 MeV is explained in the text.**

cut just discussed resulted in a suppression of the $K_L \rightarrow 2\pi^0$ background by a factor of about 30 as was found by Monte Carlo study. As a second step the $K_L \rightarrow \pi^0\gamma\gamma$ candidate was reconstructed like a $K_L \rightarrow 2\pi^0$ event and certain requirements were imposed on its χ^2 and on its reconstructed kaon mass. In particular it was required that χ^2 is greater than 1 and in addition if χ^2 was less than 10 and the invariant mass of the 4 clusters reconstructed between 0.480 GeV and 0.516 GeV the event was rejected. This cut is indicated by the solid line superimposed on Figure 53. Every $\pi^0\gamma\gamma$ candidate event reconstructing below the solid line gets rejected. The first requirement for χ^2 removes $K_L \rightarrow 2\pi^0$ background and also $K_L \rightarrow 3\pi^0$ background where two photons from the same π^0 are missing. The second requirement for χ^2 and m_K is intended to remove $K_L \rightarrow 2\pi^0$ background where mispairings led to the wrong selection of the π^0 candidate. For example if the correct pairing for a $K_L \rightarrow 2\pi^0$ decay is $\gamma_1\gamma_2$, $\gamma_3\gamma_4$ and $m_{\gamma_1\gamma_2}$ = 136.2 MeV and $m_{\gamma_3\gamma_4}$= 137.1 MeV but $m_{\gamma_1\gamma_3}$= 135.1 MeV and $m_{\gamma_2\gamma_4}$= 300.0 MeV then because the algorithm picks as π^0 candidate the pair of photons whose mass is closest to the nominal π^0 mass, the wrong pairing is picked and the event survives the first step of rejection. The second step of $2\pi^0$ rejection rejects these mispairings giving an additional rejection factor of about 24 based on Monte Carlo studies.

6.3 Background from $K_L \rightarrow 3\pi^0$

The principal background for the $K_L \rightarrow \pi^0\gamma\gamma$ signal after the rejection of the $K_L \rightarrow 2\pi^0$ background is $K_L \rightarrow 3\pi^0$ decays which can end up as four-cluster events either when photons are undetected or when they overlap in the lead glass and are not resolvable as seperate clusters. The decay $K_L \rightarrow 3\pi^0$ occurs about 3 x 10^5 more frequently than the $\pi^0\gamma\gamma$ is predicted to

occur and the challenge in observing such a signal is the effective rejection of the $K_L \rightarrow 3\pi^0$ background. This rejection occurs in several steps which are described right below.

6.3.1 Photon veto cuts

The veto counters were effective in detecting photons escaping from the fiducial volume of the decay and events with subtantial energy deposit in these counters were rejected. Out of the 14 veto planes, PA, AM, RA, CA, BA and also VA4 and LGA were in veto already at the trigger level in the "neutral" trigger. Some of the trigger cuts were tightened up in the analysis and extra cuts were applied for the remaining photon vetoes.

As mentioned in Chapter 2 the inner edge of the lead glass calorimeter is defined by the CA counters. The energies of the 4 counters surrounding each beam were summed up individually for the lower and the upper beams and it was required that the maximum of them be less than 2 μ where μ corresponds to a muon equivalent (the trigger cut was about 10 μ).

Clusters located at the outer edge of the array were handled with special care since there was no edge there defined by hardware. Events involving such clusters were rejected if any of the following conditions which are sketched in Figure 56 were satisfied: that is, if a) there was a missing corner block and the center of the cluster was located at the quarter of the central block neighboring to the missing block or b) there was a missing side block and the center of the cluster was located at the half of the central block neighboring to the missing block. In the case of a missing side block there was always a corner block missing at the same time.

Photons escaping down the holes of the calorimeter were detected by the BA counters which are described in Chapter 2. In this analysis the

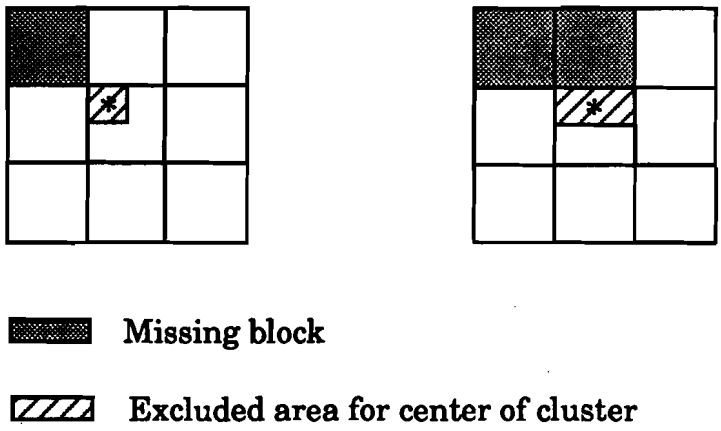

Figure 56. Disallowed topologies for cluster centers at the edges of the array.

sum of the energy of the x counters of the first two layers of BA was required to be less or equal to 4.8 GeV. For the remaining photon vetoes it was specifically required that:

1)Energy in VA1 ≤ 2.34 μ
2)Energy in VA2 ≤ 1.17 μ
3)Energy in VA3 ≤ 0.9 μ
4)Energy in VA4 ≤ 1.08 μ
5)Energy in MA ≤ 1.35 μ
6)Energy in LGA ≤ 2.25 μ
7)Energy in DRAC ≤ 0.45 μ
8)Energy in DRAN ≤ 0.54 μ

where μ represents a muon equivalent.

6.3.2 z decay vertex cut

When one or more photons from the $3\pi^0$ decay are missing then the longitudinal decay vertex gets artificially shifted towards the lead glass as can be seen by Equation (5.1). Also photons are more likely to overlap when the decays occur near the calorimeter. Therefore the $3\pi^0$ background can be reduced significantly by avoiding the downstream region. In particular we considered only decays in an 18 meter upstream decay region starting at 110 m and ending at 128 m from the target. In the decay region between 100 and 110 m from the target the $\pi^0\gamma\gamma$ acceptance is very small, at the order of 10^{-5}, due to the lead Mask. The selection of the downstream edge of the decay region, as will be discussed in Chapter 7, was based on a Monte Carlo study. In fact we derived a 90% confidence level upper limit for the $K_L \rightarrow \pi^0\gamma\gamma$ decay as a function of the downstream edge of the decay region on the basis of the $3\pi^0$ and $2\pi^0$ backgrounds and the optimum place has been picked. This will be demonstrated in Figure 136. No $\pi^0\gamma\gamma$ data candidates have been used for this optimization.

6.3.3 Center of energy cut

The center of energy of the event which was defined in Chapter 5 was required to be in the beam area and in more detail it was required that it lies within a square of side 10.5 cm centered at the center of the vacuum beam (the regenerator beam is not used for this measurement). $3\pi^0$ decays with missing energy have their center of energy reconstructed outside the beam area. To demonstrate this we show in Figure 57 the center of energy distribution for $K_L \rightarrow 3\pi^0$ Monte Carlo decays that satisfy the "four-cluster" trigger requirement and have been reconstructed as $K \rightarrow 2\pi^0$ decays. The events reconstruct in the decay region 110-134 m from the target and photon veto cuts and several of the fusion cuts have

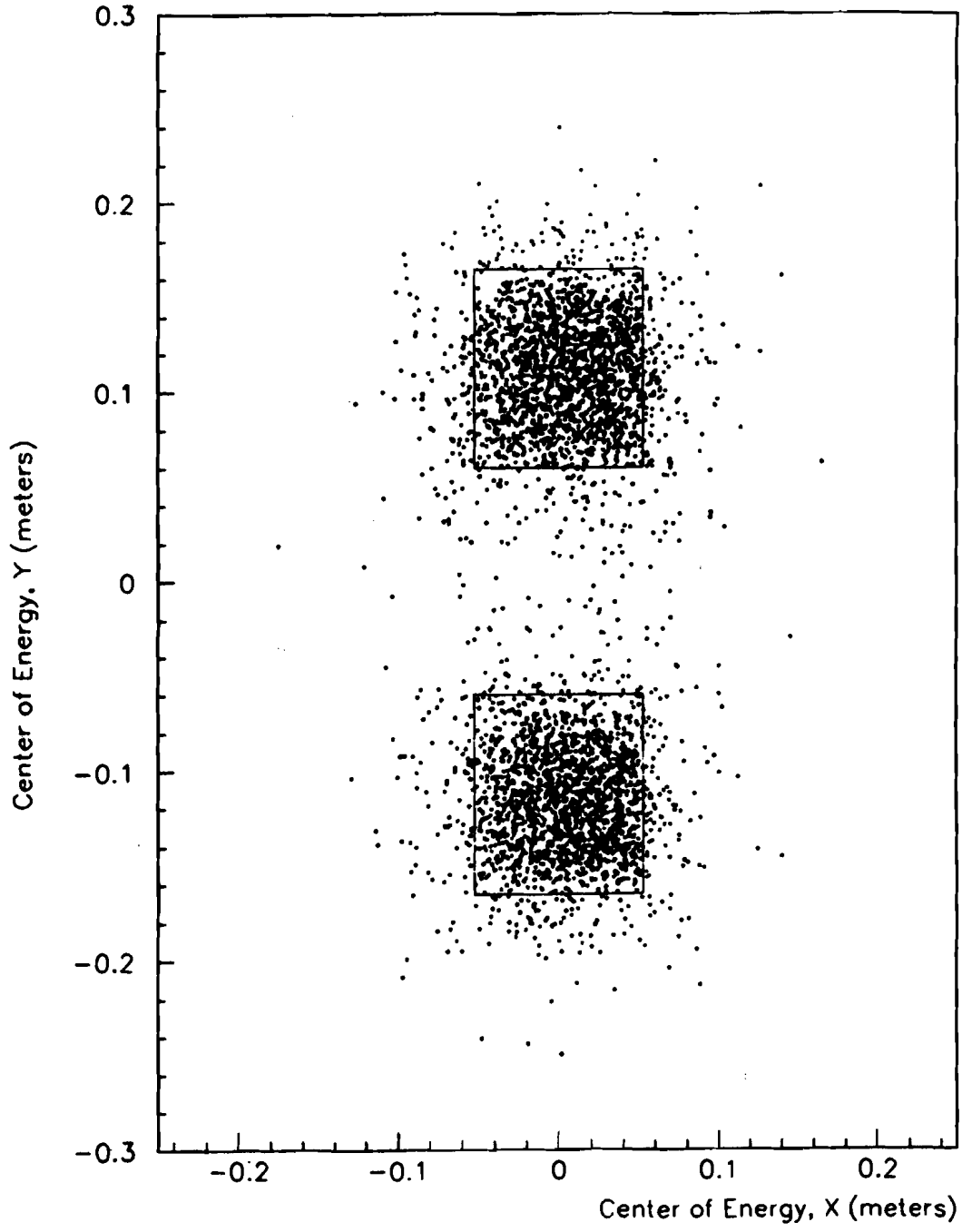

Figure 57. Center of energy distribution for $K_L \rightarrow 3\pi^0$ decays satisfying the "four-cluster" trigger requirement. Events reconstructing outside the contours are rejected.

been applied. The contour indicates the position of the cut. Events with missing energy, that have their center of energy reconstructed outside the contours are rejected. For the $\pi^0\gamma\gamma$ candidates we applied a center of energy cut already at the data reduction stage.

6.3.4 Fusion cuts

Events with unresolvable overlapping clusters at the calorimeter make the detection of the $\pi^0\gamma\gamma$ signal quite difficult and their reduction turned out to be a real challenge. We would like to remind the reader at this point that this experiment was not designed for the study of the rare decay in question and the lead glass block size of 5.8 x 5.8 cm^2 made the fusion recognition really difficult. However the number of events with unresolved overlapping clusters was subtantially reduced by rejecting events with cluster shapes inconsistent with that of a single photon. To achieve this, several fusion algorithms were developed, some of which are described below, and which were applied in addition to the fusion algorithm discussed at Chapter 5 which was applied at the data reduction level. Several times in what follows we are going to compare the effect of a fusion cut on $K_L \rightarrow \pi^0\gamma\gamma$ candidates with its effect on $K_S \rightarrow 2\pi^0$ decays because $K_S \rightarrow 2\pi^0$ gives a 4 cluster final state which is free from $3\pi^0$ background. Some of the fusion algorithms developed are the following:
1) For every cluster in the event one considers a 5 x 5 block array around the center of the cluster. The energy of the cluster is calculated by using the energies of the blocks in a central 3 x 3 block subarray only as mentioned also in Chapter 5. By stepping through the 16 block ring outside the central 9 block subarray one forms the sum of the energy of every two consecutive blocks (see Figure 58) and finds the one of the 16 such pairs of blocks in the cluster that has the maximum sum of energy, "maxsum". A block does not contribute to the sum if it belongs to the 3 x 3

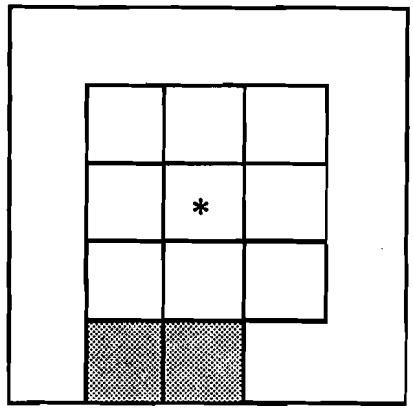

Figure 58. The 16 block ring outside the 3 x 3 blocks belonging to each cluster, on which fusion algorithm 1 operates.

central subarray of a different cluster or if although its energy is greater than 1 GeV the cluster finder trigger processor does not have any hit to the cell corresponding to the block (The Cluster Finder threshold was about 1 GeV for each block so in this sum blocks with accidental activity outside the 20 ns window of the cluster finder are excluded). Maxsum is plotted for every cluster in the event as a function of the energy of the cluster in Figure 59 for $K_S \rightarrow 2\pi^0$ and in Figure 60 for $K_L \rightarrow \pi^0\gamma\gamma$ candidates. If it is greater than 0.8 GeV for any of the clusters the event is rejected. The cut is indicated with the solid line in the same figures. In Figure 61 is presented an example of a cluster from $3\pi^0$ background that is rejected by this cut.

2) A second algorithm uses ratios of columns and rows in the 3 x 3 array that corresponds to each cluster in order to recognize fusion patterns. As shown in Figure 62, for each cluster are formed the sums E_L and E_R of the left and right column respectively in the 9 block array. Similarly are

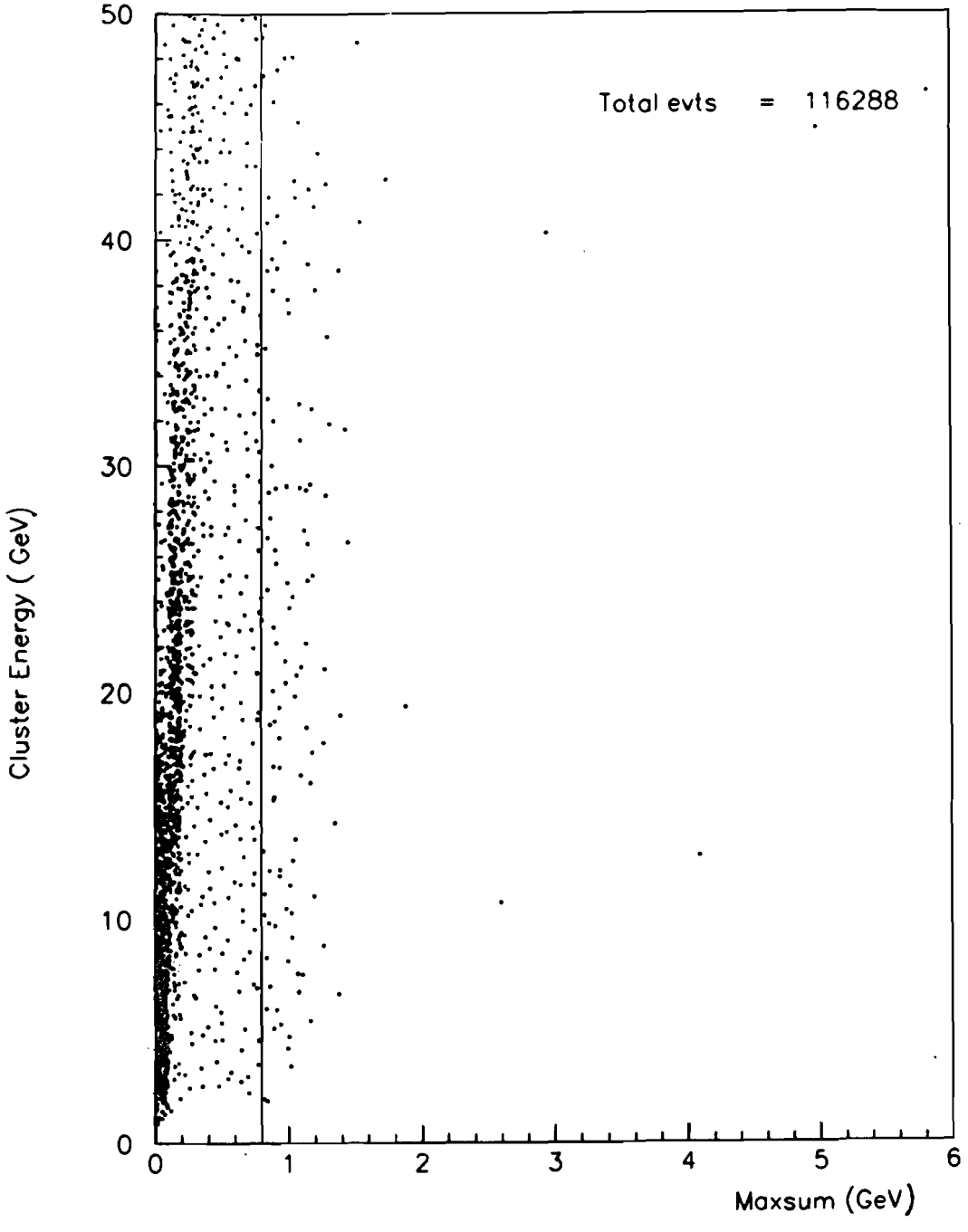

Figure 59. Maximum energy in two consecutive blocks in the 16 block ring surrounding the blocks belonging to the cluster versus the cluster energy for $K_S \rightarrow 2\pi^0$ decays.

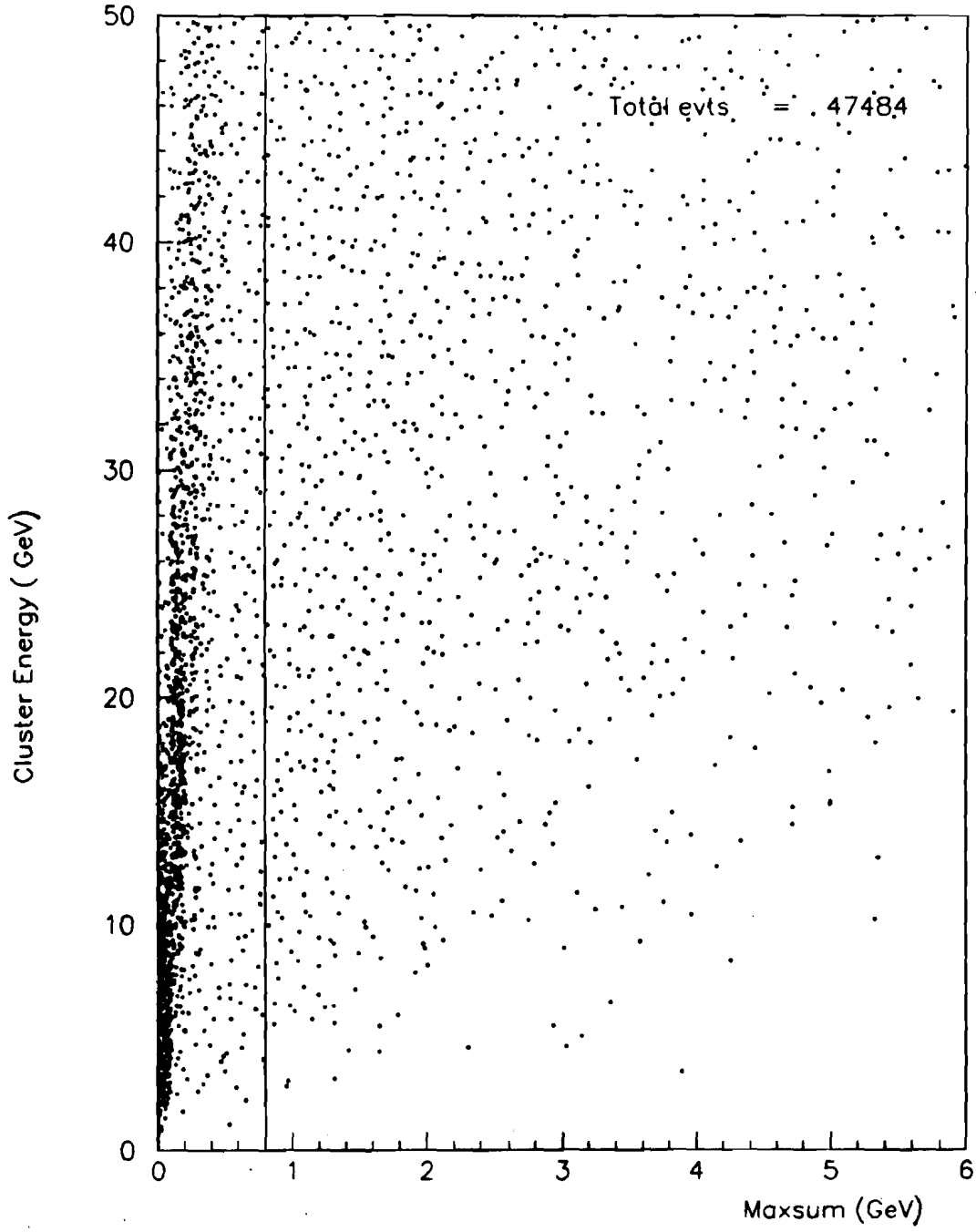

Figure 60. Maximum energy in two consecutive blocks in the 16 block ring surrounding the blocks belonging to the cluster versus the cluster energy for $K_L \rightarrow \pi^0\gamma\gamma$ candidates.

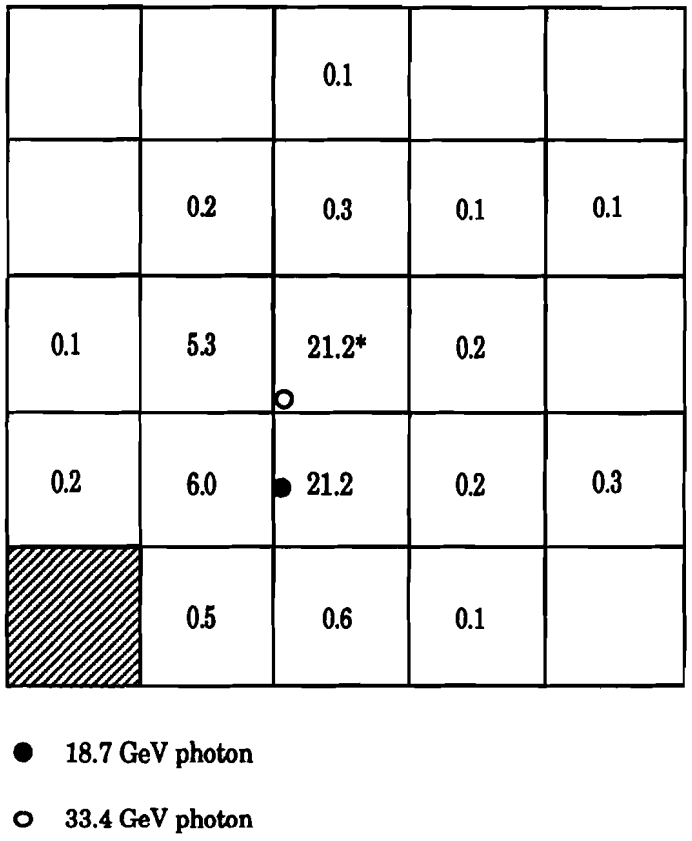

Figure 61. Example of a fused cluster from $3\pi^0$ background Monte Carlo. The circles correspond to the positions of the photons. The shaded block is a missing block in the holes of the array.

formed the sums E_T and E_B of the top and bottom rows. Next one forms the quantities:

$V_1=(E_1/Ecluster-0.02)*E_2/Ecluster$ for $E_1=min(E_L, E_R)$ and $E_2=max(E_L, E_R)$

$V_2=(E_3/Ecluster-0.02)*E_4/Ecluster$ for $E_3=min(E_T, E_B)$ and $E_4=max(E_T, E_B)$

where Ecluster is the energy of the cluster. The maximum of V_1 and V_2, "valmax", is picked and is plotted as a function of the energy of the cluster

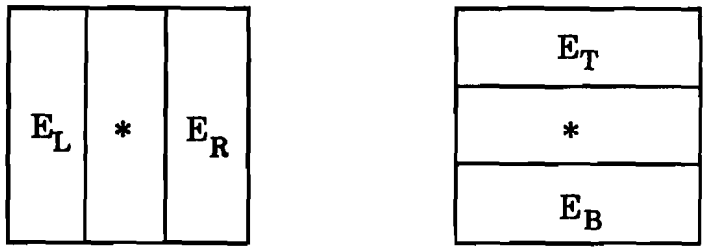

Figure 62. Rows and columns within a cluster on which fusion algorithm 2 operates.

for every cluster in the event in Figure 63 for $K_S \rightarrow 2\pi^0$ and in Figure 64 for $K_L \rightarrow \pi^0\gamma\gamma$ candidates. These plots are done after the previously discussed fusion cut was applied. Valmax is required to be at most 0.0025 for clusters with energy more than 20 GeV and at most 0.0150 for clusters with energy between 4 and 20 GeV. Otherwise the event is rejected.

3) A third algorithm considers the four corner blocks in a cluster and for each corner block forms the ratios of the energy of its two immediade side block neighbors, as in Figure 65, over the energy of the corner block. For these ratios to be formed the corner block has to have energy greater than 1 GeV and the corresponding cell of the cluster finder has to be hit. These ratios are formed for all 4 corners of a cluster and the minimum of them, "cmin", is picked and it is plotted for every cluster in the event in Figure 66 for $K_S \rightarrow 2\pi^0$ and in Figure 67 for $K_L \rightarrow \pi^0\gamma\gamma$ events after the two previous fusion requirements were applied. The event is rejected if cmin is less than 0.5.

4) Because the Cluster Finder had a threshold for each block of about 1 GeV there were cases of having soft photons in the calorimeter not seen by the proccessor. One would like to reject these events if the soft photons

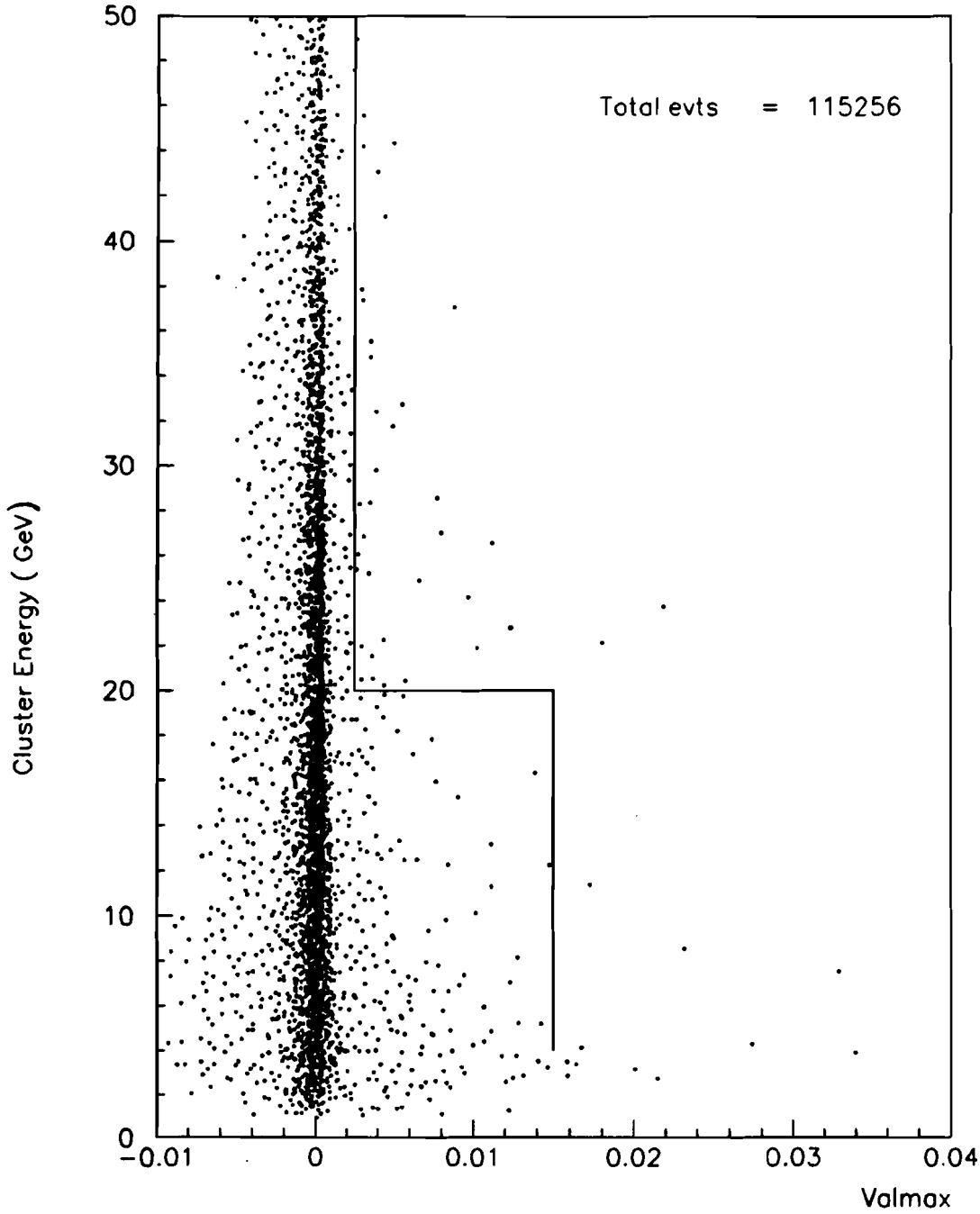

Figure 63. Valmax, as explained in the text, for each cluster versus the cluster energy for $K_S \rightarrow 2\pi^0$ decays.

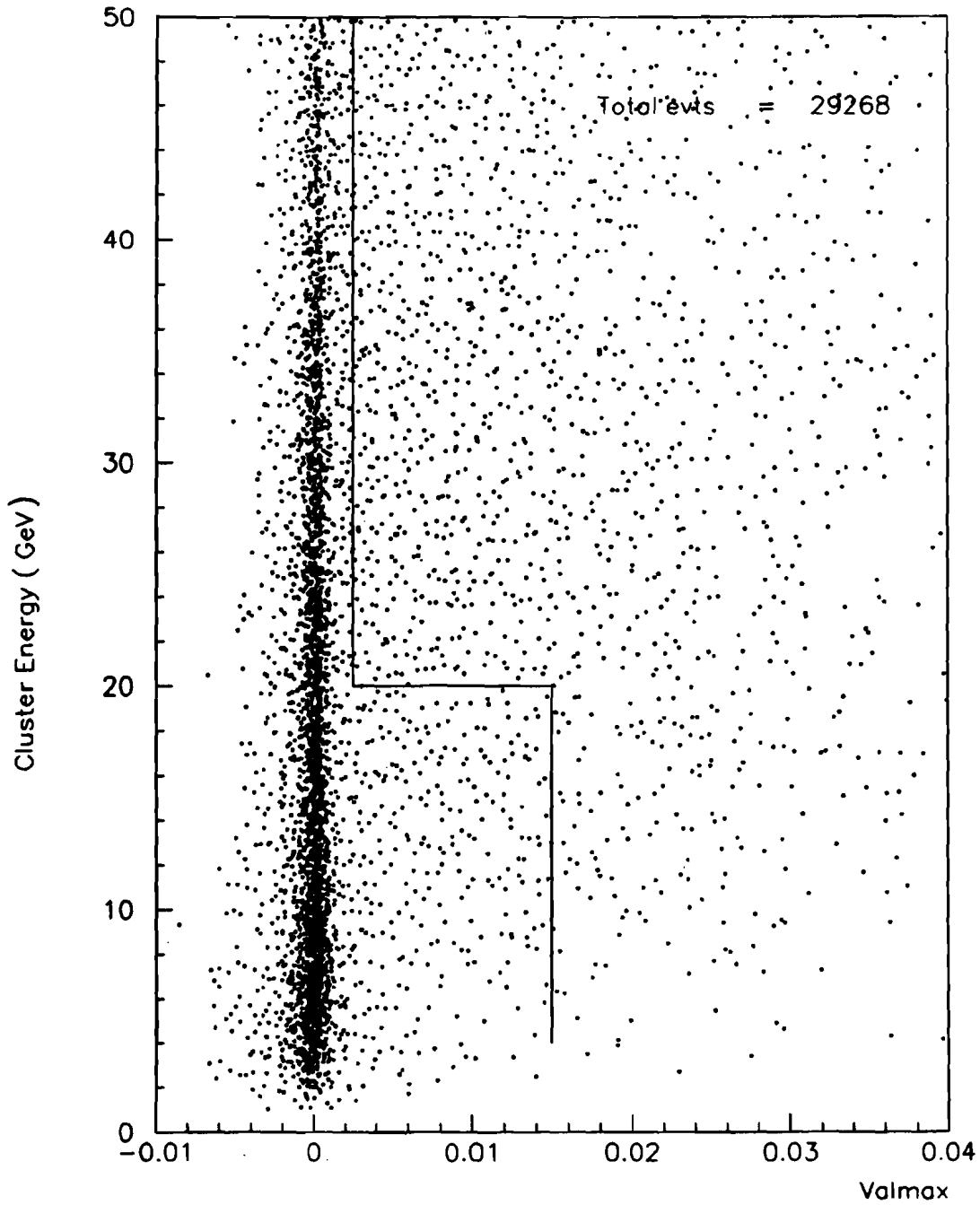

Figure 64. Valmax, as explained in the text, for each cluster versus the cluster energy for $K_L \rightarrow \pi^0\gamma\gamma$ candidates.

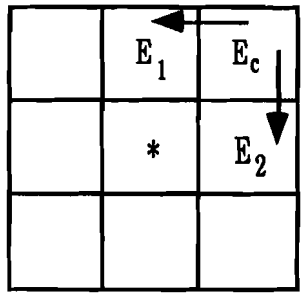

Figure 65. Corner and side blocks
on which fusion algorithm 3 operates.

originate from a $3\pi^0$ decay. This is done with the following algorithm which is applied to adders that have no lead glass block with energy above the HCF threshold and also no block belonging to the 5 x 5 block area around the center of any other cluster. For each one of these adders one forms the sum of the ADC counts for the lead glass blocks corresponding to the adder. Then the ratio of the adder ADC counts and the previous sum is formed. The adder gain is roughly 10 times less than the lead glass gain and if one takes this into account for in time photons the above ratio should be close to 1. When this ratio is greater than 0.6 and less than 1.4 , then one requires that each one of the blocks that belong to this adder have energy less than 120 ADC counts. The raw ADC counts, "maxblk", of such blocks belonging to such adders and having the maximum energy among the other blocks belonging to the adder are plotted in Figure 68 for $K_S \rightarrow 2\pi^0$ and in Figure 69 for $K_L \rightarrow \pi^0\gamma\gamma$ events. The cut is indicated by the arrow.

5) A fifth algorithm worked again with several ratios of block energies within the 3 x 3 block region around the center of a cluster. These ratios and their relationships were studied in order to seperate single clusters from fused clusters. Let us name 1, 2, 3, 4, 5, 6, 7, 8 and 9 the blocks

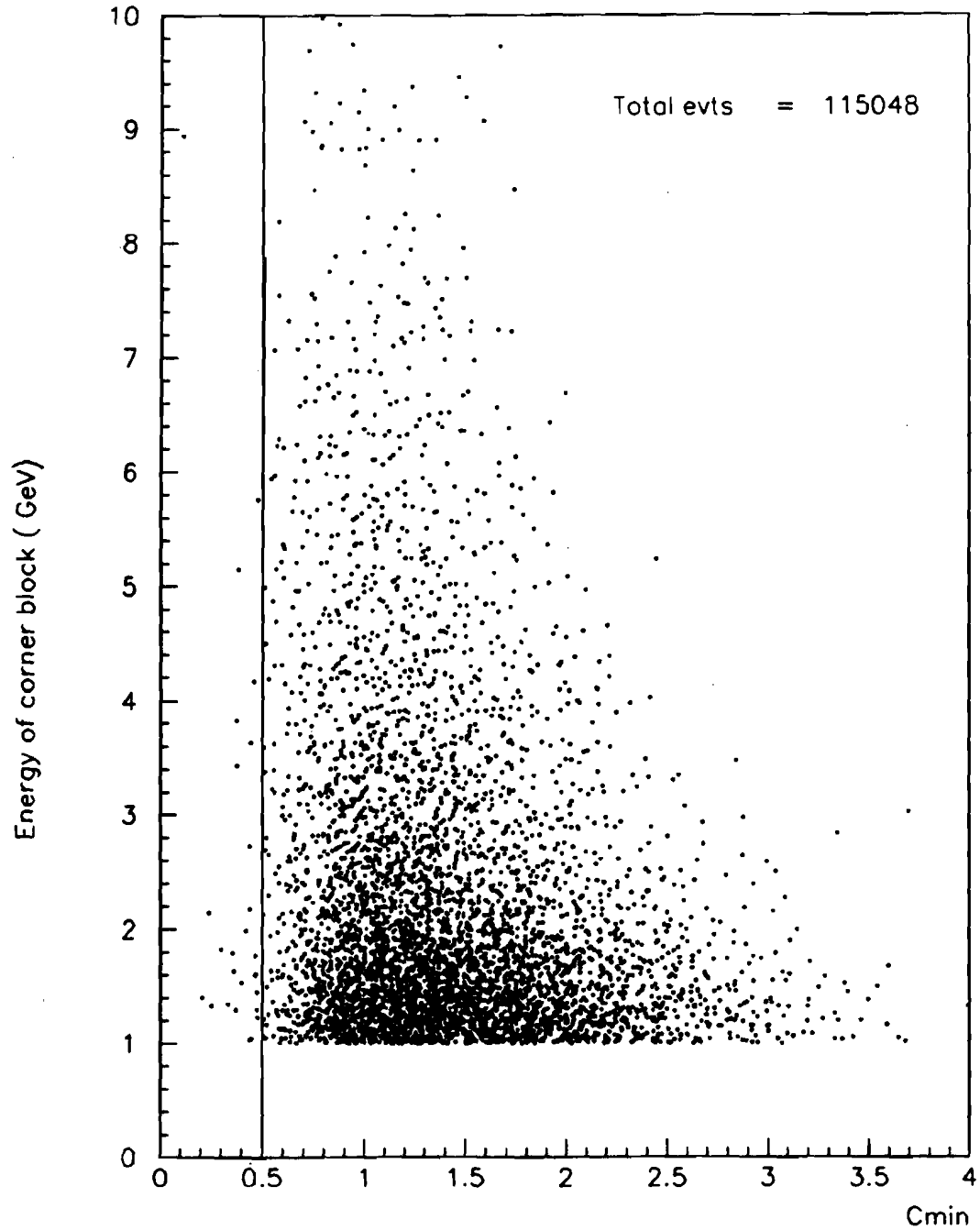

Figure 66. The minimum ratio of the energy of a side block to the energy of a corner block among all corner blocks of a cluster versus the energy of the corner block for $K_S \rightarrow 2\pi^0$ events.

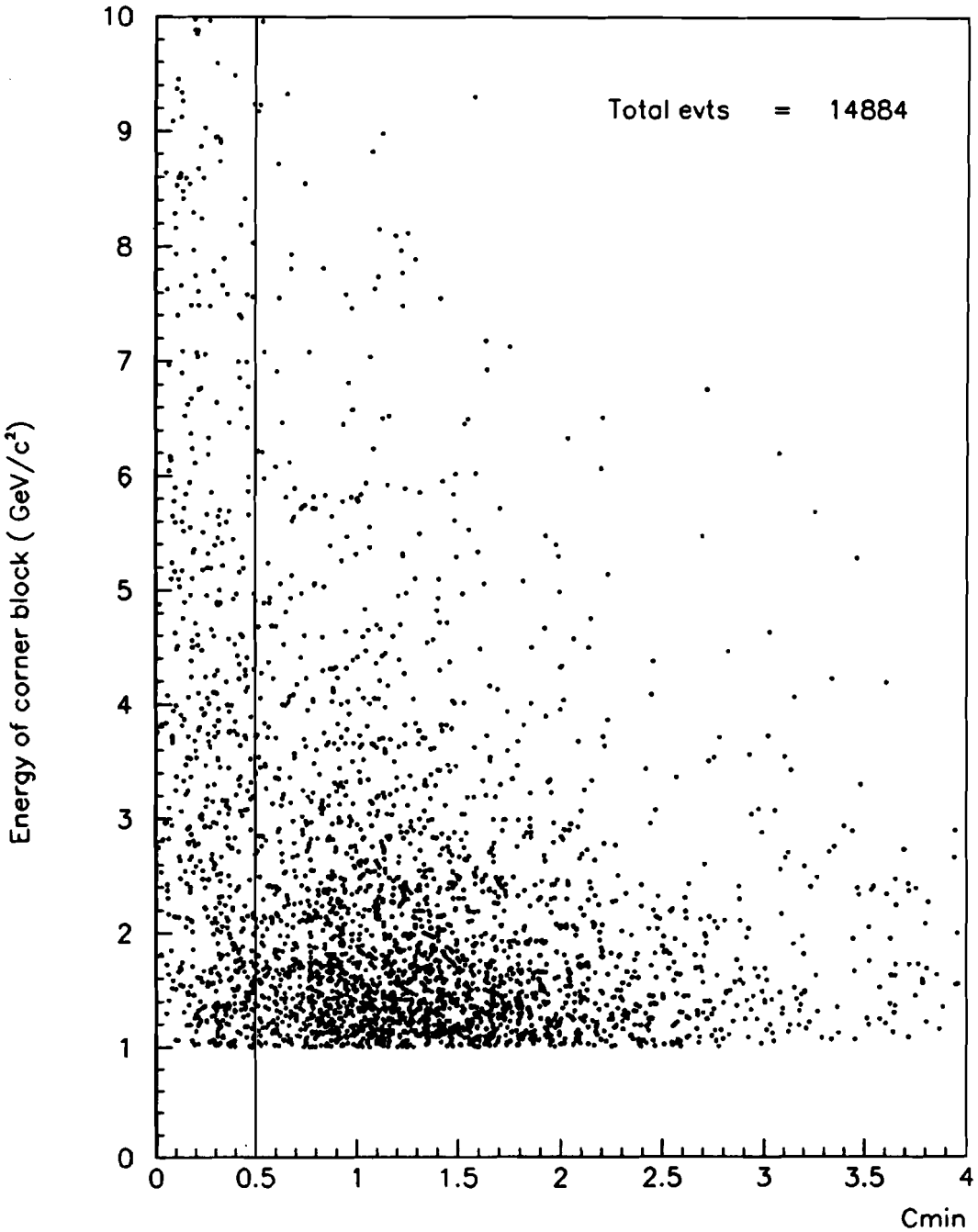

Figure 67. The minimum ratio for the energy of a side block over the energy of a corner block among all corner blocks of a cluster versus the energy of the corner block for $K_L \rightarrow \pi^0\gamma\gamma$ candidates.

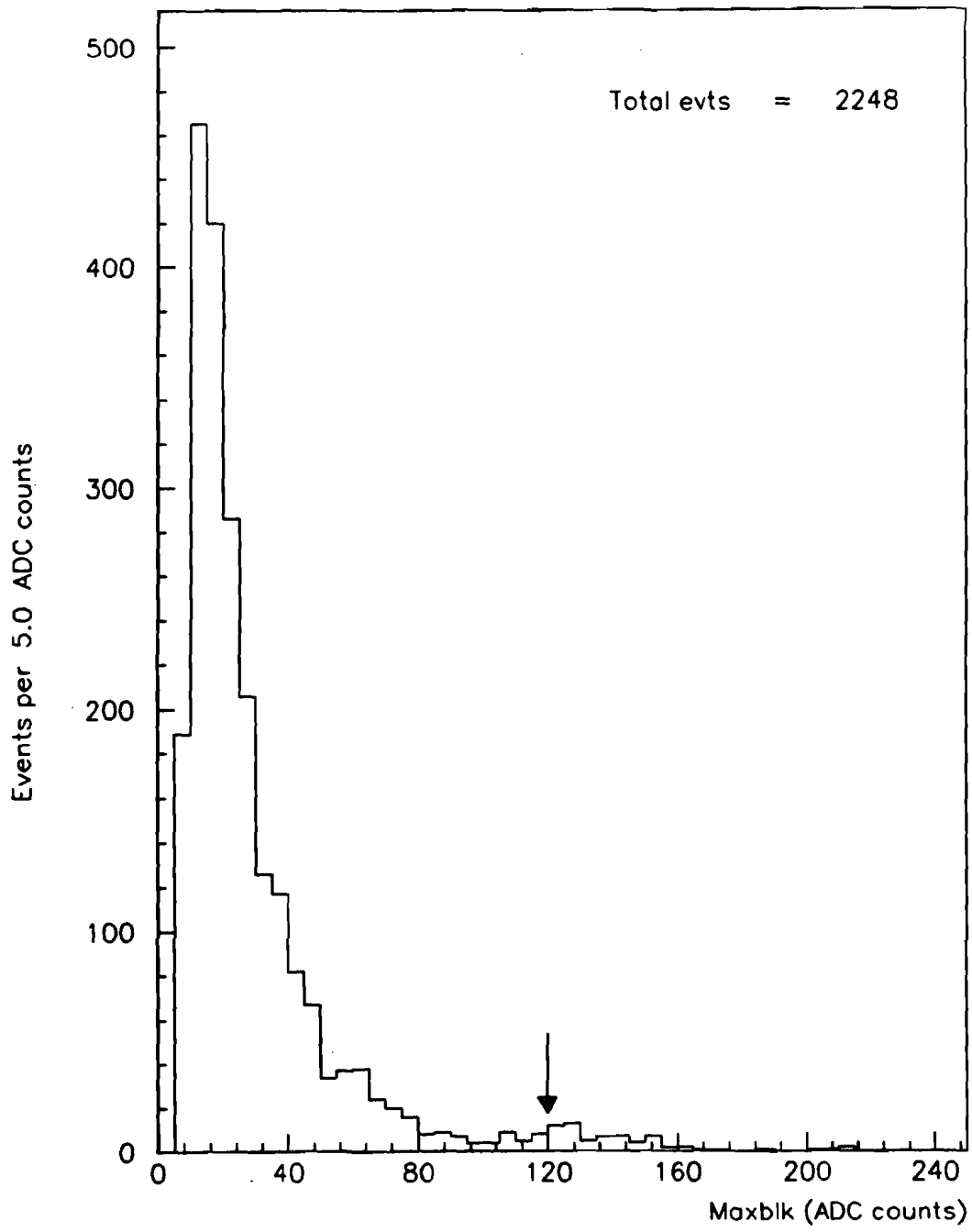

Figure 68. Distribution of the energy in ADC counts of the block with the maximum energy within an "in time" adder, as described in the text, for $K_S \rightarrow 2\pi^0$ decays.

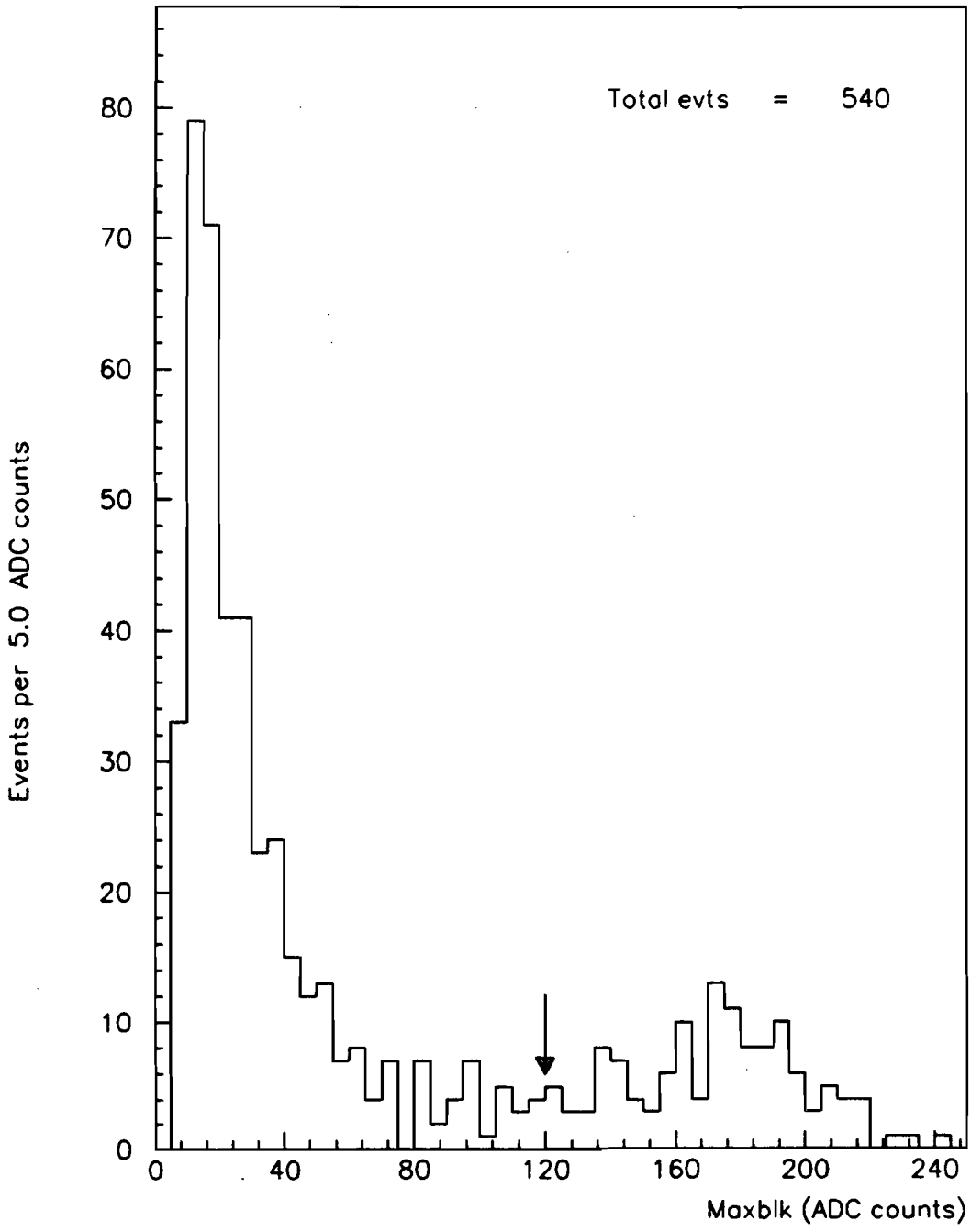

Figure 69. Distribution of the energy in ADC counts of the block with the maximum energy within an "in time" adder, as described in the text, for $K_L \rightarrow \pi^0\gamma\gamma$ candidates.

belonging to a cluster as shown in Figure 70 and E(1), E(2), E(3), E(4), E(5), E(6), E(7), E(8) and E(9) their energies. "Esum9" will be called the sum of the energies of the 9 blocks. For every cluster the block with the maximum energy among the side blocks 6, 2, 4 and 8 was picked and let us assume in this case that this is block 6. Then among blocks 2 and 8 the one with the maximum energy is found and let us assume in this example that this is block 8.

9	6	3
8	5*	2
7	4	1

Figure 70. Nine lead glass blocks belonging to a cluster.

Various ratios of block energies are formed at this point:

$$\text{Rmaxcen}=\frac{E(6)}{E(5)},\quad \text{Rtopmid}=\frac{E(9)}{E(8)},\quad \text{Rbotmid}=\frac{E(7)}{E(8)}$$

$$\text{Rmidmid}=\frac{E(8)}{E(5)},\quad \text{Rlefmid}=\frac{E(9)}{E(6)},\quad \text{Rmincen}=\frac{E(4)}{E(5)}$$

These ratios or their relationships were checked for several different ranges of Esum9 and some plots are shown in figures 71, 73 and 75 for $K_S \rightarrow 2\pi^0$ events and in Figures 72, 74 and 76 for $K_L \rightarrow \pi^0\gamma\gamma$ candidates. The cuts applied were different for the different ranges of Esum9 and they are indicated in the figures with the solid lines. Events at the left of the solid lines were rejected. These plots correspond to the same data as the previous fusion plots but after the previous 4 fusion cuts were applied.

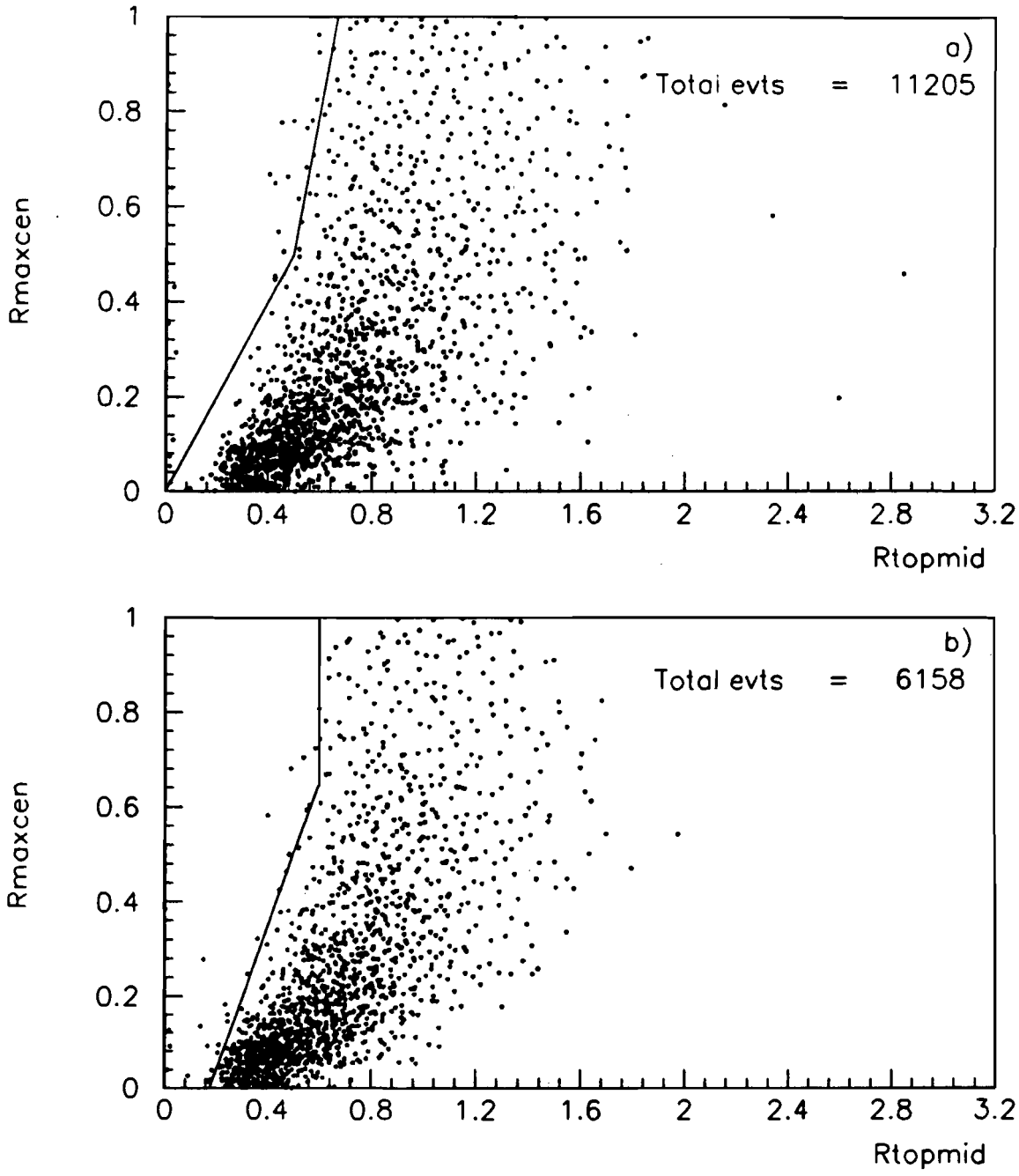

Figure 71. Rtopmid versus Rmaxcen, as defined in the text, for $K_S \rightarrow 2\pi^0$ decays. The Esum9 range is: a) 30-40 GeV; b) 40-50 GeV.

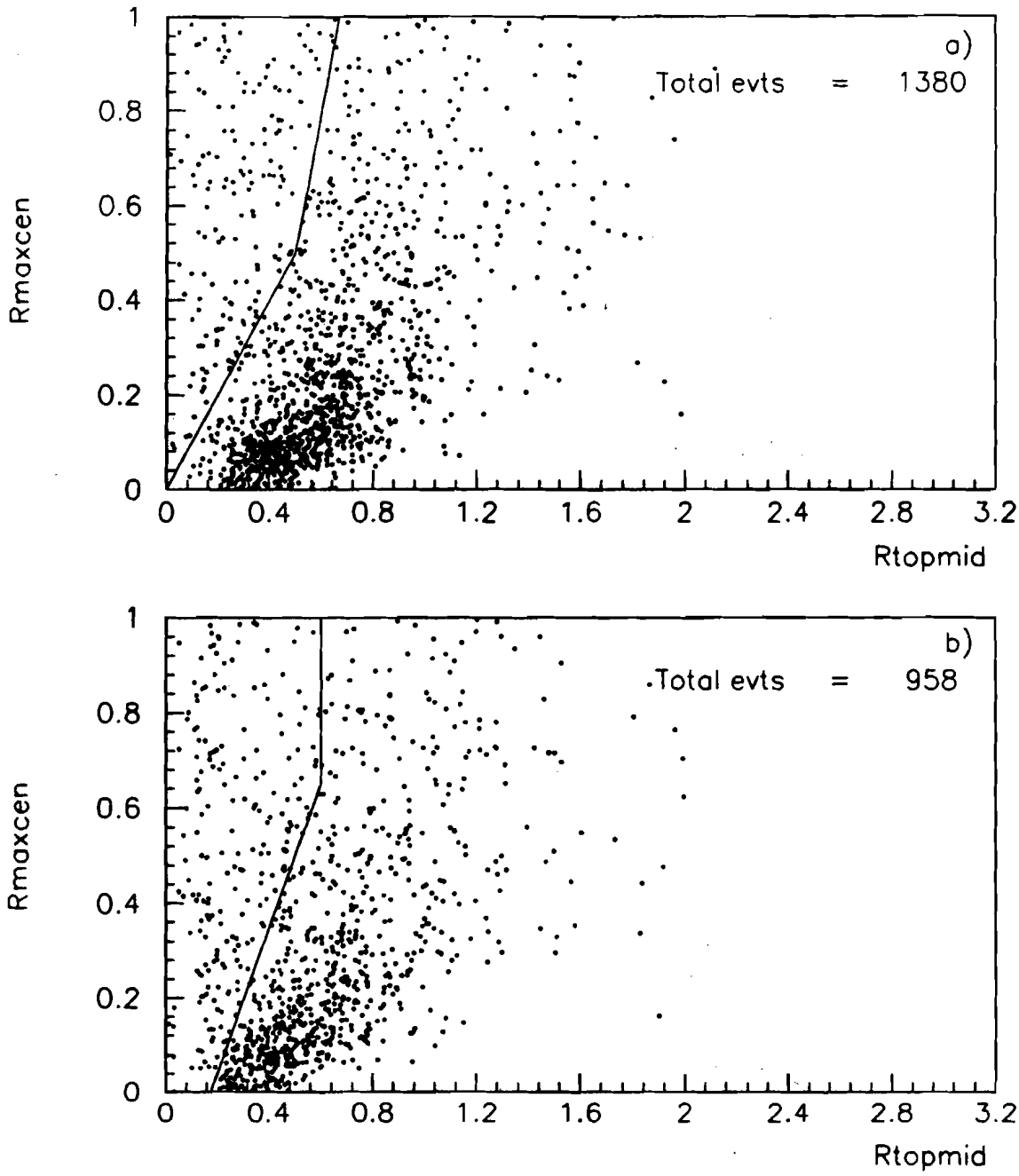

Figure 72. Rtopmid versus Rmaxcen, as defined in the text, for $K_L \rightarrow \pi^0\gamma\gamma$ candidates. The Esum9 range is: a) 30-40 GeV; b) 40-50 GeV.

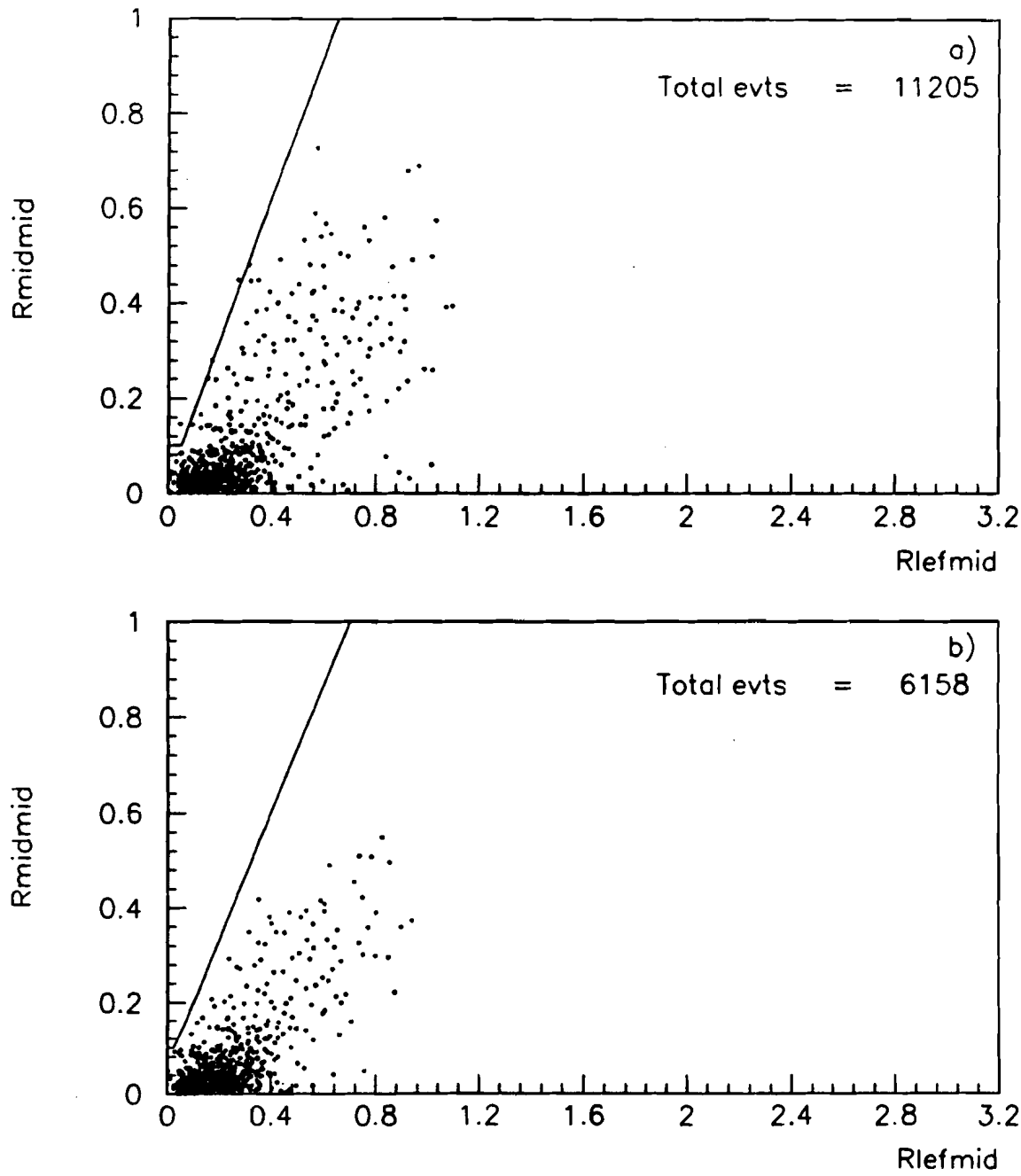

Figure 73. Rlefmid versus Rmidmid, as defined in the text, for $K_S \rightarrow 2\pi^0$ decays. The Esum9 range is: a) 30-40 GeV; b) 40-50 GeV.

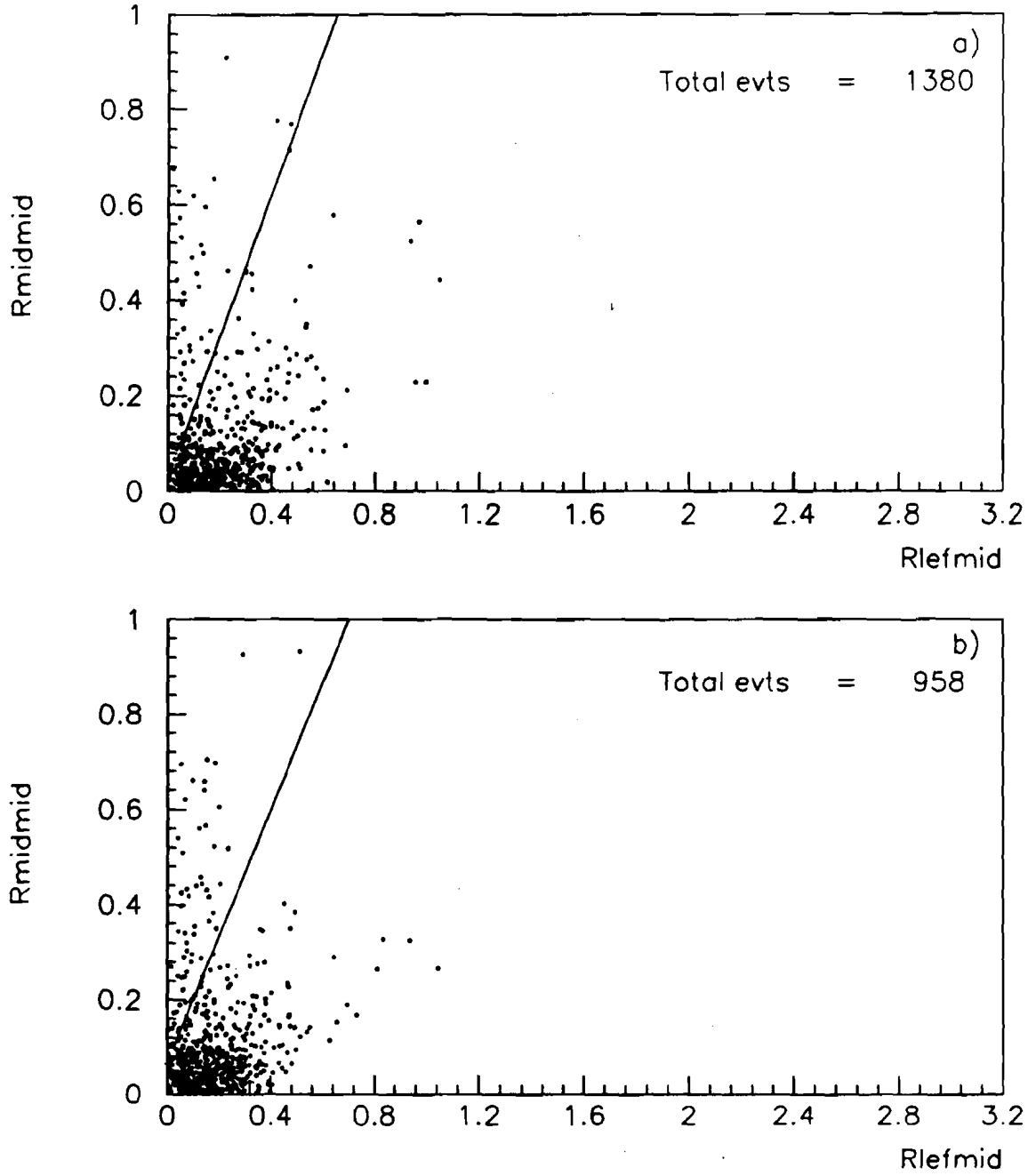

Figure 74. Rlefmid versus Rmidmid, as defined in the text, for $K_L \rightarrow \pi^0\gamma\gamma$ candidates. The Esum9 range is: a) 30-40 GeV; b) 40-50 GeV.

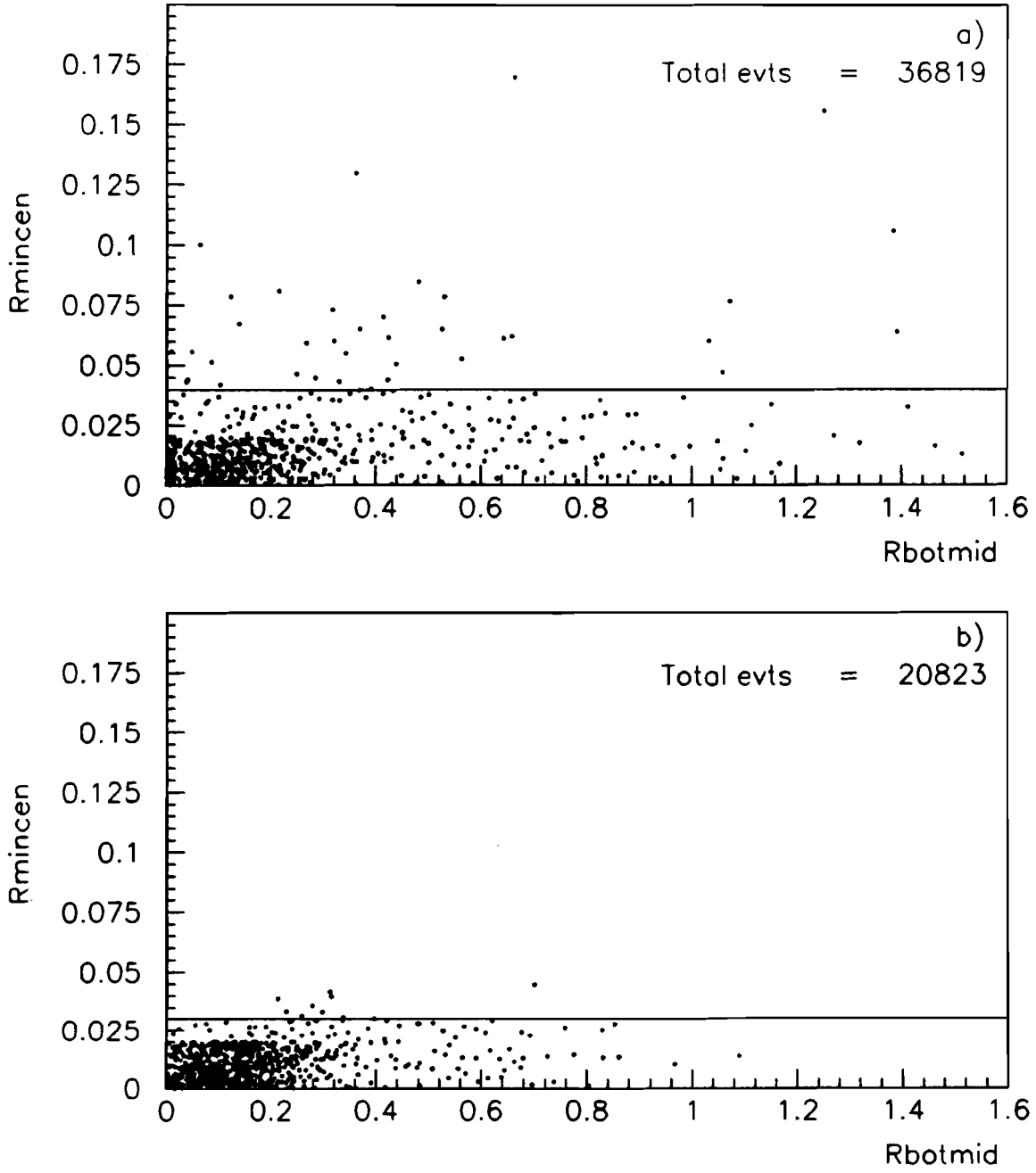

Figure 75. Rbotmid versus Rmincen, as defined in the text, for $K_S \rightarrow 2\pi^0$ decays. The Esum9 range is: a) 10-20 GeV; b) 20-30 GeV.

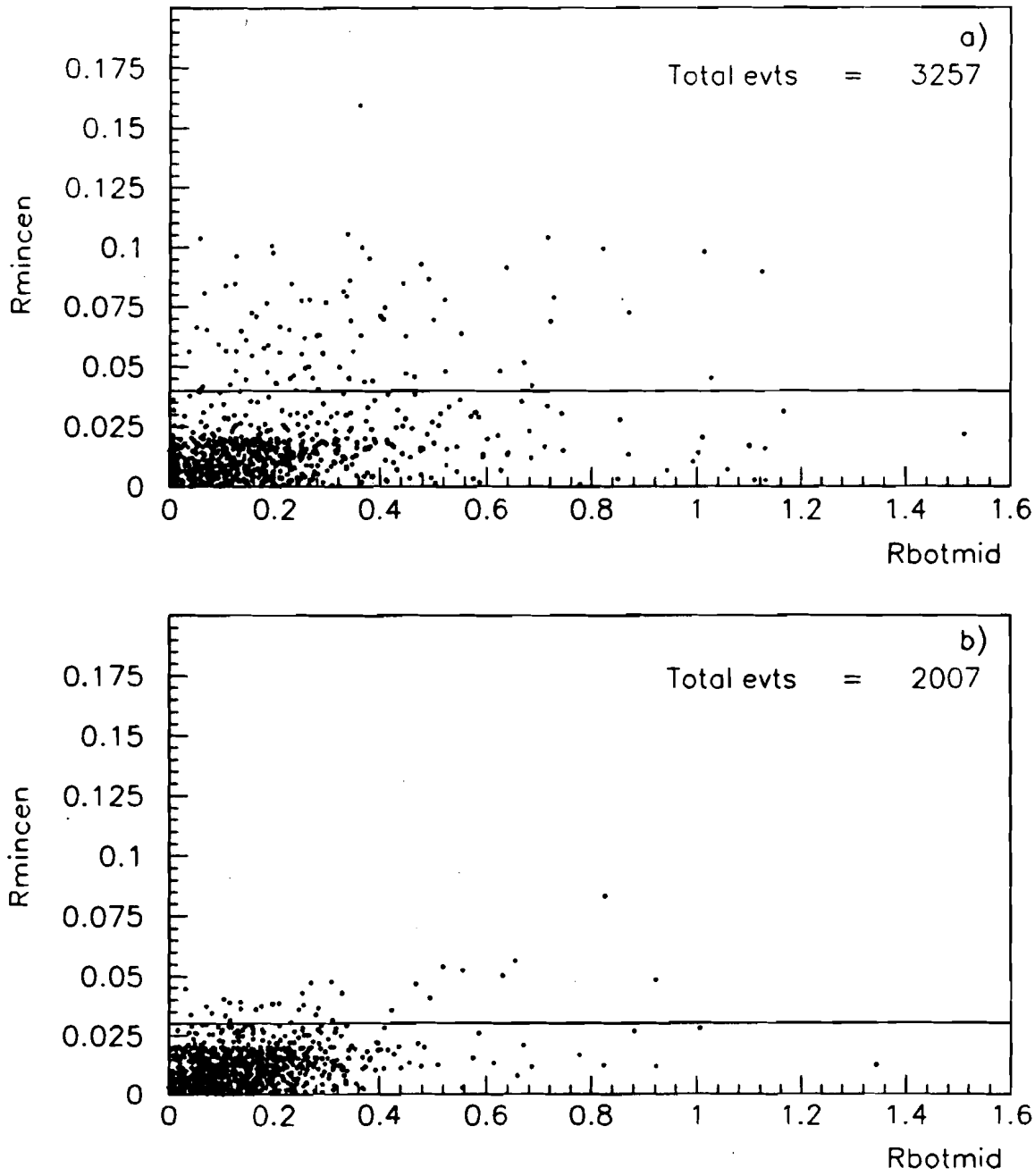

Figure 76. Rbotmid versus Rmincen, as defined in the text, for $K_L \rightarrow \pi^0\gamma\gamma$ candidates. The Esum9 range is: a) 10-20 GeV; b) 20-30 GeV.

6) Another variable sensitive to fusions is the ratio of the sum of the energy of the 9 blocks (3 x 3 around the center of the cluster) belonging to a cluster over the sum of the energy of the 25 blocks (5 x 5 around the center of the cluster) was required to be less than 0.9. Overlays of this variable, which is called 9/25, between $\pi^0\gamma\gamma$ candidates and $3\pi^0$ background Monte Carlo will be presented in Chapter 7.
7) It was also required that all the cluster energies are less than 60 GeV. Usually the fused clusters are more energetic and this cut reduces the possibilities for fusions. The cluster energy distribution before the cut is shown in Figure 88.

6.3.5 Further "double fusion" rejection

The fusion rejection cuts described till now were based on the shapes of clusters and the energy distribution within them. The cut that will be discussed in this section is mostly related with the kinematics of $3\pi^0$ "double fusion" events. In order to reduce background from $K_L \rightarrow 3\pi^0$ decays for which each photon from one π^0 overlaps with a photon from another π^0 resulting in a "double fusion" as described in Chapter 5, the following procedure was used:
As illustrated in Figure 77, one can assume that photon γ_{1b} from the decay of $\pi_b{}^0$ and photon γ_{1c} from the decay of $\pi_c{}^0$ overlap to a single cluster with energy E_1, and photon γ_{2b} from the decay of $\pi_b{}^0$ and photon γ_{2c} from the decay of $\pi_c{}^0$ overlap to a single cluster with energy E_2. We can also assume that photon γ_{1b} has energy rE_1, photon γ_{1c} has energy $(1-r)E_1$, photon γ_{2b} has energy sE_2 and photon γ_{2c} has energy $(1-s)E_2$, where $0 \leq r,s \leq 1$.

Then $$m^2_{n\pi^0} = \frac{rsE_1E_2r_{12}^2}{z^2} = \frac{(1-r)(1-s)E_1E_2r_{12}^2}{z^2} \qquad (6.3)$$

where r_{12} is the distance measured in the lead glass array between

clusters with energy E_1 and E_2 and z is the distance of the decay vertex from the calorimeter. From Equation (6.3) it turns out that r+s=1 and also that:

$$r = \frac{1 \pm \sqrt{1 - 4\left(\frac{m_{n\pi^0}^2 z^2}{r_{12}^2 E_1 E_2}\right)}}{2} = \frac{1 \pm \sqrt{1 - 4\left(\frac{m_{n\pi^0}^2}{m_{\gamma\gamma}^2}\right)}}{2}$$

Selecting as r the maximum solution then the minimum solution is s. From $3\pi^0$ background studies we know that in the decay region 110-128 m and for $m_{\gamma\gamma} \geq 0.264$ GeV, 97% of the time at least one of the photons that have been identified as not originating from a π^0 coincides with a fused cluster and 72% of the time both photons coincide with fused clusters. By

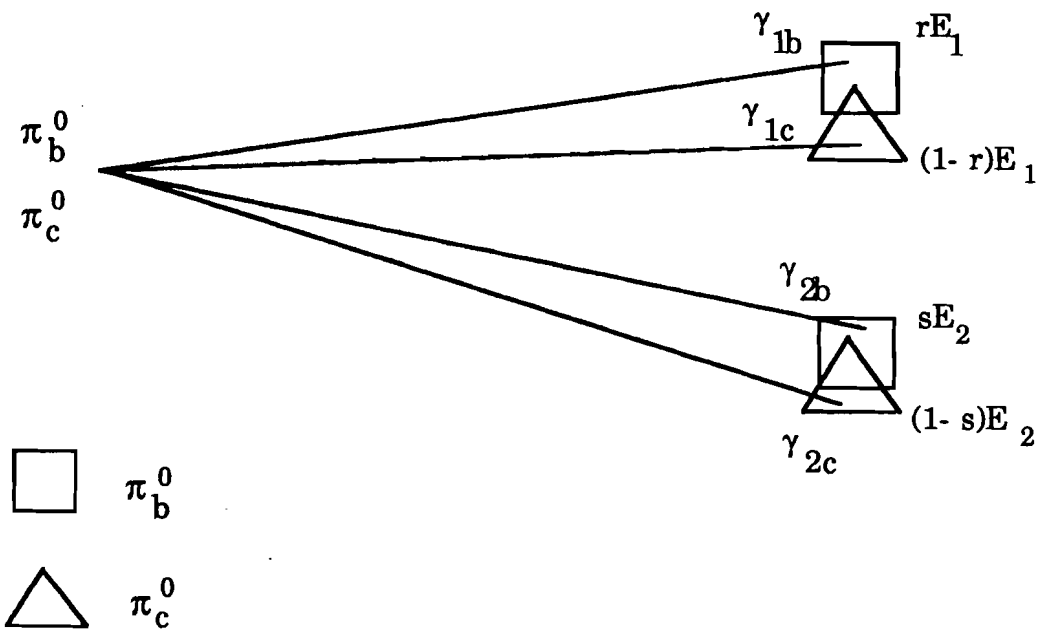

Figure 77. Overlapping clusters in a "double fusion" event from $3\pi^0$ background.

assuming that the fused clusters are the ones corresponding to the two γ's their energies were split in two according to the procedure mentioned above. By plotting the energy rE_1 of photon γ_{1b} versus the energy sE_2 of photon γ_{2b} and also the energy sE_1 of photon γ_{1c} versus the energy rE_2 of photon γ_{2c} it was realized that the distributions were noticeably different between $3\pi^0$ background Monte Carlo and signal $\pi^0\gamma\gamma$ Monte Carlo and one could gain in signal to noise ratio by accepting only events with a certain relationship between these energies. In the data these energies are plotted in Figure 78 and the cut is indicated by the solid line. Events reconstructed above the solid line are rejected.

6.4 Background from accidentals

Accidental events can interfere with the true kaon events in several ways. They may or may not be associated with clusters at the lead glass calorimeter; if no clusters are involved then one can have simply an increased activity in the chambers or in several counters due to the presence of the accidental. If the accidental event has clusters associated with it then these clusters can be "in time" or "out of time" and they may overlap with "in time" clusters from kaon decays or not. When the accidental clusters are away from the true clusters in the event, then they do not influence its reconstruction. When though we have accidental clusters in the lead glass overlapping or being close to clusters from true kaon decays then as can be seen from Equation (5.1) the z decay vertex is artificially shifted away from the lead glass. In order to reduce this background the following cuts were applied in addition to the cuts previously discussed. (Some of the cuts, like photon veto cuts or cuts

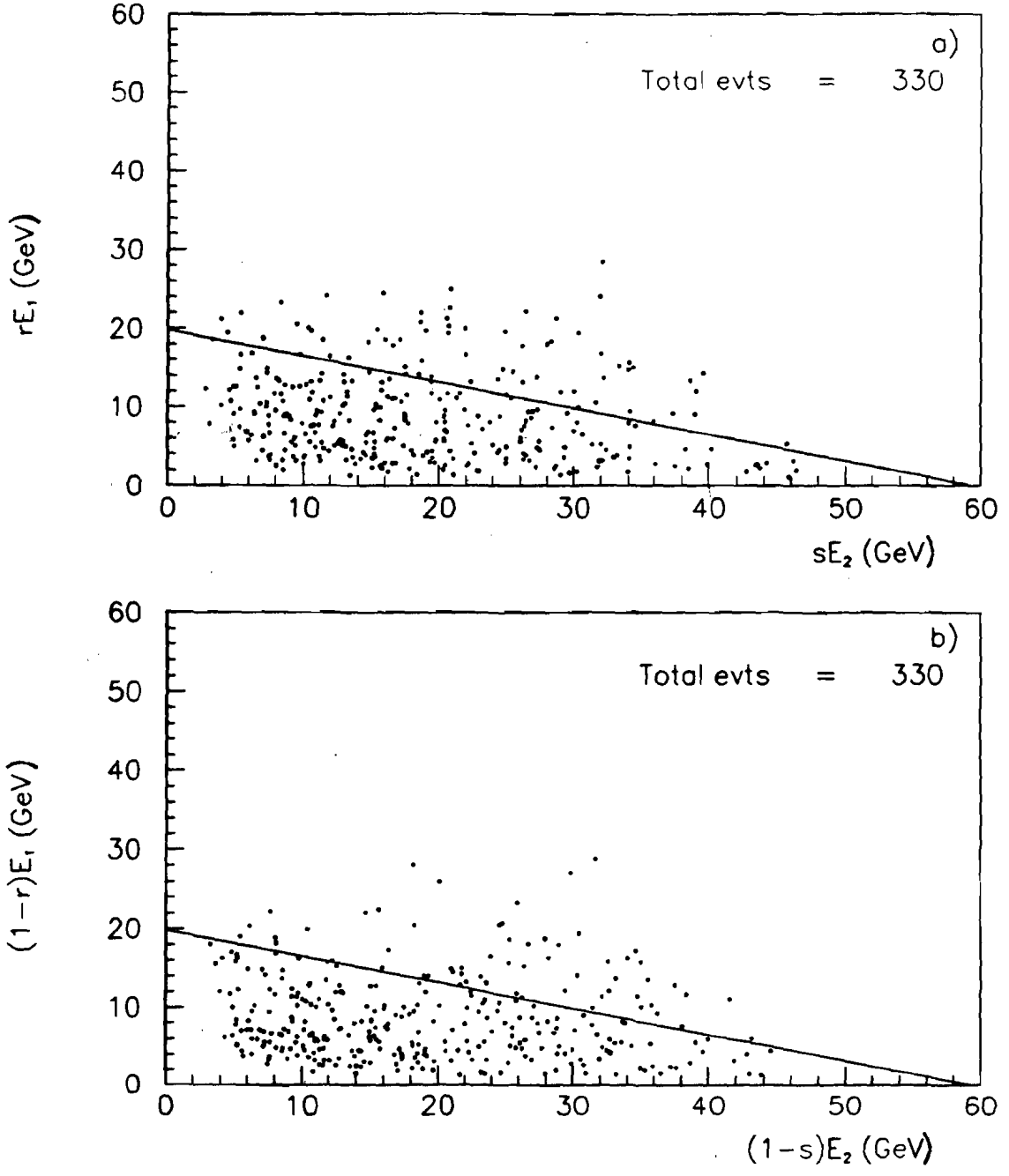

Figure 78. Energy distributions of photons belonging to the same π^0 from $K_L \rightarrow \pi^0\gamma\gamma$ events with $m_{\gamma\gamma}$ greater than about 270 MeV. a) and b) correspond, as explained in the text, to the two different π^0s.

requiring no tracks, have reduced the accidental background already)

• It was required that the drift chambers had at most 20 hits and that the TDC that measures the arrival time of signals at the T bank, Tsum TDC, does not fire.

• The extra energy in the glass, outside the 5 x 5 block area belonging to each cluster, was required to be less than 1.3 GeV. The distribution of this extra energy is shown in Figures 79 and 80 for $K_L \rightarrow \pi^0\gamma\gamma$ candidates after stage 17 in the "chg/n, neutral" and "neutral" running modes respectively. One can clearly see the higher accidental activity in the "neutral" running mode where we run at higher beam intensities.

• The adder ratios of the clusters found by the cluster finder were checked. These ratios are defined as ADC counts of the adder where the center of the cluster belongs over sum of counts in the lead glass blocks belonging to the adder and they should be around 1 (after gain correction) for "in time" clusters. It was required in this analysis that these adder ratios are greater than 0.8. In Figure 81 we show the adder ratio distribution for $K_L \rightarrow \pi^0\gamma\gamma$ candidates after stage 20. The arrow indicates the position of the cut. This cut does not remove many events because at this level the accidentals have been already reduced quite substantially in the $\pi^0\gamma\gamma$ sample. The power of this cut though to remove accidentals is demonstrated in Figure 82 where the adder ratio distribution is plotted for accidental events that have passed similar cuts with the $\pi^0\gamma\gamma$ candidates. In the accidental sample this cut removes the overwelming majority of the events.

In Table 14 we show the probability of having one and two extra clusters in the glass as a function of the analysis cuts. The trigger cuts mentioned in the table are the $BA\gamma * \overline{V_{Sum}} * \overline{CA} * \overline{Mu1}$ requirements.

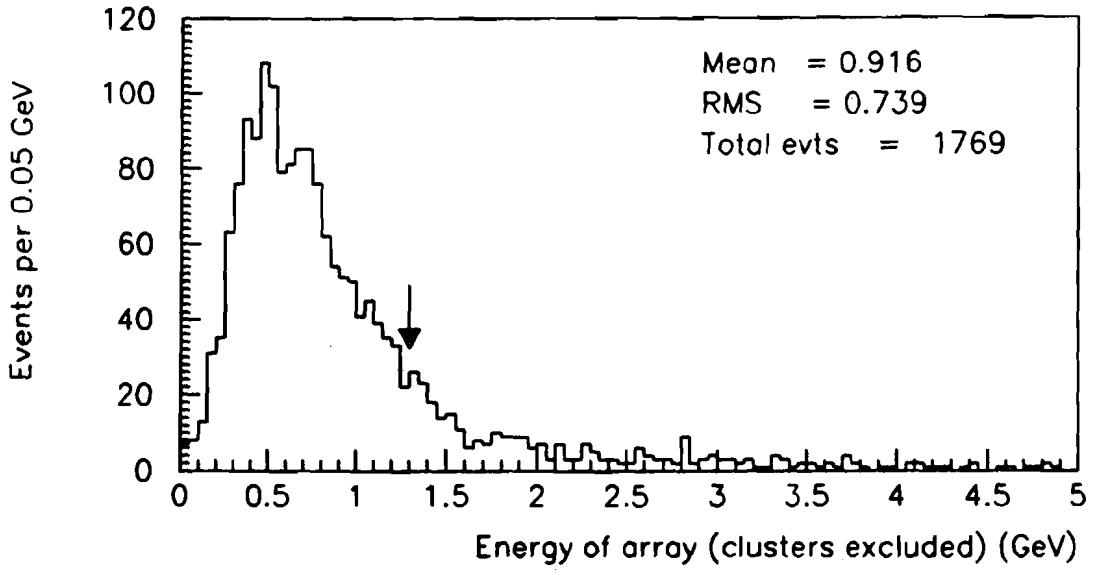

Figure 79. Energy in the lead glass calorimeter outside the 5 x 5 block area belonging to each cluster for $K_L \rightarrow \pi^0\gamma\gamma$ candidates from the "chg/n, neutral" running mode.

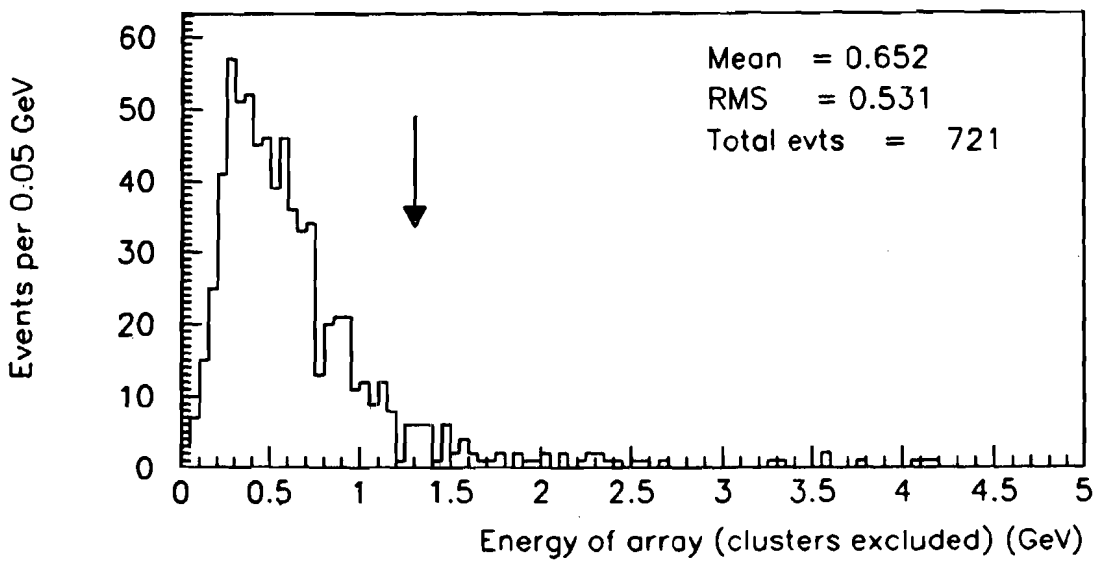

Figure 80. Energy in the lead glass calorimeter outside the 5 x 5 block area belonging to each cluster for $K_L \rightarrow \pi^0\gamma\gamma$ candidates from the "neutral" running mode.

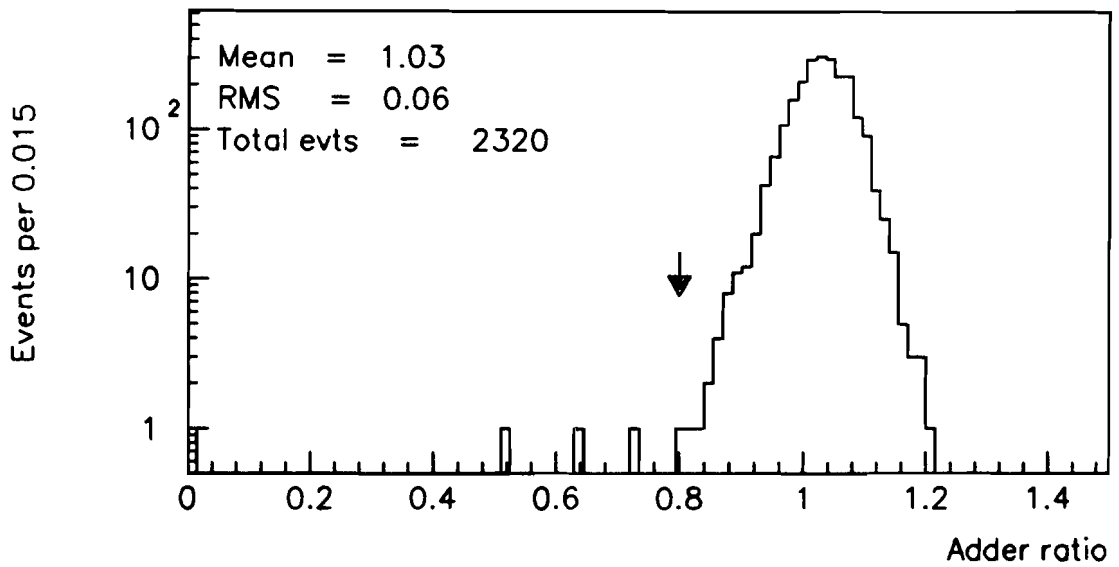

Figure 81. Adder ratio distribution for $K_L \rightarrow \pi^0\gamma\gamma$ candidates after stage 20.

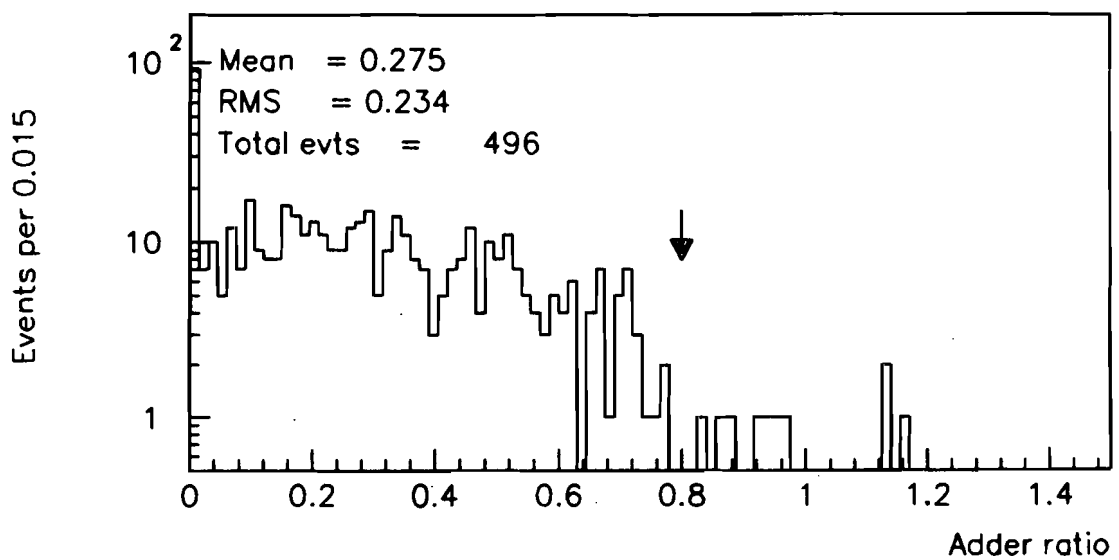

Figure 82. Adder ratio distribution for accidental events.

TABLE 14. Probability for the presence of one or two accidental clusters at the lead glass array, as a function of the $\pi^0\gamma\gamma$ analysis cuts.

cuts	Probability for	
	1 extra cluster	2 extra clusters
no cuts	$(2.83\pm0.02) \times 10^{-2}$	$(5.45\pm0.08) \times 10^{-3}$
trigger	$(1.83\pm0.02) \times 10^{-2}$	$(2.43\pm0.06) \times 10^{-3}$
photon vetoes, tracks, latches	$(6.22\pm0.12) \times 10^{-3}$	$(3.73\pm0.30) \times 10^{-4}$
fusions	$(3.76\pm0.09) \times 10^{-3}$	$(1.40\pm0.18) \times 10^{-4}$
extra energy	$(3.13\pm0.09) \times 10^{-3}$	$(9.46\pm1.55) \times 10^{-5}$
chamber hits, TDCs	$(2.75\pm0.09) \times 10^{-3}$	$(5.29\pm1.25) \times 10^{-5}$
adder	$(6.19\pm1.35) \times 10^{-5}$	$<(2.95\pm2.95) \times 10^{-6}$

6.5 Other backgrounds

We found empirically that for events with reconstructed z decay vertex upstream of the lead Mask there were photons that projected outside the lead Mask holes. We checked several possibilities to identify their source: a) The probability of them being photons that penetrate the Mask was estimated to be about 0.1% and this was put in the generation of a $3\pi^0$ background Monte Carlo which in about 64 CPU hours generated a sample equivalent to 44% of "chg/n, neutral" running mode. We generated events in a decay region starting at 70 m from the target and ending at 122 m, immediately downstream of the Mask. The events with photons projecting outside the holes at the Pb Mask plane could not be explained by this possibility. b) The positions of the photons of these events in the calorimeter were uniformly distributed across the corresponding

block and showed no indication of populating preferably the edges of the blocks. Therefore the misreconstruction was not related to missing energy at the edges of the blocks. c) The misreconstructed events do not seem to be related with accidental activity in the lead glass. As discussed in the previous section, the level of accidental activity we have after all the analysis cuts is very small. Additional checks of the ETearly and ETlate ADC distributions that were discussed in Chapters 2 and 4 and that were good monitors of the accidental activity in the glass also showed very low accidental activity.

Since the events in question were misreconstructed they were rejected from the sample. We applied a cut that removed events with photons projecting more than one centimeter away from the lead Mask holes. The effect of the cut on the sample can be seen in Table 6.2 for the 20% of the data. For $K \rightarrow 2\pi^0$ decays about 0.5% of the events with reconstructed kaon mass between 480 and 516 MeV are lost by this cut. We will discuss futher the possible sources of this background in Chapter 8.

6.6 Summary of all cuts

The cuts used to select $\pi^0\gamma\gamma$ events and the reduction they make to the original sample are briefly described in Table 14. Some of the cuts had been applied already at the data reduction stage but were reapplied at the final analysis because in the meantime several improvements occured at calibration files and in the general treatment of the data. The cuts that have been already discussed in previous sections will be clarified right below when neccessary while going through the table and some of them which have not been mentioned before will be briefly discussed.

TABLE 15. The effect of cuts (applied in series) on the sample of $\pi^0\gamma\gamma$ candidates.

	Stage	Number of Events
1	After data reduction	174330
2	Edge clusters	161370
3	Tracking	152271
4	Z decay vertex downstream (134m)	50619
5	Z decay vertex upstream (110m)	49925
6	Total energy	46929
7	m_{π^0} ($\pm$5MeV)	30588
8	$m_{\gamma\gamma}$ ($\pm$14MeV)	24840
9	Center of energy-Vaccum beam	16847
10	Tight Photon Veto cuts	13979
11	$2\pi^0$ rejection	11789
12	B bank latches	10307
13	BA,CA requirements	8975
14	Fusions	1037
15	Maximum energy < 60GeV	891
16	Double fusion rejection	812
17	Various latches	723
18	Extra energy less than 1.3 GeV	664
19	Less than 21 hits at chambers	629
20	Tsum TDC should not fire	580
21	Adder ratio > 0.80	576
22	Lead Mask requirement	572

In summary the cuts were the following:

- The event should satisfy the "neutral" trigger requirement.
- Regenerator and absorber should be in the same beam.
- 4 hardware and 4 software clusters were required.
- Events with clusters at the outer edge of the array were rejected. The edge cluster cut mentioned at stage 2 is the one described in section 6.3.1.
- There should be no tracks associated with the event.
- The z vertex of the decay should lie in the range 110 m ≤ z ≤ 128 m from the target.
- The total energy of the event was required to be between 40 and 150 GeV.

In Figure 83 is shown the energy distribution of $\pi^0\gamma\gamma$ candidates before the cut. The cut off at the low energies is due to the fact that there was a trigger requirement of at least 28 GeV energy deposition at the lead glass.

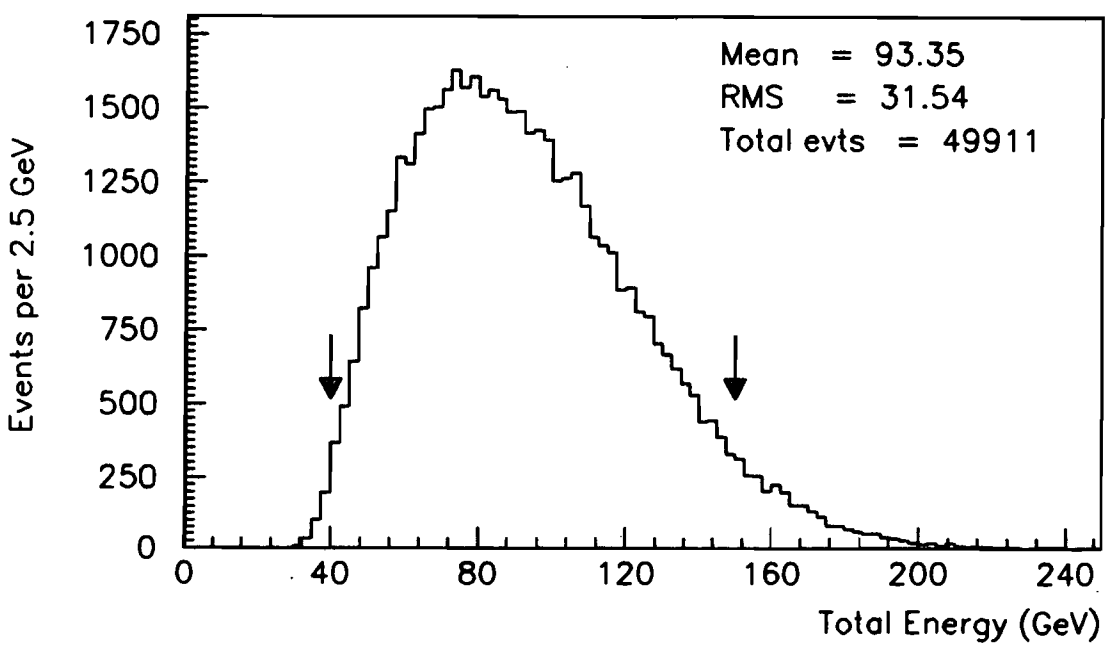

Figure 83. Total energy distribution for $\pi^0\gamma\gamma$ candidates. Only events with energy within the arrows were accepted.

• m_{π^0} should be within ±5 MeV from the nominal mass of the π^0. As will be shown in Figure 117 of Chapter 7, the m_{π^0} resolution deduced from Monte Carlo is about 3 MeV. In Figure 84 is also shown the distribution of the difference between the reconstructed π^0 mass and the nominal π^0 mass from $K_L \rightarrow \pi^+\pi^-\pi^0$ decays. The width of this distribution gives a feeling of the expected π^0 mass resolution. Of course the two analyses are not the same and one expects differences in the resolution. In particular in the $K_L \rightarrow \pi^+\pi^-\pi^0$ decay the energy available to the two photons that form the π^0 is smaller than it is for the $\pi^0\gamma\gamma$ decay and this tends to make the resolution better in $\pi^0\gamma\gamma$. On the other hand in $\pi^+\pi^-\pi^0$ the vertex is known from tracking and consequently with better precision than it is in $K_L \rightarrow \pi^0\gamma\gamma$ analysis. It would be therefore expected that this would favor the resolution in $\pi^+\pi^-\pi^0$. One should not forget though that in the $\pi^0\gamma\gamma$ analysis the calculation of m_{π^0} involves cluster energies and z vertex in such a way (Equations (5.1) and (5.2)) that an error in energy is at some extent compensated. This would argue again for a better m_{π^0} resolution in $\pi^0\gamma\gamma$.

• $m_{\gamma\gamma}$ should be away from the nominal π^0 mass by ±14 MeV.

Since several improvements occured in the energy estimation of a cluster between the data reduction and the final analysis which could influence the mass calculations it was necessary to convince ourselves that the mass cuts applied during data reduction were loose enough to allow us to take advantage of all the improvements. One may get surprised at first look by the 19% reduction that the $m_{\gamma\gamma}$ cut results in, when applied to the data at the final analysis stage. This cut was applied at the data reduction level at ±10 MeV and one would expect a smaller effect now. What is happening in reality is that after the improved energy estimation has been used, mispaired $2\pi^0$ background events that had survived the ±10 MeV hard cut during data reduction; now have their $m_{\gamma\gamma}$ mass populating the area around the nominal π^0 mass value and they are cut when the ±14

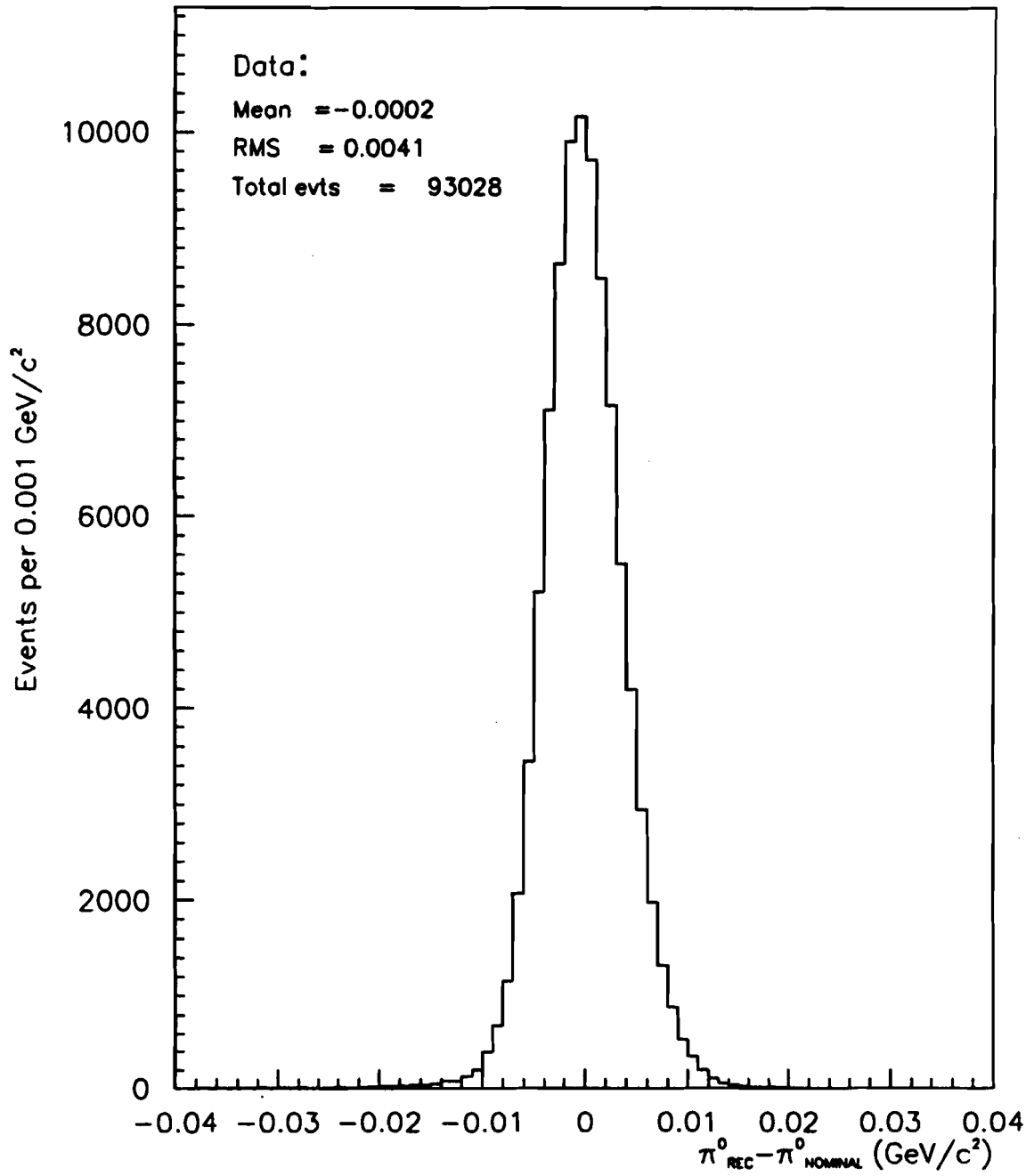

Figure 84. Distribution of the difference between the invariant mass distribution of the two photons in the $K_L \rightarrow \pi^+\pi^-\pi^0$ decay and the nominal π^0 mass.

MeV cut is applied. It turns out that the overwelming majority of these events (99.45%) would be cut out anyway by the second step of $2\pi^0$ background rejection which is described in section 6.2. In fact $m_{\pi}0$ and $m_{\gamma\gamma}$ were reconstructed with both the old and new way of energy estimation and it was found that the difference between the two ways had an rms value of 1.34 MeV for $m_{\pi}0$ and 1.57 MeV for $m_{\gamma\gamma}$. Therefore the mass cuts applied in the final analysis were safe.

- The center of energy was required to be within the vacuum beam and within the beam area.
- The photon veto cuts were tightened up from their data reduction period values
- It was required that no latches associated with the C bank fired.
- It was required that no latches associated with the Sweeper-anti veto counters fired.
- $2\pi^0$ background was further rejected as described in section 6.2 and after this stage z decay vertex, $m_{\pi}0$ and $m_{\gamma\gamma}$ distributions are presented in Figures 85, 86 and 87 respectively.
- It was required that no latches associated with the B bank fired.
- After the energy requirements for BA and CA banks and all the fusion cuts discussed in previous sections the energy of each cluster was required to be less than 60GeV. In Figure 88 is shown the maximum cluster energy distribution for $\pi^0\gamma\gamma$ candidates before the cut.

Figure 89 shows the $m_{\gamma\gamma}$ distribution after this stage and Figure 90 shows the same distribution after the kinematic "double fusion" rejection cut. As can be seen by comparing Figure 89 and 90, the reduction due to the last cut occurs only for events with $m_{\gamma\gamma}$ mass greater than $2\pi^0$ masses. Till now all the distributions were presented in the z region 110-134 m. After all cuts and the tighter downstream z decay vertex cut at 128 m the final $m_{\pi}0$ and $m_{\gamma\gamma}$ distributions are presented in Figures 91 and 92.

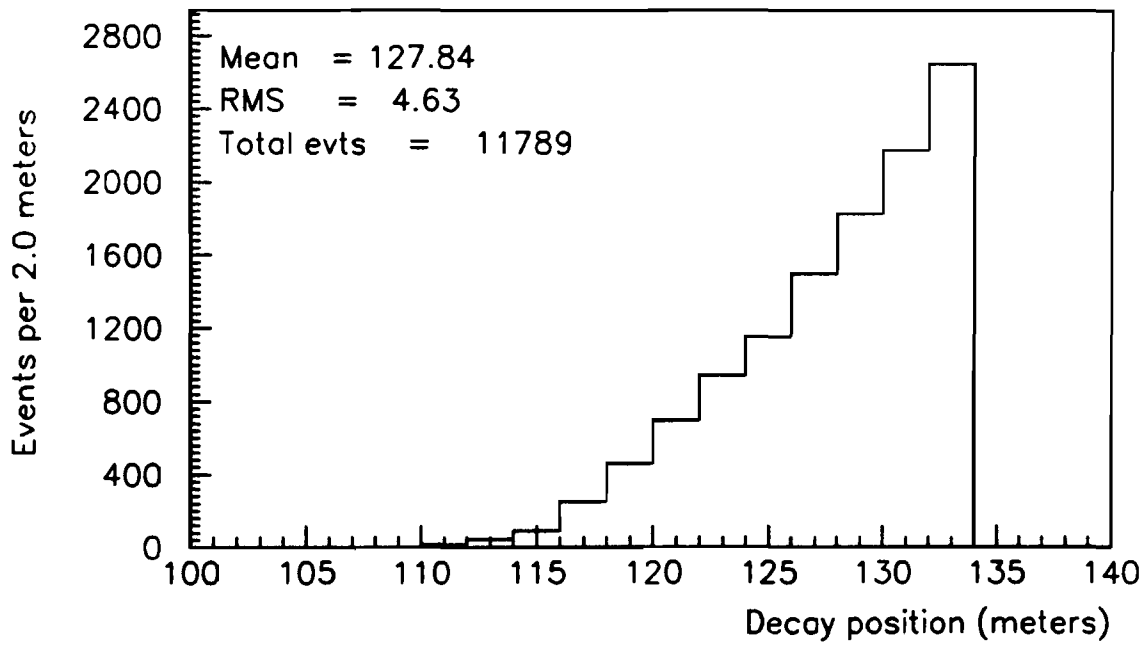

Figure 85. z decay vertex distribution for $K_L \rightarrow \pi^0\gamma\gamma$ candidate events after stage 11 (see Table 15).

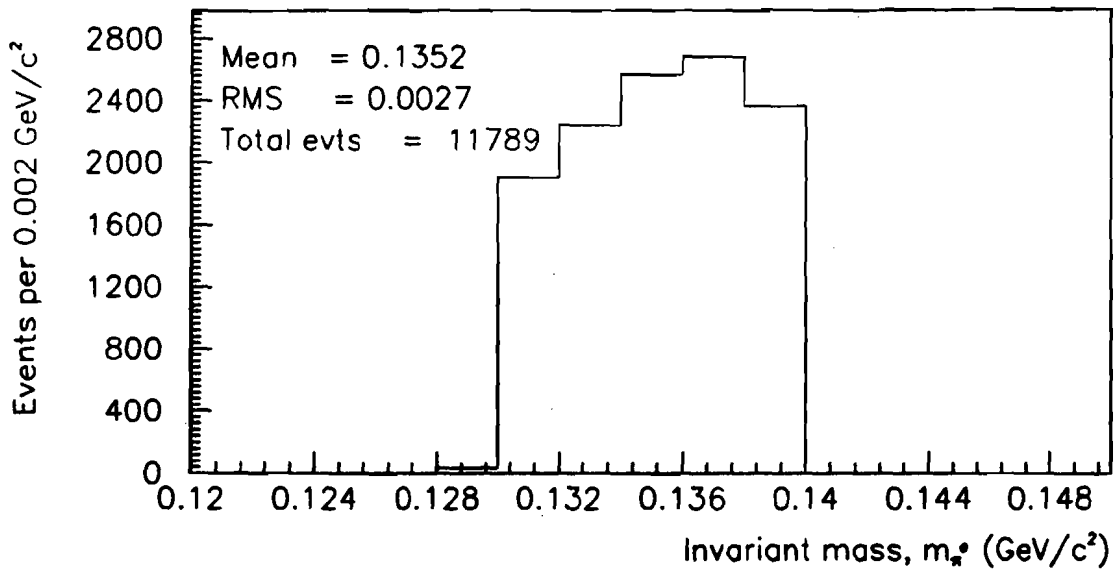

Figure 86. π^0 **invariant mass for** $K_L \rightarrow \pi^0\gamma\gamma$ **candidates after stage 11.**

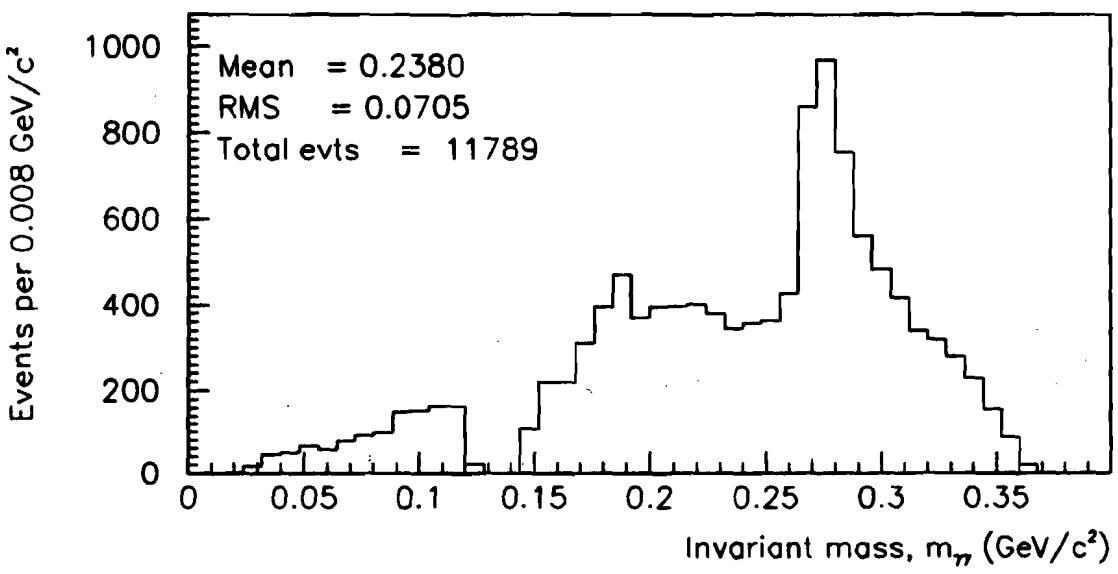

Figure 87. $\gamma\gamma$ **invariant mass for** $K_L \rightarrow \pi^0\gamma\gamma$ **candidates after stage 11.**

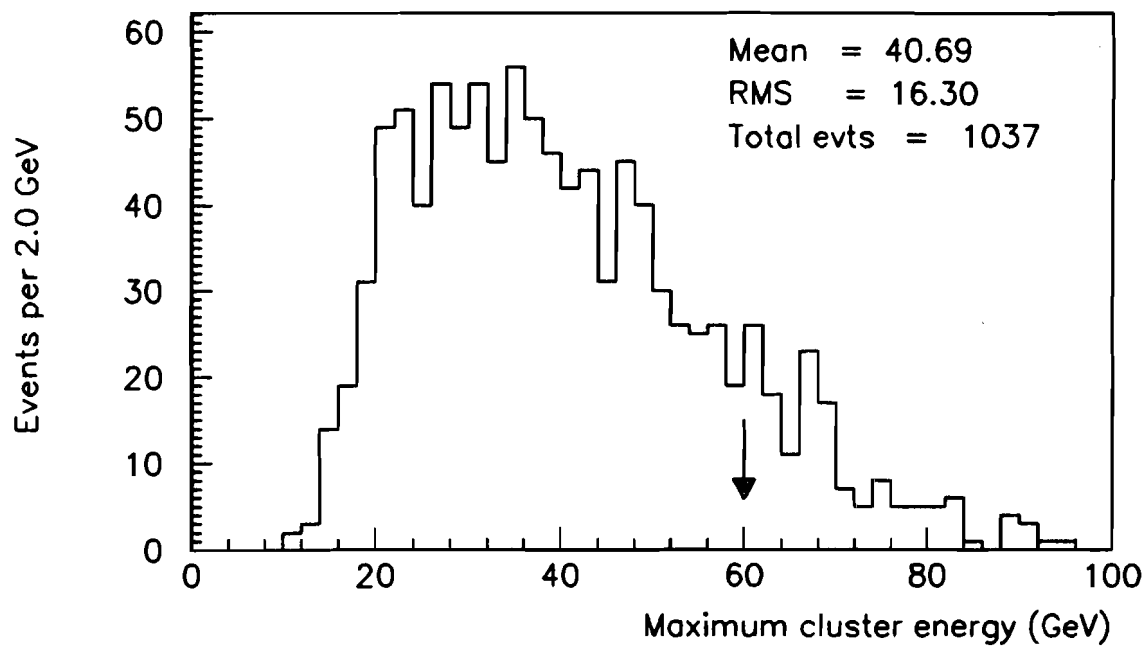

Figure 88. Distribution of the energy of the maximum energy cluster for $K_L \rightarrow \pi^0\gamma\gamma$ candidates. The arrow indicates the position of the cut.

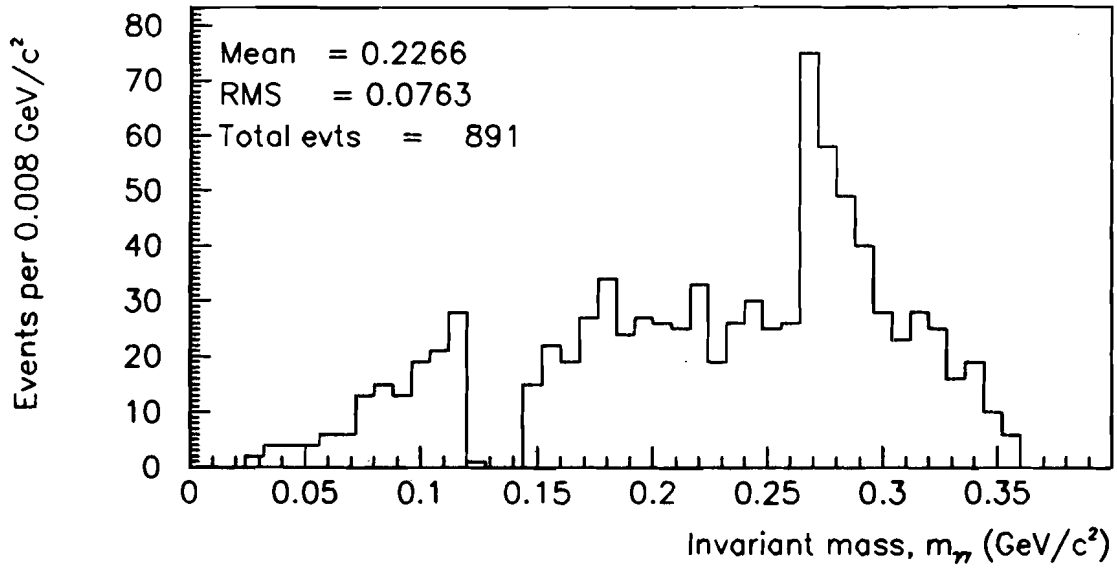

Figure 89. $\gamma\gamma$ invariant mass for $K_L \rightarrow \pi^0\gamma\gamma$ candidates after all the non kinematics related fusion cuts, that is after stage 15.

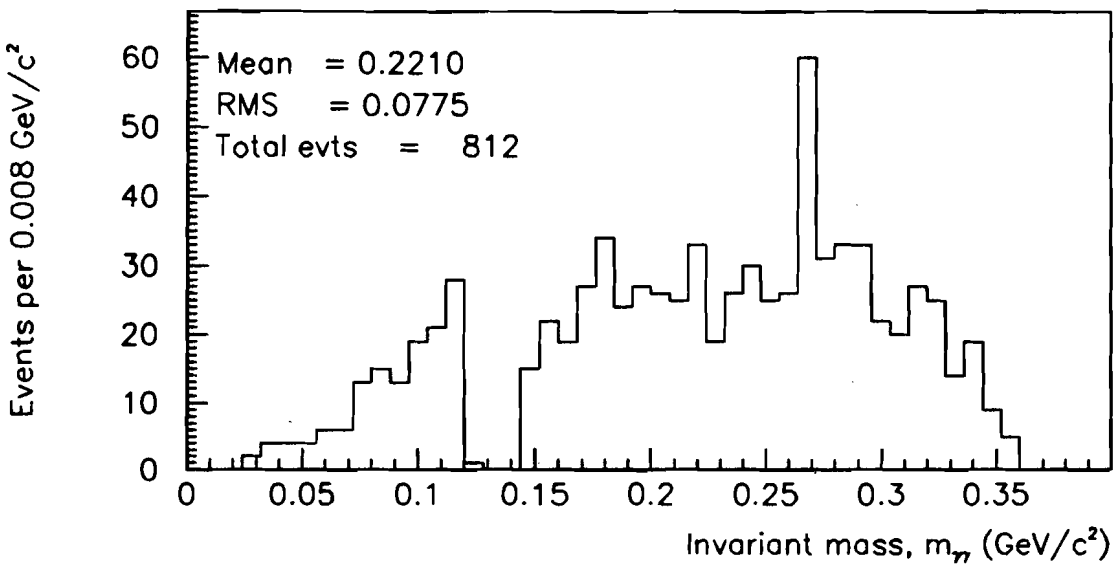

Figure 90. $\gamma\gamma$ invariant mass for $K_L \rightarrow \pi^0\gamma\gamma$ candidates after the kinematics related double fusion rejection cut.

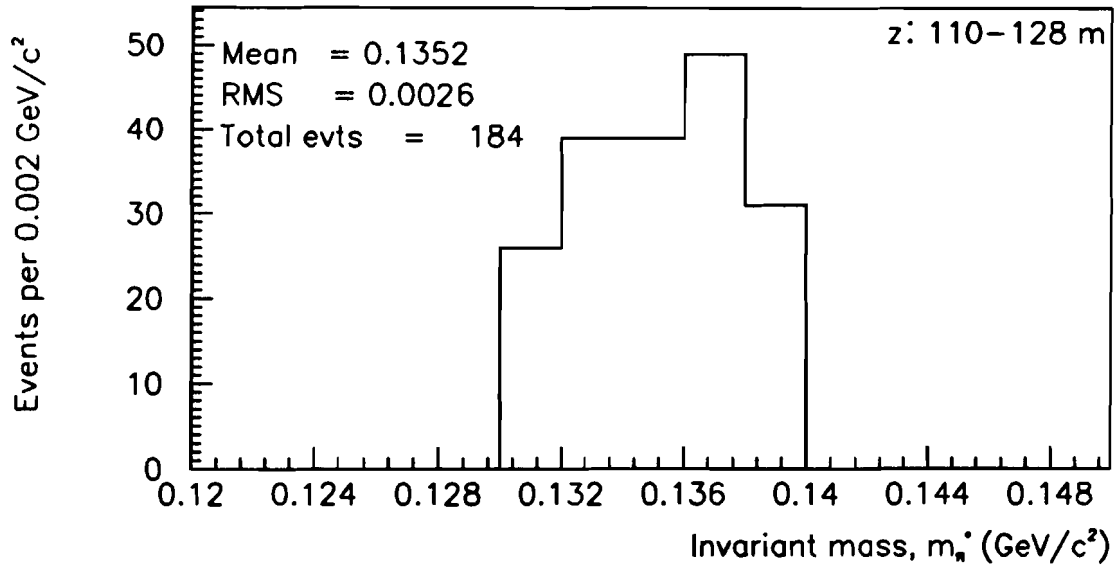

Figure 91. π^0 **invariant mass distribution for** $K_L \rightarrow \pi^0\gamma\gamma$ **candidates after all cuts.**

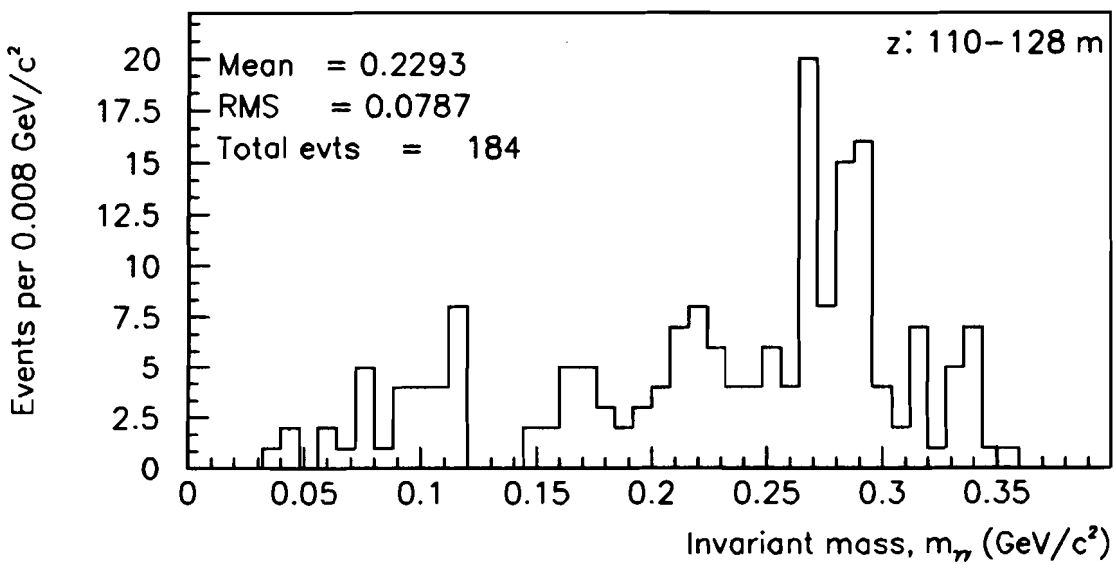

Figure 92. $\gamma\gamma$ **invariant mass for** $K_L \rightarrow \pi^0\gamma\gamma$ **candidates after all cuts.**

CHAPTER 7

MONTE CARLO

To extract an upper limit or a branching ratio for the $K_L \rightarrow \pi^0\gamma\gamma$ decay one has to determine, as mentioned in Chapter 2, the acceptances of the detector $A_{\pi^0\gamma\gamma}$ for $K_L \rightarrow \pi^0\gamma\gamma$ and and $A_{2\pi^0}$ for $K_L \rightarrow 2\pi^0$ and also understand the backgrounds that dominate the $\pi^0\gamma\gamma$ signal. All the acceptance determinations and the understanding of the background were based on a Monte Carlo program that simulated in detail the experimental conditions. The input information was the beam characteristics, the kinematics and when necessary the dynamics of each decay, the detector configuration and the trigger requirements.

This chapter is going to be divided in four major parts. In the first one we are going to discuss some general characteristics of the simulation, in the second we are going to present data-Monte Carlo comparisons and acceptance determination for signal (in contrast with background) decays like $K_L \rightarrow 3\pi^0$, $K_{L,S} \rightarrow 2\pi^0$ and $K_L \rightarrow \pi^0\gamma\gamma$. The third part is going to be devoted to special features of the background Monte Carlo and its

understanding and in the fourth part we will present the extent of the agreement for the final kinematic distributions between $\pi^0\gamma\gamma$ candidates and the considered backgrounds.

7.1 Event generation

7.1.1 Beam simulation

The first step in the generation of a kaon decay was to produce a K^0 or a $\overline{K^0}$ at a certain position at the target and with a certain cross section. The production cross section was provided by a combination of Malensek's [36] formula and a polynomial function of kaon momentum deduced by our own data. Malensek's formula which is given in Equation (7.1) describes the angular distribution and the energy distribution of secondary charged particles produced by protons hitting a Be target and was deduced by fitting data [37] of particle production by 400 GeV/c protons on beryllium targets.

$$\frac{d^2N}{dPd\Omega} = \frac{B}{400} * P * \frac{(1-X)^A * \left(1+5e^{-DX}\right)}{\left(1+\frac{P_t^2}{M^2}\right)^4} \qquad (7.1)$$

where:

$\frac{d^2N}{dPd\Omega}$ is the number of produced secondary particles per steradian, per GeV/c, per incident proton,

P is the particle momentum,

X is particle momentum / beam momentum

P_t is the transverse particle energy with respect to the proton beam direction, and

A, B, M^2, D are constants special for each secondary particle , given in Table 16 for charged kaons.

TABLE 16. Parameter values in Malensek's formula.

	K^+	K^-
A	2.924	6.107
B	14.15	12.33
M^2	1.164	1.098
D	19.89	17.78

Although the production spectra of K^0 and $\overline{K^0}$ that we are interested in have not been measured, we derived them by using the above information. By looking at the quark contents of the incident proton and of K^0, $\overline{K^0}$, K^+ and K^-, one can realize that the production cross section for K^0, $\frac{d^2N^0}{dPd\Omega}$, is an average of the production cross sections for K^+ and K^- and the production cross section for $\overline{K^0}$, $\frac{d^2\overline{N^0}}{dPd\Omega}$, is equal to the one for K^-.[1] To get the final production cross section we multiplied Malensek's formula by a fourth order polynomial in P which was determined by comparing distributions of our $K_S \rightarrow \pi^+\pi^-$ data with Monte-Carlo. Before this tuning, Malensek's formula predicts too much particle production for kaon energies greater than about 120 GeV. The tuned cross section was finally used for the generation of neutral kaon decays in both charged and neutral final states. The x and y position of kaon production at the target was initially chosen according to a gaussian distribution of σ=0.4 mm in both x and y, and the z position was generated taking into account the attenuation of the proton and kaon in the target. The x and y positions were updated by considering the finite target length and the 4.8 mr targetting angle in the x direction and the effect of the ceramic holder that keeps the target in place was also taken into account.

[1]By denoting as x the chance that a $u\bar{u}$ or $d\bar{d}$ pair is available and as y the chance that an $s\bar{s}$ is available then the production rates for the various mesons can be written as: K^+: y(2+x), K^-: xy, K^0: y(1+x), $\overline{K^0}$: xy.

After the determination of the production cross section and position in the target of K^0 or $\overline{K^0}$ we assigned to the kaon wavefunction initial K_L and K_S amplitudes which were:

$\begin{bmatrix} a_S(0) \\ a_L(0) \end{bmatrix} = \begin{bmatrix} 1 \\ 1 \end{bmatrix}$ for K^0 and $\begin{bmatrix} a_S(0) \\ a_L(0) \end{bmatrix} = \begin{bmatrix} 1 \\ -1 \end{bmatrix}$ for $\overline{K^0}$

and let the wavefunction evolve through vacuum and material. These amplitudes changed due to decays, nuclear interactions, regeneration and the mass difference between K_L and K_S and the amplitudes after the evolution were used to calculate the decay probability for a particular decay mode at a given z position within the decay volume.

The momentum spectrum (energy and direction) of the kaon is determined from a distribution which is the product of the production cross section, mentioned above, and the integrated decay probability in a given z range.

The kaon was required to pass through either holes of the two hole collimator, mentioned in Chapter 2, and it was allowed to scatter elastically at the 20" Be and 3" Pb of the absorber which is common to both beams. If it projected within the apertures of the movable absorber and the regenerator it was considered as a kaon from the regenerator beam and otherwise it was considered as a kaon from the vacuum beam. The regenerator and the movable absorber moved together, randomly from beam to beam in the Monte Carlo in order to mimic their true movement between the two beams every spill. If the kaon belonged to the regenerator beam it was also allowed to scatter elastically at the 18" Be movable absorber about 1.5 m downstream of the two hole collimator. The scattering considered in all cases was only single elastic scattering and its cross section was assummed to be of the form:

$$\frac{d\sigma}{dP_t^2} \propto \exp(-DP_t^2)$$

where P_t^2 is the square of the transverse momentum transfer and D = 55 GeV^{-2} or 400 GeV^{-2} for Be or Pb respectively. The fraction of events that intersected the absorbers and underwent single elastic scattering were

17.8% for the Pb part and 8.6% for the Be part of the common absorber and 7.8% for the movable absorber. Unscattered kaons with their original trajectory and scattered kaons with their new trajectory were propagated to the rest of the collimators that are shown in Figure 12 and they were required to project within their apertures. The configuration of the collimators could not be measured accurate enough with our data and it was adjusted to fit the observed beam profile; it was one of our tunable parameters in the Monte Carlo together with the momentum spectrum mentioned above and the targetting angle in the y direction.

For the generation of the $K_{L,S} \rightarrow 2\pi^0$ decay modes the kaon was allowed to undergo coherent and incoherent (diffractive and inelastic) regeneration at the regenerator and the HDRA. Thereby for the $2\pi^0$ decays we had coherent K_L and diffractive K_S coming out of our vacuum beam and coherent K_S, coherent K_L, diffractive K_L, diffractive K_S, and inelastic K_S coming out of our regenerator beam.

The z vertex of the kaon decay is determined so that its distribution will follow the decay probabilities mentioned earlier in this section. Kaons in the vacuum beam were usually allowed to decay between 105 m and 138 or 152 or 175 m from the target.

All the decay modes that we are concerned with in this thesis, like $K_L \rightarrow \pi^0\gamma\gamma$, $K_{L,S} \rightarrow 2\pi^0$ and $K_L \rightarrow 3\pi^0$, involve only photons. The direct photons and the ones produced by the π^0 decays propagate through the detector and if any of them hits photon counters that are in veto the event in general is rejected. If any photon hits photon counters that are not in veto or projects outside the counters, the propagation of the individual photon is terminated. For decays like $K_L \rightarrow \pi^0\gamma\gamma$ and $K_{L,S} \rightarrow 2\pi^0$ all four photons were required to hit the lead glass. For $K_L \rightarrow 3\pi^0$ background Monte Carlo decays, satisfying the "four-cluster" requirement, at least four of the six photons were required to hit the glass.

7.1.2 Detector simulation

The important geometric features of the detector were measured accurately from the data and implemented in the Monte Carlo to ensure a good representation of the various kaon kinematic distributions by the simulation program. Aperture sizes and shapes of the lead Mask, the Vacuum-antis, the HDRA, the Vacuum window, the box containing the He bags and the lead glass array were determined from Ke3 decays where we have lots of statistics available. Positions and sizes of various detector elements are given for reference in Table 1. In order to simulate properly the scattering and bremsstrahlung emission of charged particles and also conversion probabilities of photons we had to know the characteristics of the materials of which the several pieces of the detector were made. The radiation lengths of materials that were implemented in the simulation are summarized in Table 2. Information on shapes of electromagnetic showers deduced from EGS studies and from studies of real electrons and positrons of calibration data was also implemented in the Monte Carlo. Similarly was implemented the number of photo-electrons produced per unit energy at our photomultipliers and deduced from flash lamp studies . Lead glass *Čerenkov* light absorption coefficients were determined from electron calibration data and also used in the simulation. In the following subsections we are going to describe the simulation of several important elements of the detector.

7.1.2.1 Photon veto simulation

PA, AM (lead Mask), RA, CA and BA were in veto for the "neutral" trigger and among them PA, AM and RA were considered to be 100% efficient. That is if any photon hit them the event was vetoed. The characteristics of these counters are described in Chapter 2 and typical energy distributions of photons hitting them are shown in Figure 93. These distributions were produced from a special $3\pi^0$ background Monte Carlo where none of the photon vetoes was in veto. CA and BA were vetoing any

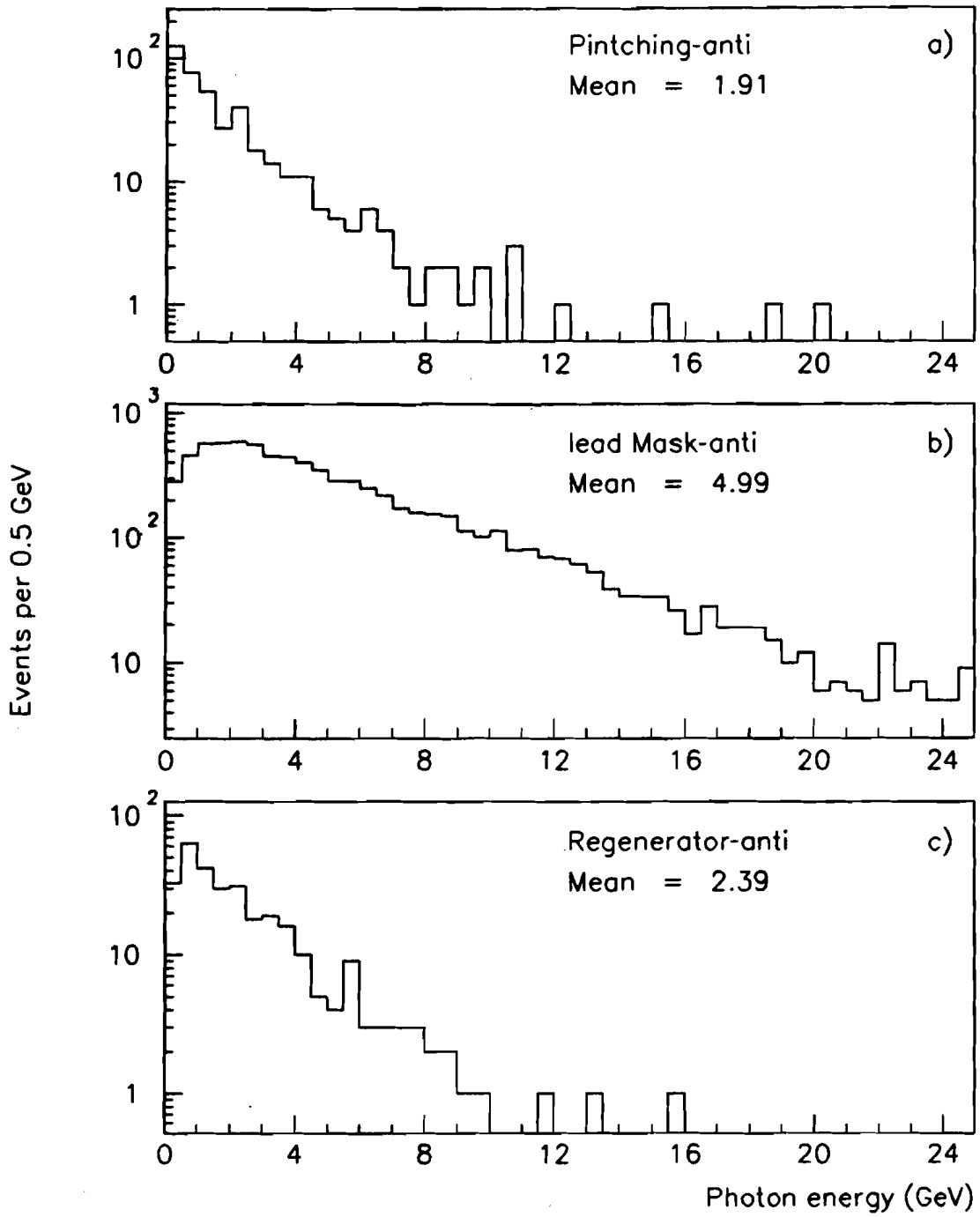

Figure 93. Monte Carlo energy distributions of photons hitting the most upstream photon veto counters. a) Photon energy distribution for PA, b) Photon energy distribution for AM, c) Photon energy distribution for RA.

photons or electrons depositing on them at least 10 μ or 5 GeV respectively. Typical energies of photons hitting these vetoes are shown in Figure 94 produced from the same Monte Carlo mentioned above. Accidental photon overlaps alter these spectra by adding on them more low energy photons. For the Collar-anti we basically simulate only photons and electrons hitting the counters. When pions hit CA they deposit about 0.8 GeV of energy in the simulation. Energies of photons and electrons underwent a gaussian smearing of 16% energy independent resolution. The fact that photons give about 20% less energy than electrons was also taken into account. Photon energy deposited at the first two layers of BA was also simulated by the Monte Carlo and energies down to 200 MeV were smeared with $\sigma = 0.2\sqrt{E}$ GeV. When we did not overlay accidental events on top of the kaon decays, we had no neutrons in the detector and there was no need for the third layer of BA to be simulated.

The lead lucite photon vetoes (VAs, MA, LGA) and DRAN were also simulated in the Monte Carlo. Photon veto gains were used to convert particle energy from GeVs to muons and the resolutions of the veto counters deduced from $K_L \rightarrow \pi^+\pi^-\gamma$ events were also implemented to smear the energies of the photons appropriately. The scintillator parts of those vetoes were not simulated though and this can cause a discrepancy in the agreement of some distributions between $\pi^0\gamma\gamma$ candidates and $3\pi^0$ background for two reasons: a) there is some small probability for photon conversion in the scintillator and b) electrons and positrons from photon conversions at the beam pipe can hit the scintillator and be vetoed during the experiment but not in the Monte Carlo. As will be discussed later this last effect has been simulated by EGS and implemented in our analysis.

The efficiencies of our photon vetoes derived from the $3\pi^0$ background Monte Carlo mentioned in the beginning of this section are presented in Table 17. The only requirements for events used in the calculation of these efficiencies are that the event has four hardware and four software clusters, its reconstructed energy is between 40-150 GeV and that under the

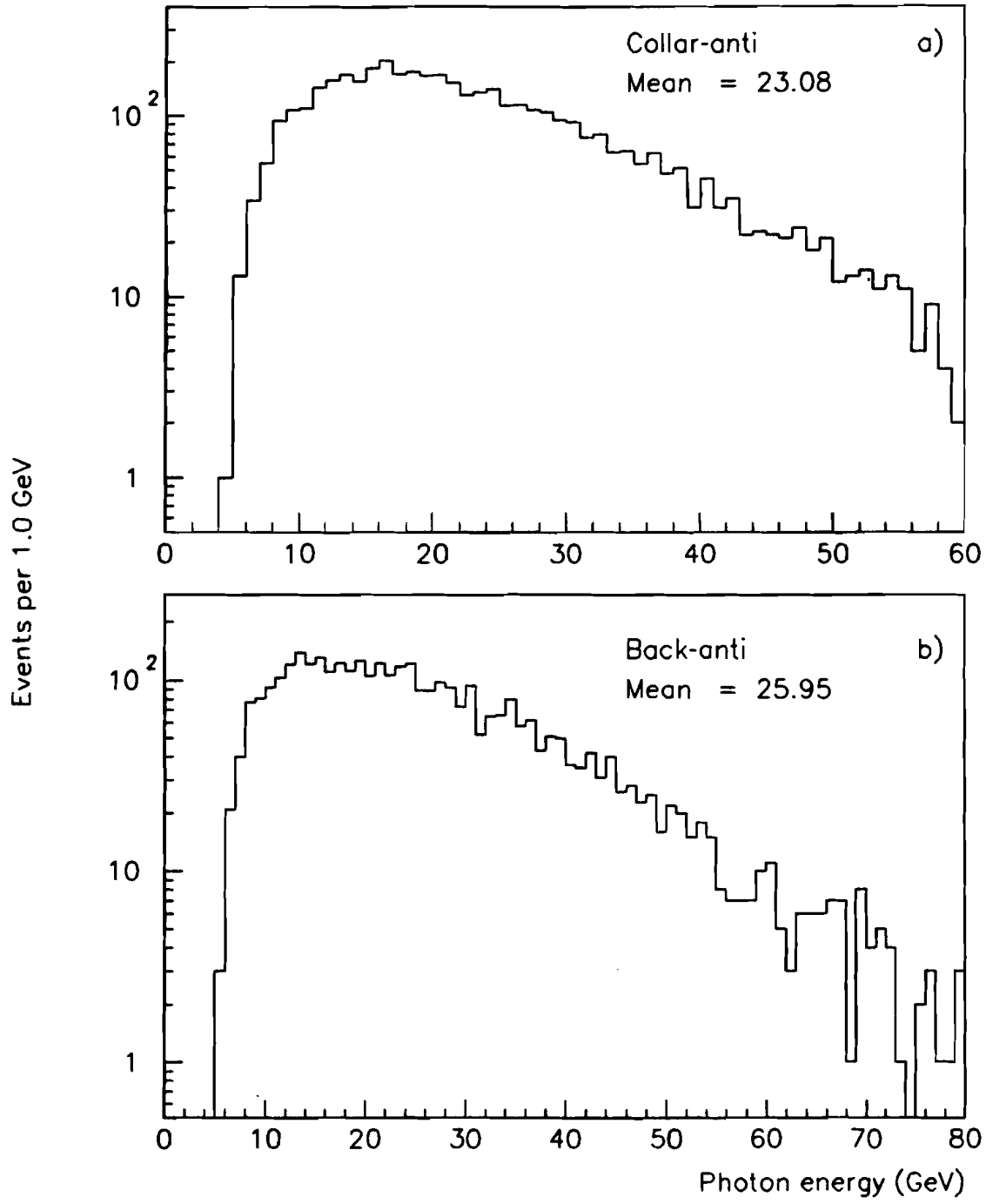

Figure 94. Monte Carlo energy distributions of photons hitting the Collar-anti and Back-anti veto counters. a) Photon energy distribution for CA, b) Photon energy distribution for BA.

TABLE 17. Photon veto efficiencies.

Photon Veto	Efficiency	Threshold
Pinching-anti (PA)	94.0 %	0.1 GeV
Sweeper-anti (SA)	97.4 %	0.05 GeV
Lead Mask-anti (AM)	99.6 %	0.1 GeV
Regenerator-anti (RA)	98.8 %	0.1 GeV
Vacuum-anti 1 (VA1)	51.9 %	2.6 μ
Vacuum-anti 2 (VA2)	90.4 %	1.3 μ
DRAN	98.1 %	0.6 μ
Vacuum-anti 3 (VA3)	99.6 %	1.0 μ
Vacuum-anti 4 (VA4)	99.2 %	1.5 μ
Magnet-anti (MA)	100 %	2.0 μ
Lead glass-anti (LGA)	97.8 %	2.5 μ
Collar-anti (CA)	100 %	5 μ
Back-anti (BA)	100 %	5 GeV

assumption that it is a kaon, it reconstructed in the decay region 110-134 m. The efficiency of a certain counter is defined as the percentage of the time that a photon that hits the counter has energy greater than a considered threshold. In the third column of Table 17 we show the threshold that was assumed for the calculation of the efficiency. The efficiency of VA1 is low because the energies of photons hitting it are low and because its threshold had to be high since it is a counter with relatively high accidental activity.

The detection efficiency of the Sweeper-anti photon veto (SA) is shown as a function of photon energy in Figure 95. This efficiency curve was produced by EGS simulation of SA having as input information the angular distribution and energy distribution of photons hitting SA as seen in $3\pi^0$ background Monte Carlo. This efficiency curve was helpful for the adjustment of the photon veto cuts in the Monte Carlo as will be described in Chapter 8.

Photons projecting outside the outer radius of the photon veto counters

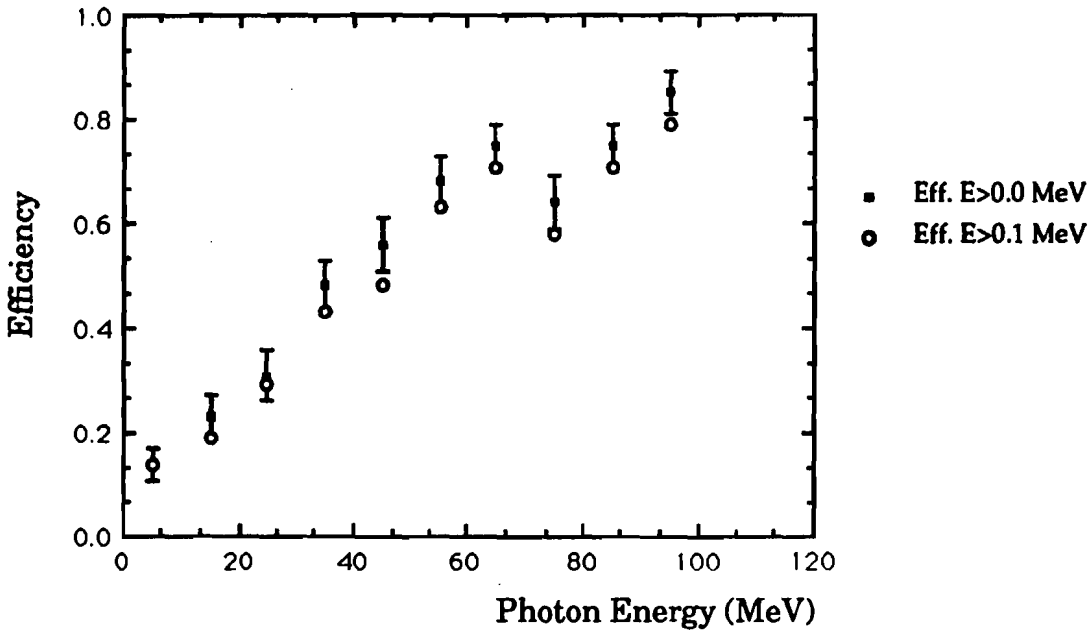

Figure 95. Detection efficiency for the Sweeper-anti photon veto as a function of photon energy. The squares correspond to deposited energy in the counters greater than 0.0 MeV while the circles correspond to energy greater than 0.1 MeV. The efficiency at 1 GeV of photon energy is 0.94.

were simply vetoed in the simulation but events with such photons were not vetoed. Using again angular distribution and energy distribution of photons hitting outside VA2 from $3\pi^0$ background Monte Carlo as input to EGS simulation we produced the probability for a photon to hit the vacuum pipe outside VA2 and deposit at least 0.1 MeV of energy. Using this probability curve as a function of photon energy which is shown in Figure 96 and generalizing it for photons hitting the pipe outside the VA1, VA3, VA4 and HDRA too, we vetoed events appropriately when analyzing the Monte Carlo data.

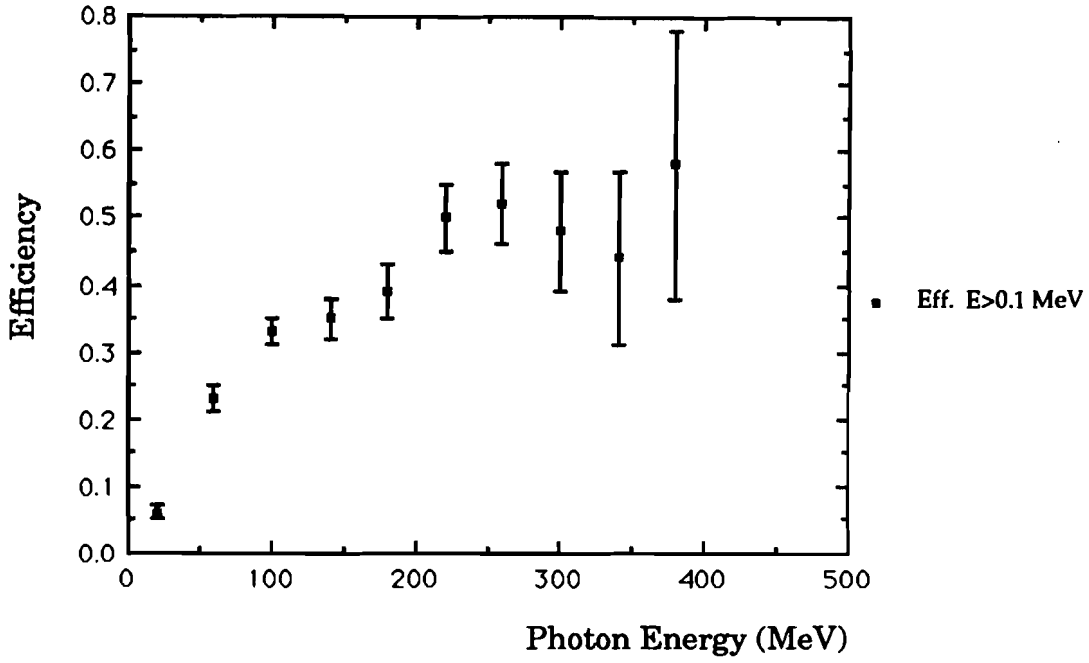

Figure 96. Photon probability for hitting the vacuum pipe outside the VA2 photon veto and depositing there more than 0.1 MeV of energy.

7.1.2.2 Chamber simulation

Wire plane efficiencies deduced from Ke3 charged mode data were implemented in the Monte Carlo. The efficiencies used for the simulation were as following: out of the 16 planes the 8 were at least 99% efficient and the rest had efficiency at least 97% with the exception of the first y plane in chamber 1 which was greater than 90% efficient and the first y plane in chamber 2 which was greater than 95% efficient. The fact that 9 of the about 2000 wires were disconnected was also implemented. Resolution smearing in the positions of the hits on the wires is implemented and the chamber 2 logic, described in Chapter 4, is also simulated.

7.1.2.3 Scintillation banks

Dimensions of the B and C bank counters and widths of gaps between them were measured from special B*μ tapes and they were implemented in the Monte Carlo. The counters of these banks were considered hit if a charged particle was intersecting with them or if the e^+, e^- from a converted photon crossed at least 1/4 of the thickness of the bank. If any of the B or C counters were hit the corresponding trigger bit was set with 99.95% or 99.94% probability for B or C bank respectively. These probabilities were deduced from study of the data.

7.1.2.4 Latches

B or C latches were set when the B or C bank counters were hit and the corresponding trigger bit was set. Latches indicating the position of the regenerator and the absorber were also implemented.

7.1.3 Cluster simulation

In order to simulate faithfully our electron and photon clusters we had to simulate properly their patterns and their energy. For the pattern simulation we used an electron cluster library based on electrons from lead glass calibration data. In order to simulate properly the energy response we had to apply to the energy of the clusters of the library, besides scaling, some additional corrections which were derived from studies of calibration data and from EGS studies.

7.1.3.1 Electron cluster simulation

The Monte Carlo generates electron and photon cluster patterns by using a sample of about 18500 electron or positron clusters collected from electron calibration data and supplemented from 10000 electron clusters generated with EGS. The electron and positron clusters from calibration data (both electrons and positrons referred to as electrons hereafter) were collected from runs with full readout mode (no sparse readout threshold

applied) to avoid the ADC threshold problem. Those clusters were selected to be clean and free from bremsstrahlung and accidental overlaps as much as possible. Some of the selection criteria applied were the following:

a) The tracks were required to match with the clusters in the calorimeter and it was additionally required that the x and y track positions at the glass do not project more than 3 mm away from the edges of the central block of the cluster to which they correspond.

b) Track quality cuts were applied.

c) It was required that $0.8 \leq \frac{E}{p} \leq 1.2$ where E is the energy of the cluster and p is the momentum of the track.

d) The Mu1 trigger latch and the AM latches were not allowed to fire and at least one V latch was required to fire. The CA was required to have small activity, less than 0.5 μ (μ stands for a muon equivalent).

e) If the time of the event with respect to the beginning of the spill was less than 1 s or the RA scaler counted less than 6 counts the event was rejected. Time into the spill and RA scaler are usually well correlated and with this cut we reduced problems relating to pedestal updating early into the spill. Pedestal problems were more severe in calibration than in normal data taking because of the very high trigger rate we had, although the intensity was low, and events with high pedestal fluctuations had to be rejected.

f) Some fusion cuts were applied and the "adder ratio" of the cluster, defined as counts of the adder where the central block of the cluster belongs over the sum of the lead glass counts in the blocks belonging to this adder, was required to be at least 0.75.

g) The x component of the center of momentum was required to be within ±2.5 cm of the center of the array to avoid electrons emitting bremsstrahlung photons upstream of the magnet.

h) The clusters were required to be well separated by at least 30 cm and none of the 25 blocks belonging to the 5 x 5 array around the center of the cluster was allowed to be missing.

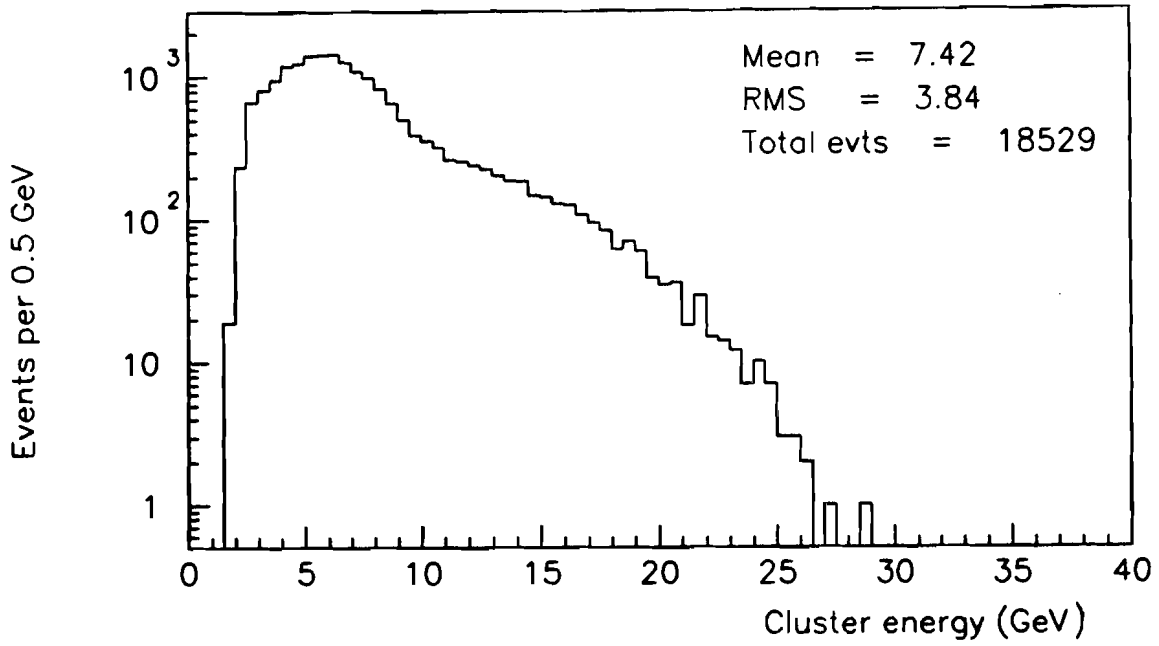

Figure 97. Energy distribution of electrons and positrons taken from calibration data and used for the cluster library.

The energy distribution of those electrons is shown in Figure 97. Since this sample did not have enough statistics for small cluster energies, it was supplemented by about 10000 electron clusters generated with EGS with energies of at most 4 GeV. For each cluster in this combined electron sample there was stored in a library the x and y position of the incident electron in the central block, the energy of each of the 5 x 5 blocks around the center of the cluster and the energy of the cluster. These electron clusters were stored in the library in position-energy bins where the position width was a fixed one of 1.45 mm and the energy width was varying from 0.25 to 3.5 GeV up to the energy of 14.5 GeV. In particular the energy widths were 0-0.25 GeV, 0.25-0.5 GeV, 0.5-1 GeV, 1-2 GeV, 2-4 GeV, 4-5 GeV, 5-6 GeV, 6-7 GeV, 7-9 GeV, 9-11 GeV, 11-14.5 GeV. Each position-energy bin had an average of 10 different cluster samples. If a cluster

pattern had to be generated for an electron that had a certain energy and position, it was formed according to the pattern of a sample electron cluster picked up randomly from the corresponding position-energy bin. Then the energy of each of the 5 x 5 blocks was multiplied by an overall factor scaling the sample electron energy to the given energy of the incident electron. The scaling was done within the energy limits of the corresponding bin but clusters beyond 14.5 GeV had to be scaled appropriately by a factor sometimes greater than 2. Cluster patterns though are not identical at high and low energies: high energy clusters have less statistical fluctuations and they are more compact and therefore the scaling results in Monte Carlo clusters being slightly wider at high energies than data clusters. Besides scaling, the cluster energy was also corrected for radial leakage and leakage from the back of the blocks and corrected for attenuation and nonlinearity.

7.1.3.2 Photon cluster simulation

When a photon hits the glass it converts to an electron positron pair and this conversion depth x was picked from an exponential distribution.[1] Then the photon energy was divided to the electron and positron according to the Bethe-Heitler spectrum [38]:

$$\phi_{E_+} dE_+ = C dE_+ \left[\left(E_+^2 + E_-^2 + \frac{2}{3} E_+ E_- \right) \ln\left(183 Z^{-\frac{1}{3}} \right) - \frac{1}{9} E_+ E_- \right]$$

where ϕ_{E_+} is the cross-section for the creation of a positron with energy E_+ and an electron with energy E_-, Z is the atomic number of the material that causes the conversion and C depends on Z and on the energy of the incoming photon. A cluster pattern was generated for the electron and positron by the same way as for single electron shower. In order to simulate properly the energy response, the energy of the photon cluster had to undergo the corrections described in the previous section. These corrections were applied in a similar way as for a single electron cluster except that the attenuation correction takes now the conversion depth into account.

[1] $I=I_0 \exp(-7x/9X_0)$ where I is the intensity of the photon beam and X_0 is the radiation length of the lead glass in this case.

Hadron showers were not simulated. Instead minimum ionizing particle energy was deposited in the calorimeter at the appropriate place.

7.1.4 ADC simulation

After the individual energies of the lead glass blocks belonging to a cluster were simulated they were digitized into ADC counts by using the gains of the blocks and the high range slopes of the ADCs (see sections 2.3.2.1 and 2.3.2.2). Similarly the adder ADC counts were simulated by using the lead glass ADC counts and the adder gains. The sparse readout threshold of 5 counts for lead glass ADCs and 2 counts for the other ADCs was applied in both cases. None of the other ADCs were simulated.

7.1.5 HCF simulation

As mentioned in Chapter 3, the 804 HCF channels are characterized by a threshold of about 200 counts (1 GeV) and a resolution (see Figures 38, 39). The individual thresholds were implemented in the Monte Carlo and a constant average resolution (σ) of 4.8 counts was used for each block. If the energy of the block was greater than 3σ from the threshold of the corresponding block then the block was considered hit. If the energy was less than 3σ from the threshold of the block, the block was considered not hit. For energies within the $\pm 3\sigma$ window, the threshold was smeared with the σ and if the block energy was above the threshold, the block was considered hit.

7.1.6 Photon conversion, Bremsstrahlung, Multiple scattering

Photons were allowed to convert at the V and T counter banks, at the Pb sheet when it was in place, at the vacuum window and at the C and B counter banks. Bremsstrahlung and multiple scattering were allowed to occur at all the places mentioned above and at the sense, field and window

wires of the chambers as well as at the chamber windows.

7.2 Signal Monte Carlo

7.2.1 Data-Monte Carlo comparison for signal

To get a feeling of how this simulation finally works it is helpful to show the agreement between data and Monte Carlo for $3\pi^0$ decays that together with the Ke3 decays consist our two very high statistics modes. In Figure 98 is shown the agreement for the z decay vertex distribution for $K_L \rightarrow 3\pi^0$ decays and in Figures 99 and 100 are shown overlays of the distributions of the total energy in the calorimeter and of the energy of the individual clusters respectively. The agreement is quite satisfactory in all three plots. In Figures 101-106, are presented data-Monte Carlo comparisons of photon illuminations at the lead Mask, at the HDRA and at the lead glass. For all three plots we used again $K_L \rightarrow 3\pi^0$ decays. The disagreement in the lead Mask aperture is due to the fact that this is the most upstream aperture and therefore a) the statistics available for its measurement from Ke3 decays are less than for other apertures and b) it is sensitive to beam shape and target position. Figure 107 shows the extent of the agreement between data and Monte Carlo for the distance between any pair of the six clusters in the $3\pi^0$ decay. The good agreement gives us confidence about the simulation program in general and the cluster distance figure especially about the cluster simulation. It would be useful at this point to see the agreement between data and Monte Carlo for $K_L \rightarrow 2\pi^0$ decays which are used for normalization in the study of the $K_L \rightarrow \pi^0\gamma\gamma$ decay. The following $2\pi^0$ plots have been produced by an analysis with similar cuts as the $\pi^0\gamma\gamma$ analysis and are shown in the decay region 110-134 m. In Figures 108 and 109 are presented overlays for the z decay vertex distribution and for the χ^2 variable which was defined in Chapter 6.

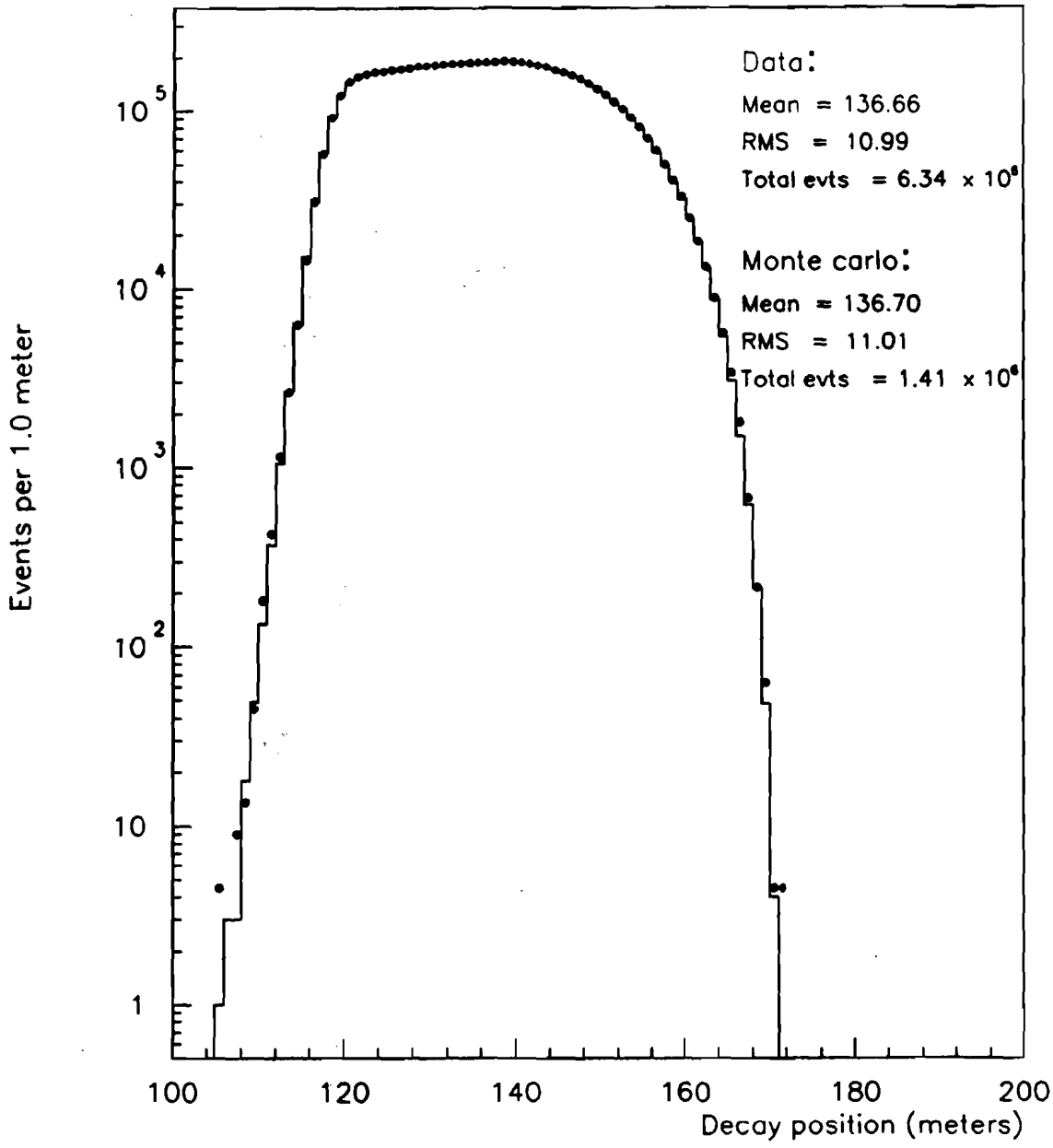

Figure 98. Data-Monte Carlo comparison for the z decay vertex distribution for $K_L \rightarrow 3\pi^0$ decays. The histogram represents the data and the solid circles the Monte Carlo.

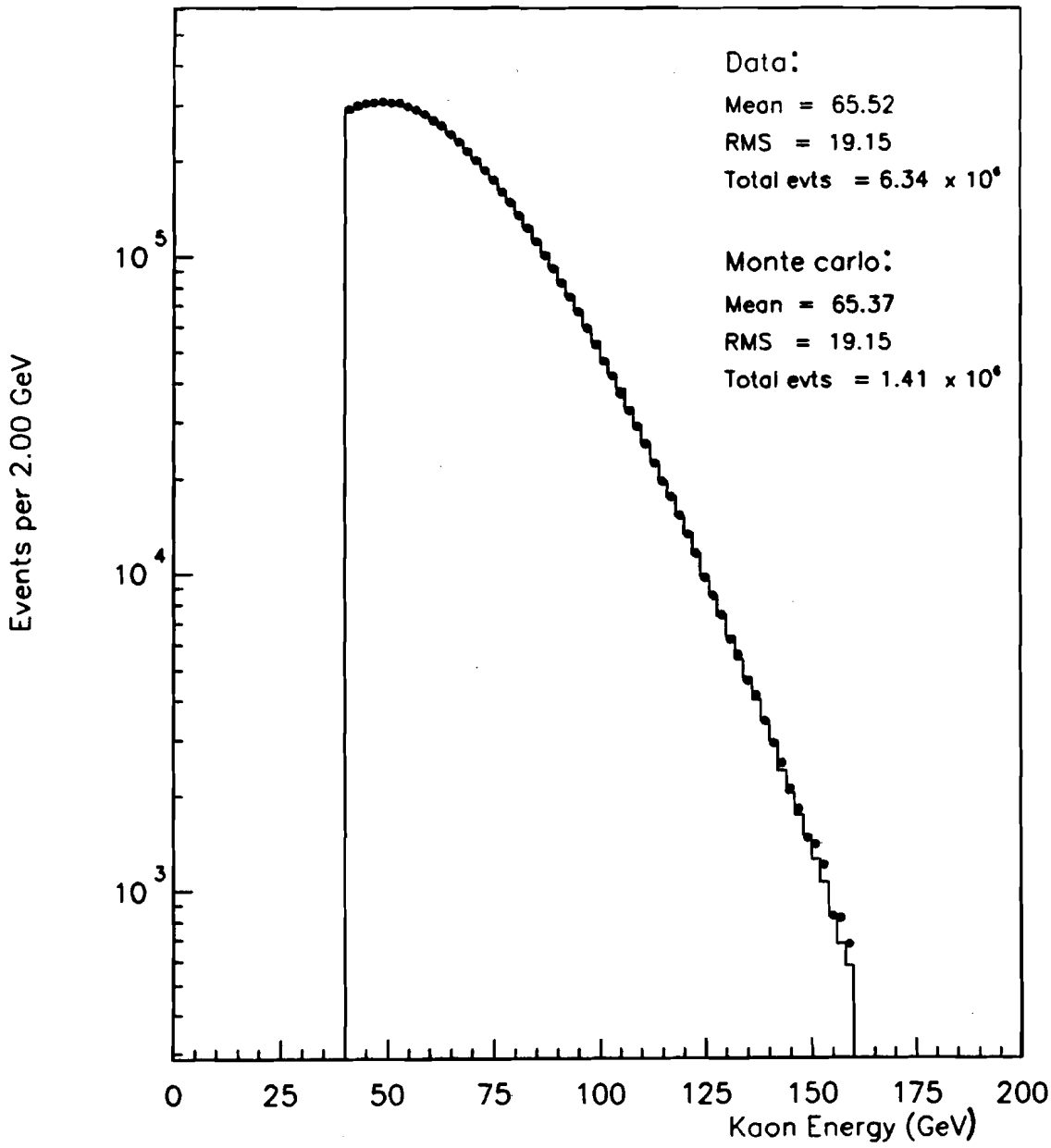

Figure 99. Kaon energy distribution for $K_L \rightarrow 3\pi^0$ decays. The histogram represents the data and the solid circles the Monte Carlo.

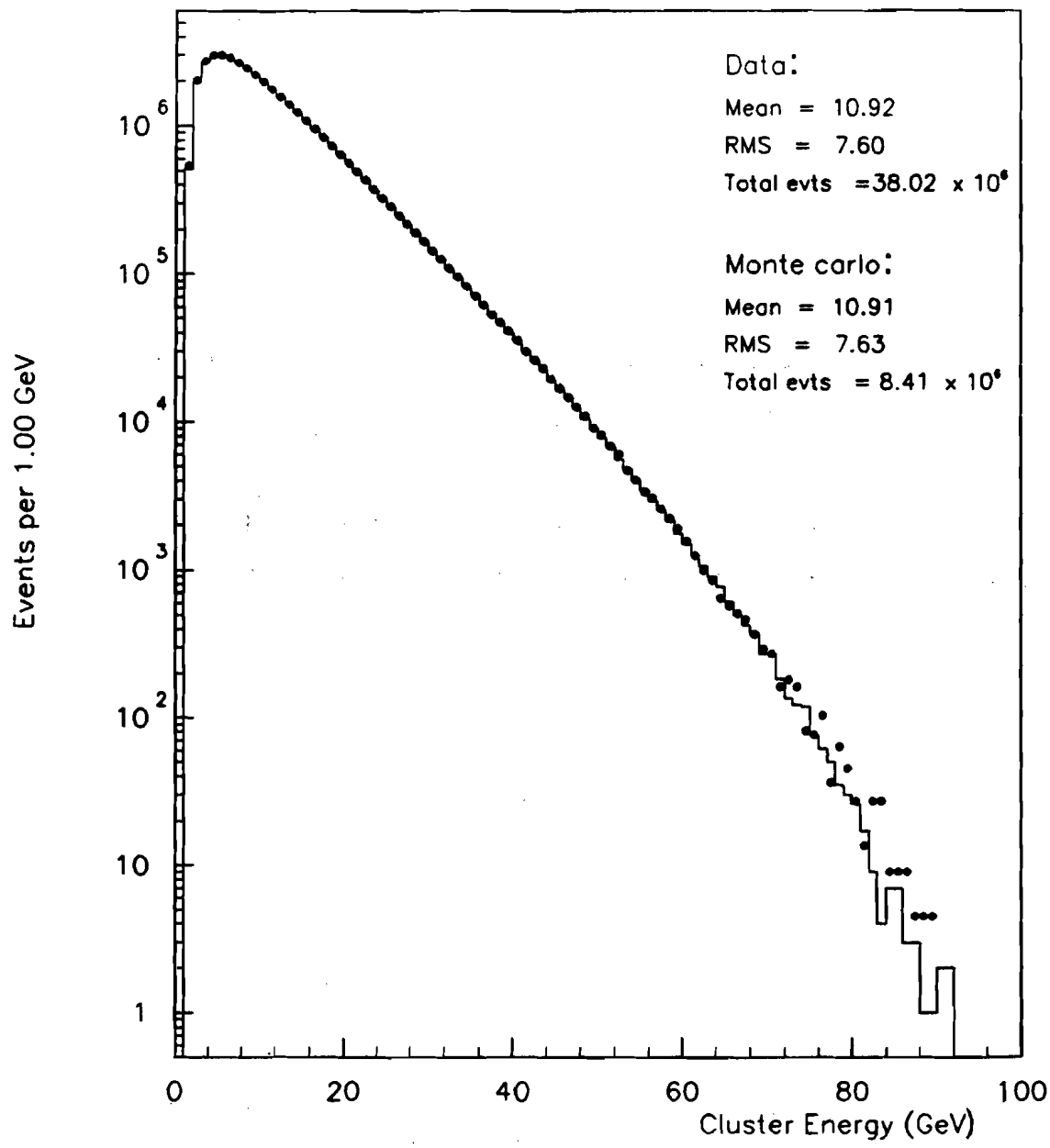

Figure 100. Cluster energy distribution for $K_L \rightarrow 3\pi^0$ decays. The histogram represents the data and the solid circles the Monte Carlo.

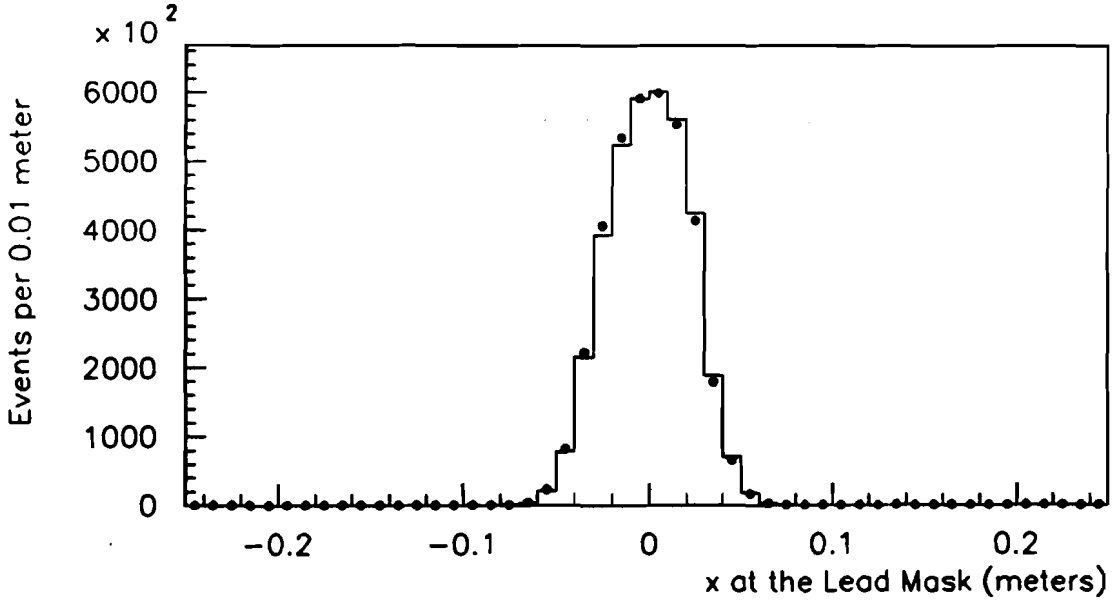

Figure 101. Photon illumination at the lead Mask, x view. The histogram represents the data and the solid circles the Monte Carlo.

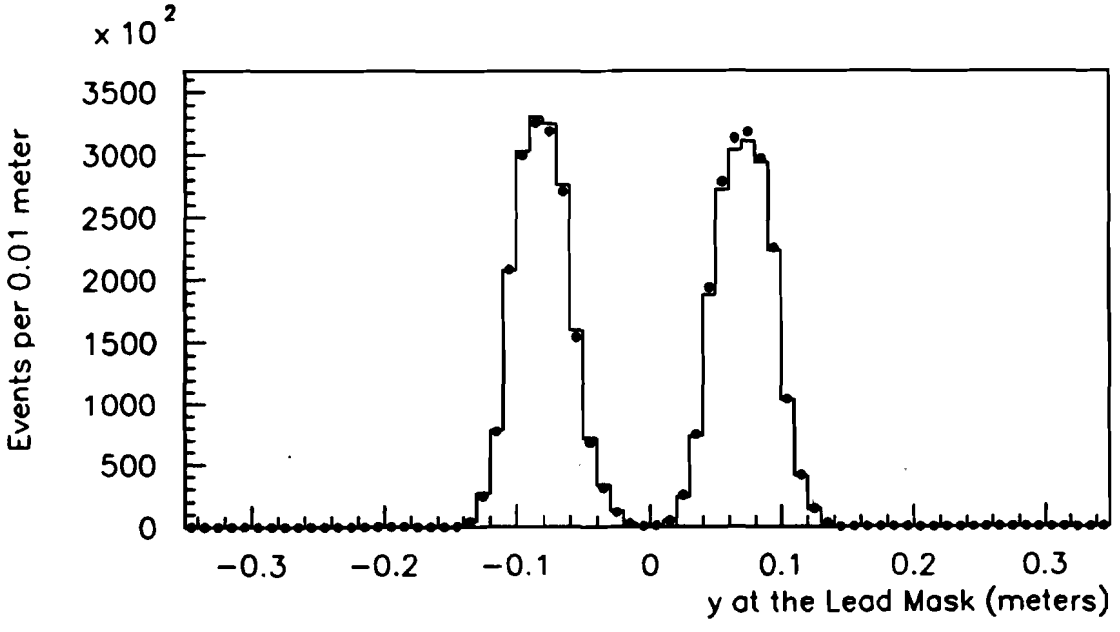

Figure 102. Photon illumination at the lead Mask, y view. The histogram represents the data and the solid circles the Monte Carlo.

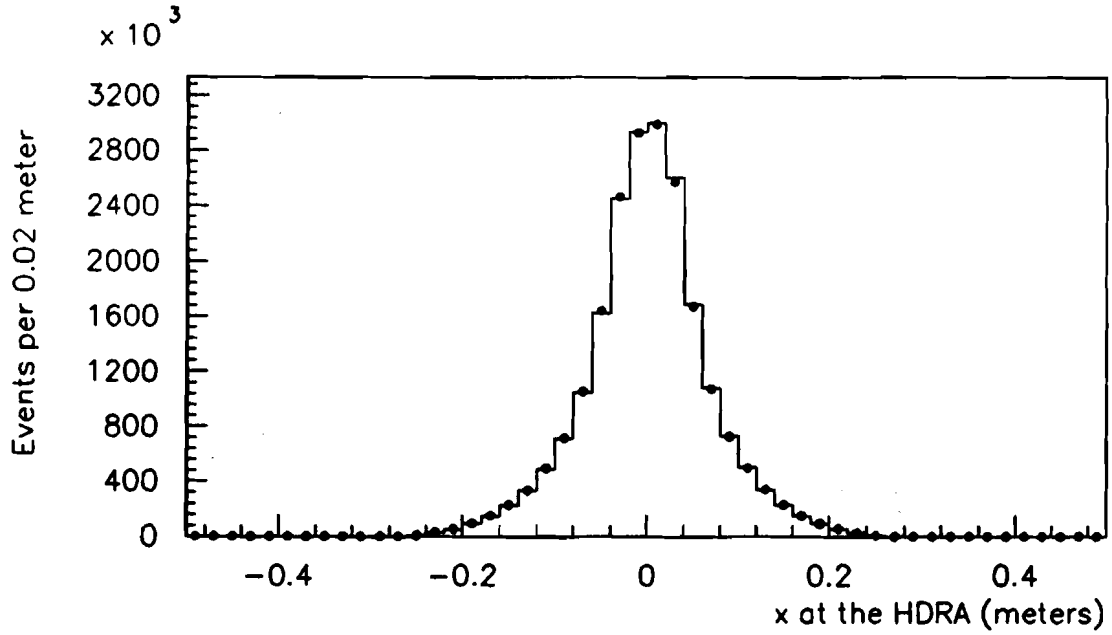

Figure 103. Photon illumination at the HDRA, x view. The histogram represents the data and the solid circles the Monte Carlo.

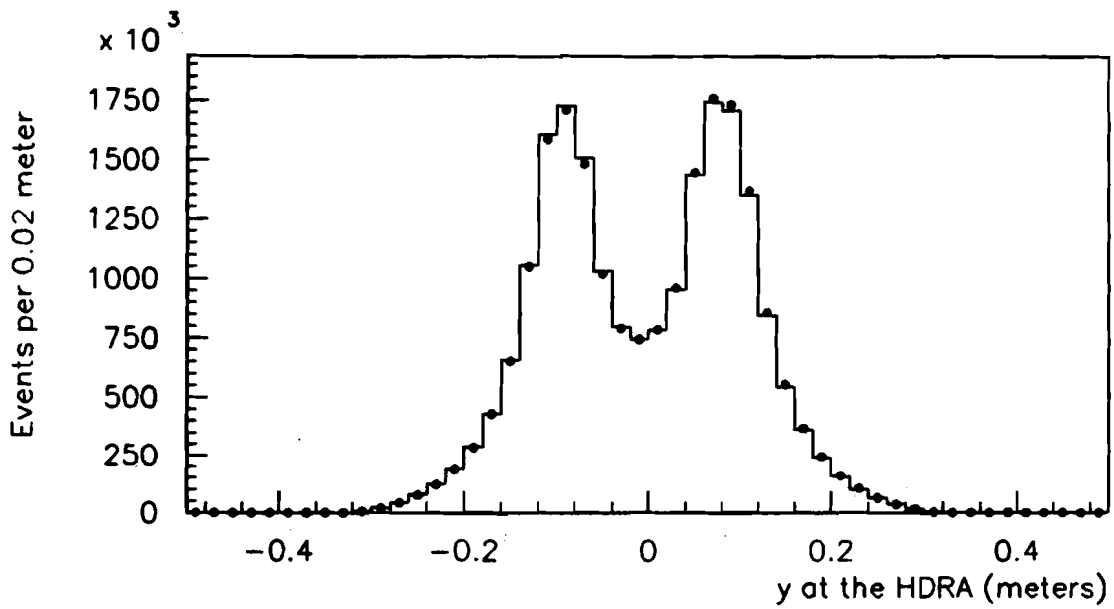

Figure 104. Photon illumination at the HDRA, y view. The histogram represents the data and the solid circles the Monte Carlo.

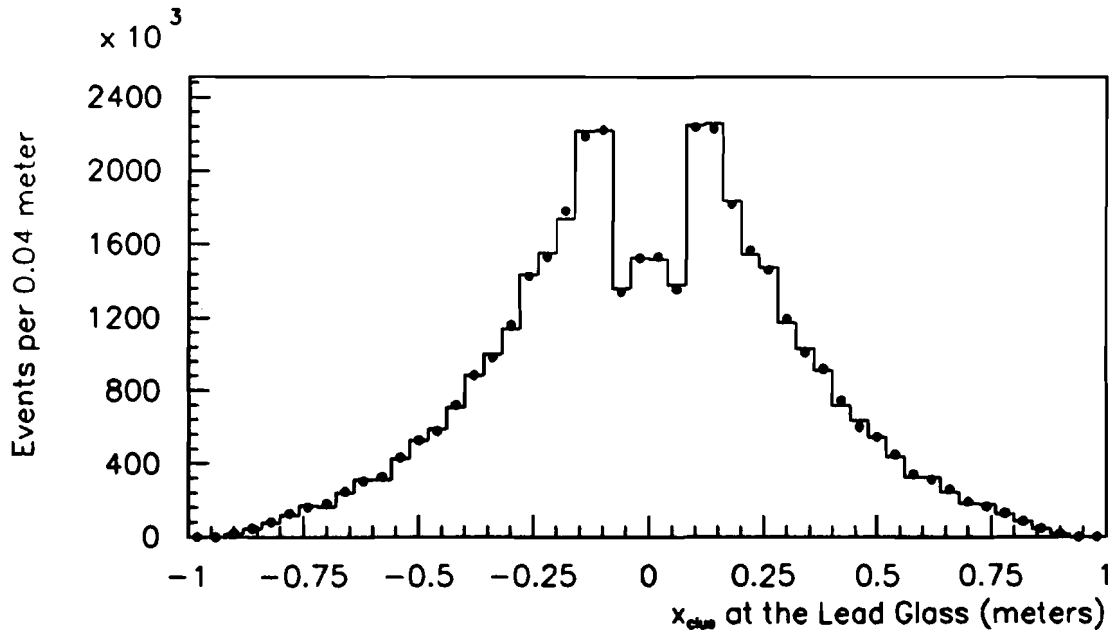

Figure 105. Photon illumination at the lead glass, x view. The histogram represents the data and the solid circles the Monte Carlo.

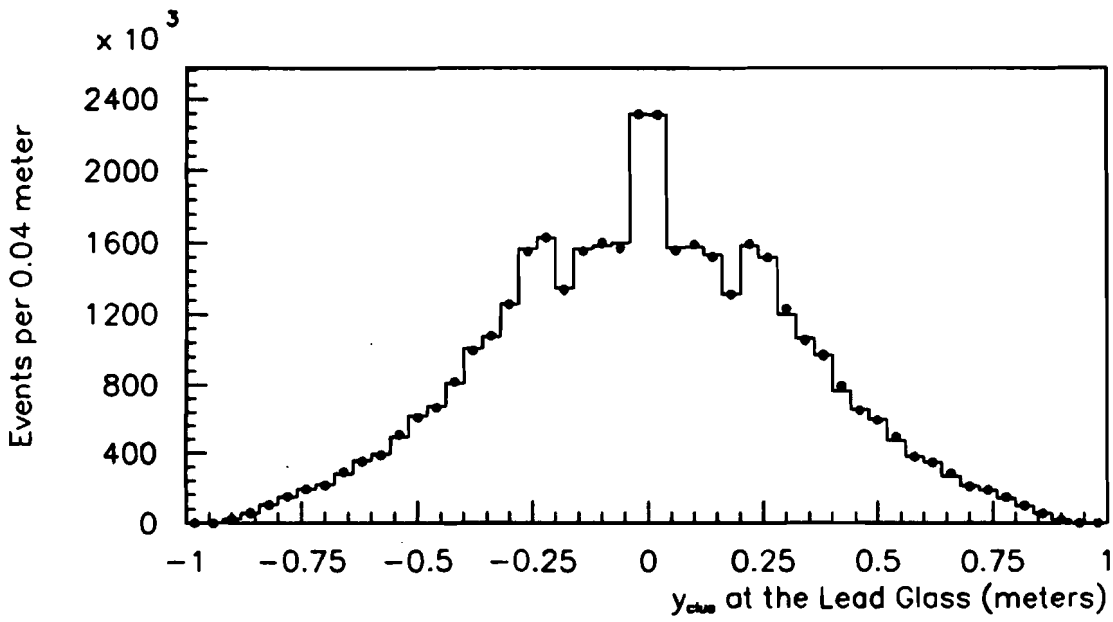

Figure 106. Photon illumination at the lead glass, y view. The histogram represents the data and the solid circles the Monte Carlo.

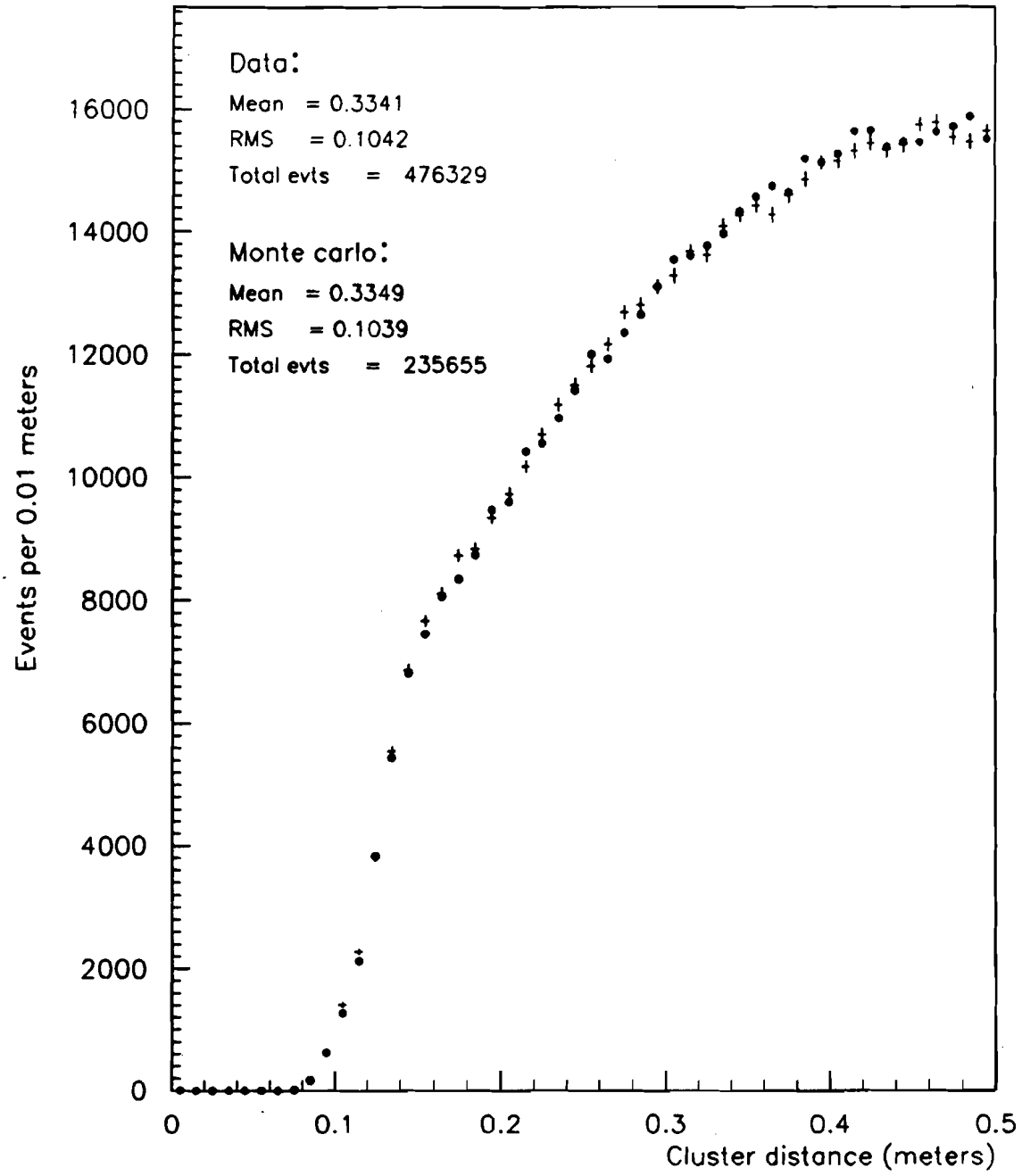

Figure 107. Distribution of the distance between clusters for $K_L \rightarrow 3\pi^0$ decays. The error bars represent the data and the solid circles the Monte Carlo.

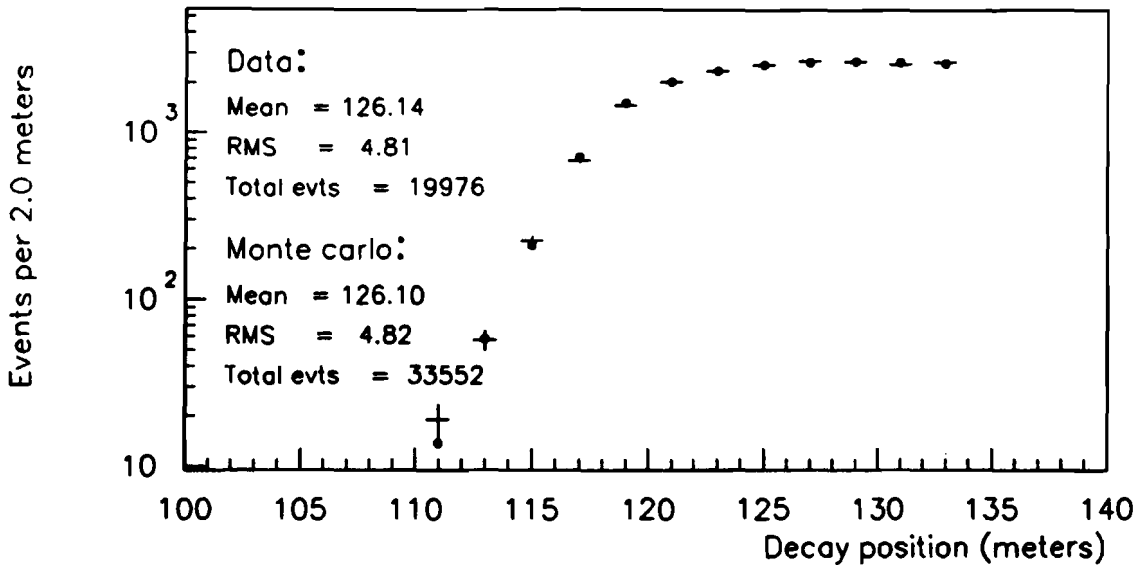

Figure 108. z decay vertex distribution for $K_L \rightarrow 2\pi^0$ decays. The error bars represent the data and the solid circles the Monte Carlo.

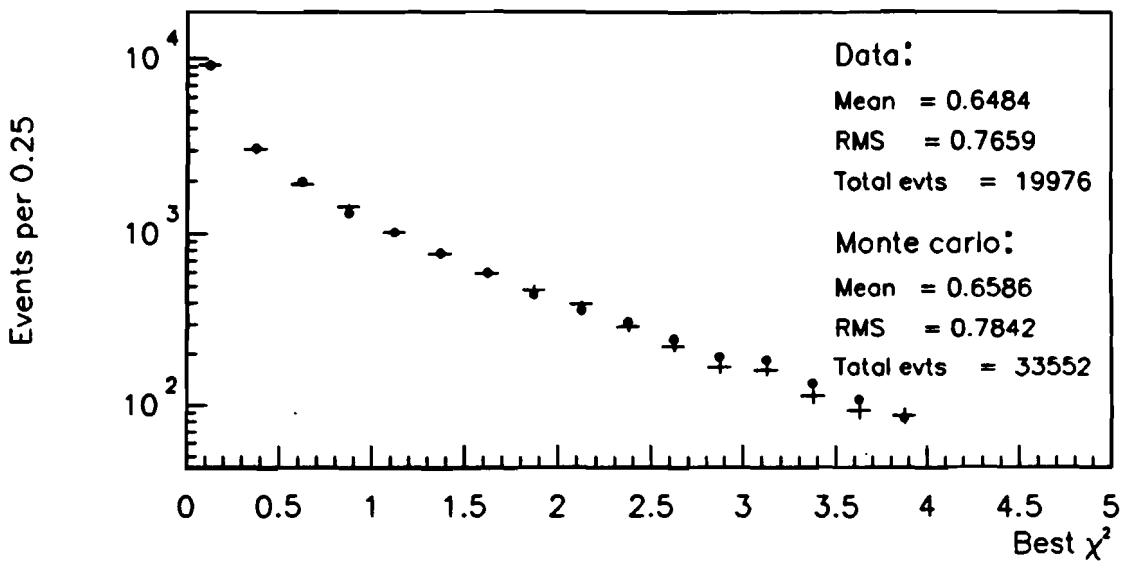

Figure 109. Distribution of the best χ^2 variable for $K_L \rightarrow 2\pi^0$ decays. The error bars represent the data and the solid circles the Monte Carlo.

Although χ^2 is sensitive to resolution and the choice of the correct pairing and therefore hard to simulate well the agreement between data and Monte Carlo is good. In Figures 110 and 111 are shown overlays of the distributions of total energy and of individual cluster energy. Finally in Figures 112-115 are shown overlays of fusion variables for $K_S \rightarrow 2\pi^0$ decays. The disagreement in "maxsum" for high energies is due to the energy scaling in the Monte Carlo as mentioned in section 7.1.3.1. Due to this, when this fusion cut is applied one cuts at the order of 1% more events in Monte Carlo than one should. This is not that important for the ε'/ε measurement because one cuts the same percentage of events in both K_L and K_S. It can affect the absolute acceptance a little but this is an effect one can correct for. Also the energies of the clusters in this analysis are required to be less than 60 GeV which makes the disagreement less important. In the determination of the $K_L \rightarrow \pi^0\gamma\gamma$ branching ratio approximately the same small error will occur in both $2\pi^0$ and $\pi^0\gamma\gamma$ acceptances and the effect will cancel out. The other fusion variables shown seem to be represented well by the Monte Carlo.

7.2.2 Acceptance determination

7.2.2.1 $\pi^0\gamma\gamma$ acceptance

The theoretical model used for acceptance determination of the $K_L \rightarrow \pi^0\gamma\gamma$ decay is the CHPT described briefly in Chapter 1. We are also discussing here the phase space hypothesis. In Figure 116 is shown the z decay vertex distribution for $\pi^0\gamma\gamma$ Monte Carlo events generated according to the CHPT model and in Figure 117 is shown the m_{π^0} distribution from the same Monte Carlo and after all cuts except the m_{π^0} cut so that the π^0 mass resolution can be easily seen. The arrows in Figure 117 indicate the position of the cut. In Figure 118 is similarly shown the $m_{\gamma\gamma}$ distribution after all cuts and in the chosen decay region of 110-128 m. The $m_{\gamma\gamma}$ distribution has a tail at the low masses which does not appear in the

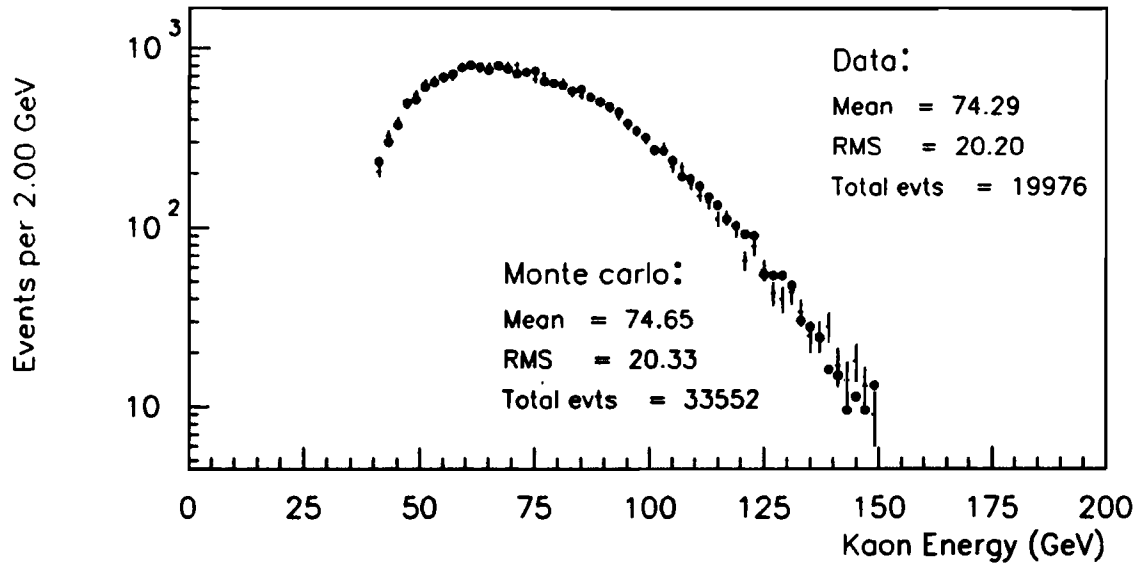

Figure 110. Kaon energy distribution for $K_L \rightarrow 2\pi^0$ decays. The error bars represent the data and the solid circles the Monte Carlo.

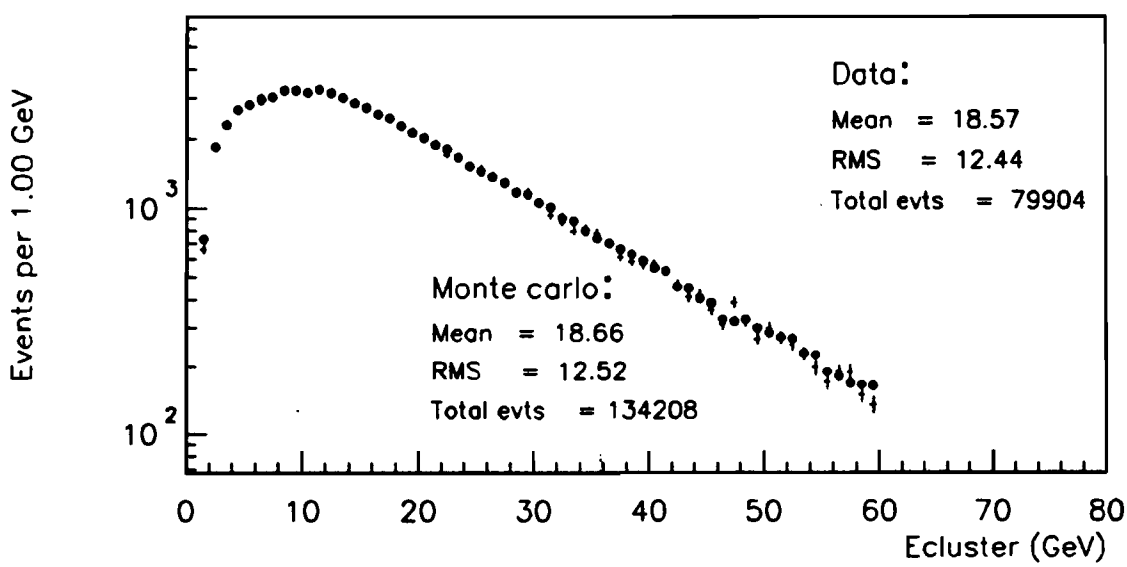

Figure 111. Cluster energy distribution for $K_L \rightarrow 2\pi^0$ decays. The error bars represent the data and the solid circles the Monte Carlo.

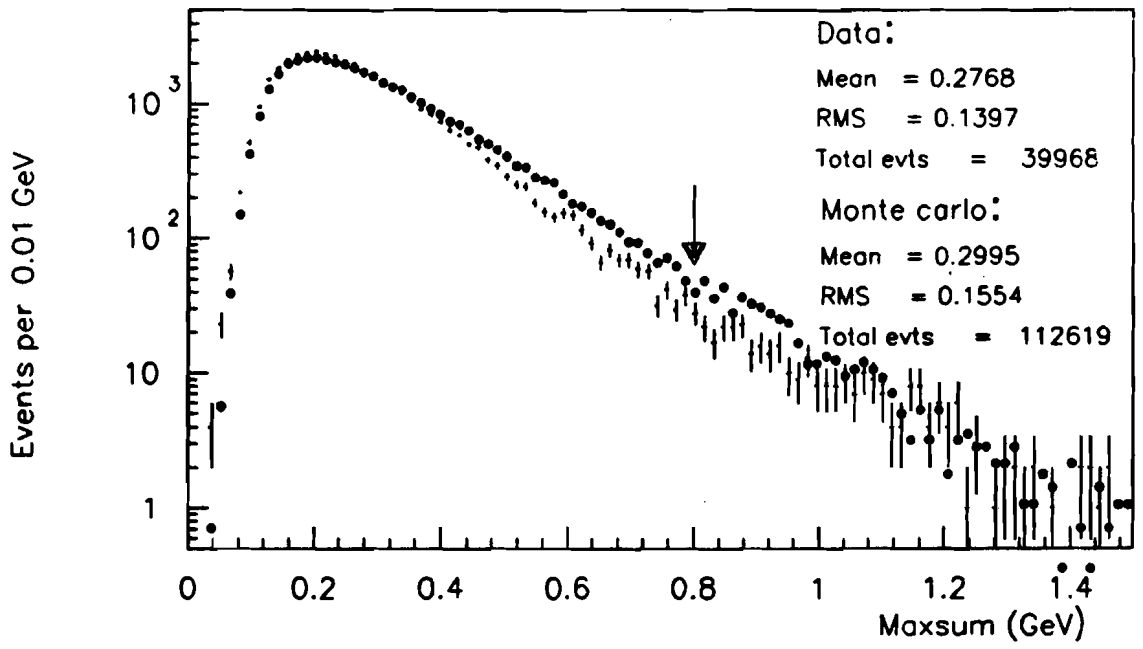

Figure 112. Data-Monte Carlo comparison in $K_S \rightarrow 2\pi^0$ decays for the maximum energy, "maxsum", in two consecutive blocks of the 16 block ring surrounding the cluster. The error bars represent the data and the solid circles the Monte Carlo.

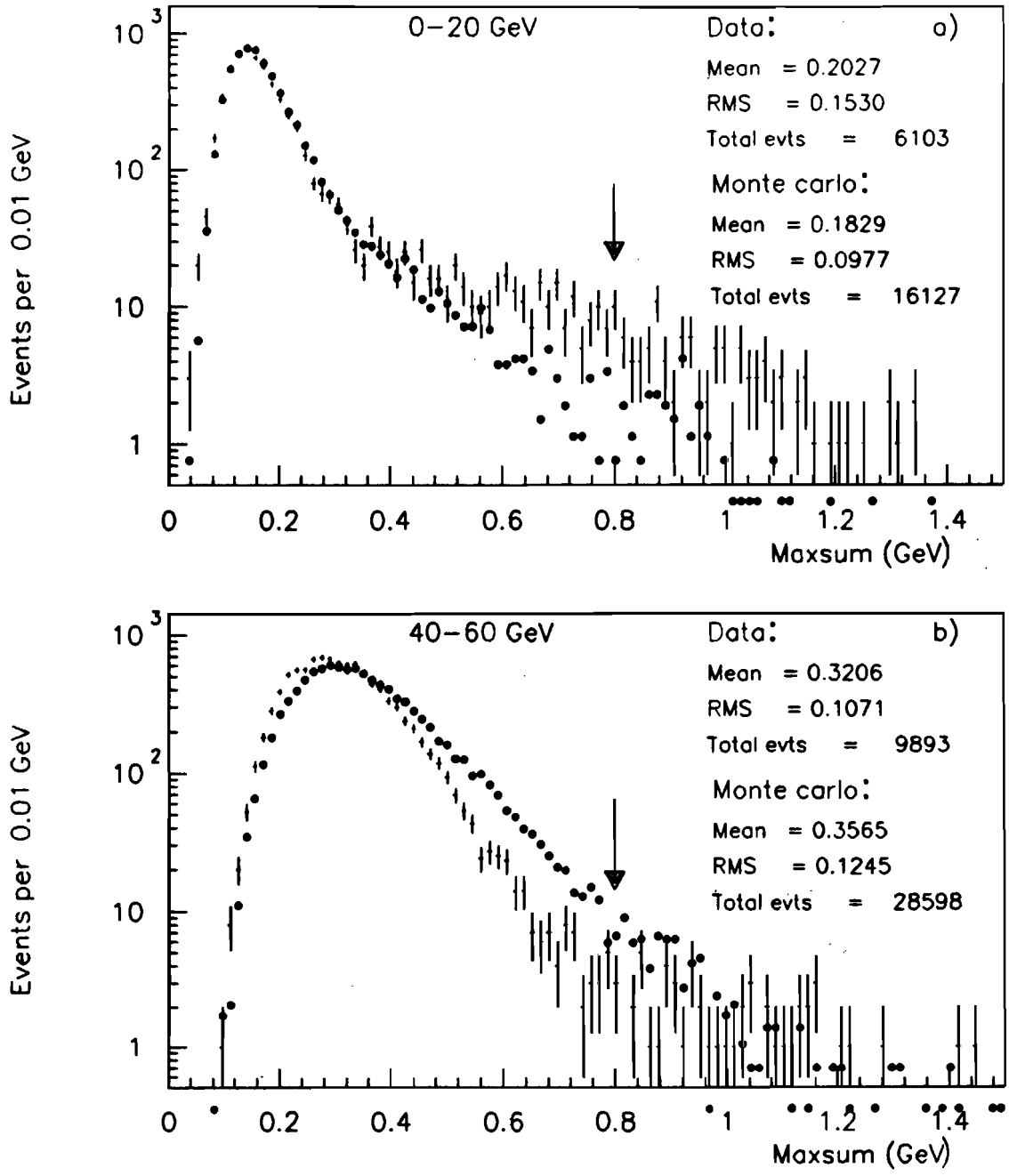

Figure 113. Data-Monte Carlo comparison for "maxsum" in $K_S \rightarrow 2\pi^0$ decays for certain cluster energy range. a) the cluster energy is in the range 0-20 GeV; b) the cluster energy is in the range 40-60 GeV. The error bars represent the data and the solid circles the Monte Carlo.

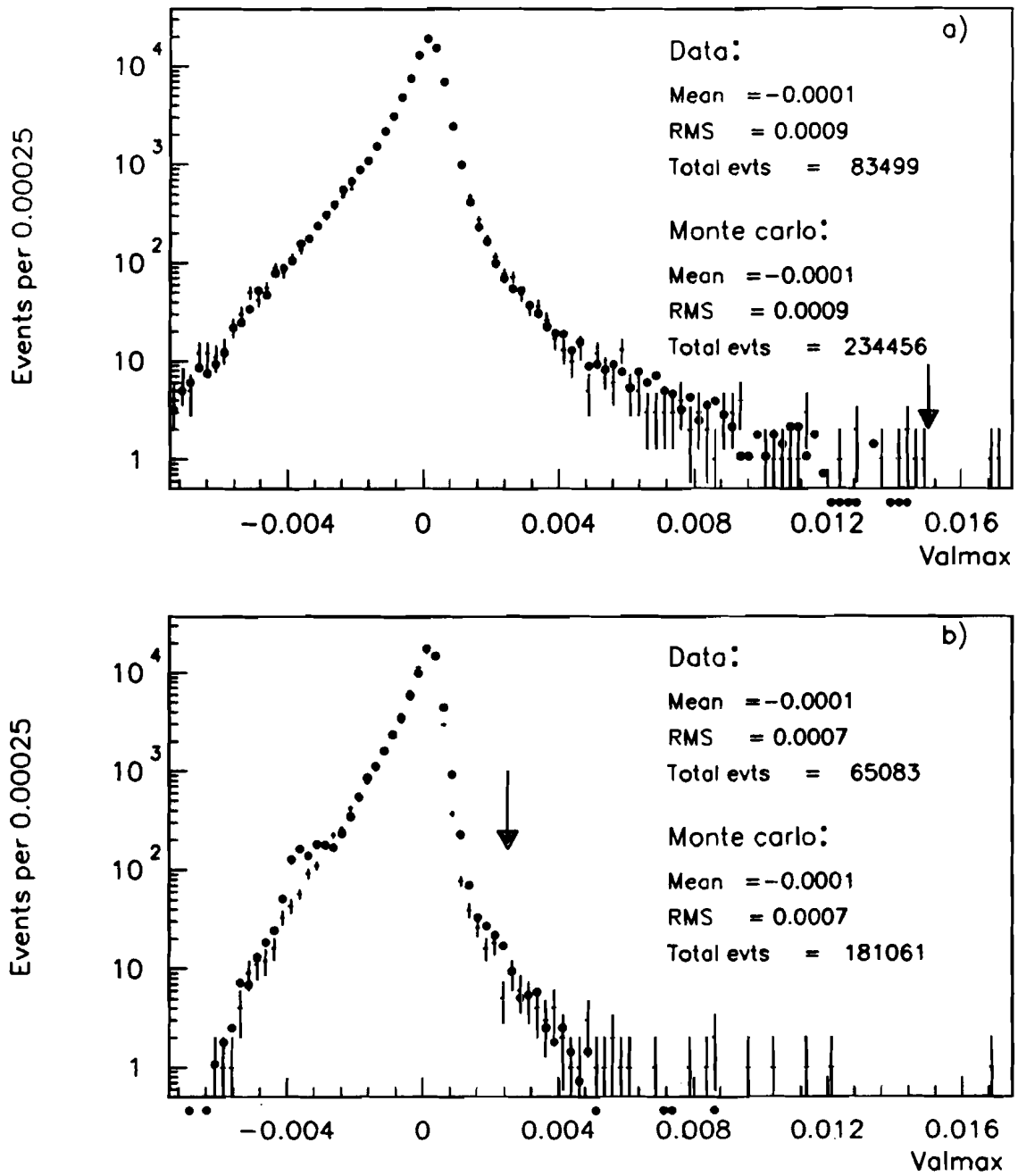

Figure 114. Data- Monte Carlo comparison for "valmax", as explained in the text, for $K_S \rightarrow 2\pi^0$ decays. a) the cluster energy is in the range 4-20 GeV; b) the cluster energy is greater than 20 GeV. The error bars represent the data and the solid circles the Monte Carlo.

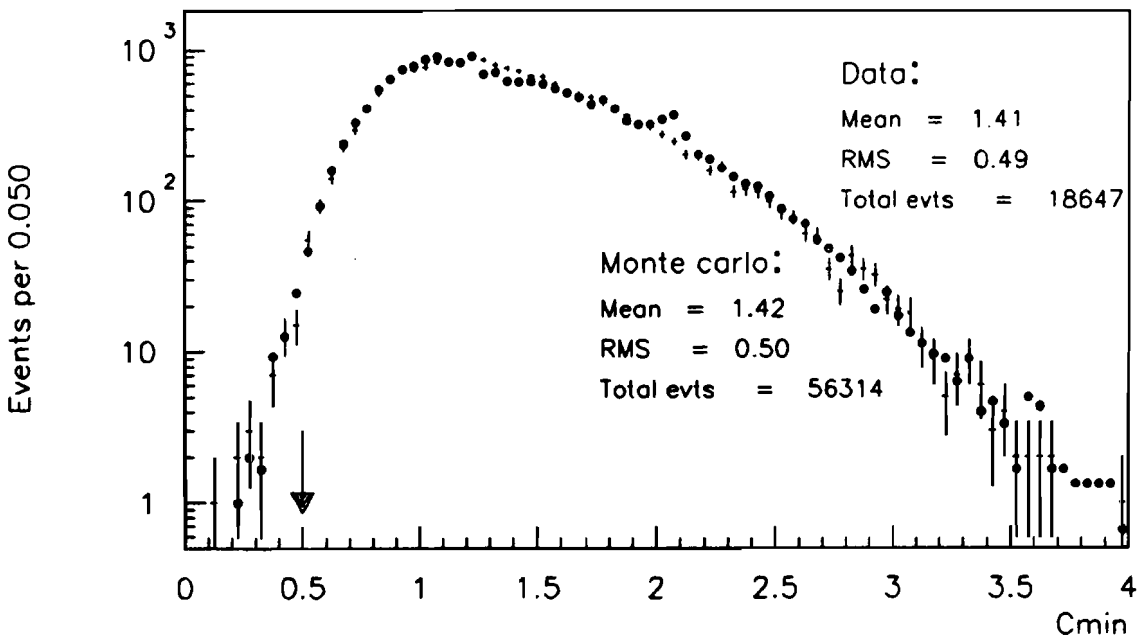

Figure 115. Data-Monte Carlo comparison for the minimum ratio of the energy of a side block to the energy of a corner block among all corner blocks of a cluster for $K_S \rightarrow 2\pi^0$ decays. The error bars represent the data and the solid circles the Monte Carlo.

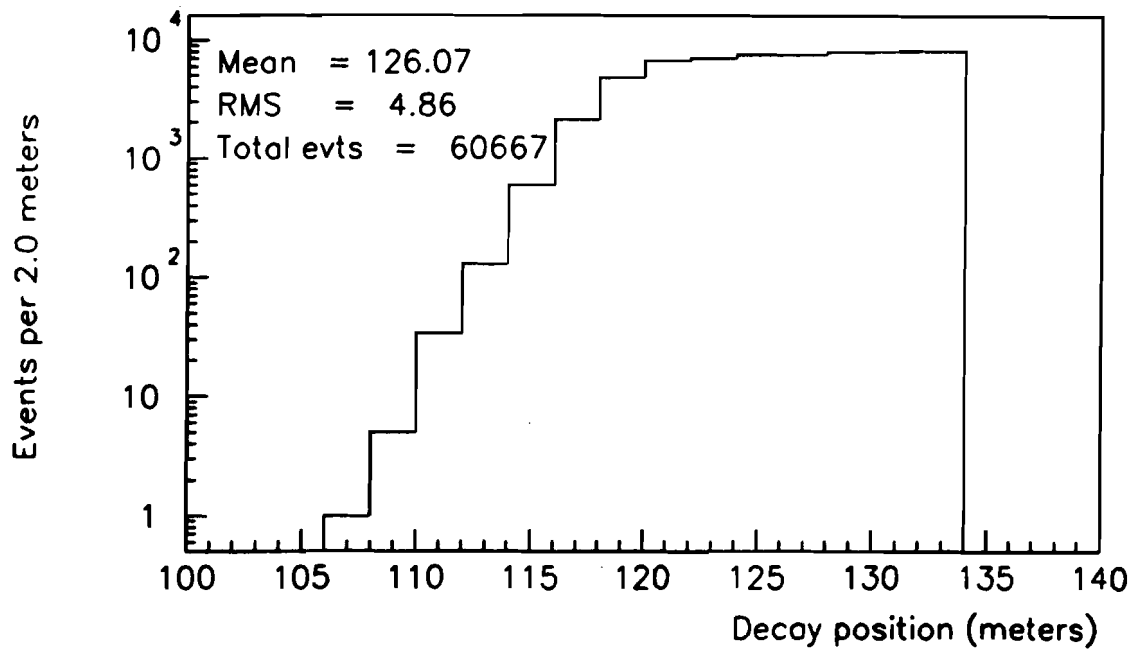

Figure 116. z decay vertex distribution for $K_L \rightarrow \pi^0\gamma\gamma$ Monte Carlo events using the CHPT model.

distribution derived directly from the theoretical model and shown in Figure 6. This tail is due to misreconsruction; in about 11.3% (8.2%) of the events, as deduced from Monte Carlo study using the CHPT (phase space) assumption, the pair of photons that forms the π^0 is selected wrong. In Figure 119 is shown the $m_{\gamma\gamma}$ distribution for the subset of events in Figure 118 for which the π^0 pairing is selected right and as can be seen the low mass tail is not there any more. In Figure 120 is shown the $m_{\gamma\gamma}$ spectrum from phase space Monte Carlo. The mass distribution here is almost flat without very prominent characteristics. The dip around 135 MeV in both models is always due to our software cut. Absolute acceptance as a function of $m_{\gamma\gamma}$ is shown in Figure 121. This curve was made by using events generated according to phase space distribution and one can see that the

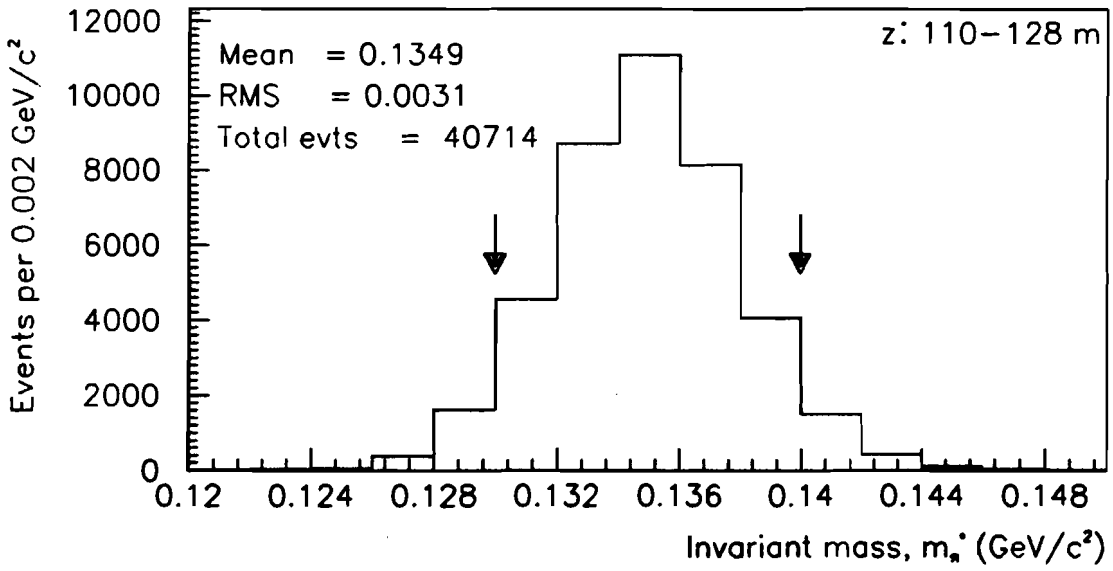

Figure 117. π^0 **invariant mass for** $K_L \rightarrow \pi^0\gamma\gamma$ **Monte Carlo events after all the analysis cuts except the** m_{π^0} **cut. (The Monte Carlo uses the CHPT assumption.)**

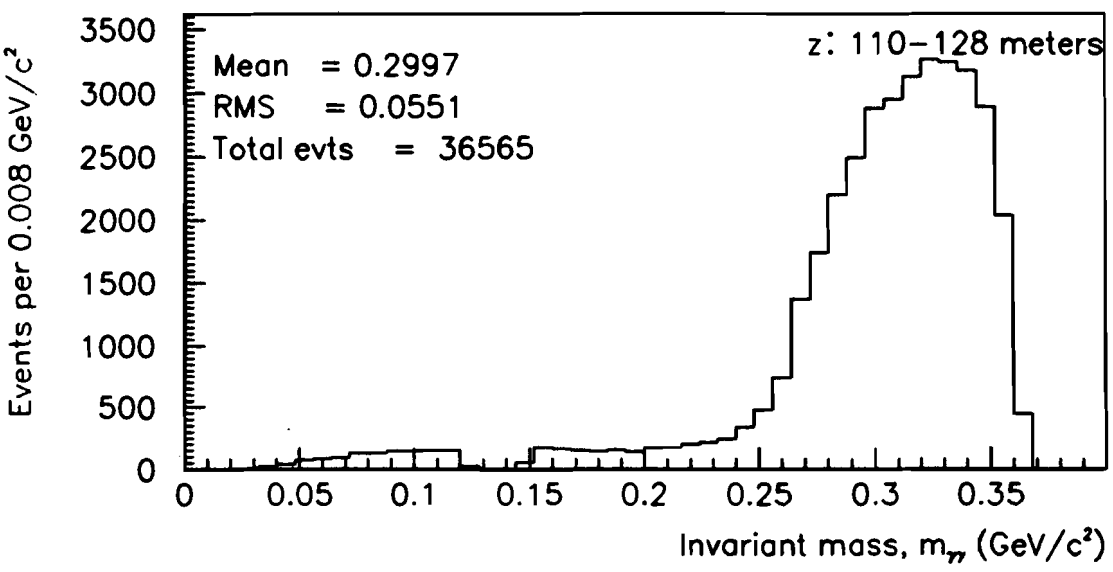

Figure 118. $\gamma\gamma$ **invariant mass for** $K_L \rightarrow \pi^0\gamma\gamma$ **Monte Carlo events after all the analysis cuts. (The Monte Carlo uses the CHPT assumption.)**

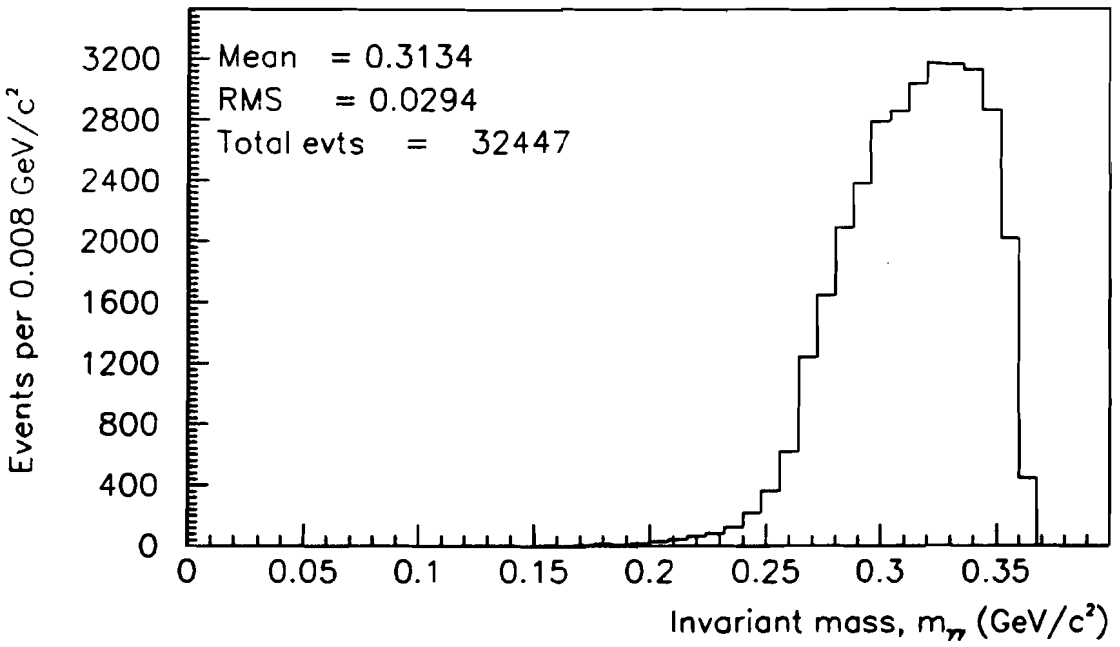

Figure 119. $\gamma\gamma$ invariant mass for $K_L \rightarrow \pi^0\gamma\gamma$ Monte Carlo events requiring that the reconstructed π^0 is also the true π^0.

acceptance is fairly flat for high $m_{\gamma\gamma}$. The dip around 135 MeV is due to the software cut mentioned above and the dip at 270 MeV is caused by the cut that kinematically rejects the "double fusion" events.

In the CHPT model $m_{\gamma\gamma}$ is peaking at high masses and therefore we are not severely hurt by considering for our limit only events with masses greater than 300 MeV. In fact with this selection we are keeping 61.8% of the events. The acceptance for the $K_L \rightarrow \pi^0\gamma\gamma$ and also for every decay mode is defined as the ratio of accepted over generated events. In order to determine the $\pi^0\gamma\gamma$ acceptance we generated events with the CHPT assumption between 100 and 138 m from the target and with momentum spectrum in the range 20-220 GeV. From those events 766.1K were generated in the regions 110-128 m and 40-150 GeV used in the analysis and 36565 passed all the analysis cuts relevant for the Monte Carlo. 22611 of the 36565 events had $m_{\gamma\gamma}$ masses greater than 300 MeV and therefore the

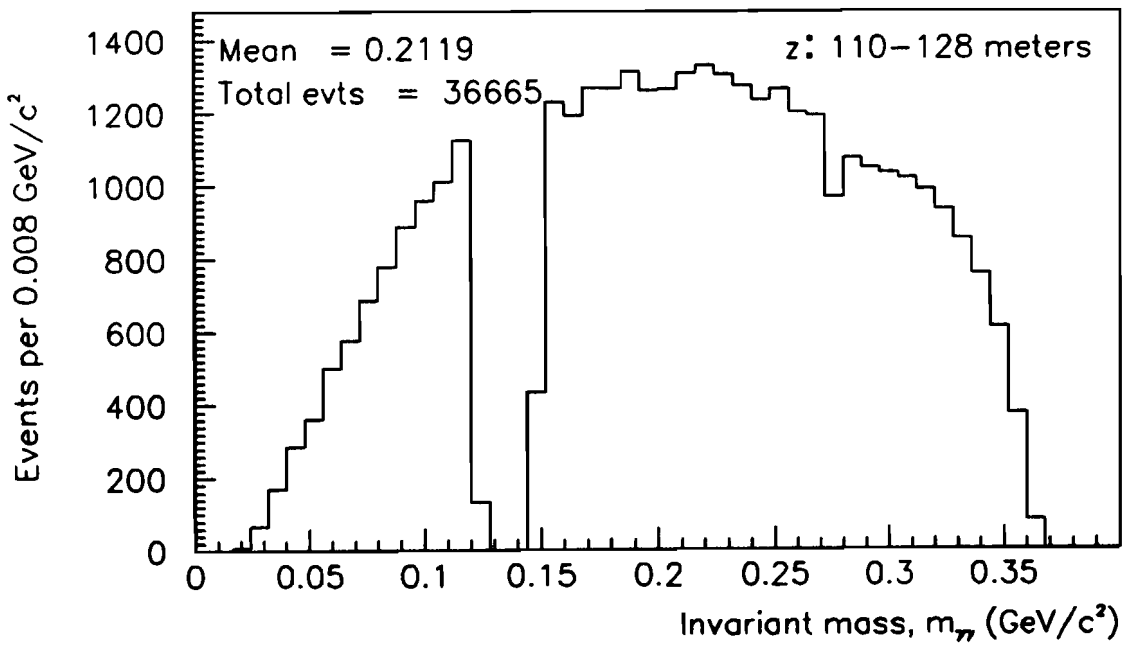

Figure 120. $\gamma\gamma$ invariant mass after all the analysis cuts for $K_L \rightarrow \pi^0\gamma\gamma$ Monte Carlo using the phase space assumption.

$\pi^0\gamma\gamma$ acceptance was calculated to be 2.95%.

Considering the phase space model which has similar distribution for $m_{\gamma\gamma}$ as the VMD model we are using for the upper limit derivation the whole mass region with the exception of the $\pm$14MeV window around $m_{n\pi^0}$ and the region from 264-280 MeV that contains in our data the "double fusion peak" and it is obvious background. The acceptance here was calculated to be 4.44% and it was derived in the same way as for the CHPT model and in the same z and energy regions.

7.2.2.2 $2\pi^0$ acceptance

To determine the $K_L \rightarrow 2\pi^0$ acceptance in the decay region 110-128 m from the target 198.5 K generated events were used which had all the features described in section 7.1.1. From these, 13520 passed all the cuts including the requirement of reconstructing in the m_K region of 480-516

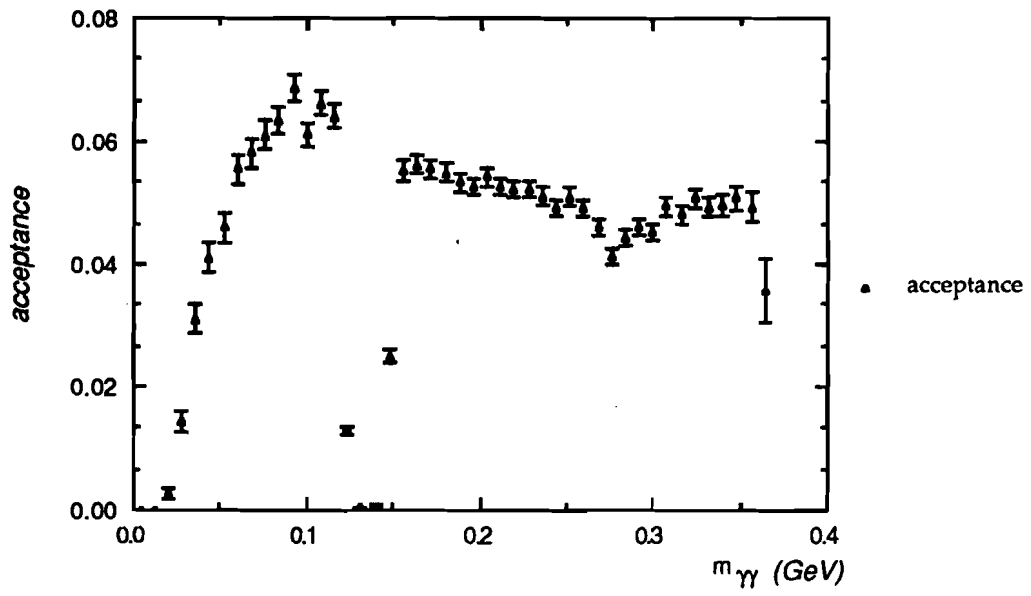

Figure 121. Acceptance versus the $\gamma\gamma$ invariant mass for $K_L \rightarrow \pi^0\gamma\gamma$ decays.

MeV. Therefore the $K_L \rightarrow 2\pi^0$ acceptance was calculated to be 6.8%. These acceptances are going to be used in Chapters 9 for the derivation of an upper limit.

7.3 Background Monte Carlo

7.3.1 The standard $3\pi^0$ background Monte Carlo

7.3.1.1 Generation conditions-characteristics

As already mentioned in Chapter 5, $3\pi^0$ decays can become background four-cluster events and mimic $\pi^0\gamma\gamma$ decays when photons escape from the fiducial decay volume or when they overlap at the calorimeter. In order to

study this background we generated $K_L \rightarrow 3\pi^0$ decays that satisfy the four-cluster trigger. This generation happened at 2 different time periods and it consumed about 500 hours of CPU time. Since it was so much time consuming we adapted some of the analysis cuts at the generation stage and we had two output streams: one for background for the $\pi^0\gamma\gamma$ candidates and one for background for the $2\pi^0$ candidates. The cuts used in this generation, which will be called standard $3\pi^0$ background Monte Carlo to be distinguished from complementary $3\pi^0$ generations used for special studies, were the following for the $\pi^0\gamma\gamma$ output stream:

- 4 hardware clusters and 4 software clusters were required.
- The z decay vertex was required to reconstruct upstream of 135 m from the target.
- The total energy of the event was required to be at least 38 GeV.
- m_{π^0} should be within 12 MeV of the nominal π^0 mass.
- The center of energy of the event was required to be within the beam area and in more detail it was required to be within a ± 6 cm window around the geometric center of the two beams in both the x and y direction.
- No latches associated with the B and C banks were allowed to fire.
- Photon veto cuts were also applied; in particular it was required that:

    1)Energy in VA1 $\leq$ 2.6 μ
    2)Energy in VA2 $\leq$ 1.3 μ
    3)Energy in VA3 $\leq$ 1.0 μ
    4)Energy in VA4 $\leq$ 1.5 μ
    5)Energy in MA $\leq$ 2.0 μ
    6)Energy in LGA $\leq$ 2.5 μ
    7)Energy in DRAC $\leq$ 0.5 μ
    8)Energy in DRAN $\leq$ 0.6 μ

where μ indicates a muon equivalent.

- Events with photons hitting the Sweeper-Anti were rejected if the photons had energy at least 100 MeV.
- The first 3 fusion cuts described in Chapter 6 were also applied.

We used this standard $3\pi^0$ background Monte Carlo to study the characteristics of our background in the $\pi^0\gamma\gamma$ decay and to check quantitavely for how much of the background we can account. There are three categories of $3\pi^0$ decays satisfying the four-cluster trigger:
i) all six photons are detected by the calorimeter,
ii) five of the six photons are detected by the calorimeter,
iii) only four of the six photons are at the calorimeter.
In category i) no energy from the event is lost and the z decay vertex is reconstructed properly with our algorithm at first order, if one assumes that the positions of the fused clusters are identical and ignores nonlinearity effects. Nonlinearity tends to decrease the final energy of a fused cluster and therefore the distance of the decay vertex from the glass too as can be realized by looking at Equation (5.1). One can see the effect of nonlinearity on the energy of a fused cluster if one considers two clusters with energies E_1 and E_2 overlapping to a single cluster. Due to nonlinearity the observed energy of a cluster is bigger than its true energy by a factor of $E^{1.021}$. Since we correct for nonlinearity in our analysis by raising basically the energies to the power 0.979 (inverse of 1.021), the ratio of the final energy of the fused cluster over the sum of the final energies of the individual clusters (after all corrections) is:

$$\frac{(E_1{}^{1.021} + E_2{}^{1.021})^{0.979}}{(E_1^{1.021})^{0.979} + (E_2^{1.021})^{0.979}}$$

If one assumes that E_1 and E_2 are equal then the corrected energy of the fused cluster is lower by 1.45%. Therefore the reconstructed distance of the vertex from the glass is reduced depending on the number of fused clusters involved. In categories ii) and iii) we have missing energy and z is reconstructed wrong anyway. Figure 122 shows the distribution of the reconstructed minus the generated decay vertex for events in category i), no missing photons, category ii), one missing photon, and category iii), two missing photons.

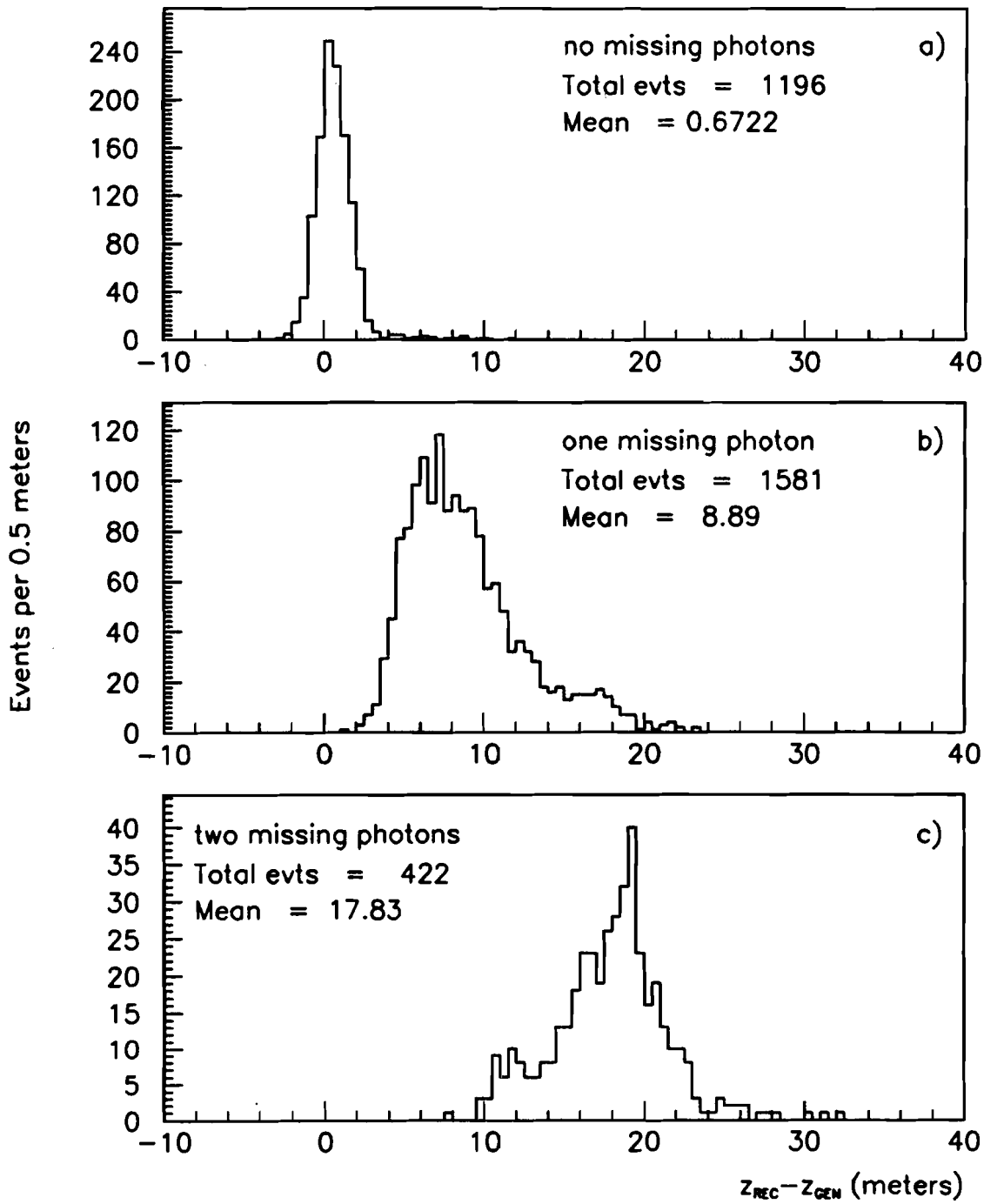

Figure 122. Difference between the reconstructed and generated decay vertex for $K_L \rightarrow 3\pi^0$ background Monte Carlo decays. a) for events with no missing photons, in b) for events with one missing photon and in c) for events with two missing photons.

In Figure 123 is plotted the fraction of events with no missing photons, one missing photon and two missing photons in 2.0 m bins of z decay vertex from the same $3\pi^0$ background Monte Carlo decays. One can see that in the region 122-124 m from the target for example ~2% of the events have two missing photons, 25% of the events have one missing photon and another 73% of the events have no missing photons. After all the $\pi^0\gamma\gamma$ analysis cuts and in the z region 110-128 m is shown in Figure 124 the $m_{\gamma\gamma}$ spectrum from $3\pi^0$ background decays. The shaded histogram corresponds to events with two missing photons or "double escapes". The area under the dashed histogram corresponds to events with one missing photon or "single fusions" and includes also the "double escapes" just mentioned. The left over area under the solid line corresponds to events with no missing photons or as usually called "double fusions". In Table 18 are shown the percentages of

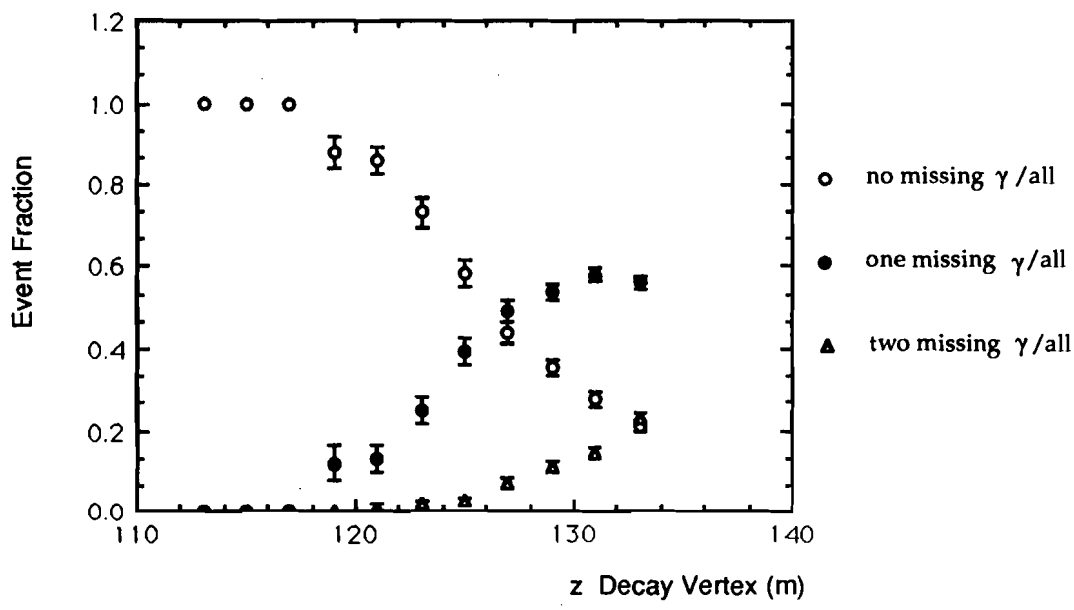

Figure 123. Fraction of events with zero, one and two missing photons as a function of the reconstructed z decay vertex from $K_L \rightarrow 3\pi^0$ background Monte Carlo decays.

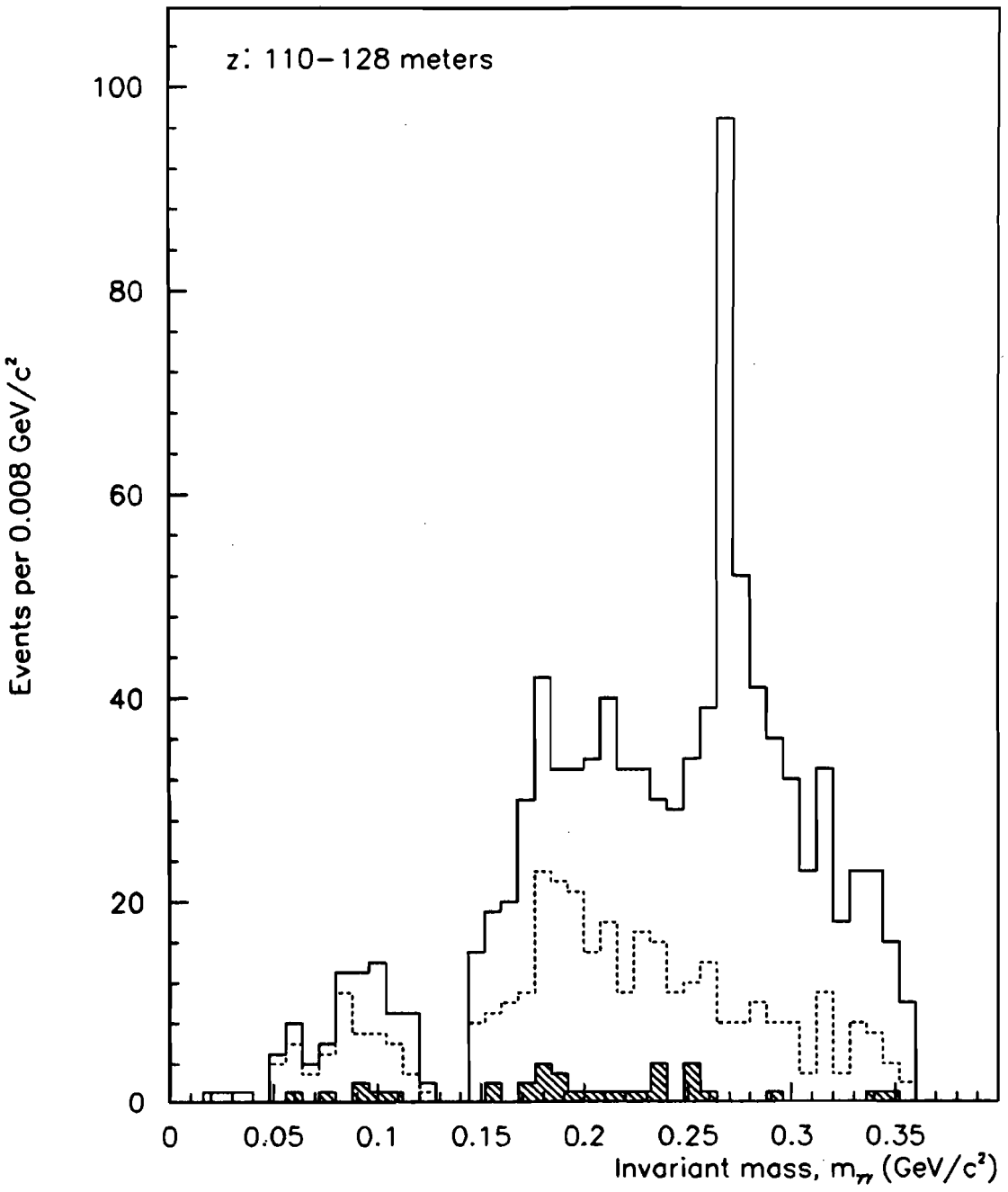

Figure 124. $\gamma\gamma$ invariant mass after all cuts from $K_L \rightarrow 3\pi^0$ background Monte Carlo events. The shaded histogram represents events with two missing photons, the area under the dashed histogram represents events with one and two missing photons and the left over area under the solid line corresponds to events with no missing photons.

TABLE 18. Percentages of events with zero, one and two missing photons in different $m_{\gamma\gamma}$ regions from $K_L \rightarrow 3\pi^0$ background Monte Carlo.

z: 110-128 m		
type of event	$0 < m_{\gamma\gamma} < 0.400$ GeV	$m_{\gamma\gamma} > 0.300$ GeV
no missing γs	62.9%	73.8%
one missing γ	33.5%	25%
two missing γs	3.6%	1.2%

events in each category.

One can try to study more the category i) mentioned above: there are three different topologies that we will examine here. In the first one our pairing algorithm picks the correct π^0 most of the time and in the other two it cannot identify the true π^0:

a) In the first topology two π^0s are superimposed, with each photon from one π^0 overlapping with a photon from the other π^0 as illustrated in Figure 51. In this case the unfused photons belong to the same π^0 and our algorithm of forming m_{π^0} and $m_{\gamma\gamma}$ finds the correct π^0 pairing about 90% of the time.

b) In Figure 125 is illustrated a case with two fused clusters where the unfused clusters belong to two different π^0s.

c) One can also have three photons from different π^0s to overlap at the same cluster as illustrated in Figure 126.

In cases b) and c) even if the algorithm forms m_{π^0} by clusters containing photons that belong to a true π^0, at least one of these clusters is fused. In Figure 127 is shown the $m_{\gamma\gamma}$ spectrum for all six photons at the calorimeter. The diagonally shaded histogram corresponds to category c). The horizontally shaded histogram corresponds to the sum of categories b) and c) and that part of a) for which we identify the wrong π^0 and the left over unshaded part corresponds to that part of category a) for which the correct

π^0 is found.

Since the majority of the events in our signal region contains fused clusters it is good to know their characteristics so that they can be reduced in a future experiment. The distance between fused photons after all cuts is shown in Figure 128. The peak of the distribution is at ~3 cm which is our limit of telling clusters apart. Illumination of the photons belonging to fused clusters at the calorimeter is shown in Figure 129. What is plotted is the distance of the projected positions of the photons from the center of the array and every cluster has two entries. In a) enter photons from events with one or two fused clusters and in b) enter photons from events with two

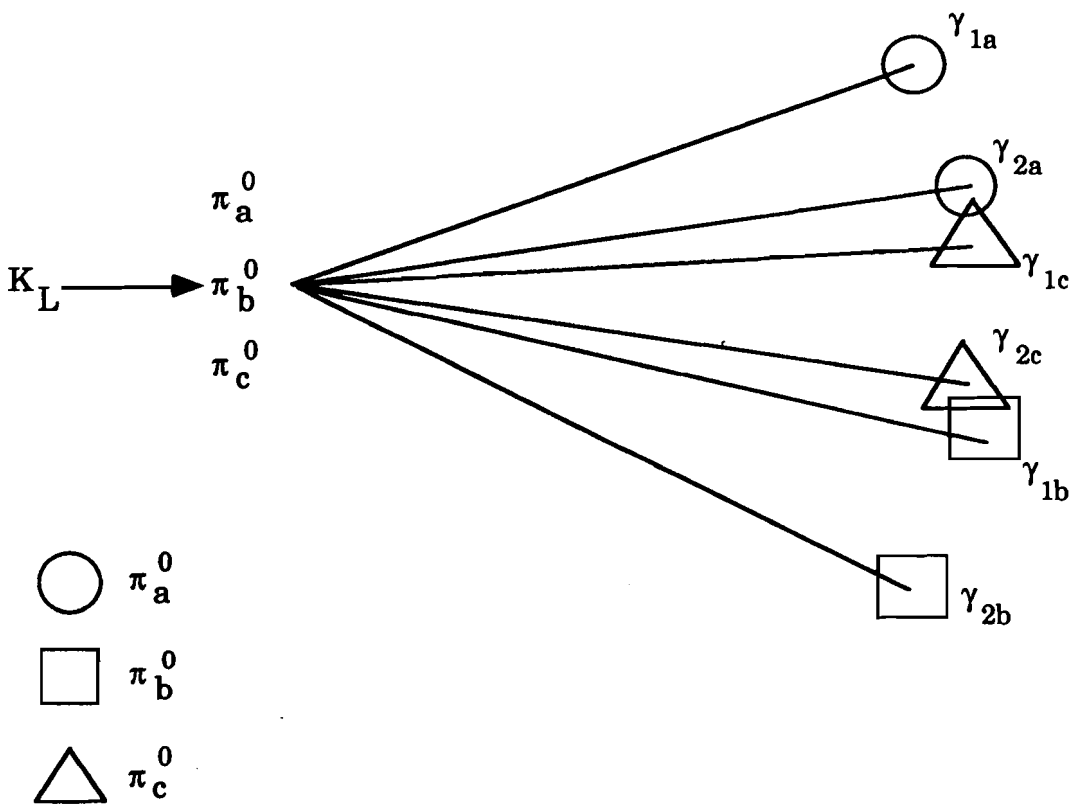

Figure 125. Illustration of a $3\pi^0$ background event with two fused clusters. The unfused clusters belong to two different π^0s.

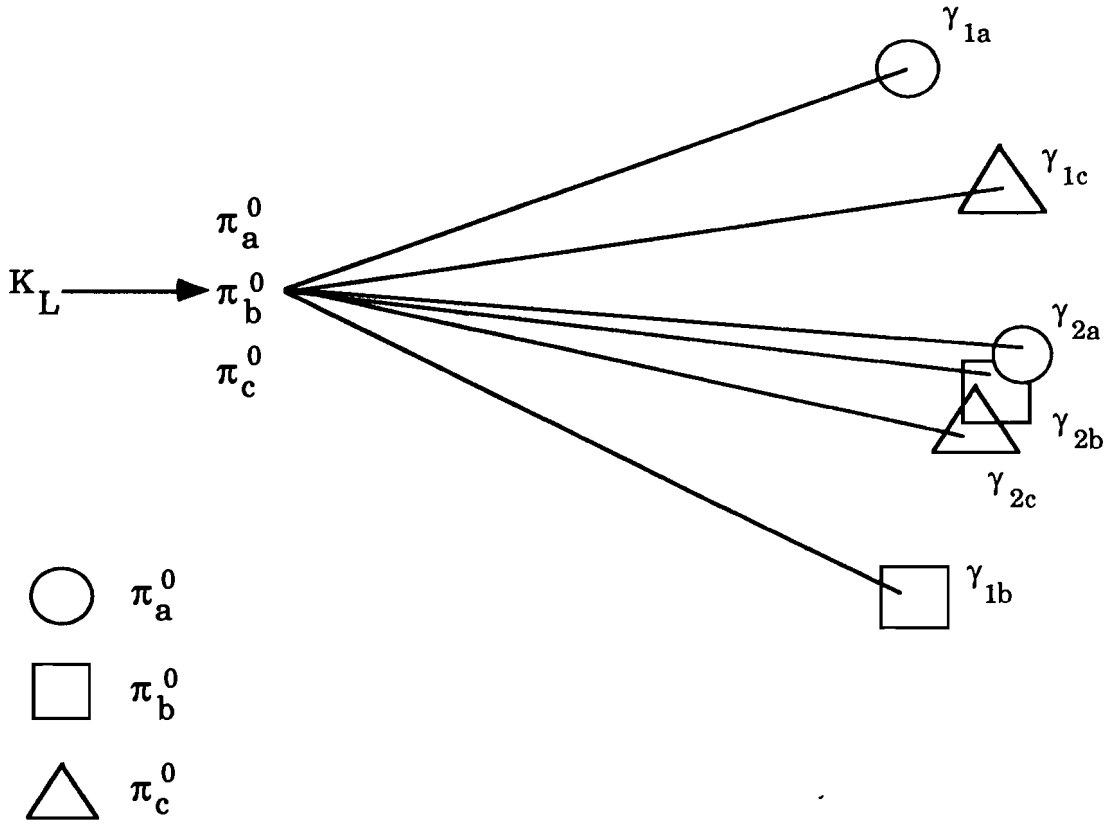

Figure 126. Illustration of three photons overlapping in a single cluster in a $3\pi^0$ background event.

fused clusters. When the event has two fused clusters in a) enter photons belonging to the cluster that is closer to the center of the array and in b) enter photons belonging to the cluster that is further away. Looking at Figure 129a one can realize that in order to reduce fusions substantially one would need a higher resolution calorimeter or a kind of preconverter for the photons that would cover an area of 1 m x 1 m around the center of the lead glass array. It looks like that if fusions can be identified within this area they can be reduced by about 93%.

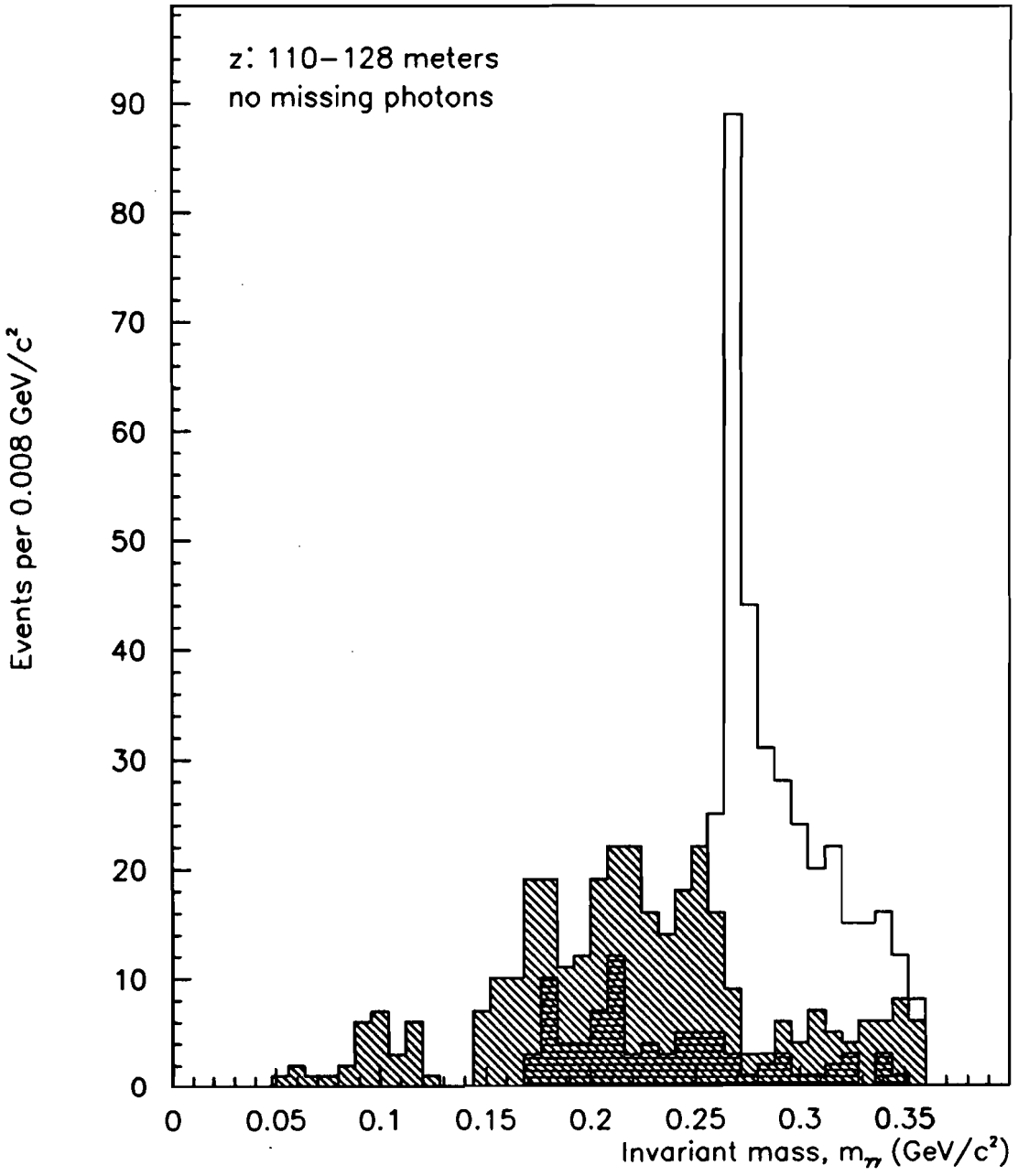

Figure 127. $\gamma\gamma$ invariant mass after all cuts from $K_L \rightarrow 3\pi^0$ background Monte Carlo events with no missing photons. The horizontally shaded histogram represents the subset of these events involving a cluster with three overlapping photons; the diagonally shaded histogram represents events with two fused clusters and the wrong selection for the π^0.

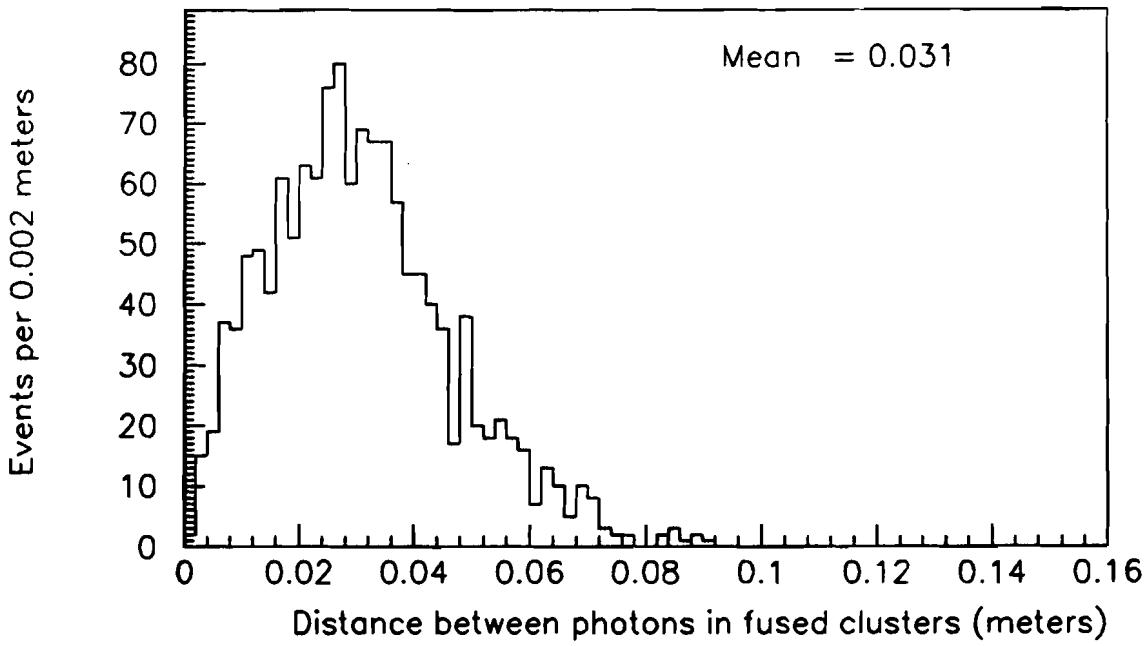

Figure 128. Distance between photons in fused clusters from $3\pi^0$ background decays after all the $\pi^0\gamma\gamma$ analysis cuts.

7.3.1.2 Data-Monte Carlo comparisons

Since the candidate $\pi^0\gamma\gamma$ events are almost completely dominated by $3\pi^0$ background it is helpful to demonstrate at this point the matching between $\pi^0\gamma\gamma$ candidates and $3\pi^0$ background at some of the fusion variables for which we have applied cuts as described in chapter 6. In Figures 130 and 131 are presented overlays of the variable "maxsum" and in Figure 132 are presented overlays of the variable "valmax" at low and high energies. Finally in Figure 133 is shown the overlay of the variable "cmin". These overlays have been done by using area normalization. The hard cuts in the distributions are due to the fact that some of the fusion cuts had been applied at the generation of the Monte Carlo. One can notice the much better agreement of "maxsum" here in comparison with Figures 112 and 113. This means that the data-Monte Carlo agreement is good for fused

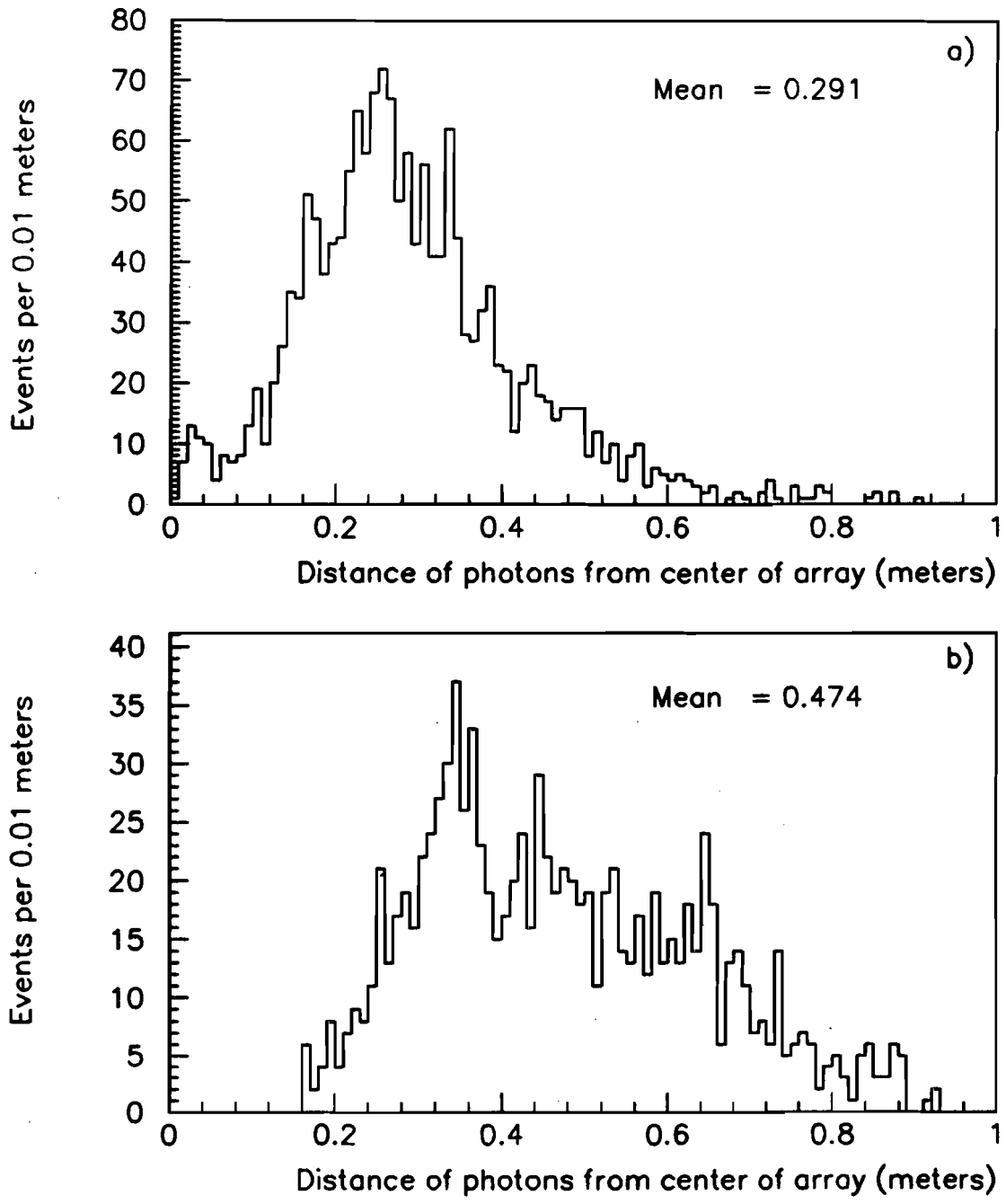

Figure 129. Illumination of photons that belong to fused clusters at the lead glass array from $3\pi^0$ background decays after all the $\pi^0\gamma\gamma$ analysis cuts. For events with two fused clusters a) corresponds to the cluster closer to the center of the array; b) corresponds to the further away cluster.

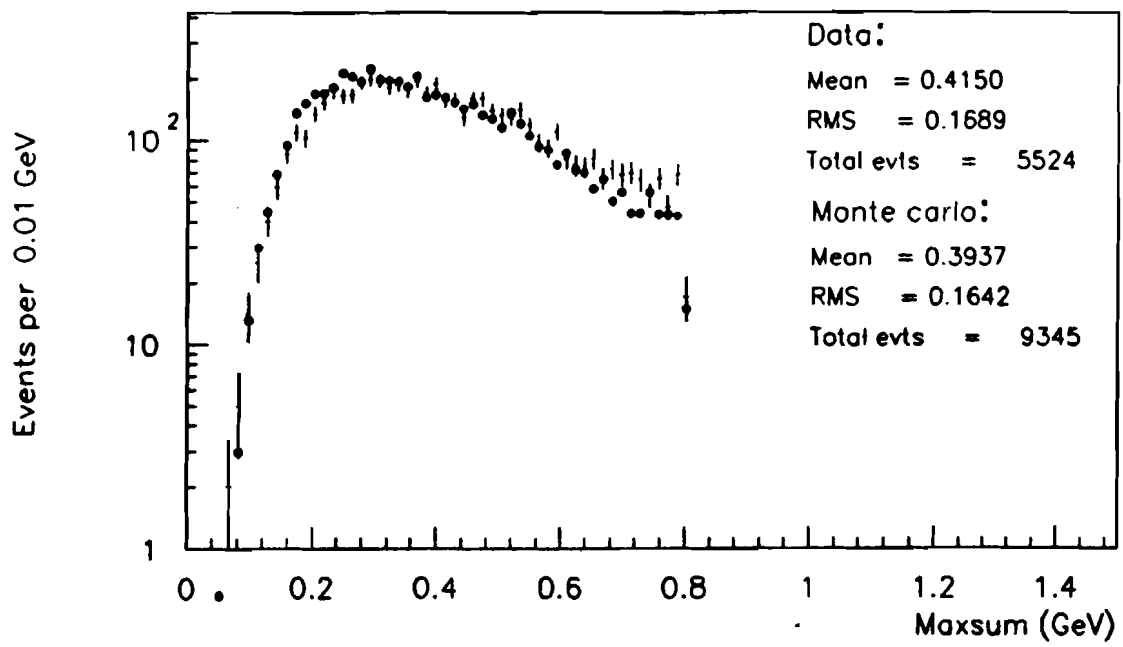

Figure 130. Data-Monte Carlo comparison between $K_L \rightarrow \pi^0\gamma\gamma$ candidates and $3\pi^0$ background events for the maximum energy, "maxsum", in two consecutive blocks of the 16 block ring surrounding the cluster. The error bars represent the data and the solid circles the Monte Carlo.

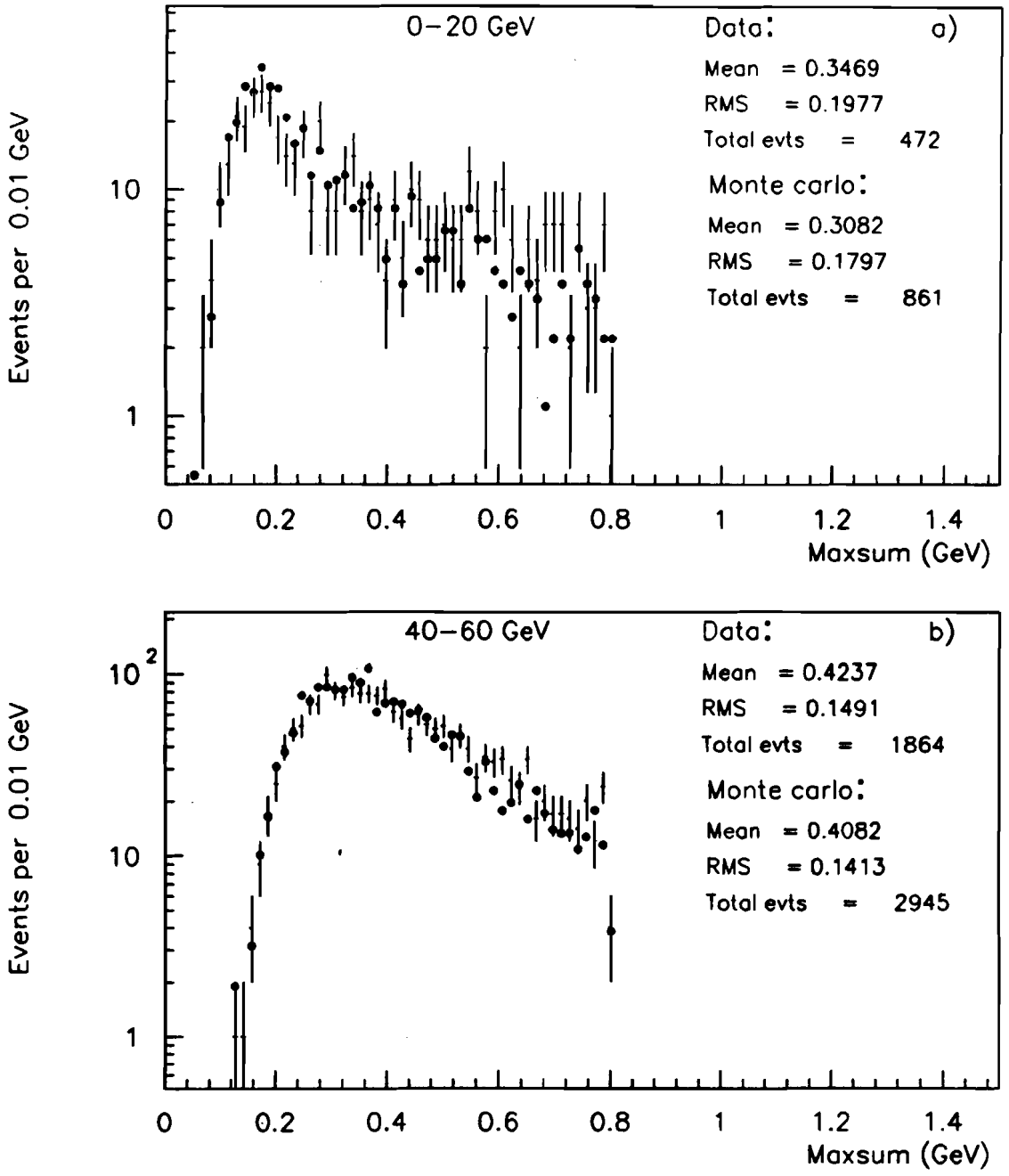

Figure 131. Data-Monte Carlo comparison for "maxsum" between $K_L \rightarrow \pi^0\gamma\gamma$ candidates and $3\pi^0$ background Monte Carlo for certain cluster energy range. a) the cluster energy is in the range 0-20 GeV; b) the cluster energy is in the range 40-60 GeV. The error bars represent the data and the solid circles the Monte Carlo.

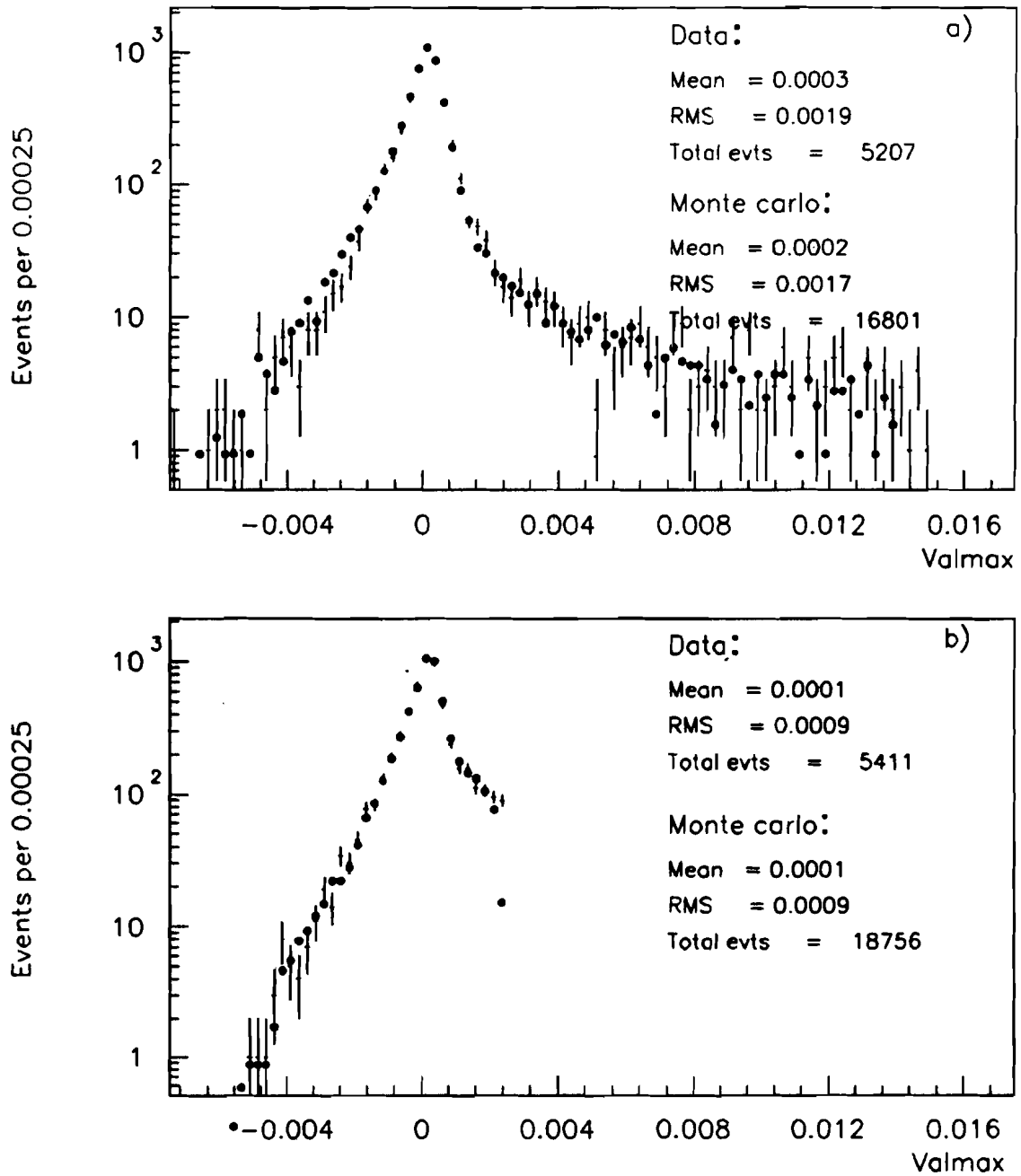

Figure 132. Data-Monte Carlo comparison for "valmax", as explained in the text, between $K_L \rightarrow \pi^0\gamma\gamma$ candidates and $3\pi^0$ background Monte Carlo.

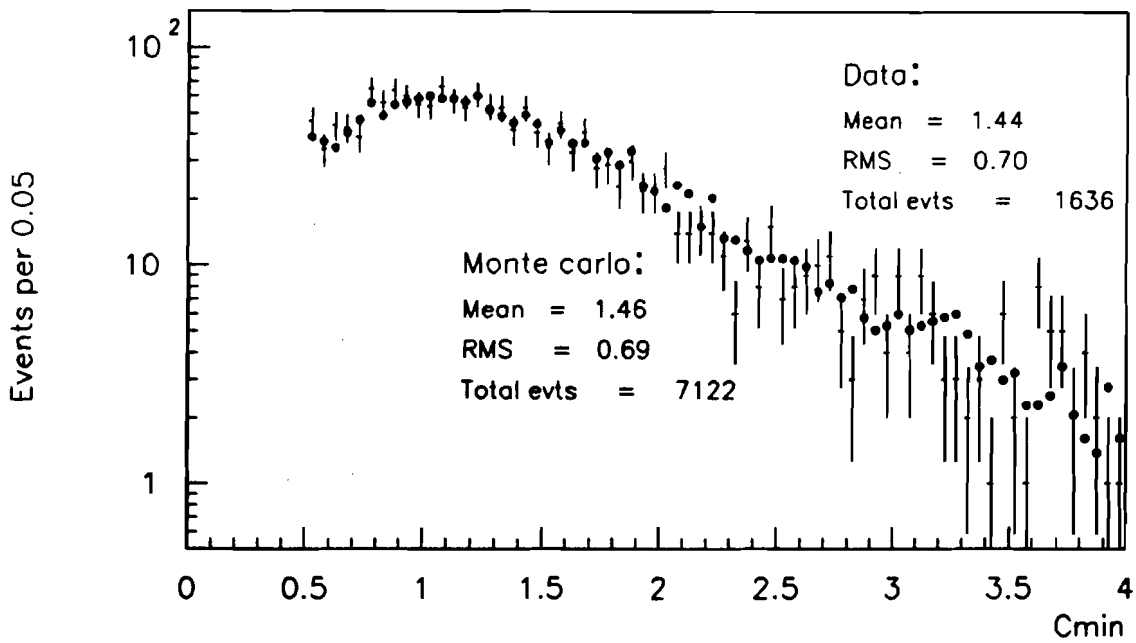

Figure 133. Data-Monte Carlo comparison between $K_L \rightarrow \pi^0\gamma\gamma$ candidates and $3\pi^0$ background Monte Carlo for the minimum ratio of the energy of a side block to the energy of a corner block among all corner blocks of a cluster.

clusters although it is less satisfactory for single clusters. The agreement is good and gives us confidence about our cluster simulation. The simulation of the variable 9/25, which was described in Chapter 6, by the $3\pi^0$ background Monte Carlo is also good and is illustrated in Figure 134.

It is useful to show at this point our understanding of the $3\pi^0$ background under the $K_L \rightarrow 2\pi^0$ mass peak which is demonstrated in Figure 135. The normalization is absolute and it shows that our prediction of the $3\pi^0$ background is very good. Some disagreement at the high masses is due to non $3\pi^0$ background coming from two π^0s produced inelastically at the HDRA. This is a fairly flat background and actually slightly higher at low masses. It is seen more prominently at high masses because there the $3\pi^0$

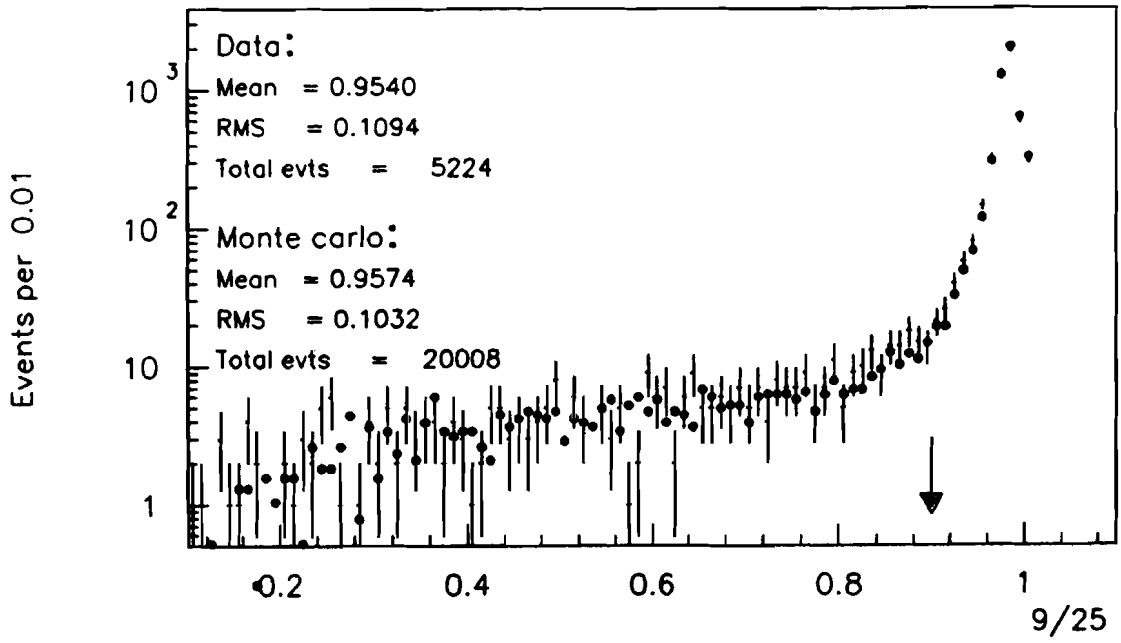

Figure 134. Data-Monte Carlo comparison between $K_L \rightarrow \pi^0\gamma\gamma$ candidates and $3\pi^0$ background Monte Carlo for the variable 9/25.

background is falling down.

7.3.1.3 Optimazation of the z decay distribution for $\pi^0\gamma\gamma$

As mentioned already in Chapter 6 the choice of the downstream end of the decay region was done on the basis of the Monte Carlo. The $\pi^0\gamma\gamma$ analysis program has been run on the standard $3\pi^0$ background and $2\pi^0$ background Monte Carlos and it has been assumed that the events passing the cuts are $\pi^0\gamma\gamma$ data candidates. Namely, it has been assumed that we completely understand the background with the $3\pi^0$ and $2\pi^0$ background Monte Carlo. Using the acceptance of $\pi^0\gamma\gamma$ signal for the events passing the cuts and using the number of $K_L \rightarrow 2\pi^0$ decays in the 20% of the data as well as their acceptance, a 90% cl. upper limit has been derived which is plotted as a function of the end of the decay region considered in Figure 136. We

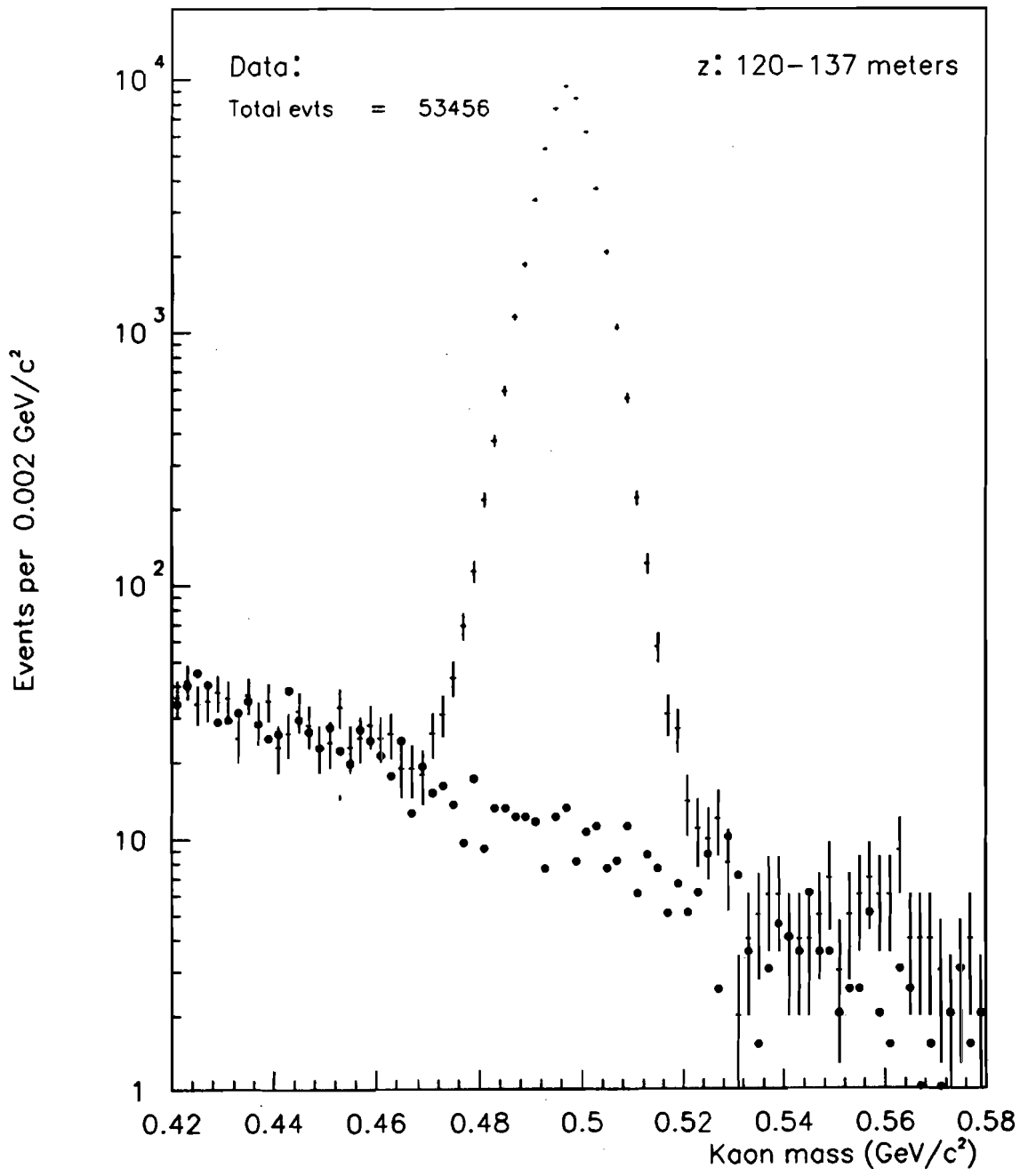

Figure 135. The four photon invariant mass distribution for $K_L \rightarrow 2\pi^0$ events. The histogram is data; the solid circles are from the Monte Carlo simulation for the residual $K_L \rightarrow 3\pi^0$ background, absolutely normalized. The arrows indicate the positions of the cuts.

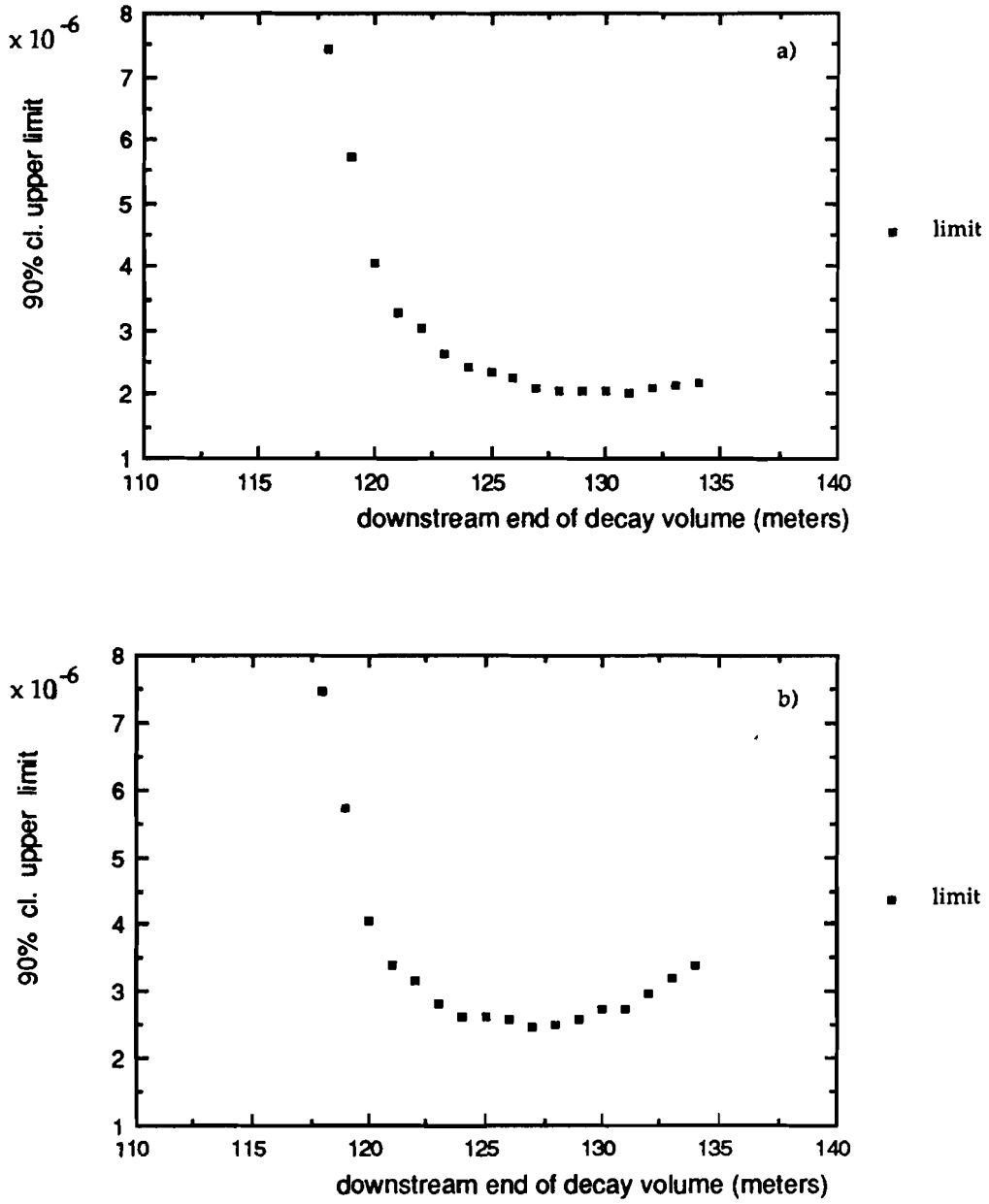

Figure 136. 90% c.l. upper limit based on $3\pi^0$ and $2\pi^0$ background. a) only statistical error included; b) systematic error of 15% has been added.

want to point out again that no $\pi^0\gamma\gamma$ candidate data have been involved in the derivation of this upper limit. In Figure 136a only the statistical fluctuations have been considered for the calculation of the limit. Adding a systematic error of 15% to the understanding of the background, independent of the z decay vertex, the upper limit was derived again and it is plotted in Figure 136b. The limit gets worse now when we include the most downstream bins because the dominant error in those bins is the systematic error. Based on these two figures it was decided that 128 m is a reasonable choice for the end of the decay region.

7.3.2 Complimentary $3\pi^0$ background Monte Carlos

Three additional $3\pi^0$ background Monte Carlo generations were performed to answer three specific questions. The first one was concerning with the effect of the vetoes on the prediction of the background, the second with the how far upstream one would have to start generating $3\pi^0$s in order to have them reconstructed in our decay region and the third with the effect of the photon penetration probability through the Mask on the prediction of the background. To answer the first question we generated $3\pi^0$ background Monte Carlo between 100-140 m from the target, with kaon energy between 35 and 220 GeV, without applying the 8 photon veto cuts mentioned in section 7.3.1.1, having the lead Mask out of the veto and not vetoing any events hitting the SA. Using this Monte Carlo we could study the events we normally reject in the standard Monte Carlo. Analyzing this sample we present in Figures 137-139, after all $\pi^0\gamma\gamma$ analysis cuts except from photon veto cuts and in the decay region 110-134 m the z decay vertex distribution of events that have at least one of their 6 photons missing because either it hits SA, or it projects outside the lead Mask (AM), or it hits AM or some other veto as indicated in the figures. We realize from these plots that the upstream vetoes like SA and AM are responsible for rejecting photons both upstream and downstream while the most downstream counters affect mostly the downstream decay region. It is also interesting to notice at this

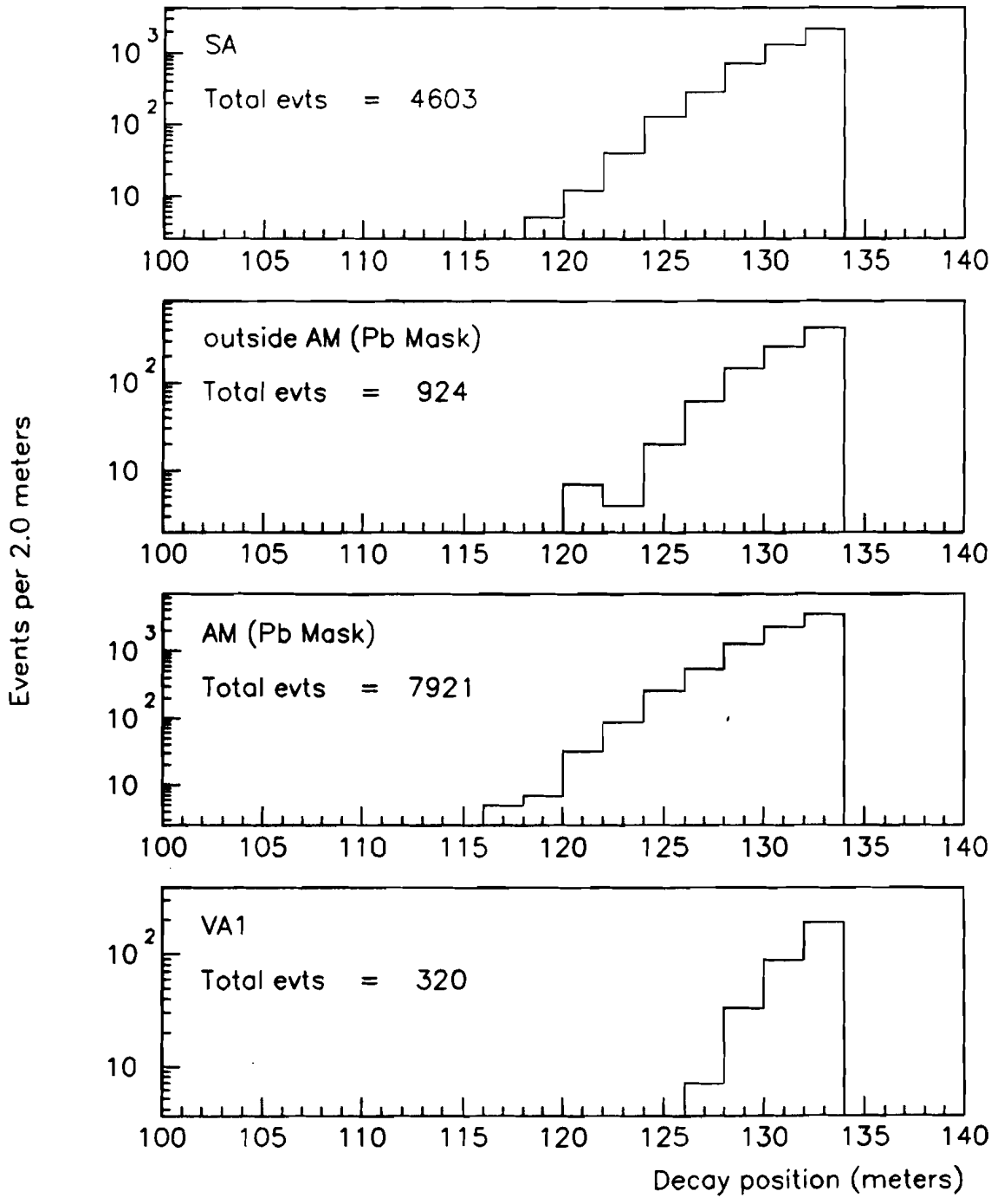

Figure 137. z decay vertex distribution for events with at least one photon hitting the SA, outside the lead Mask, the lead Mask and VA1.

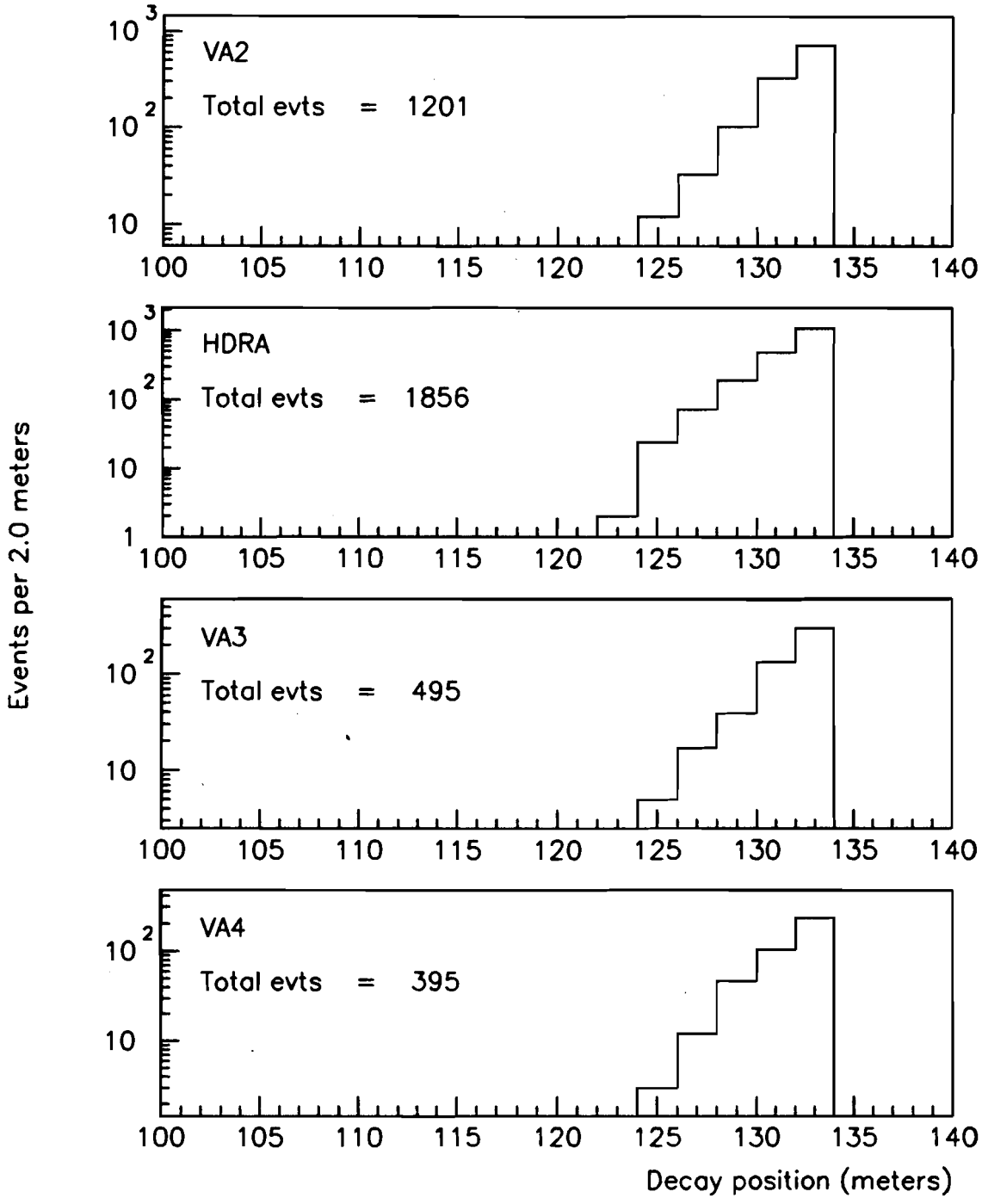

Figure 138. z decay vertex distribution for events with at least one photon hitting the VA2, the HDRA, VA3 and VA4.

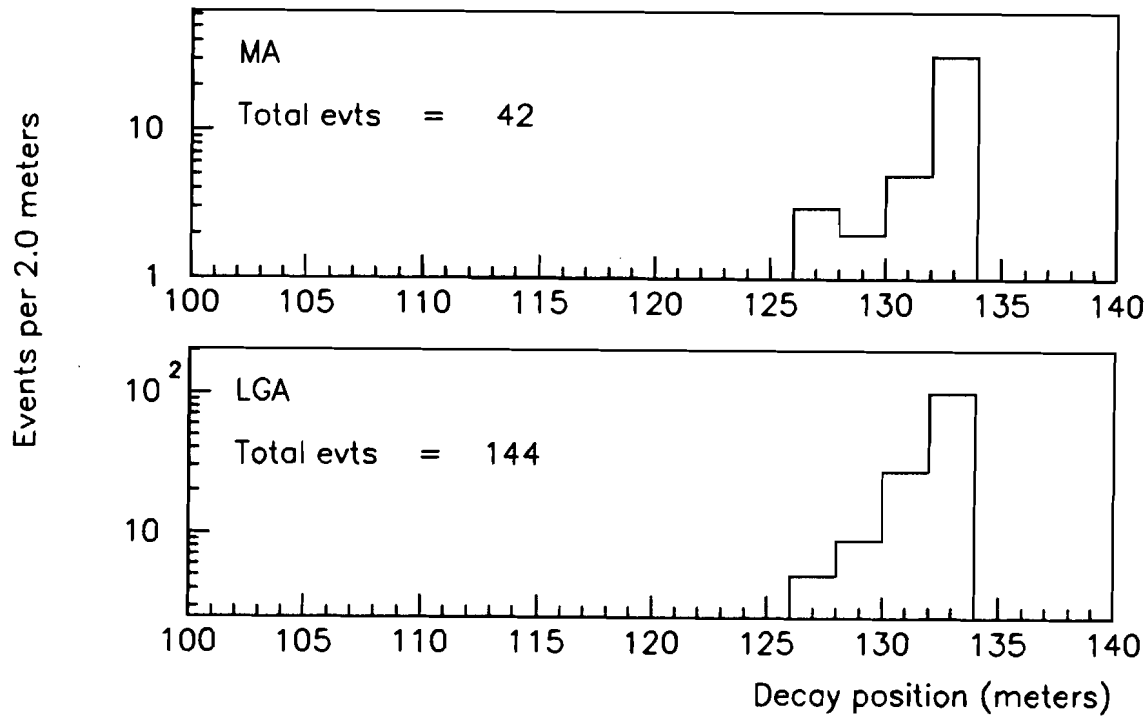

Figure 139. z decay vertex distribution for events with at least one photon hitting MA and LGA.

point that the $\gamma\gamma$ mass distribution of these events has a prominent peak centered at slightly different locations as it is illustrated in Figures 140-142. The peak is caused by the fact that the two photons selected to form the $\gamma\gamma$ mass belong to the same π^0 in the $3\pi^0$ decay. This happens usually when we have two photons escaping from two different π^0's and the other two photons belonging to those two π^0's are selected by our algorithm to form m_{π^0}. The π^0 left which is selected to form $m_{\gamma\gamma}$ has its mass shifted away from $m_{n\pi^0}$ because the z decay vertex is calculated wrong due to the missing energy.

This special Monte Carlo was also used to test the effect of loosening or

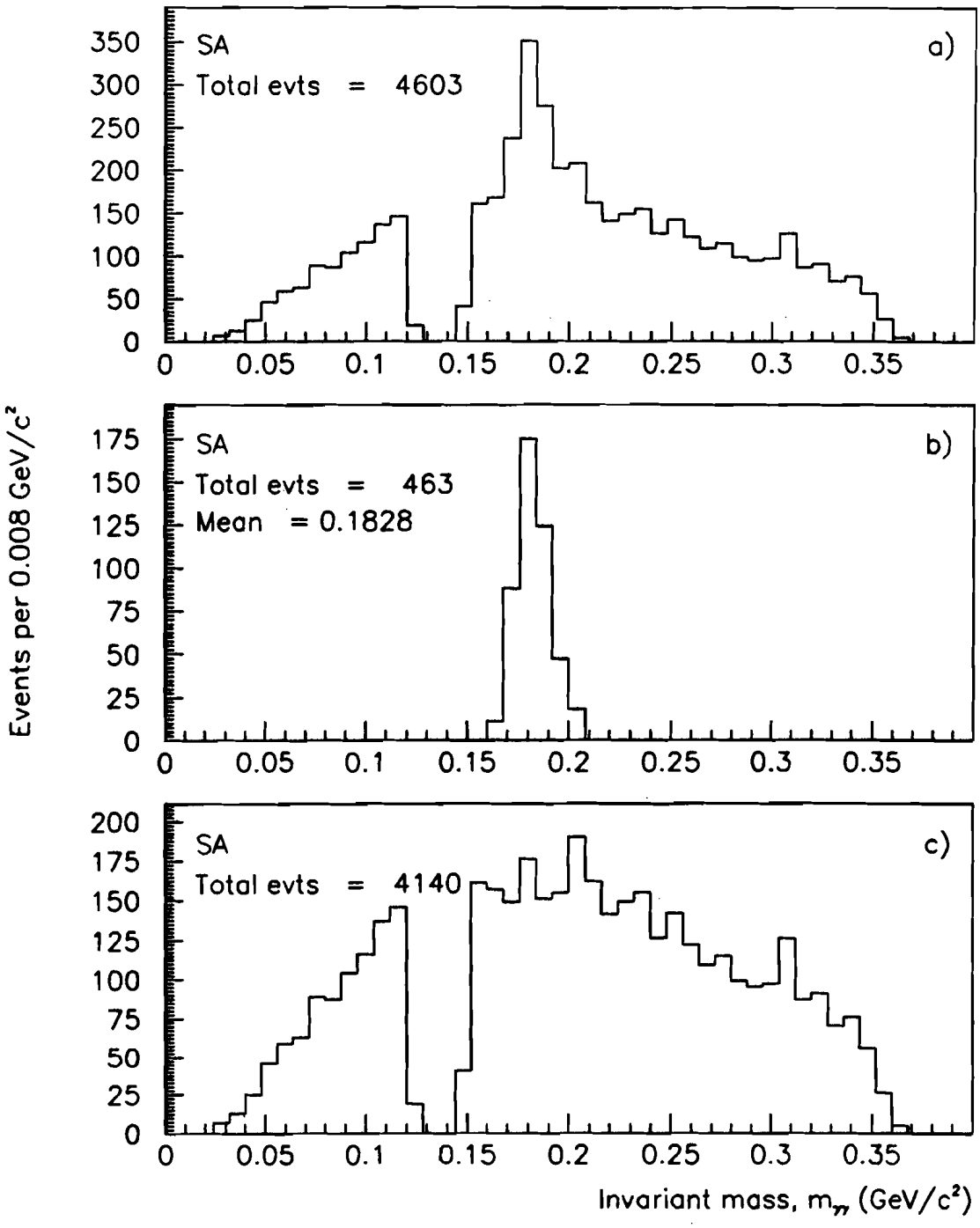

Figure 140. $\gamma\gamma$ invariant mass distribution for $K_L \rightarrow 3\pi^0$ background Monte Carlo events with at least one photon hitting the SA veto system. b) corresponds to a subset of this distribution with the $\gamma\gamma$ pair originating from the same π^0 while c) corresponds to $\gamma\gamma$ not originating from the same π^0.

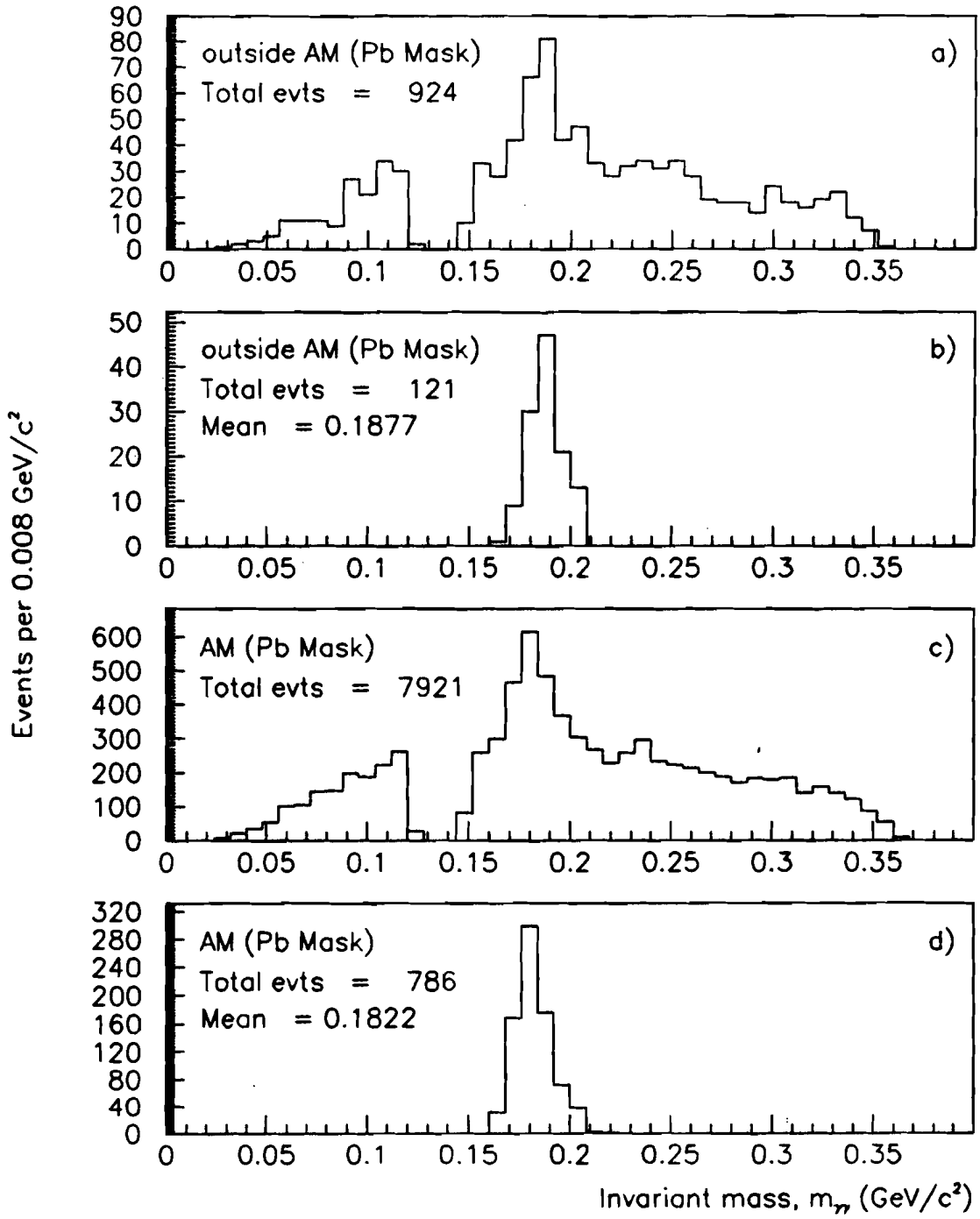

Figure 141. $\gamma\gamma$ **mass distribution for events with at least one photon hitting outside the lead Mask and the lead Mask. b) and d) correspond to** $\gamma\gamma$ **originating from the same** π^0.

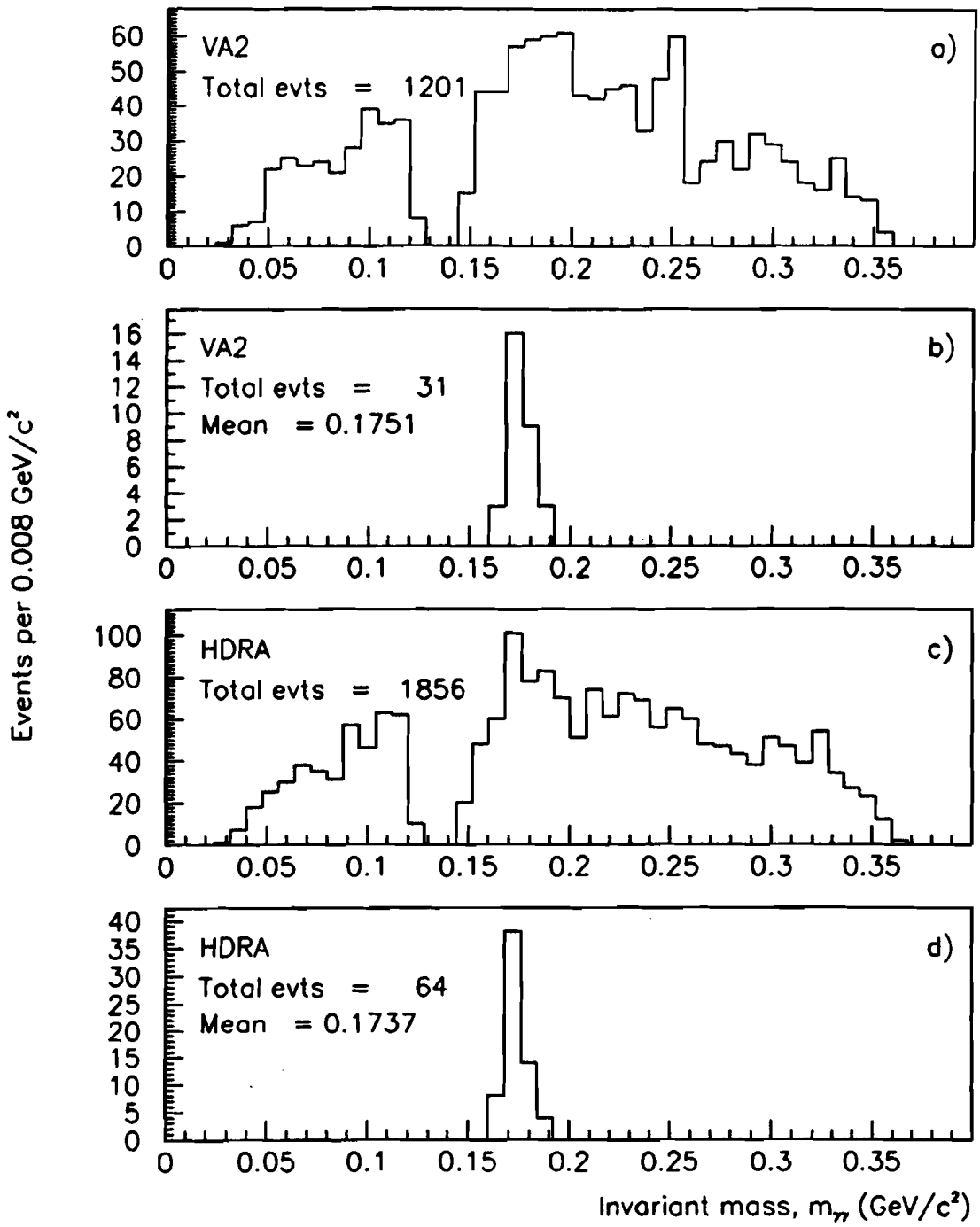

Figure 142. $\gamma\gamma$ mass distribution for events with at least one photon hitting VA2 and the HDRA. b) and d) correspond to $\gamma\gamma$ originating from the same π^0.

tightening the photon cuts or changing the photon veto resolutions in the prediction of the background as will be mentioned in the next chapter.

In order to answer the second question we generated $3\pi^0$s only upstream of 100 m. By studying in the existing standard Monte Carlo the relationship between generated energies and generated z distributions as shown in Figure 143, we were guided to generate only high energies. In this special Monte Carlo that needed about 63 hours of CPU we generated a number of events equivalent to 2.3 times of the 20% of our data; the 67% of the generated events were in the region 50-100 m from the target and their energy was between 90-500 GeV; the 16.6% of the events was generated between 70-100 m from the target and the same energy region as above. Finally the 16.4% was generated between 50-100 m and 100-500 GeV. PA, RA, AM which are the three important apertures for upstream decays were out of the veto for this generation. Also none of the 8 photon veto cuts mentioned above were applied at the generation stage. BA and CA were in veto with thresholds at 5 GeV and 10 μ respectively. The relationship

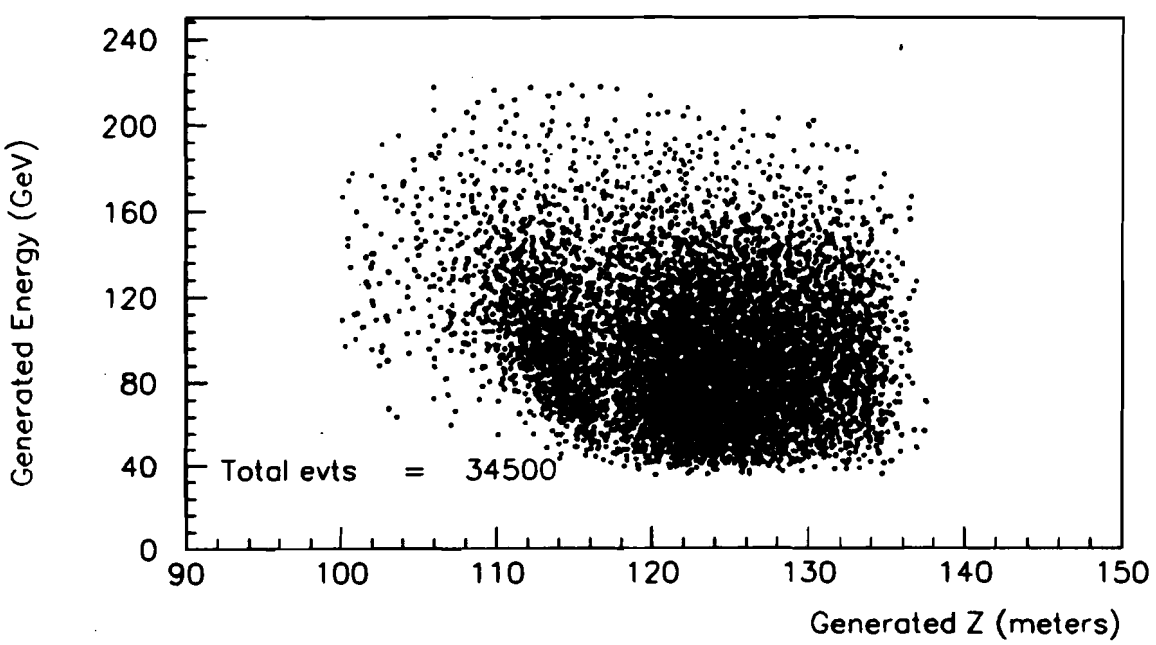

Figure 143. Generated z decay vertex versus generated energy for $K_L \rightarrow 3\pi^0$ background Monte Carlo events.

between the generated energy and z position of the events is shown in Figure 144a at the same stage as the events in Figure 143 that is after the important veto cuts have been required. Also the relationship between their generated and reconstructed z position is shown in Figure 144b. From these 27 events that correspond to 2.3 times the data only two events survived all cuts: the one was generated at 99.9 m with energy 115.0 GeV and reconstructs at 129.3 m with $m_{\gamma\gamma}$ 268 MeV; the second was generated at 99.7 m with energy 124.9 GeV and reconstructs at 133.5 m with $m_{\gamma\gamma}$ 240 MeV. On the basis of this study it is realized that the fact that the generation started at 100 m in the standard $3\pi^0$ background Monte Carlo is not going to affect in any important way our estimation of the number of expected $3\pi^0$ background events.

The answer to the third question has been already given in section 6.5.

7.4 Data-Monte Carlo comparisons for $\pi^0\gamma\gamma$ candidates

In Chapters 5 and 6 we presented in detail the algorithm and the various analysis cuts used for the reconstruction of the $\pi^0\gamma\gamma$ decay and in Figures 85, 91 and 92 we presented a z decay vertex distribution and the final $\gamma\gamma$ mass distribution. Now after studying the $3\pi^0$ and $2\pi^0$ backgrounds we are in a position to compare those distributions with Monte Carlo. In Figure 145 we present Data-Monte Carlo overlays with absolute normalization of z decay vertex distributions for three different regions of the $\gamma\gamma$ invariant mass. In the first plot we consider the mass region above 300 MeV for which we are also going to derive the upper limit. In the second plot we consider the mass region between 264 and 280 MeV which is dominated by "double fusions" and its understanding gives us confidence about our fusion simulation. Finally in the third plot we present the same distribution for the whole mass region which is very sensitive to the understanding of the photon vetoes. In Figure 146 we show an overlay of

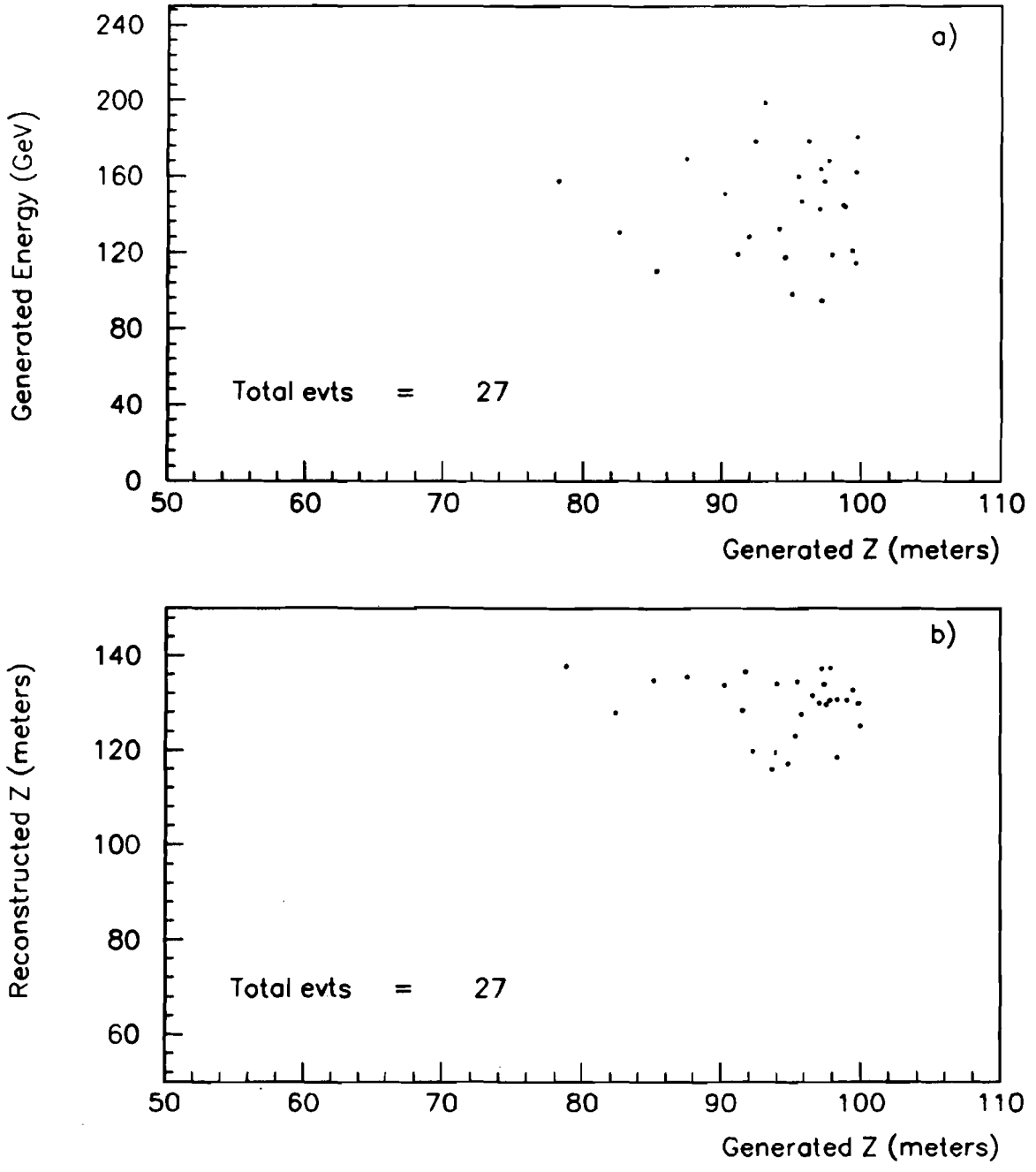

Figure 144. Generated z decay vertex versus a) generated energy and b) reconstructed z decay vertex from $3\pi^0$ background Monte Carlo.

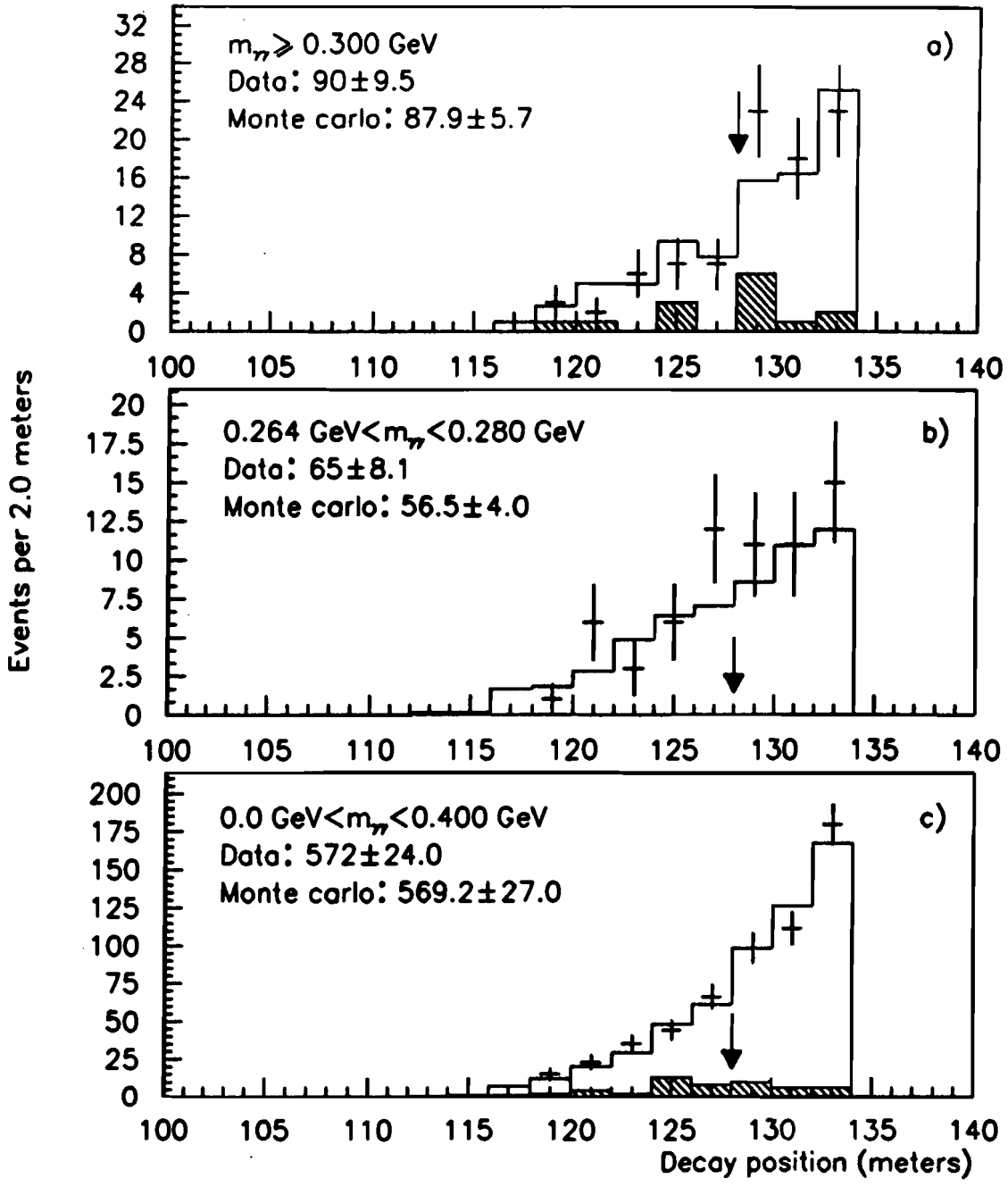

Figure 145. Data-Monte Carlo comparison for the z decay vertex distribution for $\pi^0\gamma\gamma$ candidates and background events from the 20% of the data. The error bars correspond to the data, the shaded histogram to the $2\pi^0$ background prediction and the solid line to the sum of the $3\pi^0$ and $2\pi^0$ background predictions. The normalization is absolute. The arrow indicates the position of the cut.

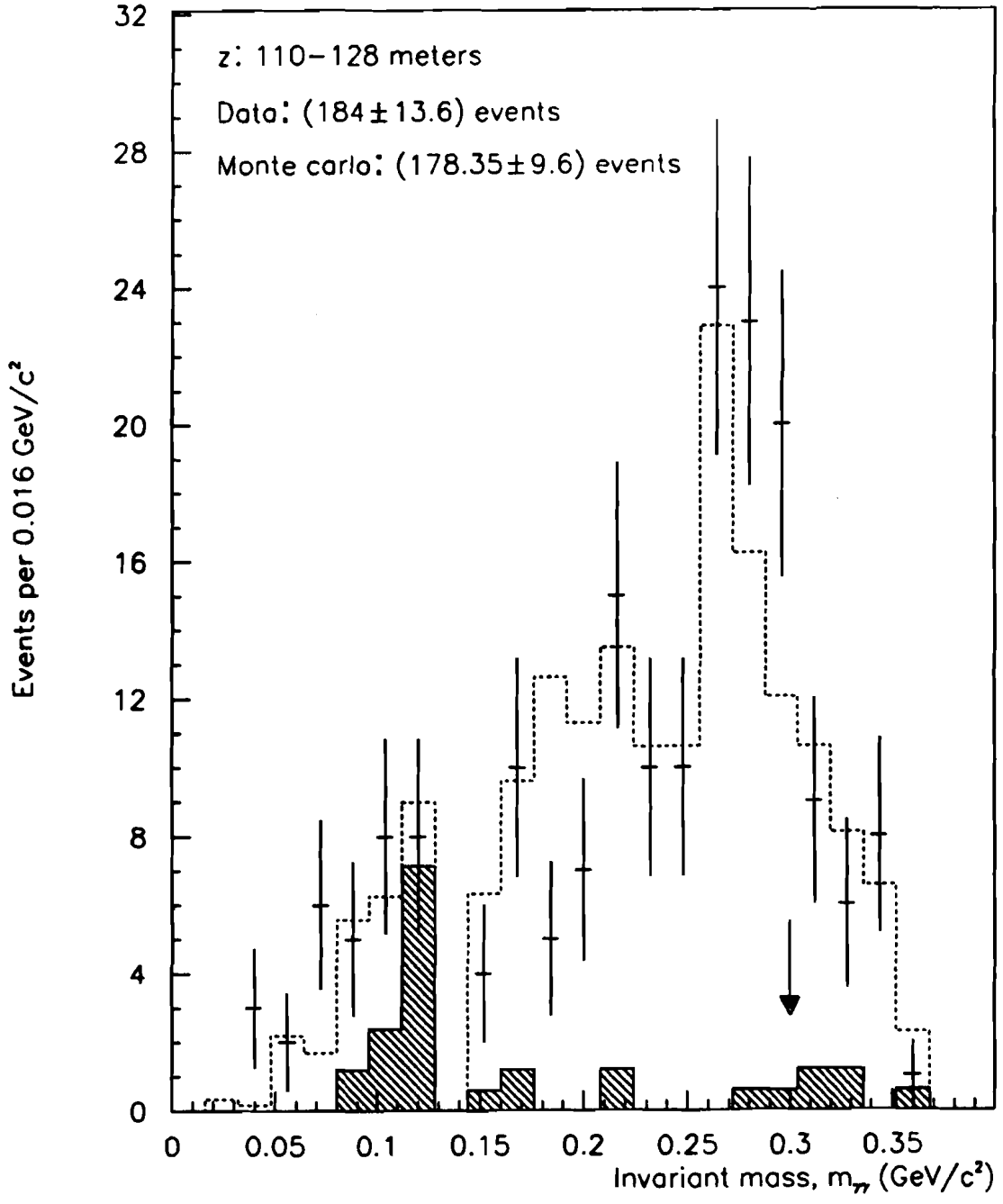

Figure 146. Data-Monte Carlo comparison for the $\gamma\gamma$ mass distribution for $\pi^0\gamma\gamma$ candidates and background events from the 20% of the data. The error bars correspond to the data, the shaded histogram to the $2\pi^0$ background prediction and the dashed histogram to the sum of the $3\pi^0$ and $2\pi^0$ background predictions. The normalization is absolute. The arrow indicates the position of the cut.

the final $\gamma\gamma$ mass for the considered decay region of 110-128 m again with absolute normalization. One can notice that the mass region on the left of the "double fusion" peak is simulated well by the Monte Carlo within statistics. The excess of Monte Carlo that we see now at around 190 MeV is less prominent when we look at the same overlay for the full data set (see Figure 156). The increase of events in the data at the "double fusion" threshold is also simulated very well by the Monte Carlo. For the extraction of an upper limit in Chapter 9 we are going to use only the $\gamma\gamma$ mass region above 300 MeV and this is indicated in Figure 147 with the arrow. All these plots and also all the plots related with fusion variables in section 7.3.1 have been produced after the photon veto adjustment during which the photon veto cuts in the $3\pi^0$ background analysis were tuned which will be described in detail in the next chapter.

CHAPTER 8

SYSTEMATIC ERROR DETERMINATION

8.1 Overview

The estimation of the systematic error is in general one of the most difficult tasks during a measurement. In this chapter we will attempt to estimate the systematic error for this particular measurement either by refering to information already given in previous chapters or by providing new information. Four sources of systematics are going to be considered: a) systematics due to photon veto uncertainty, b) systematics due to fusion understanding, c) systematics due to energy resolution and d) systematic due to the cut that rejects events with photons projecting outside the lead Mask aperture which was discussed in Chapter 6. Since we are going to present in Chapter 9 two upper limits: one for $m_{\gamma\gamma} \geq 0.300$ GeV assuming the CHPT for the $\pi^0\gamma\gamma$ signal and one for a broader mass region using the phase space hypothesis, we are going to estimate the systematic error in different $\gamma\gamma$ mass regions. We will start with the systematic due to the

photon veto uncertainty but before that we are going to describe in the next section the adjustment that we did to the photon veto cuts in the Monte Carlo as was mentioned in Chapter 7.

8.2 Photon veto adjustment and systematic error

As mentioned already in previous chapters the photon vetoes are very effective in reducing the $3\pi^0$ and accidental related backgrounds in several of the decay modes we are interested in in this experiment. For decay modes like $K_L \rightarrow 2\pi^0$ for which the $3\pi^0$ background under the kaon mass peak is less than 0.5% the detailed understanding of the photon vetoes through Monte Carlo is not that crucial. But for decay modes like $K_L \rightarrow \pi^0\gamma\gamma$ which is completely dominated by $3\pi^0$ background, the understanding of the photon vetoes becomes important. In this section we will first demonstrate our understanding of the data without any adjustment of the photon vetoes, and next we will adjust the photon veto cuts in the Monte Carlo within a reasonable range. Later in the section we will take into account this adjustment in the estimation of the systematic error.

In Figure 147 we present data-Monte Carlo overlays for the z decay vertex distribution for three different $m_{\gamma\gamma}$ regions: a) for $m_{\gamma\gamma} \geq 0.300$ GeV which is the mass region for which we set the upper limit, b) for $0.264 < m_{\gamma\gamma} < 0.280$ GeV, which is the region highly dominated by "double fusions" and c) for the whole mass region after excluding, as usual, $\gamma\gamma$ masses around the nominal π^0 mass. The last region is sensitive to both fusions and photon veto effects. We claim that we understand well, within our statistical uncertainty, regions a) and b), which are highly fusion dominated, even beyond our downstream cut for the decay volume at 128 m. We understand less well though the low $\gamma\gamma$ masses which are included in Figure 147c. The disagreement is prominent at the most

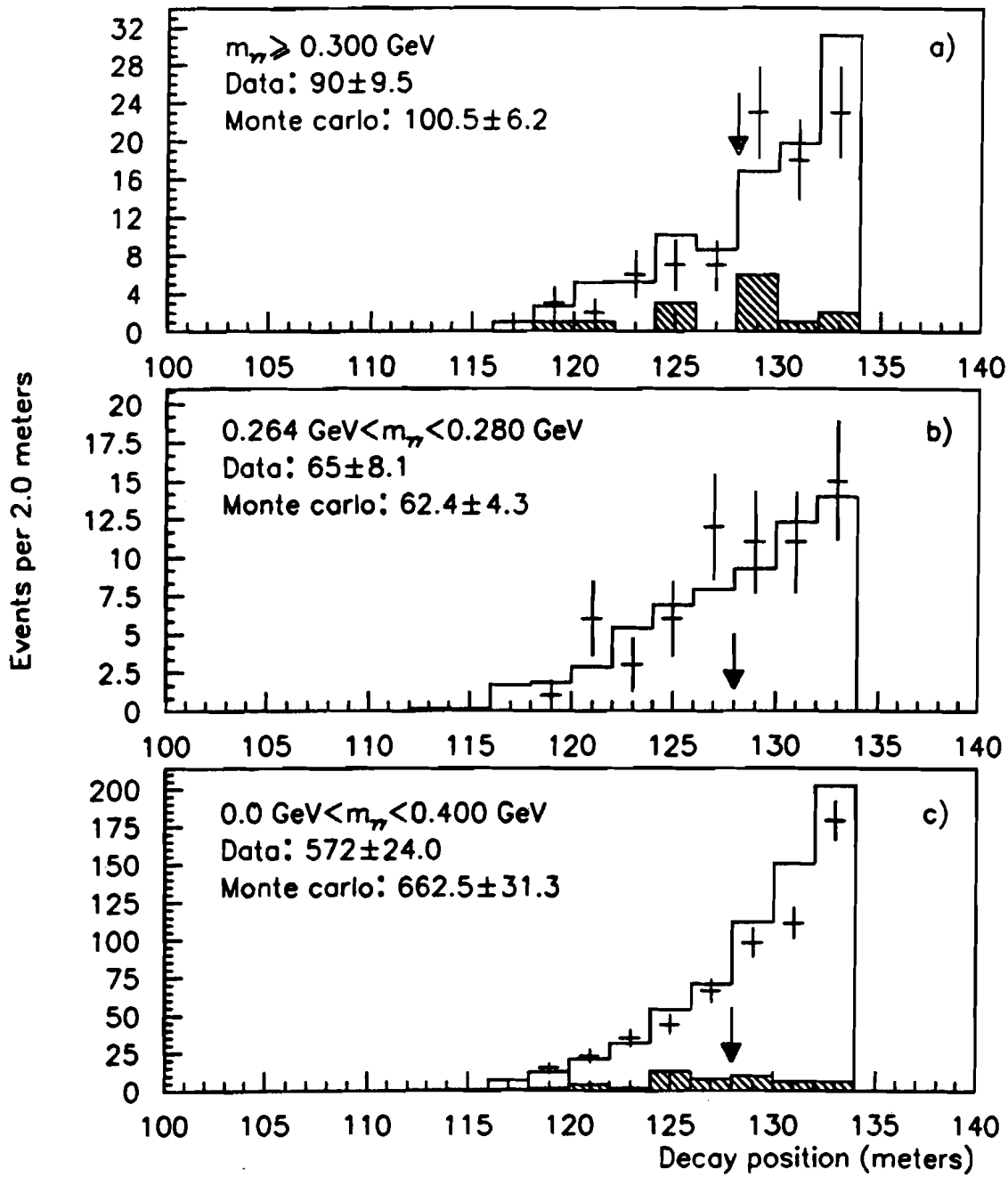

Figure 147. Data-Monte Carlo comparison for the z decay vertex distribution for $\pi^0\gamma\gamma$ candidates and background events from the 20% of the data and before any photon veto adjustment. The normalization is absolute and the arrow indicates the downstream end of the decay region. The shaded histogram corresponds to the $2\pi^0$ background contribution and the solid histogram to the sum of the $2\pi^0$ and $3\pi^0$ backgrounds.

downstream bins which are dominated by events with missing photons. This disagreement is not unexpected because we know that we have 10-20% uncertainty in the photon veto gain determination and 20-40% uncertainty in the photon veto resolution and the combined uncertainty can be quite big. We are therefore allowed to adjust the photon veto cuts in the $3\pi^0$ background Monte Carlo analysis within a reasonable range and we are going to use Figure 147c for this adjustment.

Since the $3\pi^0$ background Monte Carlo predicts more events than the data in the downstream bins of the z decay vertex distribution we can reduce them by tightening those photon veto cuts that can be tightened and that can influence this disagreement. The procedure followed for this adjustment was to tune the veto cuts in the $3\pi^0$ background Monte Carlo analysis until we obtain a good agreement between data and background plus $\pi^0\gamma\gamma$ signal. It is important to say that in this procedure the signal was allowed to vary. First of all we checked which photon vetoes influence the disagreement. We found from Monte Carlo studies that the events that reconstruct between 130-134 m from the target, the bins where the difference between data-Monte Carlo is prominent, have 44% of their missing photons projecting outside the lead Mask, 27% hitting VA1 or VA2, 10.6% projecting outside VA1 or VA2, 7% hitting SA and the rest 10.4% projecting outside the Vacuum window or hitting the HDRA or missing in other places in the detector. As can be seen in Figures 137-139 some of the photon vetoes, like VA1 and VA2, can influence only the downstream region of the z decay vertex distribution while others like AM and SA can influence both the upstream and downstream regions of this distribution. To achieve the desired agreement we chose to tighten the VA1 and VA2 cuts (downstream counters) and the SA cut (upstream counter) and also reject with some random probability events with photons projecting outside the lead Mask. (The lead Mask is also located upstream). We could not change the efficiency of the lead Mask itself because it was assumed 100% efficient in the Monte Carlo generation. We

have to point out though that its efficiency should be close to 100% because as it was mentioned in section 6.5 the probability for a photon to penetrate the Mask without conversion is about 0.1%. Since the tightening of the SA cut and the rejection of photons hitting outside the Mask should have similar effects on the z distribution and also VA1 should have similar effects with VA2 it was decided that the cut of the SA becomes fixed at 60 MeV of photon energy and then one varies both the rejection of photons projecting outside the Mask and the rejection of photons hitting VA1 or VA2 until one gets a good chi-square in the z decay vertex distribution. The choice of rejecting photons that hit SA with energy greater than 60 MeV is reasonable as can be seen from Figure 95. The chi-square just mentioned was formed by using eleven 2 m bins of the z vertex distribution from 112 to 134 m. The signal was included in the fit by using a z vertex distribution for it like the one in Figure 116 normalized properly to a variable branching ratio. The $\pi^0\gamma\gamma$ branching ratio was allowed to vary from 0-5 times the branching ratio predicted by CHPT (6.8×10^{-7}) in units of 0.2 times of itself. In Figures 148 and 149 are shown chi-square distributions as a function of change in rejection efficiency of photons hitting outside the Mask for fixed rejections caused by both VA1 and VA2. The numbers in parentheses close to the solid squares indicate the branching ratio of $\pi^0\gamma\gamma$ signal needed in units of the CHPT branching ratio in order to achieve this chi-square. The fixed rejection efficiencies of VA1 and VA2 in Figures 148 and 149 correspond, as it is also indicated on the figures themselves, to 10%, 20%, 30% and 40% reduction on both the VA1 and VA2 cuts applied on the $3\pi^0$ background sample compared to the ones applied on the data. In Figure 150 are indicated the positions of chi-square minima in a two dimensional plot where in the horizontal axis is measured the change in the rejection efficiency of photons hitting outside the lead Mask and in the vertical axis is measured the additional reduction to the cuts of both VA1 and VA2 in the Monte Carlo relative to the data. Figures 148 and 149 that we showed before are projections along

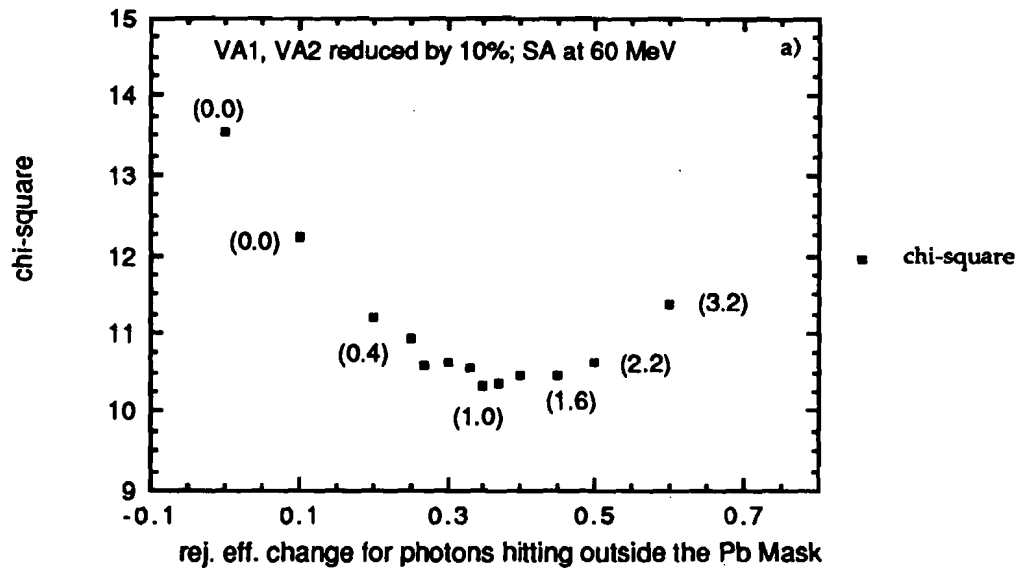

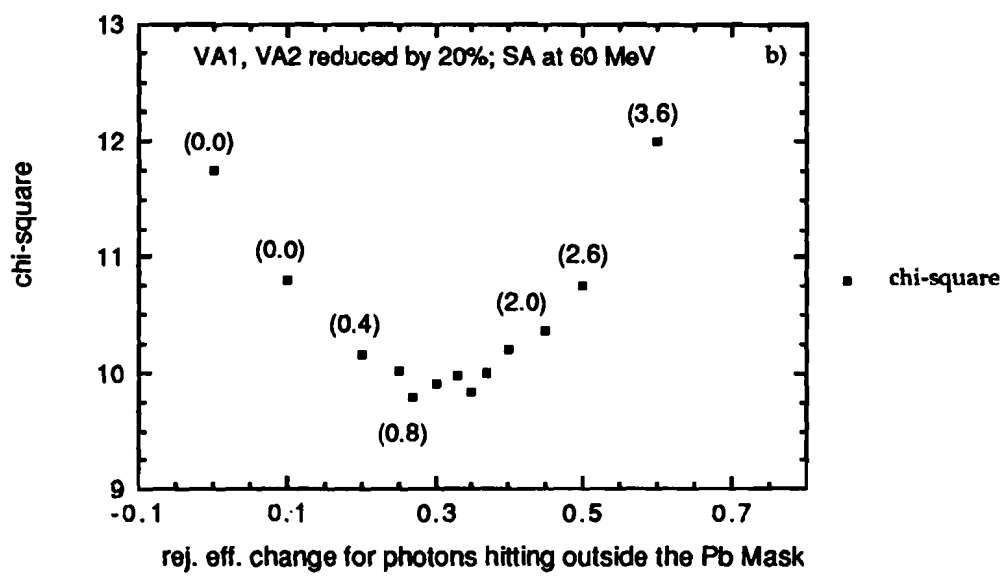

Figure 148. Chi-square for the z vertex distribution as a function of the change of rejection efficiency for photons projecting outside the lead Mask. a) and b) correspond to 10% and 20% reduction respectively to the VA1 and VA2 cuts.

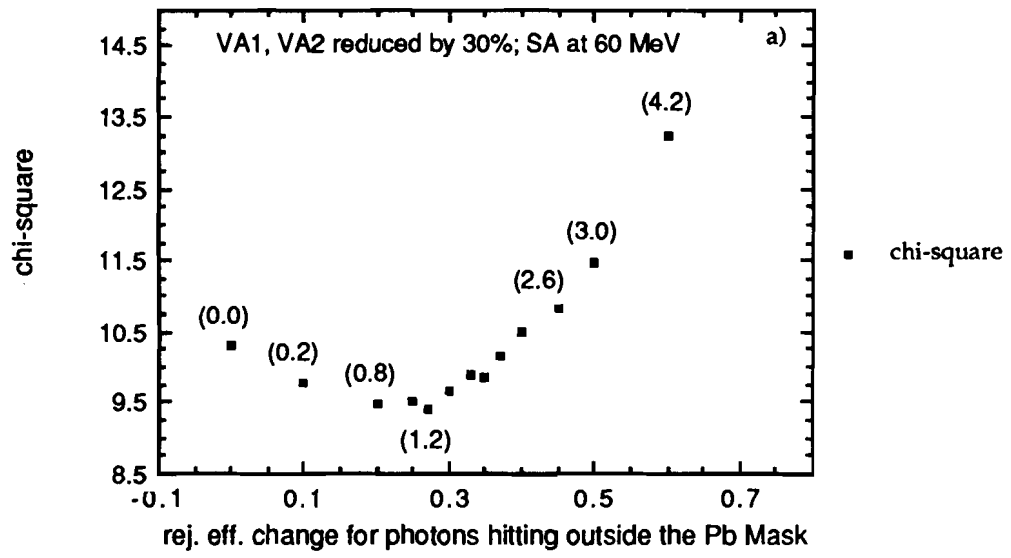

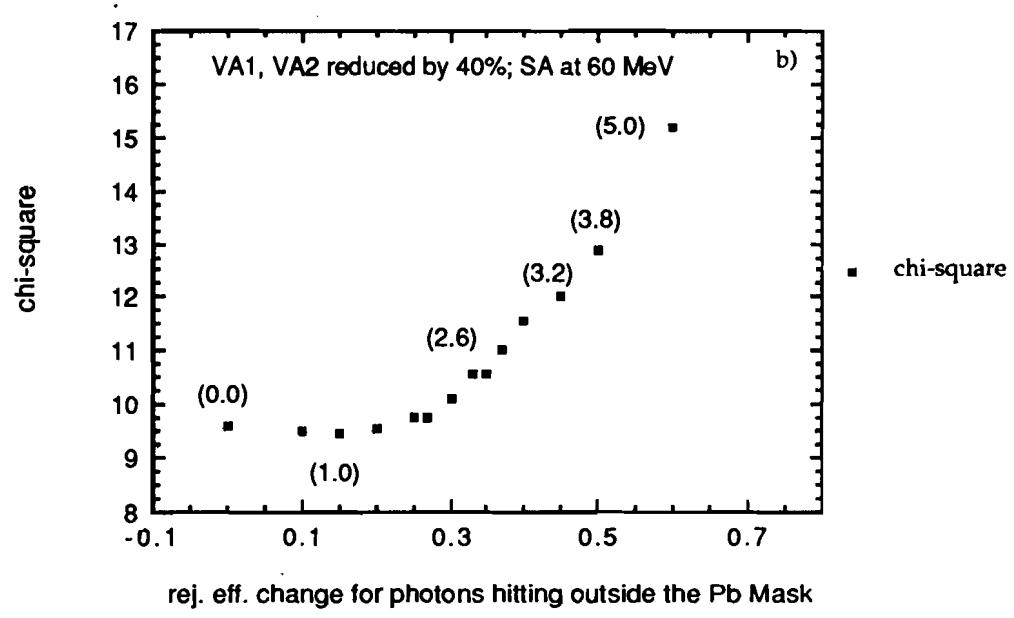

Figure 149. Chi-square for the z vertex distribution as a function of the change of rejection efficiency for photons projecting outside the lead Mask. a) and b) correspond to 30% and 40% reduction respectively to the VA1 and VA2 cuts.

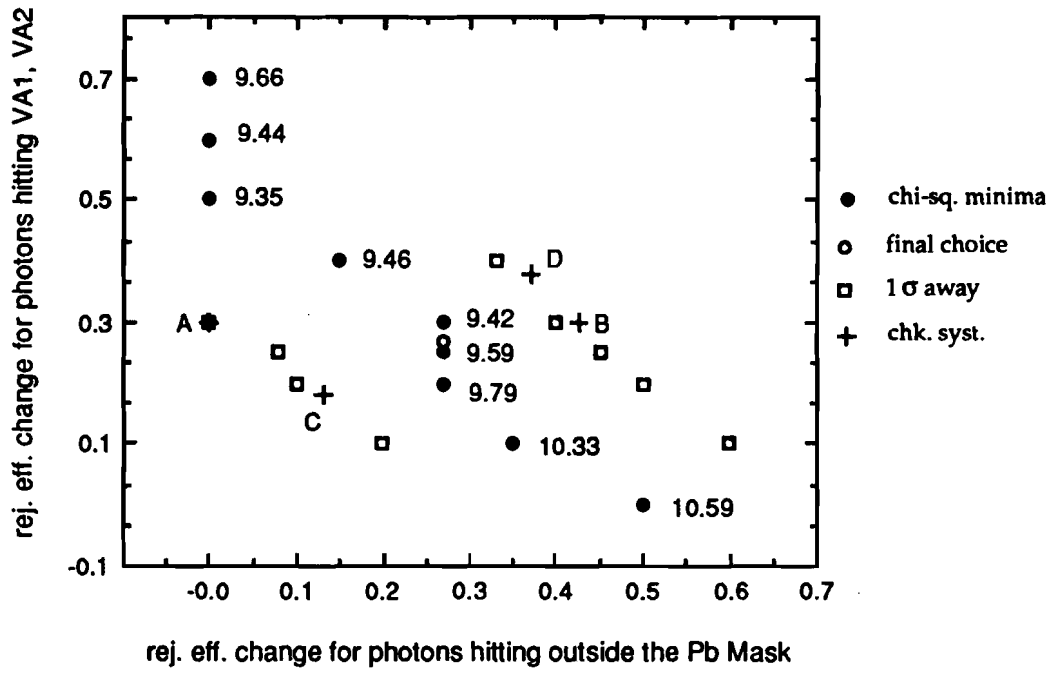

Figure 150. Chi-square minima in the plane of rejection efficiency change of photons projecting outside the lead Mask and rejection efficiency change for the VA1 and VA2 photon vetoes. The squares indicate points with chi-squares about 1σ higher than the minima, the open circle the final choice of our cuts and the "+"s the points across which the systematic was finally calculated.

the vertical axis of Figure 150. The numbers close to the solid circles are the chi-squares at the corresponding minima. The squares on the left and right of each solid circle correspond to chi-square about 1 σ bigger from the one at the circle. The open circle and the "+"s will be explained a little later. In Figure 151 we show the same two dimensional plot but now the numbers indicated next to the points are the number of events in the $3\pi^0$ background Monte Carlo (not normalized to the data) that pass the $\pi^0\gamma\gamma$ analysis cuts and reconstruct in our signal region, that is in the decay region 110-128 m from the target having $\gamma\gamma$ invariant mass at least 0.300 GeV. The number in parentheses next to the first number is a similar number of $3\pi^0$ background events with the only difference that the $\gamma\gamma$ mass reconstructs in a broader region. It reconstructs in the whole mass region after one excludes the area around $m_{n\pi^0}$ and the region 264-280 MeV that is dominated by "double fusions". This is the exact area that we are going to consider for the upper limit on the basis of the phase space hypothesis.

As one can see the variation of the number of events across the solid circles for $m_{\gamma\gamma} \geq 0.300$ GeV is very small, less than 2%, and any choice of change of rejection efficiencies would not affect the final result in any important way. This is so because in this mass region the 74% of the events have no missing photons (see Table 18) and therefore they are not affected by the photon veto cuts. Our final choice of the rejection efficiencies in the $3\pi^0$ background Monte Carlo analysis was chosen to be 27% reduction for the VA1 and VA2 cuts relative to the data and 27% rejection of photons projecting outside the lead Mask, close to a local chi-square minimum in Figure 150 and within our belief of the uncertainty in the photon vetoes. This final choice is indicated by the open circle in the same figure. Since the systematic error that would be introduced by checking the change in the number of background events across the solid circles would be small, we finally calculated the error across points where it can become bigger. The "+"s which are also named A, B, C and D in

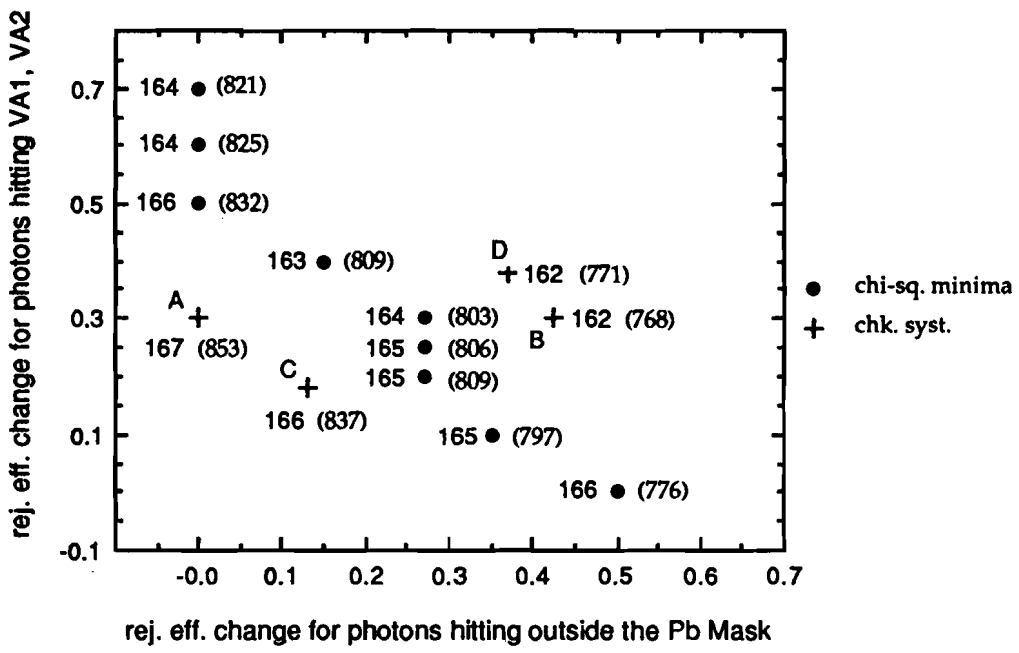

Figure 151. Chi-square minima in the plane of rejection efficiency change of photons projecting outside the lead Mask and rejection efficiency change for the VA1 and VA2 photon vetoes. The "+"s correspond to the points across which the systematic was finally calculated. The numbers next to all the points indicate the number of events for $m_{\gamma\gamma} \geq 0.300$ GeV and the ones in parentheses the corresponding number for a broader mass region.

Figures 150 and 151 correspond to the points across which the final check of the error was done. The difference in the predicted number of $3\pi^0$ background events for $m_{\gamma\gamma} \geq 0.300$ GeV is 2.5% across points C and D for which the chi-square is 10.7 and 10.8 respectively and 3.1% across points A and B for which the chi-square is 10.3 and 10.6 respectively. For the broader mass region the difference in the predicted number of $3\pi^0$ background events is 7.2% across the solid circles, 8.6% across points C and D and 11.1% across points A and B. Therefore the systematic error assigned to our photon veto uncertainty is going to be 3.1% for $m_{\gamma\gamma} \geq 0.300$ GeV and 11.1% for the broader mass region based on this test alone.

Another type of test has been done for the estimation of this systematic in which we used one of the complimentary Monte Carlos mentioned in Chapter 7 to check the effect of the change of photon veto gains and resolutions on the $3\pi^0$ background. In the generation of the Monte Carlo used, AM was not considered in veto and no cuts had been applied for the VAs, MA, LGA, DRAN and SA. For the purposes of the test though, any events with photons hitting SA and having energy at least 100 MeV or hitting AM were vetoed similarly with what is done in the standard $3\pi^0$ background Monte Carlo. The test which will be just explained was done without making any photon veto adjustment and its results are presented in Tables 19 and 20. There were two steps involved and in both we kept the cuts of the VAs, DRAN, MA and LGA at their normal values. In the first step we kept the resolutions of the photon vetoes at the values they normally have in the Monte Carlo and we loosened or tightened the values of the gains of the VAs and DRAN by 10 and 20% observing the effect of this change at the background in the decay region 110-128 m. In the second step the photon veto gains were kept at their normal values but the resolutions of the four VAs and DRAN were all of them increased or decreased by 20% or 35%. The maximum difference observed in the predicted number of $3\pi^0$ background events due to these changes, is 5.3% for $m_{\gamma\gamma} \geq 0.300$ GeV and 5.1% for the whole mass

TABLE 19. Effect of the change of photon veto gains on the $3\pi^0$ background.

change in photon veto gains	number of $3\pi^0$ background events	
	all $m_{\gamma\gamma}$	$m_{\gamma\gamma} \geq 0.300$ GeV
no change	114	19
10% reduction	115	19
20% reduction	115	19
10% increase	115	19
20% increase	114	18

TABLE 20. Effect of the change of photon veto resolutions on the $3\pi^0$ background.

change in photon veto resolutions	number of $3\pi^0$ background events	
	all $m_{\gamma\gamma}$	$m_{\gamma\gamma} \geq 0.300$ GeV
no change	114	19
20% reduction	113	18
30% reduction	113	18
35% reduction	112	18
20% increase	117	19
30% increase	118	19
35% increase	118	19

range. The statistics available for this last test are poor for $m_{\gamma\gamma} \geq 0.300$ GeV and therefore it can only give us a feeling of the range in which the systematic can vary.

The two different ways of looking at the systematic error introduced by the photon vetoes, by either estimating the effect of the change of the photon veto cuts on the background including also the signal in our fit or by observing the background change after independently varying the photon veto gains and resolutions are looking basically at the same gain and resolution effects in two different approaches. The second method can potentially introduce a bigger systematic error because it looks at maximal changes (e.g. all five resolutions or all five gains change by 35%). Using the combination of the two tests and being conservative we think we can assign a 5% systematic due to photon vetoes for $m_{\gamma\gamma} \geq 0.300$ GeV and 12% for the broader mass region.

8.3 Systematic error due to fusions

In order to estimate our understanding of fusions and the corresponding systematic error we chose to examine the agreement between data and Monte Carlo for the $\gamma\gamma$ invariant mass distribution in a region dominated by fusions. Because there is the possibility of a small signal in this data sample one has to be careful to examine a mass range dominated by background and the region selected was basically 0.264-0.280 GeV. This choice was based on the fact that this region is dominated by "double fusions" where the two pions fall on top of each other, and also on the fact that the signal expected there will not disturb the data-Monte Carlo agreement drastically for the following reasons: if the phase space model is correct then the $m_{\gamma\gamma}$ distribution is almost flat and the amount of signal in every bin is almost constant; if the CHPT is correct then in the bins we consider the amount of signal is very small as will be shown in

Tables 21-24. The mass region 0.256-0.264 GeV has been also included in the study as a check of our understanding of the "double fusion" rising step. The check was done with the "double fusion" cut that kinematically rejects the double fusions applied or removed and after the photon veto adjustment. In Figure 152 is shown the agreement between data and Monte Carlo for the $\gamma\gamma$ invariant mass with absolute normalization before and after the fusion cut that rejects kinematically fusions has been applied, and in Tables 21 and 22 we present the results of the check mentioned above. In Table 21 is presented this check for the fusion cut applied and for the decay region 110-128 m in the following form: in the second column are shown the numbers of $K_L \rightarrow \pi^0\gamma\gamma$ data candidates with their uncertainties for different $m_{\gamma\gamma}$ regions, and in the third column are similarly presented the numbers of the predicted $3\pi^0$ and $2\pi^0$ background. Finally in the last column is shown the amount of expected $\pi^0\gamma\gamma$ signal in the corresponding mass bins. In Table 22 the same test is repeated with the "double fusion" cut removed. One can see that the background prediction is statistically consistent with the data in both cases. Using this test and also the agreement between data and Monte Carlo for the z decay vertex distribution of events in the "double fusion" region shown in Figures 145 and 147; using the data-Monte Carlo agreement for the distribution of the distance between clusters shown in Figure 107 and our understanding of the fusion variables demonstrated in Figures 130-133, we conclude that the fusions are understood fairly well and therefore we will not assign a systematic error due to them.

8.4 Systematic error due to energy resolution

This systematic was estimated by changing the energy resolution in the Monte Carlo in both the $K_L \rightarrow 2\pi^0$ signal analysis and the $3\pi^0$ background analysis and checking the effect of this change on the data-

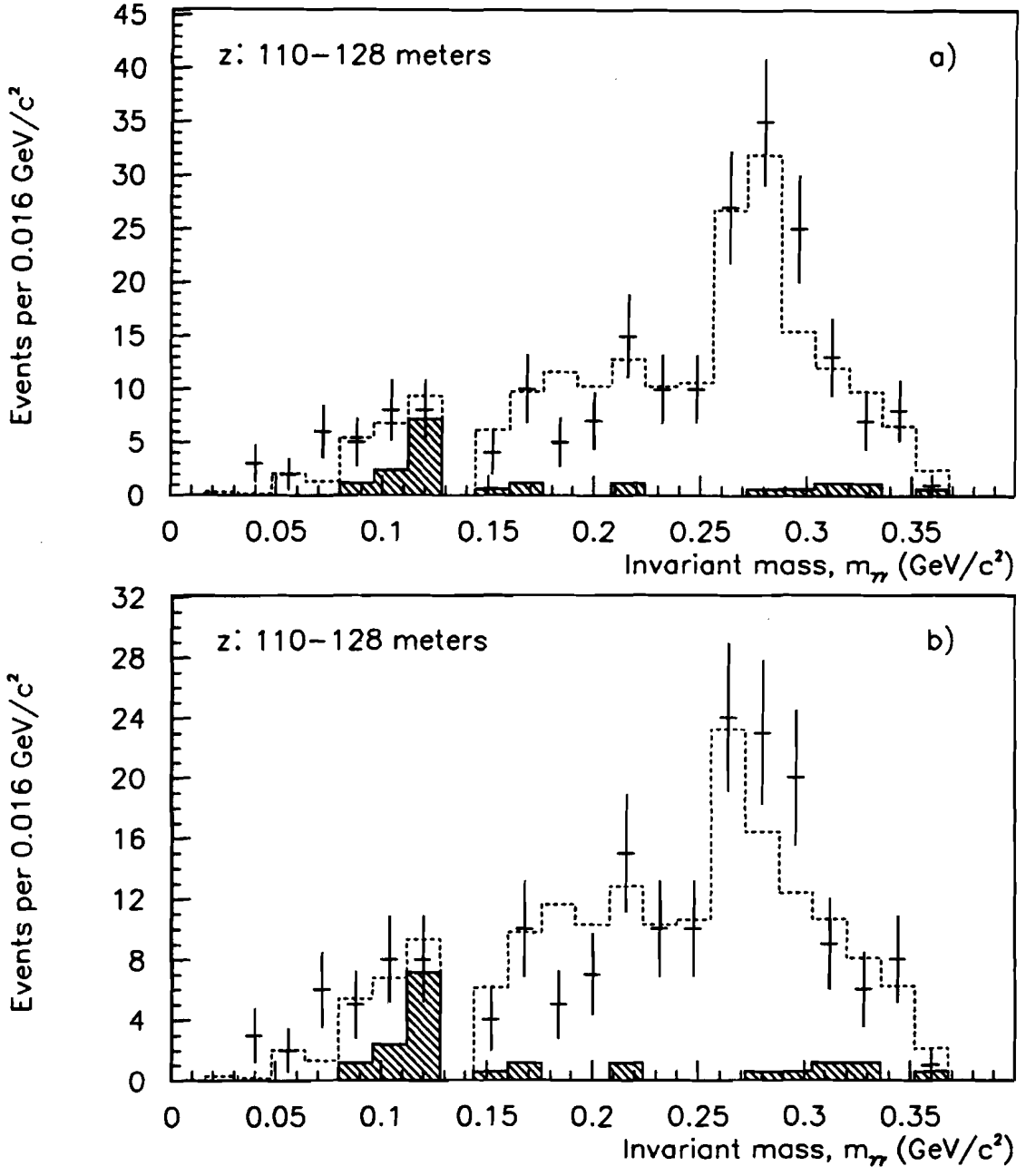

Figure 152. $\gamma\gamma$ invariant mass distribution. The error bars correspond to the data, the shaded histogram to the $2\pi^0$ background and the dashed histogram to the sum of the $2\pi^0$ and $3\pi^0$ backgrounds. a) and b) correspond to the distribution before and after the cut that kinematically rejects the double fusions.

TABLE 21. Data-Monte Carlo comparison for the $\gamma\gamma$ invariant mass distribution in the "double fusion" region. The photon veto adjustment is implemented and the kinematic "double fusion" cut is applied.

Kinematic "double fusion" cut applied

$m_{\gamma\gamma}$ interval	Data	Monte Carlo($3\pi^0$, $2\pi^0$)	Signal(CHPT)
264-280 MeV	28±5.3	25.6±2.4	0.54
256-280 MeV	32±5.7	32.1±2.8	0.67

TABLE 22. Data-Monte Carlo comparison for the $\gamma\gamma$ invariant mass distribution in the "double fusion" region. The photon veto adjustment is implemented and the kinematic "double fusion" cut has been removed.

Kinematic "double fusion" cut not applied

$m_{\gamma\gamma}$ interval	Data	Monte Carlo($3\pi^0$, $2\pi^0$)	Signal(CHPT)
264-280 MeV	38±6.2	39.5±3.2	0.64
256-280 MeV	42±6.5	46.1±3.5	0.77

Monte Carlo agreement for the best χ^2 variable discussed in Chapter 6 and also in the change of the predicted $3\pi^0$ background for the $\pi^0\gamma\gamma$ candidates. The energy in the Monte Carlo is normally smeared by $0.02+\frac{0.06}{\sqrt{E}}$. In this test we kept the mean value of the energy constant and changed the resolution by generating an additional smearing with a combination of two gaussians with widths σ_1 and σ_2 where $\sigma_1=0.005+\frac{0.005}{\sqrt{E}}$ and σ_2 is a multiple of σ_1. The first gaussian which introduces a very small additional smearing (1% for 1 GeV photons and 0.66% for 10 GeV photons) was used 80% of the time and the second gaussian was used 20% of the time during this smearing. As can be seen in Figure 153 the agreement in the best χ^2 variable becomes noticeably worse with these changes. The corresponding effect on the prediction of the $3\pi^0$ background is shown in Tables 23 and 24. The results in Table 23 correspond to smearing of only the non fused clusters in the Monte Carlo for which this smearing has a well defined meaning and which represent 74% of the total number of clusters. The results in Table 24 correspond to the application of the smearing to all clusters. For $m_{\gamma\gamma} \geq 0.300$ GeV and smearing only the non fused clusters the biggest change observed in the background prediction was 5.8%. When all clusters are smeared this maximum difference becomes 2.6%. The changes in the background prediction due to the resolution change are smaller when we consider the whole mass region. In particular they are 2.8% and 1.9% when we smear only the non fused or all the clusters respectively.

On the basis of this test we finally assign as a systematic due to energy resolution 6.0% for $m_{\gamma\gamma} \geq 0.300$ GeV and 3.0% for the broader mass region.

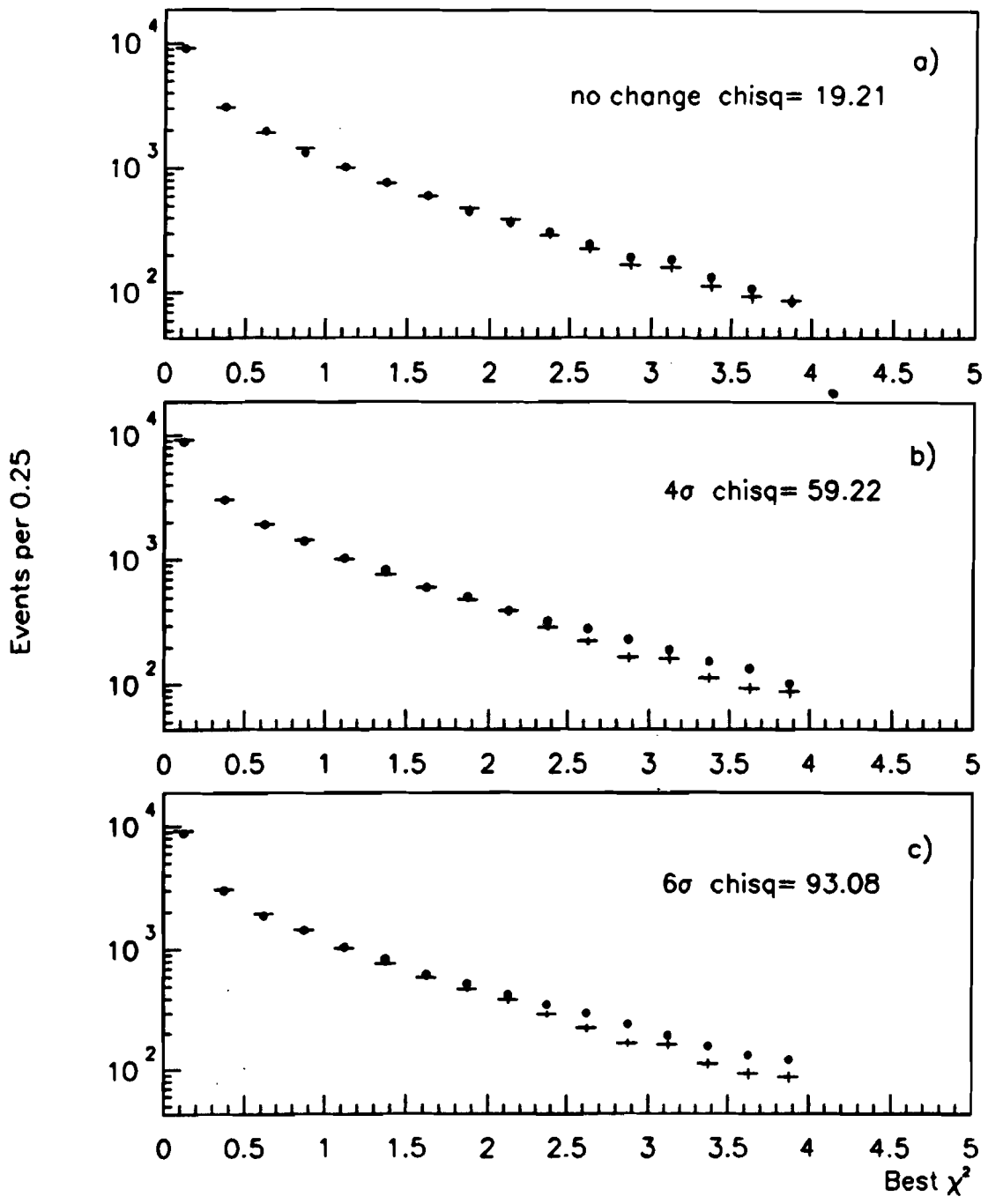

Figure 153. Data-Monte Carlo comparison for the best χ^2 distribution for $K_L \rightarrow 2\pi^0$ decays and for different resolution smearings.

TABLE 23. Effect of the change of the energy resolution in $3\pi^0$ background Monte Carlo. Only non fused clusters are smeared.

non fused clusters smeared		
smearing change	$0 < m_{\gamma\gamma} < 0.400$ GeV	$m_{\gamma\gamma} \geq 0.300$ GeV
no change	899 events	156 events
80% σ_1, 20% $4\sigma_1$	905 events	153 events
80% σ_1, 20% $6\sigma_1$	874 events	147 events

TABLE 24. Effect of the change of the energy resolution in $3\pi^0$ background Monte Carlo. All clusters are smeared.

all clusters smeared		
smearing change	$0 < m_{\gamma\gamma} < 0.400$ GeV	$m_{\gamma\gamma} \geq 0.300$ GeV
no change	899 events	156 events
80% σ_1, 20% $4\sigma_1$	888 events	152 events
80% σ_1, 20% $6\sigma_1$	882 events	154 events

8.5 Systematic error due to the lead Mask cut

In Chapter 6 we mentioned that we rejected events with photons projecting outside the holes of the lead Mask. Although we know that these events are misreconstructed and therefore they have to be rejected we do not know the exact source of this background and therefore we have to account for a systematic error due to them in a very conservative way. Because of the criteria of our rejection, the events rejected by this cut always reconstruct upstream of the Mask. It is conceivable though that the background we are rejecting extends downstream of the Mask too and we have to account for this possibility. We realized by studying the "neutral" trigger data where the cut in question is more effective that the $\gamma\gamma$ invariant mass distribution of the events that get rejected is consistent with being flat. What has been done was to find first the chi- square of the mass distribution as presented in Figure 146 for the 20% of the data or in Figure 158 for the full data set and then add to each mass bin a constant number of events and recalculate the chi-square. Here we consider this test for the full data set, where we have more statistics, but we form the chi-square only for the region 0.0 GeV < $m_{\gamma\gamma}$ < 0.272 GeV for which we have no indication of a signal. The chi-square was used to calculate the maximum likelihood function as $\exp(-\frac{chi-square}{2})$ which is plotted as a function of the number of events added per 16 MeV bin in Figure 154. We conclude at 90% confidence level that the number of events that can be added per bin is less than 1.95. Since for the region 0.0 GeV < $m_{\gamma\gamma}$ < 0.272 GeV we used 15 bins of 16 MeV and the total Monte Carlo prediction for that region is 434.6 events, one could assign a 6.7 % systematic error due to the lead Mask cut. Taking into account the facts that: a) our conclusion that the $\gamma\gamma$ mass distribution of the rejected events is flat, was based on low statistics and b) there might be z dependence on the shape of this distribution, we assigned a 9% error due to the lead Mask cut. It is worth

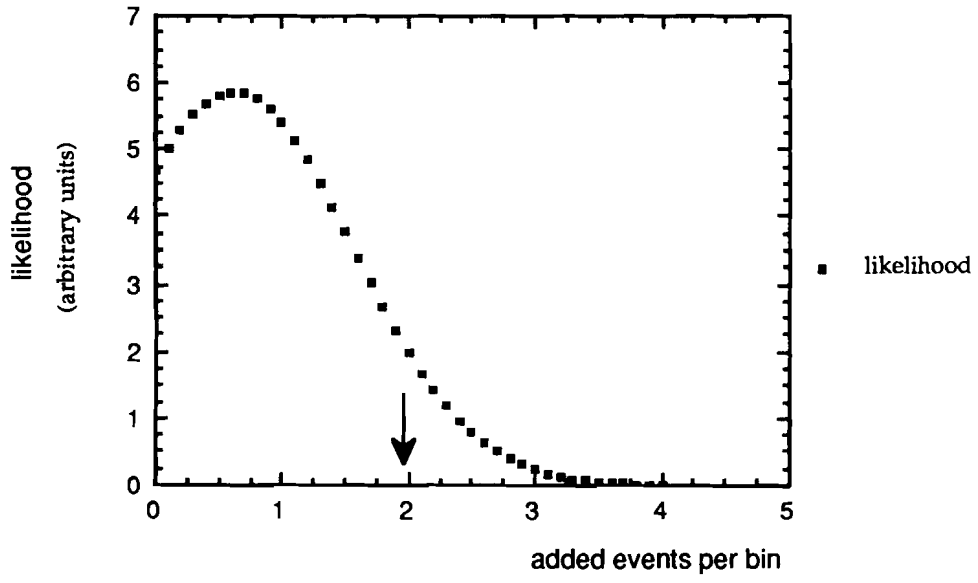

Figure 154. Likelihood function as a function of added events per bin in the $m_{\gamma\gamma}$ distribution. The arrow indicates the number of events that corresponds to the 90% confidence level.

pointing out at this point that the presence of this misreconstructed data in our sample -if we have not rejected all of them with the lead Mask cut- can only make our limit worse and not improve it artificially.

We have some thoughts on the possible sources of this background that could be checked by generating more $3\pi^0$ and $2\pi^0$ background Monte Carlo:

a) Although the photons of these misreconstructed events do not seem to penetrate the lead Mask, as already mentioned in section 6.5, they might penetrate the Regenerator-anti which has fewer radiation lengths than the Mask.

b) In reality K_L decays from the regenerator beam can scatter for example

at the regenerator and end up in the vacuum beam. Photons from such events could project badly at some aperture planes. Although this effect is simulated for the $2\pi^0$ background Monte Carlo, it is not for the $3\pi^0$ where we generate events only in the vacuum beam.
c) Noncoherent $K_S \rightarrow 2\pi^0$ decays from inelastically produced K_S could also contribute to this effect. (Production of inelastic K_S is simulated in the Monte Carlo but only up to a certain value of P_t^2).

If we knew the exact source of this background we might be able to reduce our systematic error due to the Mask. For the time being we assign a relatively large error due to it. It is encouraging to know that the m_{π^0} distribution of the events rejected by the lead Mask cut does not peak significantly at the nominal π^0 mass. This is illustrated in Figures 155 and 156 and gives us more confidence that the excess of data that we see when we analyze the full data set is true $\pi^0\gamma\gamma$ signal. In Figure 155 we show the m_{π^0} distribution of events rejected by the lead Mask cut from the full data set and after all cuts; in Figure 156 we show the same distribution at an earlier stage, namely after some of the fusion cuts applied at stage 15 (see Table 15).

8.6 Summary of systematics

We summarize in Table 25 the information given till now for the four different sources of systematic error and we finally decide to assign the total systematic by adding in quadrature the systematics due to photon vetoes, energy resolution and the lead Mask cut. We add them in quadrature because the photon veto systematic should be uncorrelated with the one due to the lead glass energy resolution and we do not know of any correlation between the systematic due to the lead Mask cut and any of the other systematics. In fact we believe that if this lead Mask effect is related at all with penetration of photons through the RA or it is related with any other photon veto effect, the correlation should be negative. This

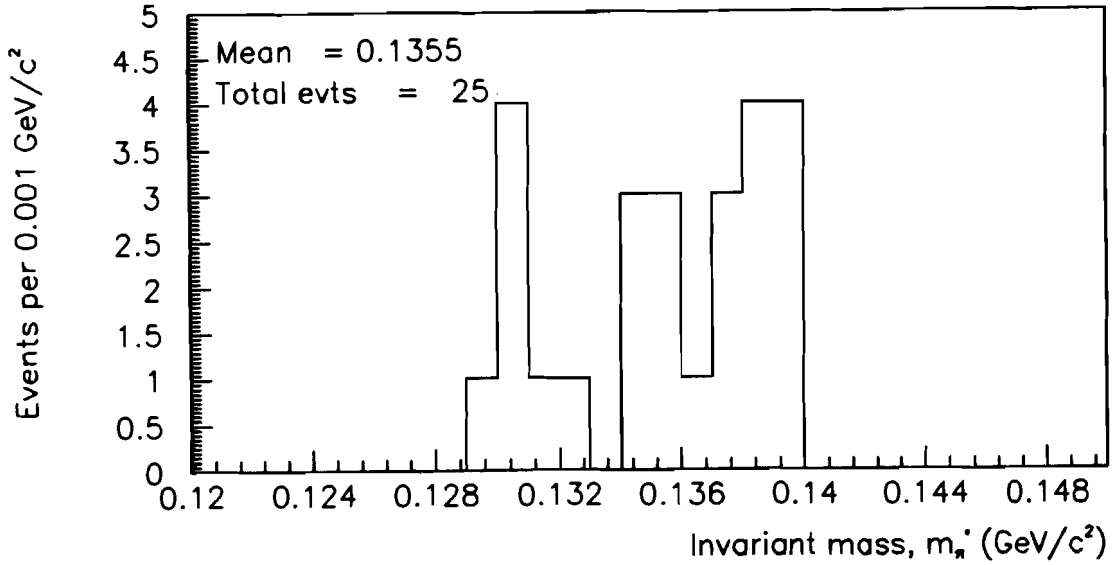

Figure 155. m_{π^0} distribution of $K_L \rightarrow \pi^0\gamma\gamma$ candidates that are rejected by the lead Mask cut after all other cuts.

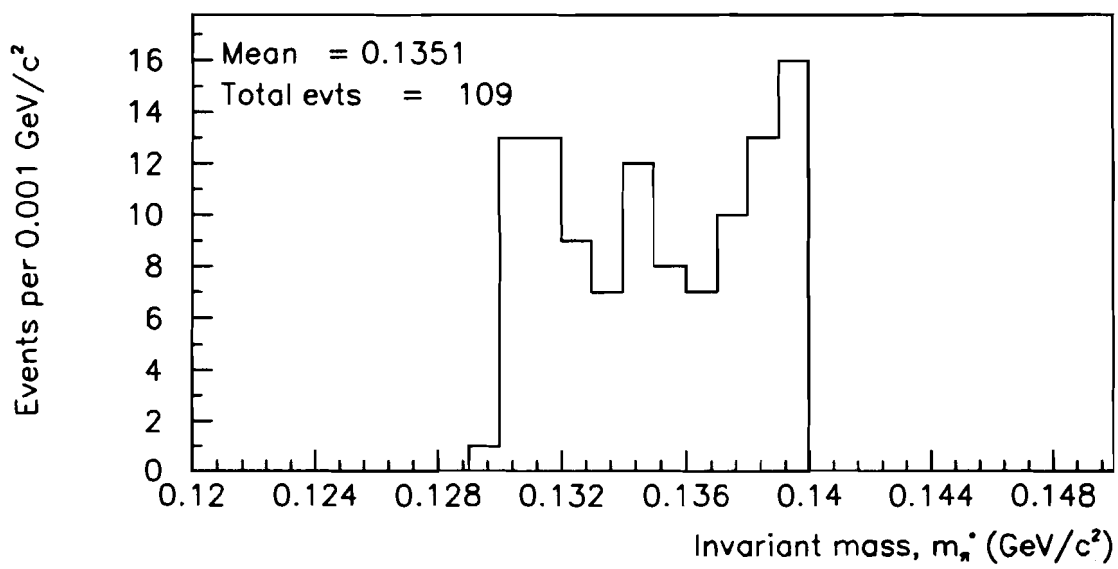

Figure 156. m_{π^0} distribution of $K_L \rightarrow \pi^0\gamma\gamma$ candidates that are rejected by the lead Mask cut after photon veto and some of the fusion cuts.

gives us a 12 % error for $m_{\gamma\gamma} \geq 0.300$ GeV and a 15 % error for the broader mass region which will be used in the next chapter for the calculation of the upper limit.

TABLE 25. Summary of systematic errors and their effects on the $3\pi^0$ background.

type of systematic error	effect of systematic error on number of $3\pi^0$ background events	
	all $m_{\gamma\gamma}$	$m_{\gamma\gamma} \geq 0.300$ GeV
photon veto	12%	5%
energy resolution	3%	6%
lead Mask cut	9%	9%
Total systematic error	15%	12%

CHAPTER 9

UPPER LIMIT CALCULATION FROM THE 20% OF THE DATA

In this chapter we are going to use information presented in previous chapters to derive an upper limit for the $K_L \rightarrow \pi^0\gamma\gamma$ decay. We will derive the limit by using two different hypotheses: a) the CHPT theory, which is one of the modern ways in treating the decay in question and b) the phase space hypothesis.

9.1 Upper limit using the CHPT model

As mentioned already in Chapter 2, the branching ratio of the decay $K_L \rightarrow \pi^0\gamma\gamma$ is given by the following equation:

$$BR(K_L \rightarrow \pi^0\gamma\gamma) = \frac{N_{\pi^0\gamma\gamma}}{A_{\pi^0\gamma\gamma}} \times \frac{A_{2\pi^0}}{N_{2\pi^0}} \times BR(K_L \rightarrow 2\pi^0) \qquad (9.1)$$

In this section we are going to discuss the calculation of each individual

variable on the right hand of this equation and we are going to start with $N_{2\pi^0}$ and $A_{2\pi^0}$ because this will give us the chance to discuss normalization factors between background Monte Carlo and data.

$N_{2\pi^0}$, the observed number of $K_L \rightarrow 2\pi^0$ decays, is deduced by reconstructing the $2\pi^0$ decays and applying to them, as much as possible, the same cuts as the ones applied in the $K_L \rightarrow \pi^0\gamma\gamma$ analysis. In Figure 157 is shown the kaon mass distribution from $K_L \rightarrow 2\pi^0$ decays after all cuts and in the decay region 110-128 m. We consider as good candidates only events reconstructing in the mass region 0.480-0.516 GeV and this is indicated by the arrows in the figure. There are 12050 events in that mass range from which the 6.9 events originate from $K_L \rightarrow 3\pi^0$ background as deduced from Monte Carlo study. After this background subtraction finally $N_{2\pi^0}$ is calculated to be 12043.1 events.

$A_{2\pi^0}$, the $K_L \rightarrow 2\pi^0$ acceptance, was calculated in section 7.2.2.1 to be 6.8%. The Monte Carlo used for this calculation simulates the experimental conditions as close as possible by generating K_L and K_S at the same time -and therefore allowing for kaons the possibility to cross over beams- and by simulating scattering and regeneration effects at several places in the detector. Therefore in order to calculate the number of coherent $K_L \rightarrow 2\pi^0$ decays that happened in the detector we can just take the ratio of $N_{2\pi^0}$ and $A_{2\pi^0}$ without need to subtract any other background from $N_{2\pi^0}$.

Since in this measurement we are dominated by background and we want to know if there is any signal on top of it, we need to normalize our background absolutely to the data and then check if there is any data excess that could be due to signal. The normalization has been done with the help of the $K_L \rightarrow 2\pi^0$ decays in the z range 110-134 m where we have more statistics and the normalization factor has smaller error. The number of $K_L \rightarrow 2\pi^0$ decays in that z range was determined from the data to be 19976 events before any background subtraction. Using the

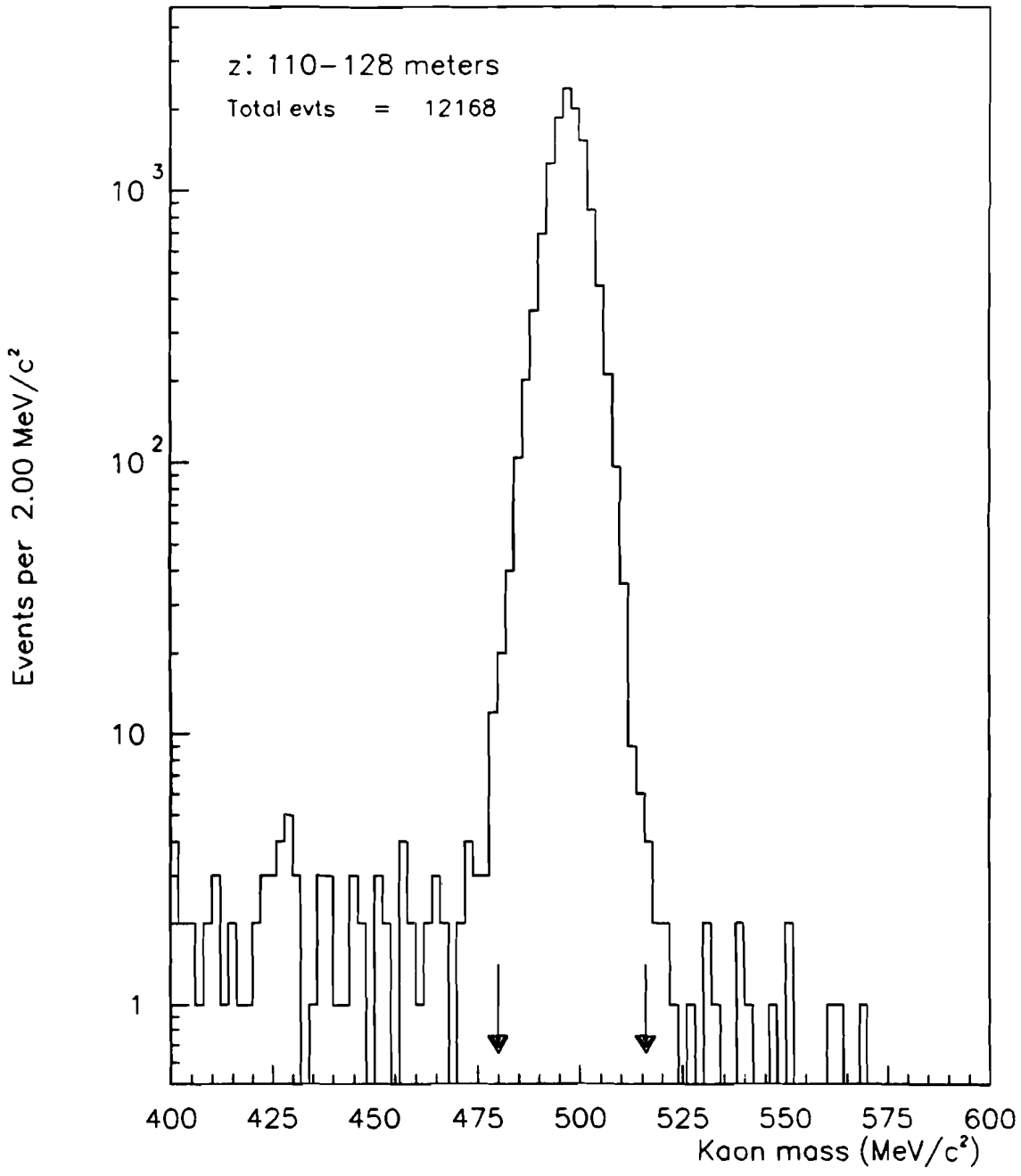

Figure 157. Kaon mass distribution for $K_L \rightarrow 2\pi^0$ decays after similar cuts with the $\pi^0\gamma\gamma$ analysis and in the decay region 110-128 m.

corresponding $2\pi^0$ acceptance which was calculated to be 8.47% and world averages for the $K_L \rightarrow 2\pi^0$ and $K_L \rightarrow 3\pi^0$ branching ratios this number was converted to the number of $3\pi^0$ decays that occured in the detector. It was compared with the number of generated $3\pi^0$ decays in the same z vertex and kaon energy regions in the $3\pi^0$ background Monte Carlo and the normalization factor was determined to be 5.936±0.275. After the subtraction of the $3\pi^0$ background which consisted only 0.13% of the $2\pi^0$ data and a couple of itterations the normalization factor for the $3\pi^0$ background stabilized to 5.944. The corresponding normalization factor for the $2\pi^0$ background is 1.682. These factors have been used already for the absolute normalization in Figures 145, 146 and 147.

$N_{\pi^0\gamma\gamma}$, the observed number of $K_L \rightarrow \pi^0\gamma\gamma$ decays, can be deduced from the information we have already presented in Chapters 6 and 7. As one can see in Figures 92 or 146, in the mass range $m_{\gamma\gamma} \geq 0.300$ GeV we have 26 candidate $K_L \rightarrow \pi^0\gamma\gamma$ events. In the same range the $K_L \rightarrow 3\pi^0$ and $K_L \rightarrow 2\pi^0$ background Monte Carlos predict that there should exist 27.6 and 3.0 events respectively giving us a total background prediction of 30.6±2.8 events where the error is only statistical. As justified in Chapter 8, we assigned to the background prediction a systematic error of 12 % in addition to the statistical error and by adding the two errors in quadrature we have a final uncertainty of 4.6 events in the background. We then used the maximum likelihood method folded with gaussian statistics to find the number of signal events, n_{s90}, allowed in our sample at 90% confidence level. n_{s90} is the number of allowed signal events that satisfies Equation (9.2).

$$0.9 = \frac{\int_0^{n_{s90}} \int_{n_{b0}-5\sigma_b}^{n_{b0}+5\sigma_b} e^{-(n_b+n_s)} \frac{(n_b+n_s)^m}{m!} e^{-\frac{(n_b-n_{b0})^2}{2\sigma_b^2}} d(n_b)d(n_s)}{\int_0^{\infty} \int_{n_{b0}-5\sigma_b}^{n_{b0}+5\sigma_b} e^{-(n_b+n_s)} \frac{(n_b+n_s)^m}{m!} e^{-\frac{(n_b-n_{b0})^2}{2\sigma_b^2}} d(n_b)d(n_s)} \qquad (9.2)$$

In the above equation, m is the observed number of candidate events, n_{b_0} is the number of predicted background events from Monte Carlo and σ_b is the uncertainty in this background prediction which in our case is 5.1 events. n_s is the number of signal events which is allowed to vary and n_b is the number of background events which is allowed to vary in a gaussian way within a window of $\pm 5\sigma_b$ around the predicted number of background events.

Using Equation (9.2) we found that the number of allowed signal events in our sample, n_{s90}, is 10.1 which is also assigned to be $N_{\pi^0\gamma\gamma}$.

Finally, the acceptance for $K_L \rightarrow \pi^0\gamma\gamma$, $A_{\pi^0\gamma\gamma}$, for $m_{\gamma\gamma} > 0.300$ GeV and in the same decay region was calculated to be 2.95% as mentioned in Chapter 7.

Using for the $K_L \rightarrow 2\pi^0$ branching ratio the world average value of 0.0909×10^{-2}, we finally conclude that $BR(K_L \rightarrow \pi^0\gamma\gamma) < 1.8 \times 10^{-6}$ (90% confidence level) for $m_{\gamma\gamma} \geq 0.300$ GeV.

Our originally published limit and our new, improved limit based on the 20% of the data are consistent with the predictions of Chiral Perturbation Theory although another factor of about 2.6 is needed in sensitivity to confirm the predictions. The CP conserving contribution to $K_L \rightarrow \pi^0 e^+ e^-$ has been better constrained and we have certainly proven that the $K_L \rightarrow \pi^0\gamma\gamma$ decay is not a serious background to the $K_L \rightarrow 2\pi^0$ mode. It is worth pointing out here that we see some excess of data in the mass range that extends between the double fusion peak and 0.304 GeV (see Figure 146). If we consider only the statistical errors of data and Monte Carlo this excess is at the 1.5σ level for $m_{\gamma\gamma} \geq 0.280$ GeV and at the 2σ level for $0.272 \text{ GeV} < m_{\gamma\gamma} < 0.304$ GeV. It is worth noticing that, because the high mass area where we see the excess is dominated by fusions which are understood by Monte Carlo quite well. We are going to wait though until the next chapter where we use the full data set to update our result to see if this excess becomes more significant.

9.2 Upper limit using the phase space hypothesis

Before closing this chapter we are going to derive also an upper limit based on the same data set but with the phase space assumption for the signal. As far as the distribution of the $m_{\gamma\gamma}$ is concerned, the phase space assumption is very similar to the VMD (Vector Meson Dominance) theory. From the variables that enter Equation (8.1) which we described in the previous section the ones that are going to change value for the derivation of the phase space limit are $N_{\pi^0\gamma\gamma}$ and $A_{\pi^0\gamma\gamma}$. As one can see from Figures 92 or 146, the number of $\pi^0\gamma\gamma$ candidate events in the whole $\gamma\gamma$ mass region after excluding the events around $m_{n\pi^0}$ and the events between 0.264-0.280 GeV, is 156. The prediction from the $K_L \rightarrow 3\pi^0$ and $K_L \rightarrow 2\pi^0$ background Monte Carlos is 144.9 and 17.8 events respectively giving us a total background prediction of 162.7±8.9 where the error is only statistical. Adding in quadrature to this error a systematic error of 15% as justified in the previous chapter, we finally have σ_b to be equal to 26 events and $N_{\pi^0\gamma\gamma}$ equal to 44.4 events. The acceptance for the corresponding mass region is calculated to be 4.44% in section 7.2.2.1 by using the information given in Figure 120 and the number of generated $\pi^0\gamma\gamma$ events in the chosen z vertex and kaon energy regions. Finally our phase space upper limit is 5.1 x 10^{-6} (90% confidence level). We want to remind the reader at this point that this limit has been derived for a wider mass region than the corresponding phase space limit in our publication.

Before proceeding to the next chapter we want to add a little more on what we already said on Chapter 1 about the observation of the $K_L \rightarrow \pi^0\gamma\gamma$ decay by Experiment NA31 at CERN. Using a similar technique to ours for the reconstruction of the $K_L \rightarrow \pi^0\gamma\gamma$ decay, that experiment observed recently a signal of 21 events from which 1.5±0.9 are expected to be

background. The branching ratio was calculated to be $(2.1 \pm 0.6) \times 10^{-6}$ for decays with $m_{\gamma\gamma} \geq 0.280$ GeV and it was based on a sample of 13.5 ± 3.8 events.

In the following chapter we will compare our updated result based on the full data set with the CERN result.

CHAPTER 10

UPDATE FROM THE FULL DATA SET

In this chapter we are going to update our result for the $K_L \rightarrow \pi^0\gamma\gamma$ branching ratio by using 100% of the data. We will use CHPT to check if the excess of data that we saw on the right of the "double fusion" peak in the analysis of the 20% of the data is more significant and we will give a branching ratio for $m_{\gamma\gamma} \geq 0.280$ GeV.

10.1 Overview

The analysis used for the full data set is identical to the one described in the previous chapters. The only thing one has to be cautious with now, is to take properly into account the different running conditions of the experiment at different times and simulate them properly with the Monte Carlo program. In fact, as was already mentioned in Chapter 4, we had three different running modes within which we collected "four-cluster"

events with neutral final states. The majority, 48%, of these data was taken in the "neutral" running mode with the Pb sheet in place; another 19% was taken in the "chg, neutral" running mode which was dominated by data with charged final states, without the Pb sheet and with a 20 count (100 MeV) threshold at each lead glass block instead of 5 counts (25 MeV); the remaining 33% was taken in the "chg/n, neutral" running mode. In fact in the last chapters we have described the analysis of the 82% of the data of this last category.

In Table 26 we show the numbers of data events that we have for the $K_L \to \pi^0\gamma\gamma$ and $K_L \to 2\pi^0$ decays in each running mode and for the full data set, before any background subtraction, after all cuts and in the decay region 110-128 m. Since in the previous chapter we derived an upper limit for $m_{\gamma\gamma} \geq 0.300$ GeV, for the $K_L \to \pi^0\gamma\gamma$ decays we give the numbers for both the $m_{\gamma\gamma} \geq 0.280$ GeV and $m_{\gamma\gamma} \geq 0.300$ GeV regions. For the calculation of the branching ratio though we are going to consider the region $m_{\gamma\gamma} \geq$ 0.280 GeV for reasons that will be explained in section 10.3.

TABLE 26. Numbers of $K_L \to \pi^0\gamma\gamma$ and $K_L \to 2\pi^0$ data events in the different running modes of the experiment.

running mode	Number of data events (z: 110-128 m)		
	$\pi^0\gamma\gamma$		$2\pi^0$
	$m_{\gamma\gamma} \geq 0.280$ GeV	$m_{\gamma\gamma} \geq 0.300$ GeV	
"neutral"	104	65	21504
"chg/n, neutral"	76	37	14684
"chg, neutral"	52	34	8818
all modes	232	136	45006

The three different running conditions mentioned above had to be mimicked in the Monte-Carlo for the acceptance determination of the

$K_L \to \pi^0\gamma\gamma$ and $K_L \to 2\pi^0$ decays and for the $K_L \to 3\pi^0$ and $K_L \to 2\pi^0$ background simulation. The acceptances for all three running modes and for both $K_L \to \pi^0\gamma\gamma$ and $K_L \to 2\pi^0$ are given in Table 27. For $K_L \to \pi^0\gamma\gamma$ we use the CHPT spectrum. The acceptances for the "chg/n, neutral" running mode are the same ones calculated in Chapter 7. For the "neutral" running mode acceptance determinations our Monte Carlo simulated the presence of the Pb sheet and the corresponding magnet settings. To simulate the "chg, neutral" running mode conditions one could proceed in two different ways: either generate more Monte Carlo with the Pb sheet out of place and with a 20 count threshold at each lead glass block or use the existing Monte Carlo events which were generated to mimic the "chg/n, neutral" running mode conditions and apply within our analysis the 20 count threshold. We chose to do the latter.

TABLE 27. Acceptances for the $K_L \to \pi^0\gamma\gamma$ and $K_L \to 2\pi^0$ decay modes for the different running modes of the experiment.

running mode	Acceptance (z: 110-128 m) $\pi^0\gamma\gamma$ $m_{\gamma\gamma} \geq 0.280$ GeV	$\pi^0\gamma\gamma$ $m_{\gamma\gamma} \geq 0.300$ GeV	$2\pi^0$
"neutral"	(2.89±0.03) %	(2.29±0.02) %	(5.27±0.05) %
"chg/n, neutral"	(3.75±0.02) %	(2.95±0.02) %	(6.81±0.06) %
"chg, neutral"	(3.67±0.02) %	(2.89±0.02) %	(6.67±0.06) %

As far as the background is concerned, we had to simulate both the $K_L \to 2\pi^0$ and the $K_L \to 3\pi^0$ backgrounds. For the $K_L \to 2\pi^0$ background we used the same Monte Carlo that was used for the determination of the corresponding acceptance of the $2\pi^0$ signal, but we simply used more

statistics. For the $K_L \rightarrow 3\pi^0$ background simulation we did not have much flexibility. Since the generation of that Monte Carlo took about 500 hours of CPU, we had to use the already existing Monte Carlo for the whole data set but treat it properly. For the "neutral" running mode conditions we had to simulate the presence of the Pb sheet. As explained in section 6.6, in the $\pi^0\gamma\gamma$ analysis we require no tracks, at most 20 hits at all four chambers and that B and C latches as well as other latches like T and V do not fire. This implies that events with photons converting at the Pb sheet will be rejected with very high probability. Therefore we simulated the presence of the Pb sheet by rejecting with 6.54% probability events with decay vertex upstream of the HDRA and with photons projecting within the HDRA aperture. This 6.54% probability has been calculated by using the thickness of our Pb sheet and the photon attenuation length in Pb. The 20 count threshold for the "chg, neutral" running mode was simulated with the way mentioned earlier for the $2\pi^0$ Monte Carlo. In order to normalize the background absolutely to the data we have to know the $K_L \rightarrow 2\pi^0$ and $K_L \rightarrow 3\pi^0$ normalization factors for each one of the data sets corresponding to the three different running modes. That is we have to know the amount of data that our $2\pi^0$ and $3\pi^0$ background Monte Carlos correspond to. These factors have been determined in the way described in Chapter 9 and they are shown in Table 28. The uncertainties in the $3\pi^0$ normalization factors are basically due to the uncertainties in the $3\pi^0$ and $2\pi^0$ branching ratios since the number of $3\pi^0$ decays is calculated by scaling the number of $2\pi^0$ decays. These factors were mainly used for the absolute normalization of the $3\pi^0$ and $2\pi^0$ backgrounds to the $\pi^0\gamma\gamma$ candidate data but also for the subtraction of a very small, about 0.1%, $3\pi^0$ background under the $2\pi^0$ mass peak.

Since we are going to use the high $\gamma\gamma$ mass region to calculate the $K_L \rightarrow \pi^0\gamma\gamma$ branching ratio, it is useful to show at this point our background prediction for this region. In Table 29 we show the expected $3\pi^0$ and $2\pi^0$ backgrounds for all three running modes and for $m_{\gamma\gamma} \geq 0.280$

TABLE 28. Normalization factors for the $K_L \to 3\pi^0$ and $K_L \to 2\pi^0$ backgrounds for the different running modes of the experiment.

running mode	Normalization factors $K_L \to 3\pi^0$	$K_L \to 2\pi^0$
"neutral"	2.58±0.12	0.99±0.01
"chg/n, neutral"	4.86±0.22	1.38±0.01
"chg, neutral"	8.02±0.37	2.27±0.02

GeV. In Table 30 we show similarly the expected background for $m_{\gamma\gamma} \geq$ 0.300 GeV. One can see the total data excess and the data excess in each running mode separately, by comparing the last columns of Tables 29 and 30 with the first two columns of Table 26. We are now ready to proceed with data-Monte Carlo comparisons that are going to be shown in the next section.

10.2 Data-Monte Carlo comparisons

Figure 158 shows data-Monte Carlo comparison for the $\gamma\gamma$ invariant mass distribution with absolute normalization. The shaded histogram represents the $2\pi^0$ background contribution and it corresponds to 11.3% of the total background for the whole $m_{\gamma\gamma}$ mass region and to 12.3% of the total background for $m_{\gamma\gamma} \geq 0.280$ GeV. The mass region on the left of the "double fusion" peak is simulated well by the $3\pi^0$ and $2\pi^0$ Monte Carlo within the statistical errors but the mass region on the right of the "double fusion peak" has four consecutive bins with prominent data excess which is suggestive of $\pi^0\gamma\gamma$ signal. In Figure 159 we show data-Monte Carlo

TABLE 29. Background prediction corresponding to the different running modes of the experiment, for $m_{\gamma\gamma} \geq 0.280$ GeV.

running mode	Number of background events absolutely normalized to the $\pi^0\gamma\gamma$ data (z: 110-128 m, $m_{\gamma\gamma} \geq 0.280$ GeV)		
	$3\pi^0$	$2\pi^0$	Total bkg
"neutral"	67.07	13.09	80.16
"chg/n, neutral"	52.43	5.09	57.52
"chg, neutral"	31.16	3.02	34.18
all modes	150.66	21.20	171.86 ± 11.47

TABLE 30. Background prediction corresponding to the different running modes of the experiment, for $m_{\gamma\gamma} \geq 0.300$ GeV.

running mode	Number of background events absolutely normalized to the $\pi^0\gamma\gamma$ data (z: 110-128 m, $m_{\gamma\gamma} \geq 0.300$ GeV)		
	$3\pi^0$	$2\pi^0$	Total bkg
"neutral"	43.13	8.06	51.18
"chg/n, neutral"	33.72	3.63	37.35
"chg, neutral"	20.04	2.16	22.20
all modes	96.89	13.85	110.74 ± 8.99

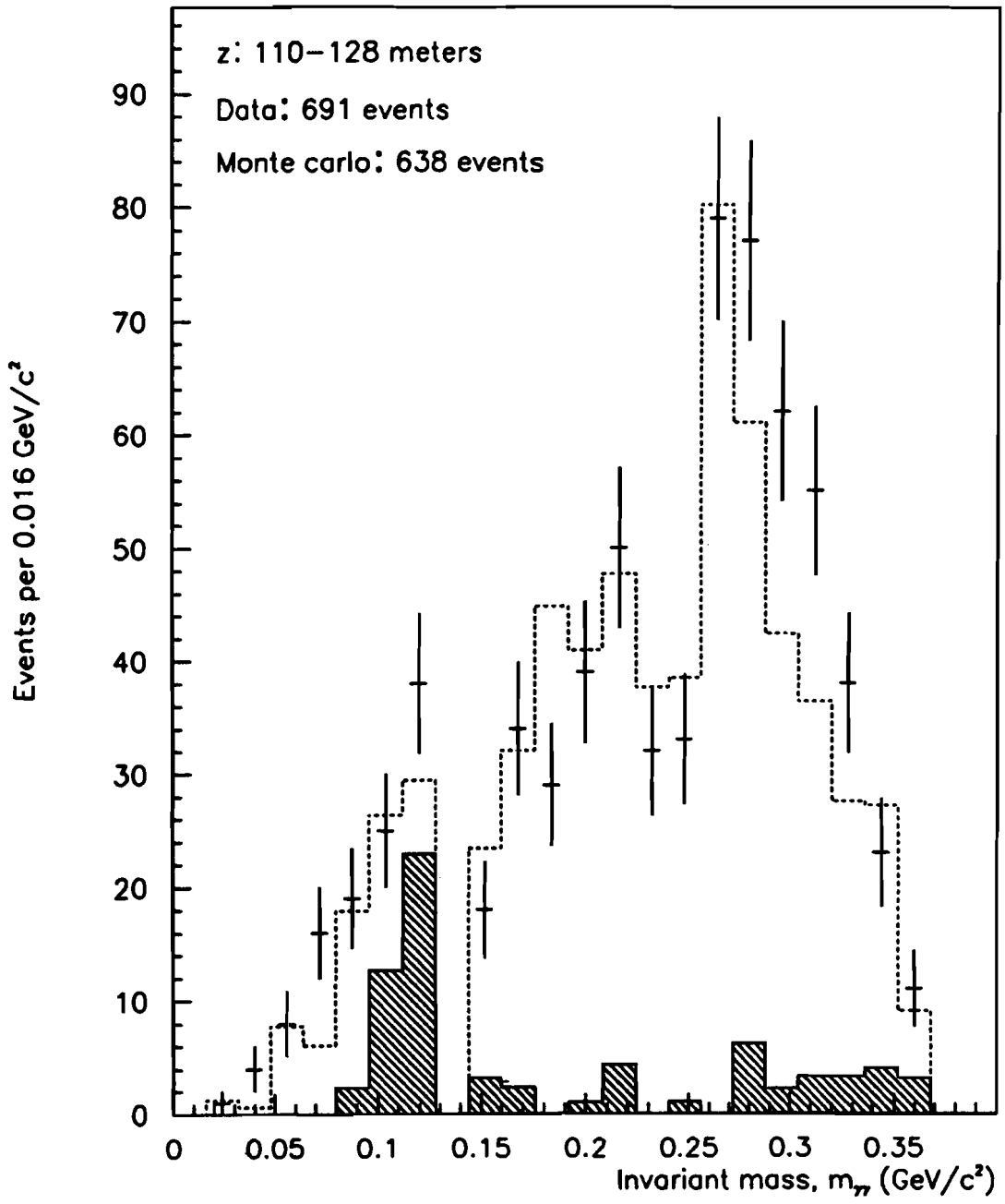

Figure 158. Data-Monte Carlo comparison for the $\gamma\gamma$ mass distribution between $\pi^0\gamma\gamma$ candidates and background events based on the full data set. The normalization is absolute. The error bars correspond to the data, the shaded histogram to the $2\pi^0$ background Monte Carlo and the dashed histogram to the sum of the $3\pi^0$ and $2\pi^0$ background Monte Carlo.

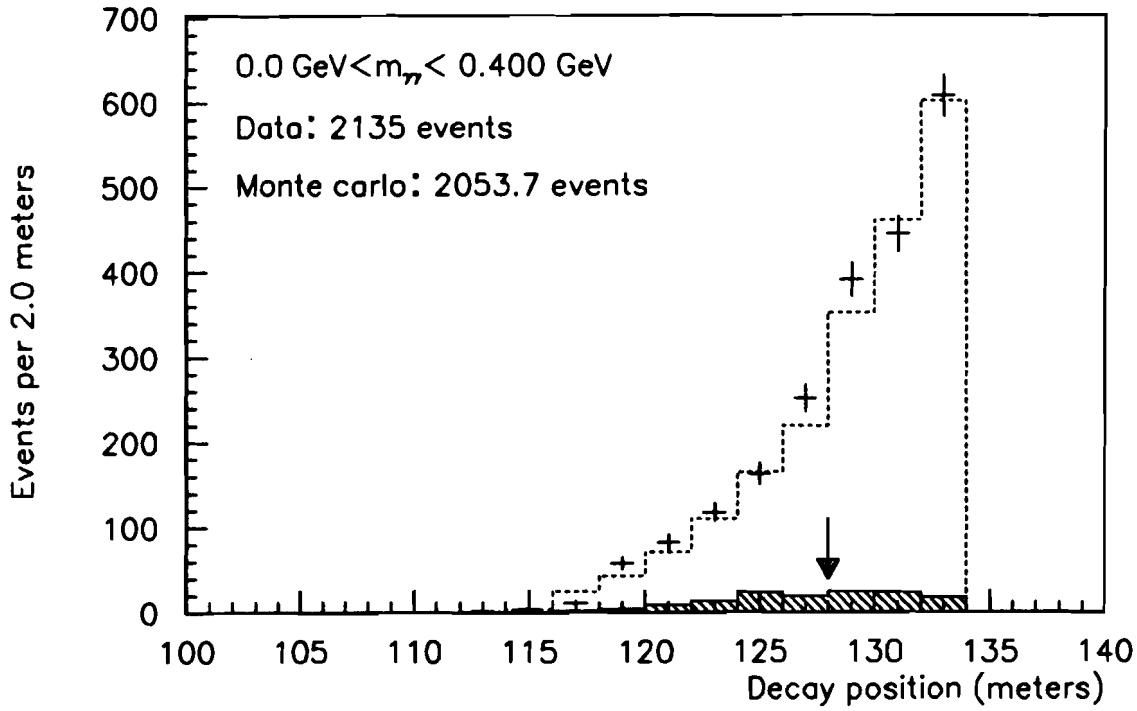

Figure 159. Data-Monte Carlo comparison for the z decay vertex distribution between $\pi^0\gamma\gamma$ candidates and background events for the whole $\gamma\gamma$ mass region. The error bars correspond to the data, the shaded histogram to the $2\pi^0$ background Monte Carlo and the dashed histogram to the sum of the $3\pi^0$ and $2\pi^0$ background Monte Carlo. The normalization is absolute. The arrow indicates the position of the cut.

comparison of the z decay vertex distribution for the whole mass region ($\gamma\gamma$ masses around the nominal π^0 mass value, $m_{n\pi^0}$, are always excluded) and in Figure 160 we show similar comparison for $m_{\gamma\gamma} \geq 0.280$ GeV and for $m_{\gamma\gamma} \geq 0.300$ GeV. One can notice that for $m_{\gamma\gamma} \geq 0.280$ GeV most of the bins have data excess. If the excess of the data at high $\gamma\gamma$ masses is $\pi^0\gamma\gamma$ signal, then the invariant mass of the two photons that originate from the π^0 has to be centered around the nominal π^0 mass while backgrounds are expected to have wider distributions. Before we test this hypothesis we

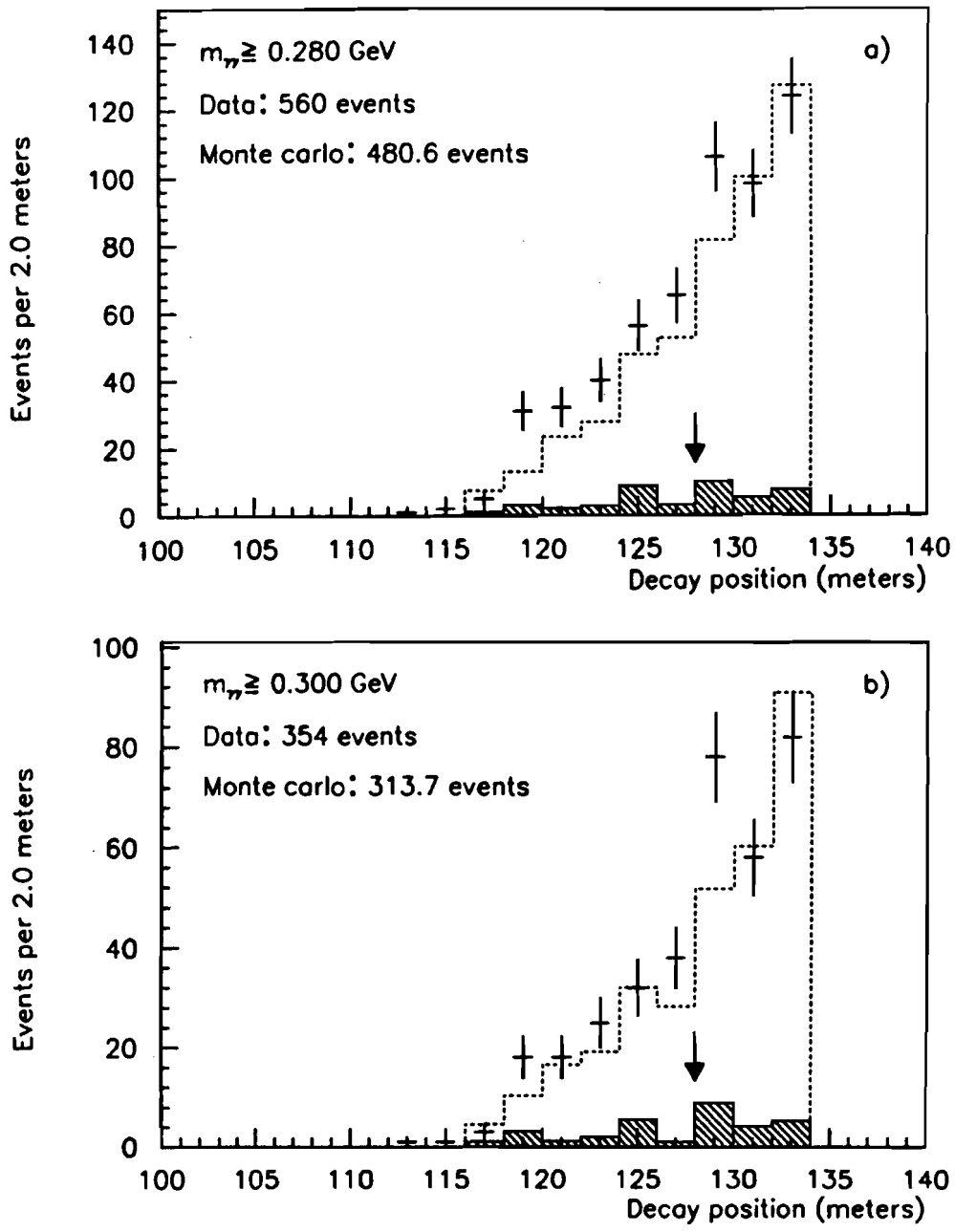

Figure 160. Data-Monte Carlo comparison for the z decay vertex distribution between $\pi^0\gamma\gamma$ candidates and background events for the high $\gamma\gamma$ mass region. The normalization is absolute. The error bars correspond to the data, the shaded histogram to the $2\pi^0$ background Monte Carlo and the dashed histogram to the sum of the $3\pi^0$ and $2\pi^0$ background Monte Carlo. a) $m_{\gamma\gamma} \geq 0.280$ GeV and b) $m_{\gamma\gamma} \geq 0.300$ GeV.

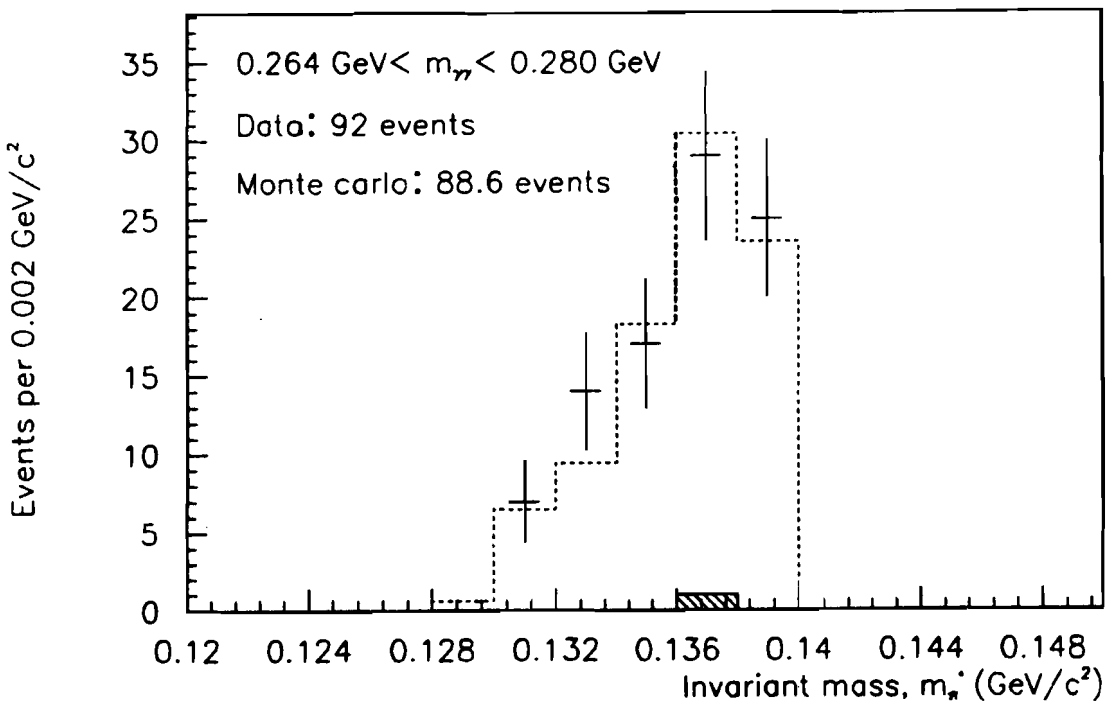

Figure 161. Data-Monte Carlo comparison for the m_{π^0} distribution between $\pi^0\gamma\gamma$ candidates and $3\pi^0$ and $2\pi^0$ background events in the range 0.264 GeV < $m_{\gamma\gamma}$ < 0.280 GeV. The shaded histogram corresponds to the $2\pi^0$ background contribution. The normalization is absolute.

want to demonstrate our level of understanding of the m_{π^0} distribution in a region dominated by background. In Figure 161 we show data-Monte Carlo comparison for the m_{π^0} distribution after all the analysis cuts for events with $\gamma\gamma$ invariant mass in the range 0.264 GeV - 0.280 GeV which is dominated by "double fusions". The agreement is very good and this assures us that the "double fusion" peak is understood well. The peak of this distribution is shifted to the high masses as it is expected from the nonlinearity effect that was defined in section 2.3.2.1 and was explained in section 7.3.1.1. Figure 162 shows data-Monte Carlo overlays for the m_{π^0}

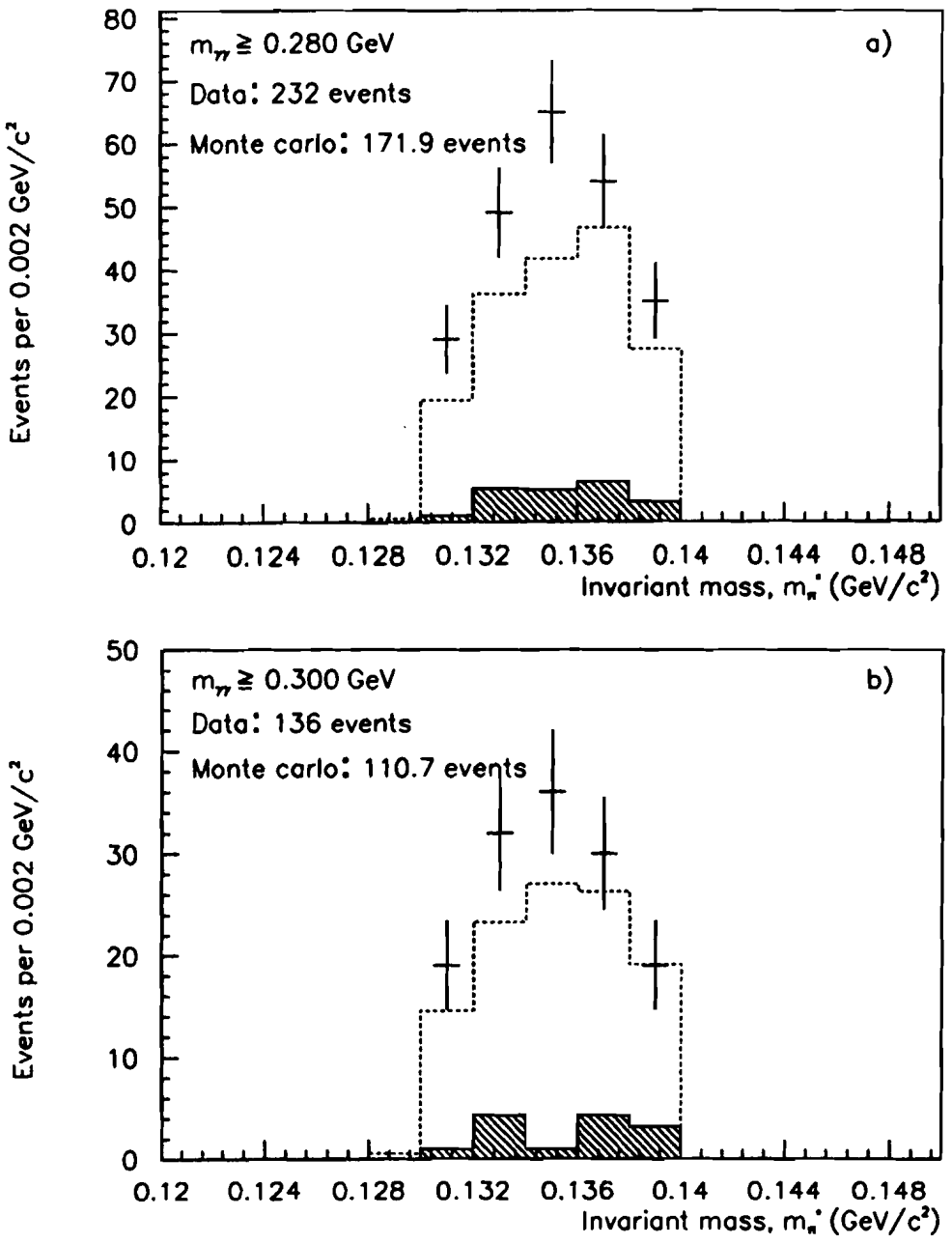

Figure 162. Data-Monte Carlo comparison for the m_{π^0} distribution between $\pi^0\gamma\gamma$ candidates and background events for the high $\gamma\gamma$ mass region. a) $m_{\gamma\gamma} \geq 0.280$ GeV; b) $m_{\gamma\gamma} \geq 0.300$ GeV. The error bars correspond to the data, the shaded histogram to the $2\pi^0$ background prediction and the dashed histogram to the sum of the $3\pi^0$ and $2\pi^0$ background predictions. The normalization is absolute.

distribution for $m_{\gamma\gamma} \geq 0.280$ GeV and for $m_{\gamma\gamma} \geq 0.300$ GeV. One can see that the data excess is quite prominent for $m_{\gamma\gamma} \geq 0.280$ GeV and is centered around m_{π^0} for both distributions. We are going to overlay the signal m_{π^0} distribution on top of this distribution shortly, after being more quantitative about the data excess and deriving a branching ratio.

10.3 Calculation of the branching ratio for the $K_L \rightarrow \pi^0\gamma\gamma$ decay

The definition of the branching ratio for the $K_L \rightarrow \pi^0\gamma\gamma$ decay is basically the same one given by Equations (2.1) and (9.1). We will, however, write it here in a more general form since we have to deal with three different data sets where each one has its own acceptances and normalization factors. We define this branching ratio to be:

$$BR(K_L \rightarrow \pi^0\gamma\gamma) = \frac{Nc_{\pi^0\gamma\gamma}}{Nc_{2\pi^0}} \times BR(K_L \rightarrow 2\pi^0) \qquad (10.1)$$

where $Nc_{\pi^0\gamma\gamma}$ stands for the number of $K_L \rightarrow \pi^0\gamma\gamma$ decays and $Nc_{2\pi^0}$ stands for the number of $K_L \rightarrow 2\pi^0$ decays that occurred through our beamline (after acceptance correction). If we number the three different data sets as 1, 2, 3 where 1 corresponds to the "neutral", 2 corresponds to the "chg/n, neutral" and 3 corresponds to the "chg, neutral" running modes respectively, then we can write $Nc_{\pi^0\gamma\gamma}$ and $Nc_{2\pi^0}$ as following:

$$Nc_{\pi^0\gamma\gamma} = \frac{N_{\pi^0\gamma\gamma 1}}{A_{\pi^0\gamma\gamma 1}} + \frac{N_{\pi^0\gamma\gamma 2}}{A_{\pi^0\gamma\gamma 2}} + \frac{N_{\pi^0\gamma\gamma 3}}{A_{\pi^0\gamma\gamma 3}} \qquad (10.2)$$

$$Nc_{2\pi^0} = \frac{N_{2\pi^0 1}}{A_{2\pi^0 1}} + \frac{N_{2\pi^0 2}}{A_{2\pi^0 2}} + \frac{N_{2\pi^0 3}}{A_{2\pi^0 3}} \qquad (10.3)$$

In the above Equations $N_{\pi^0\gamma\gamma i}$ and $N_{2\pi^0 i}$ stand for the observed number of excess of $\pi^0\gamma\gamma$ data or $2\pi^0$ data respectively over the expected background

for each one of the three data sets. Of course for the $2\pi^0$ case the expected background is very small, on the order of 0.1%. Similarly $A_{\pi^0\gamma\gamma i}$ and $A_{2\pi^0 i}$ stand for the $\pi^0\gamma\gamma$ and $2\pi^0$ acceptances for each one of the three sets.

Using Equations (10.1, 10.2 and 10.3) and the information provided in Tables 26, 27, 29 and 30 on $\pi^0\gamma\gamma$ and $2\pi^0$ data and acceptances, and on expected backgrounds for the $K_L \rightarrow \pi^0\gamma\gamma$ decay, we conclude that:

$$BR(K_L \rightarrow \pi^0\gamma\gamma) = (2.2 \pm 0.7 \pm 0.8) \times 10^{-6} \qquad \text{for } m_{\gamma\gamma} \geq 0.280 \text{ GeV},$$

where the first error is statistical and the second is systematic.

The statistical error on this number has been derived by taking into account the Monte Carlo statistics, the correlations in the backgrounds due to the fact that we used the same Monte Carlo for different data sets, the uncertainties in the normalization factors and also the uncertainty in the $2\pi^0$ branching ratio. The systematic error in the branching ratio corresponds to the 12% systematic uncertainty in the background prediction for the high $\gamma\gamma$ mass region as estimated in Chapter 8: by changing both our $3\pi^0$ and $2\pi^0$ backgrounds by $\pm 12\%$ we observed a change in the central value of the branching ratio by $\mp 0.8 \times 10^{-6}$.

As we promised in the previous section, we used this branching ratio to normalize the m_{π^0} distribution from signal $\pi^0\gamma\gamma$ Monte Carlo, we added this normalized distribution on top of the $3\pi^0$ and $2\pi^0$ backgrounds and we compared with the data. We demonstrate this check in Figure 163 where we plot m_{π^0} for a wider mass range than in Figure 162. The agreement is very good and gives us additional confidence that the excess of data we see is $\pi^0\gamma\gamma$ signal.

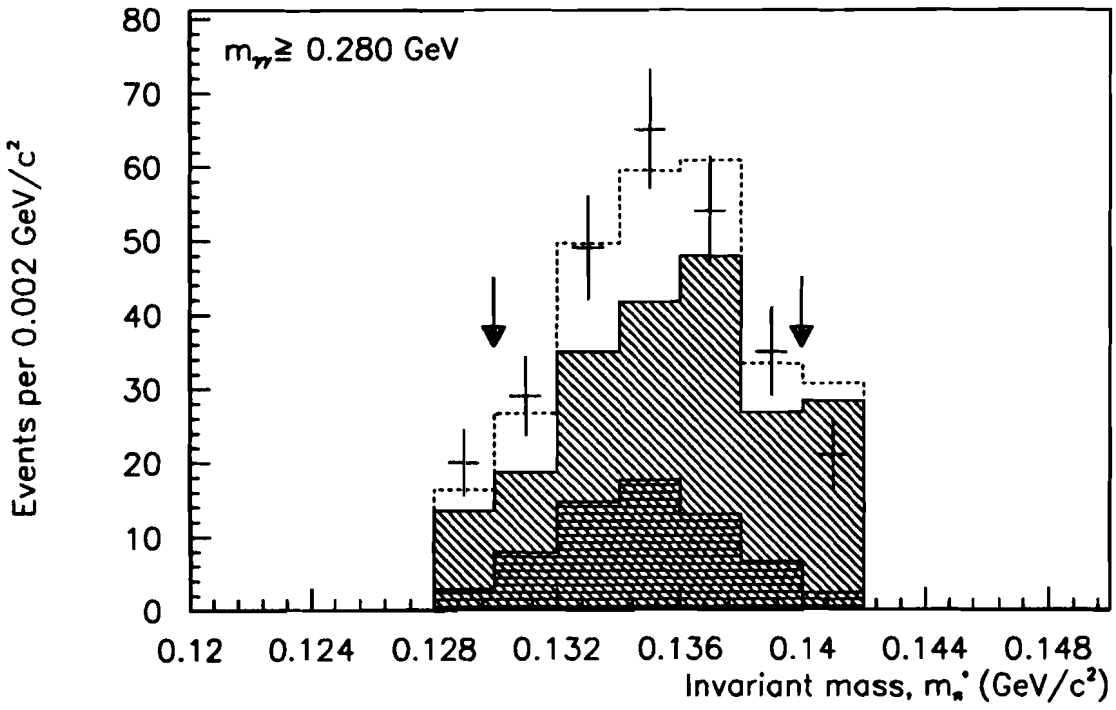

Figure 163. Data-Monte Carlo comparison for the m_{π^0} distribution between $\pi^0\gamma\gamma$ candidates and background events plus $\pi^0\gamma\gamma$ signal Monte Carlo, for $m_{\gamma\gamma} \geq 0.280$ GeV. The error bars correspond to the data; the diagonally shaded histogram to the sum of the $3\pi^0$ and $2\pi^0$ background Monte Carlo; the horizontally shaded histogram corresponds to the $\pi^0\gamma\gamma$ signal normalized with the branching ratio of 2.2×10^{-6} and the dashed histogram to the sum of the background and signal. The normalization is absolute. The arrows indicate the position of the cut.

10.4 Summary - Conclusions

By using our full data set we see an excess of events in our data sample over the considered backgrounds. This excess cannot be explained with the $3\pi^0$, $2\pi^0$ and $\pi^+\pi^-\pi^0$ assumptions. We have also no indication that they are related with accidental activity. These events have a well centered m_{π^0} distribution and we believe they are $\pi^0\gamma\gamma$ signal. We measured a branching ratio of:

$$BR(K_L \rightarrow \pi^0\gamma\gamma) = (2.2 \pm 0.7 \pm 0.8) \times 10^{-6} \qquad \text{for } m_{\gamma\gamma} \geq 0.280 \text{ GeV}.$$

It is natural to look for a signal in this mass range for two reasons:
a) This region is above the $\pi^+\pi^-$ energy threshold which is favored by both the Chiral Perturbation Theory and the pion rescattering models as was discussed in Chapter 1.
b) Although the double fusions start at 0.264 GeV and extend all the way up to the kinematical limit, we still avoid a big fraction of the "double fusion" peak by looking for signal in the region $m_{\gamma\gamma} \geq 0.280$ GeV. With our cut that kinematically rejects double fusions we are in a better position now than we were at the time of our publication to look for signal even in the region dominated by double fusions.
Since it is desirable to use for the calculation of the branching ratio the broader possible $\gamma\gamma$ mass range, after exploring with the full data set statistics the whole $m_{\gamma\gamma}$ spectrum, we decided to use for the branching ratio calculation the mass range $m_{\gamma\gamma} \geq 0.280$ GeV.

Our branching ratio is a 3σ measurement if one considers only the statistical error and it is a 2σ measurement if both the statistical and systematic errors are considered. This branching ratio is consistent with the NA31 measurement for the same mass region. It is also consistent, within errors, with the CHPT predictions favoring the $\gamma\gamma$ pair in an S state, although the central value of our branching ratio is a factor of three

higher. As far as the comparison of our result with the NA31 result is concerned we would like to point out that: although the central values of our branching ratios look the same, they should not be compared directly. When we use the CHPT spectrum to find the signal acceptance for $m_{\gamma\gamma} \geq$ 0.280 GeV for example, we generate events in the whole mass spectrum and define our acceptance as the percentage of the generated events that pass the analysis cuts and reconstruct above 0.280 GeV. NA31 however, uses as acceptance the ratio of accepted events above 0.280 GeV to the generated events in the same mass region. That is to say that our branching ratio would have to be lowered by about 15% if it had to be compared directly with the NA31 branching ratio.

For completeness, and since we already had a publication of an upper limit for $m_{\gamma\gamma} \geq 0.300$ GeV we want to summarize in Table 31 our calculations for a branching ratio and an upper limit for both mass regions considered.

TABLE 31. Branching ratio for $m_{\gamma\gamma} \geq 0.280$ GeV and $m_{\gamma\gamma} \geq 0.300$ GeV using the Chiral Perturbation Theory.

Full data set measurement	$m_{\gamma\gamma} \geq 0.280$ GeV	$m_{\gamma\gamma} \geq 0.300$ GeV
Branching ratio	$(2.2 \pm 0.7 \pm 0.8) \times 10^{-6}$	$(1.2 \pm 0.7 \pm 0.6) \times 10^{-6}$
Upper limit		$< 2.46 \times 10^{-6}$

Our branching ratio for $m_{\gamma\gamma} \geq 0.300$ GeV is a factor of 2 lower than the branching ratio for $m_{\gamma\gamma} \geq 0.280$ GeV but the two ratios are still consistent within errors. Both branching ratios have been derived with the Chiral Perturbation Theory assumption. If that theory is right then the two branching ratios are expected to be consistent. If it is not, then the difference between the two branching ratios would indicate that the $\gamma\gamma$

mass spectrum is peaking between 0.280 and 0.300 GeV.

Since for the region $m_{\gamma\gamma} \geq 0.300$ GeV our measurement is only a one σ measurement we would like to give for completeness an upper limit for the branching ratio. Since for this mass region all our data excess over background comes from the "neutral" and "chg, neutral" running modes, we expect the limit to be less strong than the one we derived in the previous chapter on the basis of the "chg/n, neutral" running mode. This limit has been calculated in the way described in Chapter 9, using the maximum likelihood method folded with Gaussian statistics. The only difference is that for the number of measured events, the number of predicted background events and the uncertainty in this prediction we now use the numbers of the full data set given in Tables 26 and 30. Using an additional 12% systematic uncertainty for the background prediction we find that there should be 52.9 events allowed in that region at 90% confidence level. Using as a $\pi^0\gamma\gamma$ acceptance a weighted average of the acceptances in the three different running modes (2.58%) and the K_L flux in the full data set we conclude that the upper limit for the $K_L \rightarrow \pi^0\gamma\gamma$ branching ratio for $m_{\gamma\gamma} \geq 0.300$ GeV is 2.46×10^{-6}.

If we check the data Monte Carlo predictions for the mass below 0.280 GeV then we find that the number of data events is 459 ± 21.4 and the Monte prediction is 466.2 ± 21.1. Therefore we have no indication of a signal in the low $\gamma\gamma$ mass region.

We would like to conclude that we observed the $\pi^0\gamma\gamma$ signal at the branching ratio of :

$BR(K_L \rightarrow \pi^0\gamma\gamma) = (2.2 \pm 0.7 \pm 0.8) \times 10^{-6}$ for $m_{\gamma\gamma} \geq 0.280$ GeV.

More statistics and bigger background rejection would be necessary for confirming this observation and for studying the Dalitz plot distribution of the decay.

REFERENCES

[1]. S. Oneda, Phys. Rev. **158**, 1541 (1967).

[2]. S. Pakvasa, Univ. of Hawaii, Internal Report 21-67 (1967) and references therein.

[3]. M. Atiya et al., Phys. Rev. Lett. **65**, 1188 (1990).

[4]. M. Banner, J. W. Cronin, J. K. Liu, and J. E. Pilcher, Phys. Rev. **188**, 2033 (1969).

[5]. L. M. Sehgal, Phys. Rev. D **6**, 367 (1972).

[6]. L. K. Gibbons et al., Phys. Rev. Lett. **61**, 2661 (1988); A. Barker et al., Phys. Review D **41**, 3546 (1990).

[7]. G. D. Barr et al., Phys. Lett. B 214, 303 (1988).

[8]. E. Jastrzembski et al., Phys. Rev. Lett. **61**, 2300 (1988); K. E. Ohl et al., Phys. Rev. Lett. **64**, 2755 (1990).

[9]. See, for example, C. O. Dib, I. Dunietz, and F. Gilman, Phys. Rev. D **39**, 2639 (1989) and references therein.

[10]. Particle Data Group, G. P. Yost et al., Phys. Lett. **204 B**, 1 (1988).

[11]. J. R. Patterson et al., Phys. Rev. Lett. **64**, 1491 (1990).

[12]. H. Burkhardt et al., Phys. Lett. **206 B**, 169 (1988).

[13]. X. He, B. McKellar, and N. Tupper, Univ. of Melbourne Preprint UM-P 88/40.

[14]. G. Ecker, A. Pich and E. De Rafael, Phys. Lett. **189 B**, 363 (1987).

[15]. L. Cappiello and G. D' Ambrosio, IL Nuovo Cimento **99 A**, 155 (1988).

[16]. J. Gasser and H. Leutwyler, Annals of Phys. **158**, 142 (1983).

[17]. J. Gasser and H. Leutwyler, Nucl. Phys. **250 B**, 465 (1985).

[18]. C. Bernard et al., Phys. Rev. D **32**, 2343 (1985).

[19]. A. Pich, CERN-TH. 5194/88.

[20]. P. Ko and J. L. Rosner, Phys. Rev. D **40**, 3775 (1989).

[21]. T. Morozumi and H. Iwasaki, KEK report KEK-TH 206, KEK-Preprint 88-4, April 1988 (unpublished).

[22]. T. Morozumi and H. Iwasaki, Proceedings of the Second Meeting on Physics at TeV Energy Scale, May 1988.

[23]. T. Truong, EFI 89-57.

[24]. L. M. Sehgal, Phys. Rev. D **41**, 161 (1990).

[25]. P. Ko, Phys. Rev. D **41**, 1531 (1990).

[26]. G. Ecker, A. Pich and E. De Rafael, UWThPh-1989-65, FTUV /89-44.

[27]. V. Papadimitriou et al., Phys. Rev. Lett. **63**, 28 (1989).

[28]. G. D. Barr et al., Phys. Lett. B 242, 523 (1990).

[29]. J. R. Patterson, Ph.D. Thesis (University of Chicago, December, 1990).

[30]. H. Sanders, V. Papadimitriou, J. Ting, Y. W. Wah, E. Weatherhead, *IEEE* Trans. Nucl. Sci. **36**, 358 (1988).

[31]. M. Asner, V. Papadimitriou, H. Sanders, J. Ting, Y. W. Wah, E. Weatherhead, *NIM* A291, 577 (1990).

[32]. A+PLUS, Altera Corporation, Santa Clara, CA 95051.

[33]. M. Karlsson, et al., Phys. Rev. Lett. **64**, 2976 (1990).

[34]. Fermilab Proposal E-773; Spokesman: G.D.Gollin.

[35]. Fermilab Proposal E-799; Spokesmen: Y. Wah and T. Yamanaka.

[36]. A.J. Malensek, et al. (FNAL report FN-341, Oct. 1981).

[37]. H.W. Atherton, et al. (CERN report 80-07, 1980).

[38]. W. Heitler, *The Quantum Theory of Radiation* (Clarendon Press, Oxford, Eng., 1954).